UNIVERSIDAD DE CANTABRIA

PROGRAMA DE DOCTORADO EN
Ciencia y Tecnología

TESIS DOCTORAL

PRODUCCIÓN DE DOS BOSONES W^+W^- EN COLISIONES PROTÓN-PROTÓN A UNA ENERGÍA DE CENTRO DE MASAS DE $\sqrt{s} = 13$ TeV CON EL DETECTOR CMS DEL LHC

PH.D. THESIS

W^+W^- BOSON PAIR PRODUCTION IN PROTON-PROTON COLLISIONS AT CENTER-OF-MASS ENERGY OF $\sqrt{s} = 13$ TeV WITH THE CMS DETECTOR AT THE LHC

Realizada por:
Pedro José Fernández Manteca

Dirigida por:
Dra. Alicia Calderón Tazón
Dra. Rocío Vilar Cortabitarte

Santander, 2021

To my supervisors, Alicia and Rocío. Thank you for your effort, commitment, scientific enthusiasm, and for the huge number of hours invested in my learning. It has been a great honor to be your student.

To the University of Cantabria for the funding, and to the CMS Collaboration at CERN (in a broad sense), for the scientific support during the last four years.

This thesis would not have been possible without all of you.

Abstract

A measurement of the W^+W^-boson pair production cross section in proton-proton collisions at a center-of-mass energy of 13 TeV is presented. The data used in this study are collected with the CMS detector at the LHC, corresponding to an integrated luminosity of 35.9 fb^{-1}. The W^+W^-candidate events are selected by requiring two oppositely charged leptons. The total W^+W^-production cross section measurement has been 117.6 ± 6.8 pb, which agrees well with the theoretical prediction. Fiducial cross sections and differential cross sections are also reported, which also agree well with the theoretical prediction. Finally, constraints on the dimension-6 operators in the context of an effective field theory are derived. This analysis provides some of the strongest constraints compared with previous results.

A search for dark matter in proton-proton collisions at a center-of-mass energy of 13 TeV is performed using events with a W^+W^-boson pair and large missing transverse momentum. The data used in this study are collected with the CMS detector at the LHC, corresponding to an integrated luminosity of 137 fb^{-1}. The W^+W^-candidate events are selected by requiring two oppositely charged leptons. No significant excess over the expected standard model prediction is observed. Limits are set on dark matter production in the context of the dark Higgs simplified model, with a dark Higgs mass above the W^+W^-pair mass threshold. The results presented correspond to the first measurement carried out in the CMS experiment using this novel interpretation.

Deep learning techniques are applied to estimate the transverse momentum of highly energetic muons in the CMS detector. The main goal of these studies is to improve the results of the current procedure, and if so, consider including these types of methodologies in the future data taking of the experiment. The preliminary results obtained, based on simulation, show an improvement of about 25% in the resolution of the transverse momentum for muons with $1500 \leq p_T \leq 2500$ GeV and $|\eta| < 0.9$.

Key words: LHC, CMS experiment, W^+W^-boson pair, cross section measurement, dark matter, dark Higgs, deep learning, highly energetic muons.

Contents

1 Introduction

Particle physics is a branch of physics which studies the fundamental particles that constitute the universe. The most complete theoretical framework that explains the features of these fundamental particles is the Standard Model (SM) [1]. The SM of particle physics is a relativistic theory of quantum fields developed in the early 70's in its current formulation, including information from many theories and discoveries done since 1930. It is based on the symmetries that describes the structure of matter considering elementary particles, shown in Figure 1, as irreducible entities whose kinematics are driven by the three fundamental interactions: the electromagnetic, weak, and strong interactions. The fourth fundamental interaction, the gravity, is driven by the general theory of relativity, but until now it has not been accommodated within the mathematical formulation of the SM.

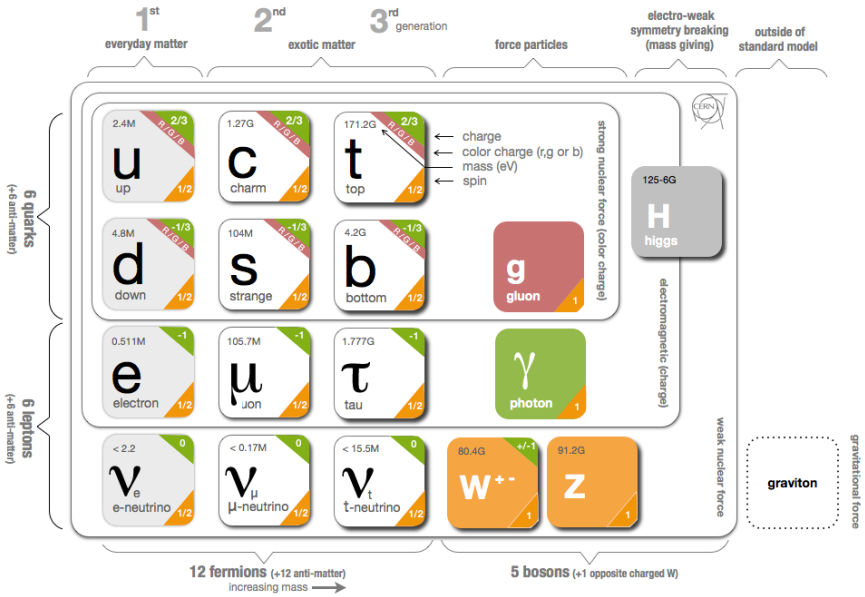

Figure 1: Table showing the SM fundamental particles and their properties. Image taken from [2].

The elementary particles of the SM can be split into fermions and bosons.

- Fermions have spin 1/2 and are divided into leptons and quarks, each of them are split into three generations with different masses, and for each fermion there is an equivalent anti-fermion, with same mass and spin, and opposite charge. Leptons interact only through the electromagnetism and the weak forces, and each generation contains a charged lepton with charge -1, and an electrically neutral neutrino. Quarks also interacts through the strong force, and are observed in bounded states in hadrons, such as

mesons (bounded quark-antiquark particles) and baryons (bounded quark-quark-quark or antiquark-antiquark-antiquark particles). Each generation of quarks contains a quark with charge +2/3 and a quark with charge -1/3. First generation of fermions (electrons, quarks *up* and *down*) constitute the ordinary matter of the universe.

- The mediators of the fundamental interactions are bosons with spin 1. Photons are the mediator particles of the electromagnetic force, and couple to charged particles. Gluons are the mediator particles of the strong force, and couple to quarks and among themselves. $W^{\pm}$ and Z are the mediator particles of the weak force, couple with leptons, quarks, and among themselves, and are the only mediator bosons that are massive. Finally, the Higgs boson has spin 0, it is electrically neutral, massive, and was introduced in the SM to be able to explain the origin of the mass of the fermions and the weak bosons [3, 4].

Up to now, the SM has shown huge successes in providing predictions for the three forces described by it, which have been experimentally contrasted. However, the SM falls short of being a complete theory of fundamental interactions due to several unresolved issues, such as the existence of Dark Matter (DM), the hierarchy problem [5], or the matter-antimatter asymmetry [6].

There are strong experimental evidences for the existence of DM [7], all of them through its gravitational interaction. The first evidence was pointed out by Zwicky in 1933 [8], where he introduced the concept of *dunkle Materie* to be able to fit the orbital speeds of galaxies in clusters. Later, Vera Rubin [9] studied the rotation curves of spiral galaxies in the 70's. She measured the radial velocity of the different components of the spiral galaxies with a precise spectrograph as function of the distance to the galaxies' center. Since the matter density drops with the distance to the center, one would expect that the radial velocity of the visible matter would progressively drop when the distance increases. However, she observed flatness for long distances, indicating that there must be a significant amount of invisible matter, gravitationally bound to the galaxies, to be able to explain the observed rotation curves distribution.

Other evidences come from gravitational lensing [10] that allows to obtain position and density information taking the deviation of light when attracted by matter, and in particular, the study of the Bullet Cluster [11] played an important role. The Bullet Cluster (1E 0657-56) consists of two colliding clusters of galaxies, where the kinematic behavior of the main components of the joined cluster (stars, gas and DM) can be studied separately during the collision. The gravitational lensing of background objects showed that the DM is concentrated in two separated regions from the gas, where the gas components (ordinary baryonic matter) interact electromagnetically, and then they are slowed down and mostly concentrated in the center of the collision. This fact indicated that the DM is able to

pass through the gas regions without interacting electromagnetically, and it seems to only interact through gravity.

The existence of DM leaves a characteristic imprint on the Cosmic Microwave Background (CMB) observations, as it clumps into dense regions and contributes to the gravitational collapse of matter, but is unaffected by the pressure from photons. The oscillations in the CMB can be predicted with and without DM, which is presented in the form of a power spectrum. The power spectrum of the CMB shows us the strength of oscillations at different sizes of the photons and matter, and its observed spectrum agrees with the existence of DM. Latest results from the Plank mission [12], provide a precise measurement for the DM density ($\Omega_c h^2 = 0.120 \pm 0.001$), and with this experimental result, we know that the ordinary matter represents only a 5% of the total mass of the universe. In summary, DM has been experimentally shown to exist, to be neutral, non-baryonic, stable (at least during the age of the universe), it does not interact with the electromagnetic force, and its existence has only inferred from the gravitational effect.

For many years, it was thought that neutrinos could explain DM. However, neutrinos follow the Fermi-Dirac distribution, which imposes a maximum space density that is in some cases inconsistent with the observed DM mass of several galaxies [13]. Thus, it is required to look for other candidates beyond the SM.

One of the most extended DM candidates, among others, are stable weakly interactive massive particles (WIMPs or χ) [14], assuming that DM can interact weakly. Their presence is mainly motivated by the measured DM relic abundance within the DM *freeze out* interpretation [15]: DM, at the early stages of the universe, was expected to be in thermal equilibrium (balance between production and annihilation). The universe expanded and got colder progressively, until a certain state is reached where the probability of both production and annihilation was very low. The population then came out of equilibrium and froze (*freeze out*), and the remaining density is the relic abundance that we see today. To match the observed DM relic density, WIMPs must have a mass in the GeV-TeV mass range, which can currently be produced at high-energy colliders. Thus, although WIMPs have not been observed yet, they are target of many of the current searches for DM at colliders.

Several Beyond the Standard Model (BSM) interpretations for DM with WIMPs have been postulated by theoretical physicists. In addition, the hypothesis that DM is part of a hidden sector, so-called the *dark sector*, with several new types of dark particles, has taken strength in the last few years. In that sense, the postulated dark particles would not couple to SM fields, but would be able to interact with SM particles through a mediator that would provide a portal to the DM candidates or even be the candidates.

Simplified models[1] are commonly used for DM searches at the Large Hadron Collider (LHC), which is the largest and highest energy particle accelerator in existence, to model generic processes yielding to simple signatures in the detector. This scenario gives rise to a potential signature at the LHC collider where one SM particle, 'X', is produced and detected, and it recoils against an substantially large energy imbalance associated with the non-interacting DM particles. Recent searches at the LHC consider 'X' to be a hadronic jet [17, 18], a heavy-flavor jet [19, 20], a photon [21, 22] or a W/Z boson [23, 24, 18, 25]. On the other hand, the discovery of the Higgs boson [26, 27] opened a production channel for DM; DM particles production in association with a Higgs boson, denoted as *mono-Higgs*. Since any new particle that has mass should in some way couple to the Higgs boson, the Higgs boson could be a generic portal to new physics, not just to DM. Several *mono-Higgs* searches have been already carried out at the LHC in the different Higgs decay channels. The most recent published search includes the combination of $b\bar{b}$, WW, $\gamma\gamma$, $\tau\tau$ and ZZ [28] decay modes, but so far no hints of new physics have been found in the sensitive phase space.

The LHC was originally built for testing the predictions from the SM, and in particular to search for the Higgs boson using proton-proton collisions. Once the Higgs boson was discovered in 2012, a new LHC era took place from 2016 to 2018, so-called *LHC Run 2*. During that time, the LHC operated a center of mass energy ($\sqrt{s}$) of 13 TeV, corresponding to the largest energy ever reached in a collider. With this energy, two kind of measurements can be performed:

- Precision measurements of SM processes.
- Searches for deviations from SM predictions to test BSM interpretations.

The main objective of this thesis is to perform both precision measurements and searches for deviations from SM predictions. For these purposes, the production of processes involving at least a W^+W^-boson pair at the LHC are studied. Data collected in the *LHC Run 2* by the Compact Muon Solenoid (CMS) experiment will be analyzed.

The cross section of the W^+W^-diboson pair production is measured, for which the full 2016 CMS data set is used, corresponding to a total integrated luminosity[2] of 35.9 fb^{-1}. The most precise theoretical prediction from the SM at $\sqrt{s} = 13$ TeV for the W^+W^-production cross section is $\sigma_{theo} = 118.8 \pm 3.6$ pb [29]. It is important to mention that the study of the production of two opposite charged W bosons at the LHC is important to test the SM electroweak sector at $\sqrt{s} = 13$ TeV, given that the vector boson pair production is one of the most

[1]Models based on a minimal amount of new particles and operators constrained by the requirement of renormalizability which are used to generate the desired phenomenology [16].

[2]Number of particles per unit area and per unit time in a beam. It is measured in inverse barn unit.

important electroweak processes, and in particular the W^+W^-production due to its larger cross section compared to the WZ and ZZ production. Its understanding is also relevant because it represents one of the most dominant backgrounds in BSM searches involving a W^+W^-pair in the final state, and in SM precision measurements of the Higgs boson properties. Furthermore, any deviation in the electroweak SM predictions may be an indication of a BSM effect, such as the presence of anomalous triple gauge boson couplings (aTGCs) [30], or other BSM interpretations.

A previous measurement of the W^+W^-production cross section with CMS data was already published at $\sqrt{s} = 13$ TeV [31], using an integrated luminosity of 2.3 fb^{-1}, with a result of $\sigma_{W^+W^-} = 115.3 \pm 5.8$ (stat) $\pm$ 5.7 (syst) $\pm$ 3.6 (lumi) pb. Another measurement at $\sqrt{s} = 8$ TeV (during the so-called *LHC Run 1*), with an integrated luminosity of 19.4 fb^{-1} [32], provided a measured value of $\sigma_{W^+W^-} = 60.1 \pm 0.9$ (stat) $\pm$ 3.2 (syst) $\pm$ 1.6 (lumi) pb. Both measurements agree with the theory prediction [29] within the uncertainties. In this work, 2016 CMS data is analyzed, corresponding to a total integrated luminosity of 35.9 fb^{-1}. The latest and most precise detector calibrations and corrections, and about 15 times more luminosity than in the previous measurement at $\sqrt{s} = 13$ TeV will be used. In addition, events with same-flavour leptons are analyzed for the first time in this analysis during the *LHC Run 2*. With these conditions, the experimental precision of that result is expected to be improved. Moreover, the increased luminosity allows to precisely measure fiducial and differential cross sections as function of several kinematic quantities. Finally, a search for aTGCs that could potentially affect the W^+W^-production is performed, where limits on the corresponding coupling constants are set.

Regarding the search for DM, the so-called the *dark Higgs* simplified model [33] proposed by the ATLAS/CMS Dark Matter Forum [34] is used for interpreting the experimental results. This model provides a new signature of DM production at the LHC resulting from the emission of a dark Higgs boson, s, that mixes with the SM Higgs boson and would provide mass to the DM particles via a Higgs mechanism. Also, if the dark Higgs boson decays into SM states via a small mixing with the SM Higgs boson, then it is feasible to perform searches at high-energy colliders, such as at the LHC. Furthermore, since s can be lighter than the DM particle, it would be possible to relax constraints from the DM relic abundance by introducing a new annihilation channel $\chi\,\chi \to s\,s$, with the subsequent decay of s into SM particles. Assuming that s couples also to other SM particles, similar final states than in the *mono-Higgs* case can be obtained, including for instance a W^+W^-pair.

Using the same W^+W^-final state, a search for DM is performed, for which the previously studied SM W^+W^-process corresponds to one of the dominant backgrounds. In this search, the total data collected by the CMS detector during

the *LHC Run 2* is used in order to squeeze the whole amount of available data, corresponding to a total integrated luminosity of 137 fb^{-1}. The results presented correspond to the first measurement carried out in the CMS experiment using this novel interpretation.

This work focuses on the leptonic decay of the W bosons. Therefore, the characteristic signature of the selected CMS data events will consist of two very energetic leptons with opposite charge, and an energy imbalance. This energy imbalance is due to the presence of neutrinos, which do not interact with the detector in case of the SM W^+W^-production, or due to the presence of neutrinos and DM particles in case of the dark Higgs search.

Moreover, the identification of the physics objects that intervene in the final state signature has been improved by applying several techniques. For instance, studies on supervised deep learning techniques for the transverse momentum assignment of highly energetic muons are performed. The aim of these studies is to improve the resolution and muon p_T assignment with respect to the current CMS assignment procedure. This methodology will be potentially useful for most of the BSM searches at the LHC with boosted topologies including muons in the final state during the next *LHC Run 3* run, that will start in 2022.

This thesis is divided into the following sections. In section 2, the used experimental device will be shown: the CMS detector, including a description of its subdetectors, the CMS event reconstruction procedure, and the triggering system used for the data taking. A description of the used data and simulated samples for background and signal processes will be presented in section 3. In Section 4, the chosen definitions for the physics objects will be shown. The followed strategy for the signal extraction will be presented in Section 5. In Sections 7 and 8, the performed data analyses will be detailed, including discussions on the obtained results. In Section 9 the studies for the muon high momentum assignment with machine learning techniques will be shown. Finally, the conclusions of the performed work will be given in Section 10.

2 The CMS experiment

The CMS detector, represented schematically in Figure 2, is located at one of the points of the LHC accelerator where the proton beams collide. It is composed, from the innermost region to the outermost, by a tracker of silicon pixels and strips for the detection of charged particles with high spatial resolution, an electromagnetic tungstate crystal calorimeter (ECAL) for the measurement of electrons and photons, a hadronic calorimeter made up of dense and absorbent material (HCAL) specialized in the measurement of hadrons, and muon chambers that placed at the outermost part of the detector. Between the HCAL and the muon chambers there is a superconducting magnet that reaches a magnetic field of 3.8 T, enough to bend high energetic charged particles to be able to measure their momentum accurately.

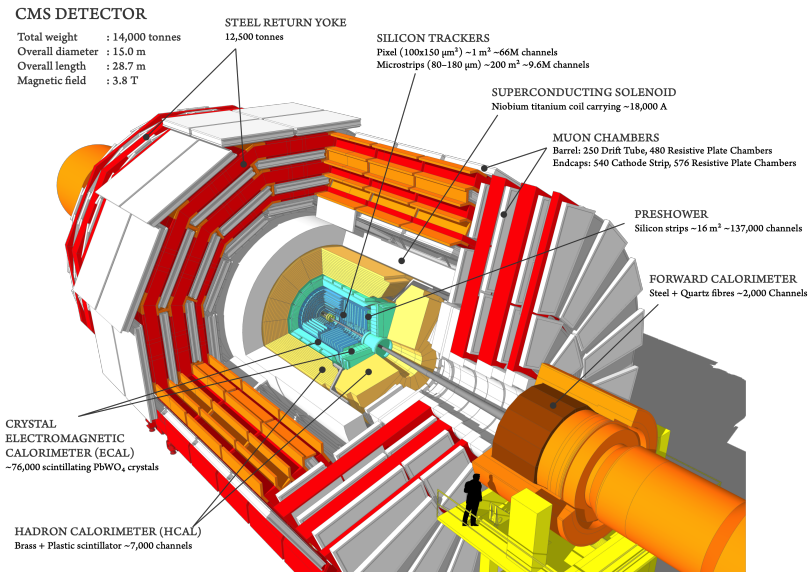

Figure 2: Graphical representation of the different parts of the CMS detector. Image taken from [35].

Regarding its geometry, the coordinate system has its origin at the collision point, with the y-axis pointing vertically upwards, the x-axis radially from the origin, and the z-axis in the direction of the beams. The azimuth angle ϕ is measured from the x-axis in the x-y plane transverse to the beam, while the polar angle θ is measured from the z-axis in the x-z plane. Another important angular variable that will be used in this work is the pseudorapidity η, since differences in η are invariant under Lorentz transformations on the z-axis for high momentum particles. It is defined as a function of the polar angle as:

$$\eta = -\ln\left(\tan\frac{\theta}{2}\right) \tag{1}$$

Other variables defined in the plane transverse to the direction of the particle beam are usually used, such as the transverse momentum p_T, as there is no initial momentum in the transverse plane, so the transverse momentum of the final state particles must cancel one another out due to the law of conservation of momentum.

The following subsections briefly describe the features of the different CMS subdetectors.

2.1 Subdetectors

2.1.1 Tracker

The tracker system [36] aims to reconstruct the interaction vertices and the tracks of the charged particles. It is placed in the innermost part of the CMS and is made of silicon devices: The Silicon Pixel Detector (SPD) is located at the core of the subdetector and therefore receives the highest particle fluence, and the Silicon Strip Detector (SSD), which is made of silicon strips that surround the layers of pixels (see Figure 3).

As the particles travel through the tracker, the pixels and strips produce small electrical signals that are amplified and detected. The tracker has a total of 75 million electronic channels, giving rise to about 6000 connections per square centimeter that allow to measure the trajectories of the charged particles with an accuracy of about 10 μm, reaching a momentum resolution of 0.9% (6%) for $p_T = 10$ GeV tracks, and 2% (15%) for $p_T = 100$ GeV for isolated muons (electrons) in the barrel region $|\eta| < 0.9$ [37].

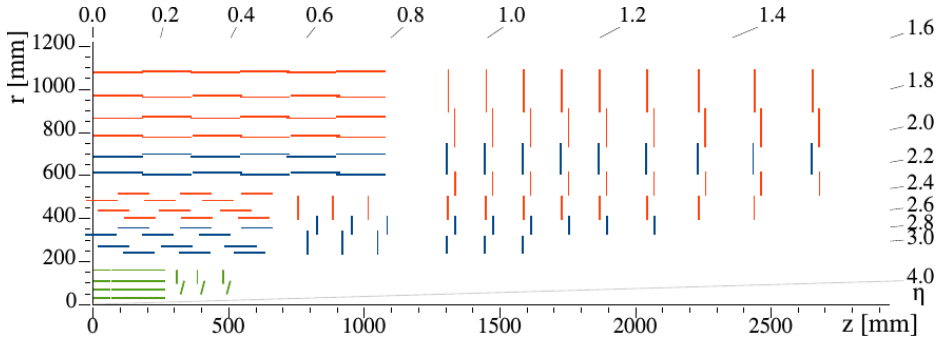

Figure 3: Quadrant of the CMS tracker in the r-z plane, where r refers to the radial distance in the x-y plane. The pixel detector is displayed in green, while the single-sided and double-sided strip modules are displayed as red and blue segments respectively. Image taken from [38].

It is worth to mention that the original pixel detector layout [39], used in the 2016 data taking, was replaced for 2017/2018 [40] to maintain good performance under the high luminosity and pileup conditions.

2.1.2 Electromagnetic Calorimeter (ECAL)

The ECAL [41] is made of scintillating lead tungstate crystals. Due to its high-density, this subdetector is able to catch electrons and photons that pass through it, providing a very fast response in form of light. The scintillation light is converted into electrical signal and then it is amplified in order to get the energies of the emerging particles with high resolution.

The ECAL layer is placed between the tracker and the HCAL as shown in Figure 2. It is formed by a cylindrical barrel with 61200 crystals located in 36 modules, and two endcaps made up about 15000 crystals that seal the barrel at its boarders.

Calibrations and corrections are carefully measured using electrons from W and Z boson decays and photons from π^0 decays. Those corrections allow to achieve an excellent energy resolution along all the ECAL regions: about 2% in the barrel region, and about 4% in the endcaps for electrons in Z decays [42].

2.1.3 Hadron Calorimeter (HCAL)

The HCAL [43] is made of layers of brass (dense absorber) and scintillators. When a hadronic particle interacts with a brass absorber, a cascade of particles is produced, and the emerging particles activate the scintillation material, producing light that is converted and amplified into fast electronic signals by photodetectors, that translate the light into energy.

The HCAL layer is placed between the ECAL and the muon system as shown in Figure 2. It is formed by a cylindrical barrel with 36 parts of 26 tonnes each, 36 endcap wedges, and two hadronic forward calorimeters that are placed out of the CMS cylinder, aiming to catch particles from the collision region at small angles relative to the beam pipe.

The HCAL has maintained a good energy resolution during the *CMS Run 2* data taking, archiving a energy resolution measured in pions of about 20% for a pion energy of 20 GeV, and below 15% for pions with energy greater than 60 GeV [44].

2.1.4 Muon system

The muon system has three parts: the Drift Tubes (DTs), the Catode Strip Chambers (CSCs), and the Resistive Plate Chambers (RPCs).

The Drift Tubes [45] cover the CMS barrel ($|\eta| < 1.2$) on the outermost part of the detector. Each tube is made up of a positively charged collector wire and is filled with gas, so that a charged particle extracts electrons from the gas atoms while it passes through the tube, and these electrons are electrically attracted and collected by the collector wire. In this way, the coordinates of the muon through the tube are obtained from the position of the wire where the electrons impact, and from the distance from the muon to the wire (which is calculated by multiplying the drift speed of the electron in the tube by the travel time to it).

In Figure 4, the spatial position of the different DT chambers are graphically represented, denoted as MBZ/N/S, where Z = -2 ... + 2 corresponds to the wheel number along the z axis, N = 1 ... 4 refers to the concentric station number in the xy plane, and S = 1 ... 12 to the circular sector number.

The whole subdetector consists of 250 chambers, each of them with an average dimensions of 2 x 2.5 m. The chambers of the first three innermost stations are composed of three layers with about 60 tubes per layer, so that one of them measures signals in the r-z plane and the other two in the r - ϕ plane (where r refers to the radial distance in the x-y plane). The last station consists only of two layers of tubes oriented in the r - ϕ plane, so the z coordinate is not measured at this outermost station.

The Cathode Strip Chambers [46] are located on the CMS endcaps ($0.9 < |\eta| < 2.4$), and their operation is similar to that of the DTs. In this case, there are positively charged wires (anodes) crossed with negatively charged copper strips (cathodes) within a gas volume. When the muons pass through the chamber, they extract electrons out of the gas atoms, producing an avalanche of electrons that go to the anode wires, while the positive ions move away from the wire and go to the copper cathode, which also induces a charging pulse in the strips (in a direction perpendicular to the anode). Because the strips and wires are perpendicular, two position coordinates are obtained for each particle that passes through the chamber.

The CSC subdetector contains 540 chambers in total, and is made of rings of trapezoidal cameras up to 3.4 m long and 1.5 m wide (placed on eight disks, four on each endcap). The CSCs cameras are spatially denoted as ME$\pm$S/R, where the sign indicates which CMS endcap, S = 1 ... 4 refers to the station number (parallel on the z axis), and R corresponds to the ring number, concentric in the x-y plane. Figure 5 shows a real image of the ME-1 wheel, with its three concentric rings in the x-y plane.

Each of the DTs and CSCs chambers is made up of several layers, and the signals or impacts left by the muons in their path are reconstructed in each of them. From these impacts, small straight traces, so-called segments, are built by joining the

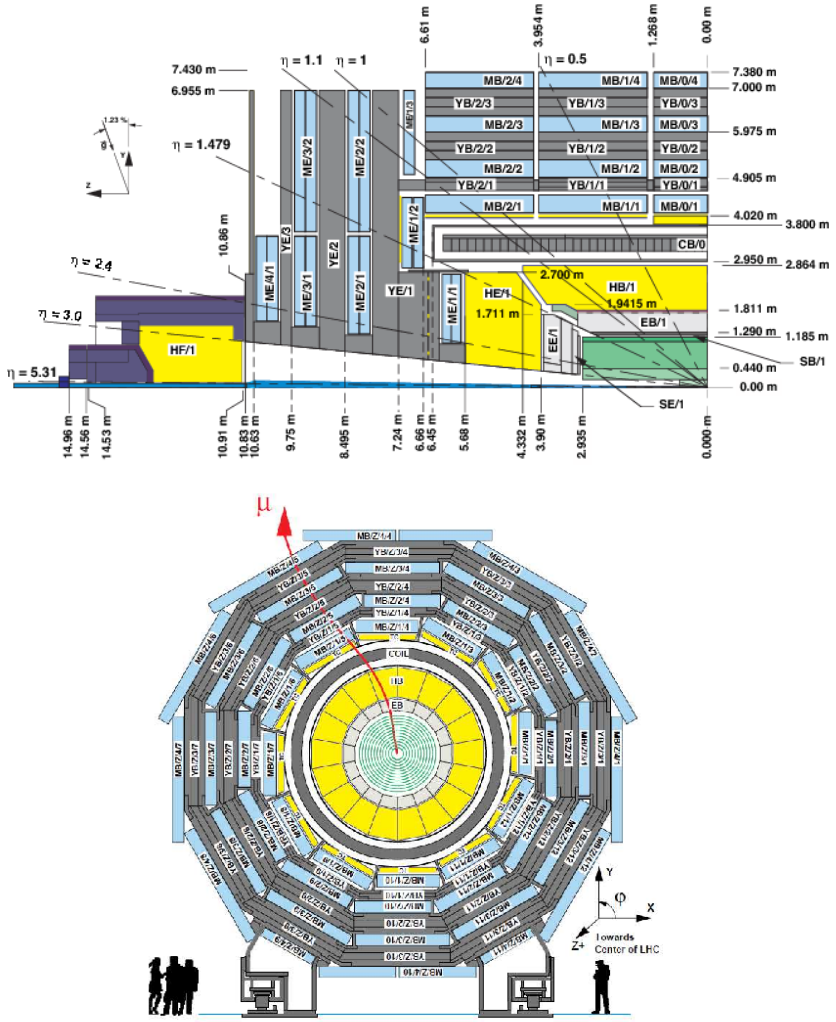

Figure 4: Schematic view of the CMS detector. Above: longitudinal view of a quarter of the detector. Bottom: cross-sectional view at $z = 0$. Both figures have been taken from [45].

signals found in the different layers within each DT or CSC chamber. These segments are formed by the position and direction both in the transverse plane and in the longitudinal coordinate, except for the outermost DTs chamber (station 4), in which longitudinal information is not available. In this way, the segments left by the muons as they pass through the different chambers will be used for the *Run 3* studies as will be detailed in Section 9.

The Resistive Plate Chambers [48] are gas detectors, placed both on the CMS barrel and on the endcaps, whose fast response is exploited mainly for the trig-

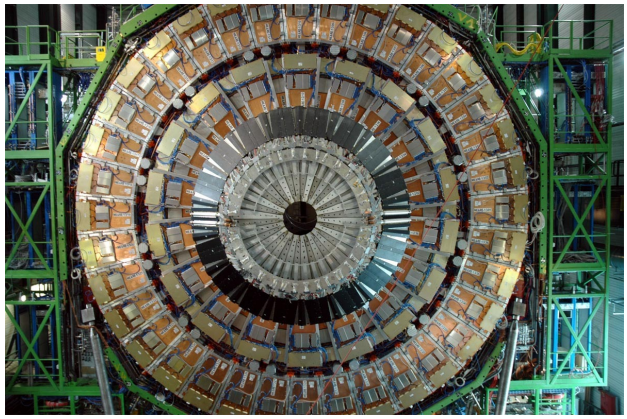

Figure 5: Photo of the ME-1 station. Image taken from [47].

ger. RPCs consist of 1056 plates (two parallel each) separated by a gas volume. When a muon goes through a RPC chamber, the gas atoms are ionized, and the extracted electrons hit other atoms producing an avalanche of electrons that are collected by external metallic strips (hits). The pattern of collected hits provides a quick measure of the muon momentum, which is used by the trigger to make quick decisions about whether to keep the data or not.

The *global* muon track (tracker track plus muon system track) allows to improve the muon momentum resolution by 25% for muons with $p_T > 200$ GeV compared to the tracker track only resolution [49].

2.2 Event reconstruction

As they pass through the detector, the particles generate electrical signals in the millions of channels of the CMS subdetectors. The reconstructed particles from these signals, using dedicated software, are called physics objects.

The first objective of the reconstruction process of physical objects is to transform these signals into relevant physical information, such as energy, momentum or direction. Subsequently, the information of the produced particles in the collision is collected by the CMS subdetectors, and combined by the Particle Flow algorithm (PF) [50]. In this way it is possible to identify and rebuild each physics object individually. Figure 6 illustrates the characteristic signatures left in the different layers of the detector by some of the particles that will be used in this work: muons, electrons, and hadrons, whose features are detailed in Section 4. For reconstructing the different physics objects, the PF algorithm uses the following logic:

- Muons: Muons are reconstructed and identified by joining the information of the hits that they leave in the muon chambers (the four outermost layers

in Figure 2) and the hits they leave in the silicon layers close to the interaction point. The PF track reconstruction is done independently in the tracker (tracker tracks) and in the muon system (standalone tracks) by fitting the found hits with a Kalman filter [51]. The Kalman filter is a technique that allows obtaining the parameters associated with a trajectory from a series of points belonging to that trajectory which are provided sequentially, producing a new estimation of fit parameters dynamically as more information is added to the algorithm. Then, two different reconstruction procedures are performed: for *global* muons, the standalone tracks are matched to tracker tracks (outside-in) and a combined fit of the tracker and muon system hits is performed with the Kalman filter. This approach reduce the misidentification rate, and improve the p_T resolution for high p_T muons. On the other hand, for *tracker* muons, the tracker tracks are propagated to the muon system (inside-out) by matching them with locally reconstructed CSC/DT segments, aiming to improve the reconstruction efficiency for low-p_T muons.

- Electrons: The electrons are reconstructed and identified from the energy they deposit in the ECAL and the track they leave on the tracker. On the ECAL, the PF reconstruction aims to identify individual particles from the reconstructed energy deposits in the $\eta - \phi$ plane by a clustering technique that looks for local maximums. Since electrons usually arrive to the ECAL accompanied by multiple secondary particles, contiguous crystals are combined into *SuperClusters* if their energy deposit is above a certain threshold. On the tracker, Gaussian Sum Filter (GSF) technique [52] is used to reconstruct the electron track from the tracker hits by accounting for changes in the curvature due to radiative energy loss by Bremsstrahlung. This technique also allows to associate Bremsstrahlung radiation and photon conversion tracks to the *SuperCluster* (refined *SuperCluster*). Finally, the refined *SuperClusters* and the tracker track are matched.

- Photons: Since photons are neutral particles, they do not leave hits on the tracker nor are bent by the magnetic field. Thus, PF reconstruction relies only on the energy deposits on the ECAL following the same clustering procedure as for electrons.

- Jets: jets are bundles of particles collimated in a certain direction, which come from the fragmentation of quarks and gluons (so-called hadronization [53]). The reconstruction of these objects is done using the recursive *anti-k_T* algorithm [54], which sequentially takes into account the distance between the different pairs of particles, and the distance between each individual particle with respect to the direction of the candidate jet. The *anti-k_T* algorithm provides a set of reconstructed jets in the event, and their corresponding energy is measured by the calorimeters.

- Missing Transverse Energy: The Missing Transverse Energy (MET, E_T^{miss}, or p_T^{miss}) is built by applying the principle of conservation of momentum in the

transverse plane, which must be fulfilled in each collision: the momentum before and after the collision is zero in the transverse direction to the beam pipe. This quantity is mainly associated with neutrinos as they pass through the detector with little interaction. On the other hand, it is a common key variable in searched for new physics, such as the dark Higgs, since the interaction of the WIMPs with the detector is also expected to be null.

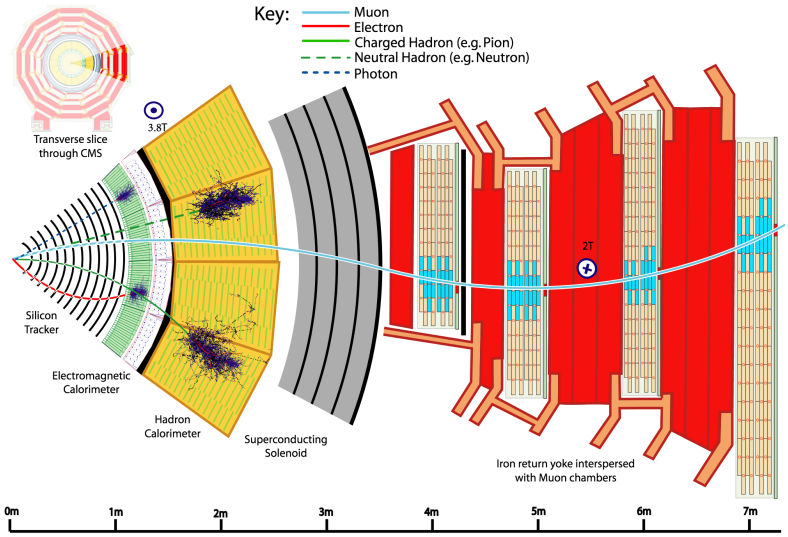

Figure 6: Reconstruction of some types of particles with the CMS subdetectors. Image taken from [50].

The reconstruction is carried out during the data processing, and for each type of analysis the most appropriate criteria for identification and isolation of physics objects are chosen.

2.3 Trigger

It should be noted that the large amount of data produced by the accelerator makes its full storage unviable. However, not all the collisions are of physical interest in this type of experiment, and storing them would therefore not be useful. In this way, CMS has an integrated intelligent data acquisition system called trigger that decides which data is stored and which is discarded.

The CMS trigger is formed by the Level 1 Trigger [55], that reduces the initial rate of 40 MHz to 100 kHz, and the High Level Trigger (HLT) [56] that keeps about 1 kHz for the usual physics analyses.

The Level 1 Trigger is implemented in hardware by dedicated electronics that take a summary information from the calorimeters and from the muon detectors,

so called *trigger primitives*, to decide in a few μs if an event must be accepted or rejected.

Events that pass the Level 1 filters go to the HLT trigger, that combines information from the different parts of the detector to build high-level variables, such as the p_T, the isolation, or the invariant mass of a single or a set of physics objects. These quantities are used as filters to reduce the data rate. The HLT trigger is split into different *paths*, and each *HLT path* targets different objects and consequently different physics processes. Thus, a certain *HLT path* may select events with two electrons, with high E_T^{miss}, or with one high p_T muon.

The *HLT paths* can be un-prescaled, meaning that all the events passing the specific requirements are stored, while others with higher rate are pre-scaled, meaning that only one passing event is stored every certain number of events. Pre-scaled *paths* are usually used for instance for performing specific subdetector studies, for inspecting certain kinematic regions (see Section 7.4.1), or for performing B-physics and QCD analyses. The events passing the HLT criteria, define the data sets that are used in the physics analyses.

3 Data and simulated samples

This section describes the data and the simulated samples used in this work.

3.1 Data

A sample of proton-proton collisions collected in 2016, 2017, and 2018, with the CMS experiment at the LHC at $\sqrt{s} = 13$ TeV is used, corresponding to an integrated luminosity of 36.3, 41.5, and 59.8 fb^{-1}, respectively [57, 58, 59]. The mean pileup (PU) measured for these data periods, defined as the mean number of interactions per bunch crossing, has been 23, 32, and 32 respectively. Only certified data that passed the quality criteria by all the detector subsystems is used.

Events are stored in disk if the selection criteria of HLT triggers are satisfied. The used *HLT paths* in this work, denoted as *MuEG*, *DoubleMuon*, *DoubleElectron*, *SingleMuon*, and *SingleElectron*, require one or two leptons (electrons or muons) with a minimum p_T threshold, and are used together to ensure a very high trigger efficiency.

The lowest p_T thresholds for the double-lepton triggers are 23 GeV for the leading lepton and 12 GeV for the trailing lepton. The single-lepton triggers in 2016 have p_T thresholds of 25 GeV for $|\eta| < 2.1$ and 27 GeV for $2.1 < |\eta| < 2.5$ for electrons, and of 24 GeV for muons. In 2017, the corresponding thresholds are increased to 35 and 27 GeV, while in 2018 they are 32 and 24 GeV. The overall trigger efficiency is about 98%, measured using Z+jets events. The names of the used *HLT paths* are listed in Tables 1-3.

Data Set	Run range	HLT path
MuonEG	B-F	HLT_Mu8_TrkIsoVVL_Ele23_CaloIdL_TrackIdL_IsoVL HLT_Mu23_TrkIsoVVL_Ele12_CaloIdL_TrackIdL_IsoVL
	F-H	HLT_Mu12_TrkIsoVVL_Ele23_CaloIdL_TrackIdL_IsoVL_DZ HLT_Mu23_TrkIsoVVL_Ele12_CaloIdL_TrackIdL_IsoVL_DZ
SingleMuon	B-H	HLT_IsoMu24 HLT_IsoTkMu24
SingleElectron	B-H	HLT_Ele27_WPTight_Gsf HLT_Ele25_eta2p1_WPTight_Gsf
DoubleMuon	B-G	HLT_Mu17_TrkIsoVVL_Mu8_TrkIsoVVL HLT_Mu17_TrkIsoVVL_TkMu8_TrkIsoVVL
	H	HLT_Mu17_TrkIsoVVL_Mu8_TrkIsoVVL_DZ HLT_Mu17_TrkIsoVVL_TkMu8_TrkIsoVVL_DZ
DoubleEG	B-H	HLT_Ele23_Ele12_CaloIdL_TrackIdL_IsoVL_DZ

Table 1: 2016 HLT un-prescaled paths used in this work.

Data set	Run range	HLT path
MuonEG	B	HLT_Mu23_TrkIsoVVL_Ele12_CaloIdL_TrackIdL_IsoVL_DZ
		HLT_Mu12_TrkIsoVVL_Ele23_CaloIdL_TrackIdL_IsoVL_DZ
	C-F	HLT_Mu23_TrkIsoVVL_Ele12_CaloIdL_TrackIdL_IsoVL
		HLT_Mu12_TrkIsoVVL_Ele23_CaloIdL_TrackIdL_IsoVL_DZ
SingleMuon	B-F	HLT_IsoMu27
SingleElectron	B-F	HLT_Ele35_WPTight_Gsf
DoubleMuon	B	HLT_Mu17_TrkIsoVVL_Mu8_TrkIsoVVL_DZ
	C-F	HLT_Mu17_TrkIsoVVL_Mu8_TrkIsoVVL_DZ_Mass8
DoubleEG	B-F	HLT_Ele23_Ele12_CaloIdL_TrackIdL_IsoVL

Table 2: 2017 HLT un-prescaled paths used in this work.

Data set	Run range	HLT path
MuonEG	A-D	HLT_Mu23_TrkIsoVVL_Ele12_CaloIdL_TrackIdL_IsoVL_DZ
		HLT_Mu12_TrkIsoVVL_Ele23_CaloIdL_TrackIdL_IsoVL_DZ
SingleMuon	A-D	HLT_IsoMu24
SingleElectron	A-D	HLT_Ele32_WPTight_Gsf
DoubleMuon	A-D	HLT_Mu17_TrkIsoVVL_Mu8_TrkIsoVVL_DZ_Mass3p8
DoubleEG	A-D	HLT_Ele23_Ele12_CaloIdL_TrackIdL_IsoVL

Table 3: 2018 HLT un-prescaled paths used in this work.

3.2 Simulated samples

Several Monte Carlo (MC) event generators are used to simulate the signal and the background processes, in order to optimize the event selection, evaluate the selection efficiencies and the systematic uncertainties, and compute the expected yields for most of the processes as will be detailed in Sections 7.4 and 8.3. In all the cases, the detector response is simulated using a detailed description of the CMS detector, based on the GEANT4 package [60], and the event reconstruction is performed with the same algorithms used for data. The simulated samples also include additional interactions per bunch crossing (pileup).

For all the MC samples, each reconstructed lepton is matched to a real generated lepton. With this requirement it is ensured that the selected leptons are real leptons and not leptons inside jets. The effect of this matching in the selection efficiency is less than 0.2%.

The parton distribution function (PDF) used for all samples is NNPDF3.0 for the 2016 samples and NNPDF3.1 [61, 62] for the 2017 and 2018 samples, while for the dark Higgs samples the NNPDF3.1 is used for the three data periods. In all the samples, the simulation of the parton shower (PS), the hadronization, and

the underlying event (UE) are provided by Pythia 8.2 [63, 64]. UE and multiple interactions are based on the CUETP1 tune [65] for the 2016 samples, and on the CP5 tune [66] for the 2017 and 2018 samples, while for the dark Higgs samples the CP5 tune is used for the three data periods.

The qq $\rightarrow W^+W^-$ production, via quark-antiquark annihilation, is generated at Next-To-Leading-Order precision (NLO) with POWHEG2.0 [67, 68, 69, 70]. The gluon-gluon fusion component, gg $\rightarrow W^+W^-$, is generated without Higgs boson diagrams using MCFM v7.0 [71] at Leading-Order (LO).

The WZ and ZZ production, via quark-antiquark annihilation, are generated with POWHEG2.0 at NLO. The $t\bar{t}$ and tW samples are also generated with POWHEG2.0 at NLO, while the Z+jets, Zγ, Wγ, t$\bar{t}$V, WZZ, and WWZ samples are generated with MadGraph5_aMC@NLO [72] at NLO.

All the Higgs boson production modes, the gluon-gluon fusion [73], the vector boson fusion (VBF) [74], the associated production with a vector boson (WH and ZH) [75], and with a $t\bar{t}$ pair (ttH) [76], are generated with the POWHEG generator at NLO. The decay of the Higgs boson into a W^+W^-pair, and the subsequently decay of the W bosons into leptons is done with Pythia 8.1 [77] for WH and ZH, and with JHUGen [78] for all the other production processes.

The whole set of used MC samples is listed in Tables 4 and 5.

All the simulation samples are further tuned with the following event-by-event weights to better approximate the simulation to collision data in terms of kinematics and object identification efficiencies.

- Pileup: The simulated events are weighted so that the pileup distribution matches the equivalent distribution in data. The ratio between the data distributions of the number of inelastic collisions for each year and the MC pileup profile is used as an event weight, that is applied as function of the true number of generated inelastic collisions in the event. Proton inelastic cross section value of (69.2 $\pm$ 4.6%) mb is used to derive the distributions of the number of collisions in MC.

- Trigger efficiency: Trigger HLT selections are not applied on the MC samples. Instead, the MC samples are weighted event-by-event by a function dependent on the p_T and η of the two lepton candidates. This function is derived as a combination of the measured triggering efficiencies per lepton leg, which are measured in data with the Tag-And-Probe method [49].

- Lepton identification efficiency scale factors: Data over MC scale factors are applied to the simulated events to correct for the different identification efficiencies found in data and in simulation (more details will be provided

process	year	dataset name
qqWW	2016	WWTo2L2Nu_13TeV-powheg
	2017	WWTo2L2Nu_NNPDF31_TuneCP5_PSweights_13TeV-powheg-pythia8
	2018	WWTo2L2Nu_NNPDF31_TuneCP5_13TeV-powheg-pythia8
ggWW	2016	GluGluWWTo2L2Nu_MCFM_13TeV
	2017	GluGluToWWTo*_13TeV_MCFM701_pythia8
	2018	GluGluToWWTo*_TuneCP5_13TeV_MCFM701_pythia8
EWK WW	2016	WWJJToLNuLNu_EWK_13TeV-madgraph-pythia8
	2017, 2018	WWJJToLNuLNu_EWK_TuneCP5_13TeV-madgraph-pythia8
$t\bar{t}$	2016	TTTo2L2Nu_TuneCUETP8M2_ttHtranche3_13TeV-powheg-pythia8
	2017, 2018	TTTo2L2Nu_TuneCP5_13TeV-powheg-pythia8
Single top s-ch	2016	ST_s-channel_4f_leptonDecays_13TeV-amcatnlo-pythia8_TuneCUETP8M1
	2017, 2018	ST_s-channel_4f_leptonDecays_TuneCP5_13TeV-amcatnlo-pythia8
Single top t-ch	2016	ST_t-channel_(anti)top_4f_inclusiveDecays_13TeV-powhegV2-madspin-pythia8_TuneCUETP8M1
	2017	ST_t-channel_(anti)top_4f_inclusiveDecays_TuneCP5_13TeV-powhegV2-madspin-pythia8
	2018	ST_t-channel_(anti)top_4f_InclusiveDecays_TuneCP5_13TeV-powheg-madspin-pythia8
Single top tW	2016	ST_tW_(anti)top_5f_inclusiveDecays_13TeV-powheg-pythia8_TuneCUETP8M1
	2017, 2018	ST_tW_(anti)top_5f_inclusiveDecays_TuneCP5_13TeV-powheg-pythia8
ggHWW	2016	GluGluHToWWTo2L2Nu_M125_13TeV_powheg_pythia8
	2017, 2018	GluGluHToWWTo2L2Nu_M125_13TeV_powheg2_JHUGenV714_pythia8
VBF HWW	2016	VBFHToWWTo2L2Nu_M125_13TeV_powheg_JHUGen_pythia8
	2017, 2018	VBFHToWWTo2L2Nu_M125_13TeV_powheg2_JHUGenV714_pythia8
W^+HWW	2016	HWplusJ_HToWW_M125_13TeV_powheg_pythia8
	2017, 2018	HWplusJ_HToWW_M125_13TeV_powheg_pythia8_TuneCP5
W^-HWW	2016	HWminusJ_HToWW_M125_13TeV_powheg_pythia8
	2017, 2018	HWminusJ_HToWW_M125_13TeV_powheg_pythia8_TuneCP5
ZHWW	2016	HZJ_HToWW_M125_13TeV_powheg_pythia8
	2017, 2018	HZJ_HToWWTo2L2Nu_M125_13TeV_powheg_jhugen714_pythia8_TuneCP5
ggZHWW	2016	GluGluZH_HToWW_M125_13TeV_powheg_pythia8
	2017, 2018	GluGluZH_HToWWTo2L2Nu_M125_13TeV_powheg_pythia8_TuneCP5
ttH	all	ttHToNonbb_M125_TuneCP5_13TeV-powheg-pythia8
ggH$\tau\tau$	all	GluGluHToTauTau_M125_13TeV_powheg_pythia8
VBF H$\tau\tau$	all	VBFHToTauTau_M125_13TeV_powheg_pythia8
W^+H$\tau\tau$	2016, 2017	WplusHToTauTau_M125_13TeV_powheg_pythia8
	2018	WplusHToTauTau_M125_13TeV_powheg_pythia8
W^-H$\tau\tau$ W^-	2016, 2017	WminusHToTauTau_M125_13TeV_powheg_pythia8
	2018	WminusHToTauTau_M125_13TeV_powheg_pythia8
ZH$\tau\tau$	2016, 2017	ZHToTauTau_M125_13TeV_powheg_pythia8
	2018	ZHToTauTau_M125_13TeV_powheg_pythia8

Table 4: Used MC samples in this work (I).

process	year	dataset name
DY$\tau\tau$	2016	DYJetsToTT_MuEle_M-10to50_TuneCUETP8M1_13TeV-madgraphMLM-pythia8
		DYJetsToTauTau_ForcedMuEleDecay_M-50_TuneCUETP8M1_13TeV-amcatnloFXFX-pythia8
		DYJetsToLL_M-5to50_HT-70to100_TuneCUETP8M1_13TeV-madgraphMLM-pythia8
		DYJetsToLL_M-5to50_HT-100to200_TuneCUETP8M1_13TeV-madgraphMLM-pythia8
		DYJetsToLL_M-5to50_HT-200to400_TuneCUETP8M1_13TeV-madgraphMLM-pythia8
		DYJetsToLL_M-5to50_HT-400to600_TuneCUETP8M1_13TeV-madgraphMLM-pythia8
		DYJetsToLL_M-5to50_HT-600toInf_TuneCUETP8M1_13TeV-madgraphMLM-pythia8
		DYJetsToLL_M-50_HT-70to100_TuneCUETP8M1_13TeV-madgraphMLM-pythia8
		DYJetsToLL_M-50_HT-100to200_TuneCUETP8M1_13TeV-madgraphMLM-pythia8
		DYJetsToLL_M-50_HT-200to400_TuneCUETP8M1_13TeV-madgraphMLM-pythia8
		DYJetsToLL_M-50_HT-400to600_TuneCUETP8M1_13TeV-madgraphMLM-pythia8
		DYJetsToLL_M-50_HT-600to800_TuneCUETP8M1_13TeV-madgraphMLM-pythia8
		DYJetsToLL_M-50_HT-800to1200_TuneCUETP8M1_13TeV-madgraphMLM-pythia8
		DYJetsToLL_M-50_HT-1200to2500_TuneCUETP8M1_13TeV-madgraphMLM-pythia8
	2017, 2018	DYJetsToTT_MuEle_M-10to50_TuneCP5_13TeV-madgraphMLM-pythia8
		DYJetsToLL_M-50_TuneCP5_13TeV-amcatnloFXFX-pythia8
		DYJetsToLL_M-4to50_HT-100to200_TuneCP5_13TeV-madgraphMLM-pythia8
		DYJetsToLL_M-4to50_HT-200to400_TuneCP5_13TeV-madgraphMLM-pythia8
		DYJetsToLL_M-4to50_HT-400to600_TuneCP5_13TeV-madgraphMLM-pythia8
		DYJetsToLL_M-4to50_HT-600toInf_TuneCP5_13TeV-madgraphMLM-pythia8
		DYJetsToLL_M-50_HT-100to200_TuneCP5_13TeV-madgraphMLM-pythia8
		DYJetsToLL_M-50_HT-200to400_TuneCP5_13TeV-madgraphMLM-pythia8
		DYJetsToLL_M-50_HT-400to600_TuneCP5_13TeV-madgraphMLM-pythia8
		DYJetsToLL_M-50_HT-600to800_TuneCP5_13TeV-madgraphMLM-pythia8
		DYJetsToLL_M-50_HT-800to1200_TuneCP5_13TeV-madgraphMLM-pythia8
		DYJetsToLL_M-50_HT-1200to2500_TuneCP5_13TeV-madgraphMLM-pythia8
		DYJetsToLL_M-50_HT-2500toInf_TuneCP5_13TeV-madgraphMLM-pythia8
Wγ	2016	WGToLNuG_01J_5f_TuneCUETP8M1_13TeV-amcatnloFXFX-pythia8
	2017, 2018	WGToLNuG_01J_5f_TuneCP5_13TeV-amcatnloFXFX-pythia8
Zγ	2016	ZGTo2LG_TuneCUETP8M1_13TeV-amcatnloFXFX-pythia8
	2017, 2018	ZGToLLG_01J_5f_TuneCP5_13TeV-amcatnloFXFX-pythia8
$W/Z\gamma^*$	2016	WZTo3LNu_mllmin01_13TeV-powheg-pythia8
	2017, 2018	WZTo3LNu_mllmin01_NNPDF31_TuneCP5_13TeV_powheg_pythia8
WZ (2ℓ2q)	all	WZTo2L2Q_13TeV_amcatnloFXFX_madspin_pythia8
ZZ (2ℓ2ν)	2016, 2017	ZZTo2L2Nu_13TeV_powheg_pythia8
	2018	ZZTo2L2Nu_TuneCP5_13TeV_powheg_pythia8
ZZ (2ℓ2q)	2016	ZZTo2L2Q_13TeV_powheg_pythia8
	2017, 2018	ZZTo2L2Q_13TeV_amcatnloFXFX_madspin_pythia8
ZZ (4ℓ)	2016, 2017	ZZTo4L_13TeV_powheg_pythia8
	2018	ZZTo4L_TuneCP5_13TeV_powheg_pythia8
ZZZ	2016	ZZZ_TuneCUETP8M1_13TeV-amcatnlo-pythia8
	2017, 2018	ZZZ_TuneCP5_13TeV-amcatnlo-pythia8
WZZ	2016	WZZ_TuneCUETP8M1_13TeV-amcatnlo-pythia8
	2017, 2018	WZZ_TuneCP5_13TeV-amcatnlo-pythia8
WWZ	2016	WWZ_TuneCUETP8M1_13TeV-amcatnlo-pythia8
	2017, 2018	WWZ_4F_TuneCP5_13TeV-amcatnlo-pythia8
WWW	2016	WWW_4F_TuneCUETP8M1_13TeV-amcatnlo-pythia8
	2017, 2018	WWW_4F_TuneCP5_13TeV-amcatnlo-pythia8

Table 5: Used MC samples in this work (II).

in Sections 4.1 and 4.2). Scale factors for each lepton are independently considered, and the product of the two correction factors is taken as the event weight. Lepton scale factors are applied as function of the lepton p_T and η.

- Heavy-flavor tagging efficiency scale factor: For each jet in the event where the b-tagging discriminator is evaluated (more details will be given in Section 4.4), a scale factor provided centrally by the *b-tag & Vertexing Physics Object Group* of CMS [79], is applied to the event, depending on the jet p_T, η, flavour, and the b-tagging discriminator value. The scale factors are designed to make the distribution of the discriminator value in the simulation close to that found in data.

- L1 prefiring correction: In the course of the 2016 and 2017 data taking, progressing transparency loss in the forward parts of the ECAL endcap led to a time-dependent gradual shift in the timing of the trigger primitives. The shift had become large enough that a significant fraction of trigger primitives were sent to the Level 1 trigger in the earlier neighboring bunch crossing, causing the Level 1 trigger to fire spuriously and subsequently veto the bunch crossing of the current collision of interest. As the HLT receives empty events under such circumstances, these collisions of interest were discarded immediately even if they contained high-p_T e/γ objects and/or jets. Trigger inefficiency due to this prefiring effect has been measured as a function of pseudorapidity of high-p_T e/γ objects and jets, and provided centrally by the CMS collaboration [55]. MC samples are weighted by this inefficiency arising from any physics object (following the central recommendation).

4 Identification of physics objects

In this section, the identification criteria of the physics objects used in this work are described.

4.1 Muons

Once the track of the muons is reconstructed, additional quality criteria are used based on the information from the different subdetectors.

For any analysis that contains muons in the final state, it is important to distinguish between those muons that come from decays produced directly at the interaction point (so-called *prompt* muons), mainly from W and Z bosons decays, and those other muons (so-called *fakes* or *non-prompt* muons) that can come from secondary decays, such as kaons or pions, or from muons inside jets. To improve the *prompt* muons purity, identification (ID) and isolation (ISO) selection criteria have been studied.

Muons with very restrictive ID criteria (tight ID [49]) are used. The tight ID selections, listed in Table 6, consist of a series of quality criteria applied on the reconstructed *global* muon track, providing a selection efficiency of about 97% for muons with $p_T > 20$ GeV. Moreover, to further reject muons that come from secondary vertices, tighter distance selections with respect to the primary vertex (PV) are included, distinguishing between the radial distance, d_0, between the PV and the muon, and the longitudinal distance, d_z, of the tracker track with respect to the PV: $d_0 < 0.01$ cm, $d_z < 0.1$ cm. These selections have been optimized by maximizing the signal efficiency for $H \to W^+W^-$ events while reducing the backgrounds [80].

Muon tight ID selections
Reconstructed as PF *global* muon
Normalized χ^2 of the *global* muon track fit < 10
Number of muon chambers with hits included in the fit > 0
Muon segments in at least two muon stations
Number of pixel hits > 0
Number of tracker layers with hits > 5
$d_0 < 0.2$ cm
$d_z < 0.5$ cm

Table 6: Summary of the muon tight ID criteria.

Also, the presence of high energy around the muon track for leptons in jets, due to the bunch of particles that the jet contains, can be used to discriminate whether or not a lepton is inside a jet. In this way, relative isolation variables can thus

defined as the sum of the energy deposited of all the reconstructed particles in a cone of radius $\Delta R = (\Delta\eta^2 + \Delta\phi^2)^{1/2}$ around the muon, relative to its transverse momentum:

$$ISO = \Big(\Sigma \mathrm{p_T}(\text{charged hadrons from PV}) + \max\Big(0, \Sigma Et(\text{neutral hadrons}) + \Sigma Et(\text{photons}) - 0.5 \times \Sigma \mathrm{p_T}(\text{charged hadrons from PU})\Big)\Big) / \mathrm{p_T}(\mu) \ , \tag{2}$$

where the last term is an additional correction to mitigate the effect of the PU [81]. It is estimated by subtracting the energy deposited in the isolation cone coming from charged particles not associated with the PV. This contribution is multiplied by a 0.5 factor, which corresponds approximately to the ratio of neutral to charged hadron production in the hadronization process of PU interactions.

Muons are selected if ISO < 0.15 within a cone ΔR $= 0.4$, with an overall efficiency of about 95% for muons with $\mathrm{p_T} > 20$ GeV.

In summary, well identified and isolated muons are selected in this work, requiring $\mathrm{p_T} > 20$ GeV and $|\eta| < 2.4$ (see Figure 2) to exploit the entire volume of the detector. On the other hand, for the study of the background due to *non-prompt muons*, as detailed in Section 7.4.1, a looser selection on ISO is used, $ISO_{loose} < 0.4$, while keeping the ID criteria.

The total efficiency of a muon can be measured as the product of the different reconstruction, trigger, identification and isolation efficiencies as:

$$\epsilon_{total} = \epsilon_{Trk} \times \epsilon_{ID} \times \epsilon_{ISO} \times \epsilon_{Trigger} \ , \tag{3}$$

where ϵ_{Trk} refers to the *global* track reconstruction efficiency, $\epsilon_{Trigger}$ to the efficiency of the trigger selection, ϵ_{ID} to the efficiency of the identification selection, and ϵ_{ISO} to the isolation selection efficiency. The track reconstruction efficiency is typically of the order of 99% [82], while the efficiency of the used triggers is of the order of 98% as commented in Section 3.

To measure the efficiency of the muon identification and isolation selections, the so-called *Tag-and-Probe* method [49] is used. In this method, the resonance of a well known particle, such as the electroweak neutral boson Z, is used to select muon pairs from its decay. From a given sample, a set of *prompt* muons, denoted as *tag* muons, is defined by applying very strict identification and isolation requirements, such that the probability that a *fake* muon passes these requirements is very low ($<< 1\%$). Once the *tags* are selected, they are paired with potential muon tracks, in such a way that the *tag-probe* invariant mass matches the Z boson mass, giving rise to another set of objects called *probes*. Then, the efficiency of a

certain ID or ISO selection is defined as the quotient between the number of *probe* muons that pass the imposed selection and the total number of *probes* obtained from the mass resonance:

$$\epsilon = \frac{N_{pass}}{N_{all}} \ , \tag{4}$$

where N_{pass} is the number of *probes* that pass the certain selection and N_{all} is the total number of *probes*. These efficiencies are usually measured as function of $\mathrm{p_T}$ and η of the lepton, since they depend on both variables.

The events previously selected are not totally pure in signal, which means that they may contain background events that do not come from the Z resonance and therefore may introduce a bias in the efficiency measurement. In order to obtain more precise results in the calculation, and to be able to subtract the background, a simultaneous fit to signal and background has been performed for the *probes* that pass (passing *probes*) and those that do not pass the selection (failing *probes*). The efficiency is then computed as:

$$\epsilon = \frac{passing\ probes}{passing\ probes + failing\ probes} \tag{5}$$

The fits are performed in a mass window wider than the Z boson width in order to properly fit the background shape: from 70 to 130 GeV for ID efficiencies, and from 77 to 130 GeV for ISO efficiencies.

As the efficiency is measured in bins of $\mathrm{p_T}$ and η, the fits will depend on the amount of signal and background events in each bin, and hence on the available statistics. Therefore, a group of bins has been defined to have enough statistics and then to ensure a good fit quality, and to properly account for the detector features:

- $\mathrm{p_T}$ = [20, 25, 30, 40, 60, 100, 200] GeV
- η = [-2.4, -2.1, -1.6, -1.2, -0.8, -0.3, -0.2, 0.0, 0.2, 0.3, 0.8, 1.2, 1.6, 2.1, 2.4]

Moreover, the shape of the *tag-probe* mass distribution depends on the amount of background in each bin, that is directly related to the applied selection on the *probes* and on the $\mathrm{p_T}$ and η of the *probe* muon. In this way, the fit has been optimized using different functions, and the one that gives the lowest value of χ^2 has been chosen. The used fit functions are the following:

- In case of ID efficiencies, the signal is fitted by the sum of two Voigtians (Breit-Wigner convoluted with a Gaussian to account for the detector resolution), and the background by the product of an exponential function and

the error function. This background function reproduces well the low $m_{\ell\ell}$ part of the spectrum for *probes* that fail the selection, where the background can be large specially at low p_T.

- In case of ISO efficiencies, the signal is fitted by the sum of two Voigtians and the background by an exponential function. Here the background contribution for the failing *probes* is expected to be lower, since the *probe* ID definition is tighter.

Data events passing a HLT trigger that requires at least one isolated muon with $p_T > 24$ (27) GeV for the 2016 and 2018 (2017) data sets, matched to the *tag* muon, have been used to measure the data efficiencies. Regarding MC, a Drell-Yan (DY) + Jets sample produced by the MADGRAPH generator has been used, for which a pile-up reweighting is applied to match the number of vertices in data. Efficiencies for both data and MC are computed for each data period independently.

The applied selection criteria on the *tag* muons are the following: $p_T > 29$ GeV, tight ID criteria, and ISO < 0.2. On the other hand, the *probe* muons are requested to be *tracker* muons (see Section 2.2) with $p_T > 20$ GeV when measuring the tight ID efficiencies, and to pass the tight ID criteria when measuring the ISO efficiencies.

Some fits for the passing, failing, and all *probes* are shown in Figures 7 and 8 for ID in the p_T and η ranges $20 < p_T < 25$ GeV, $-0.3 < \eta < -0.2$ for 2017 data, and for ISO in the p_T and η ranges $60 < p_T < 100$ GeV, $-1.6 < \eta < -1.2$ for 2017 MC, respectively. These figures are just an example; fits are performed in each bin for the ID and ISO chosen selections, for data and MC, and for each data period independently.

As shown in Figures 9 and 10, the efficiencies obtained separately for data and MC as function of p_T and η show discrepancies in certain regions, such as in the CMS endcaps. To correct this effect, scale factors (SFs) are computed as the ratio of the efficiency in data over the efficiency in MC, as function of p_T and η. These SFs are applied directly to the simulation in order to preserve the observed efficiency in data.

To estimate the systematic uncertainties of the efficiencies obtained by the *Tag-And-Probe* method, four variations are considered with respect to the nominal parameters described previously. First, the isolation of the tag muon is moved from $ISO < 0.2$ to $ISO < 0.3$ and $ISO < 0.1$. Second, the signal fit function is changed from two Voigtians to a single Voigtian. Third, the number of mass bins where the fit is done is moved from 40 to 50 and 30. Finally, the mass range in which the fit is performed is shifted up and down: for ID it is the shifted from [70-130] GeV to [75,140] GeV and to [65,120] GeV, while for ISO it is shifted from

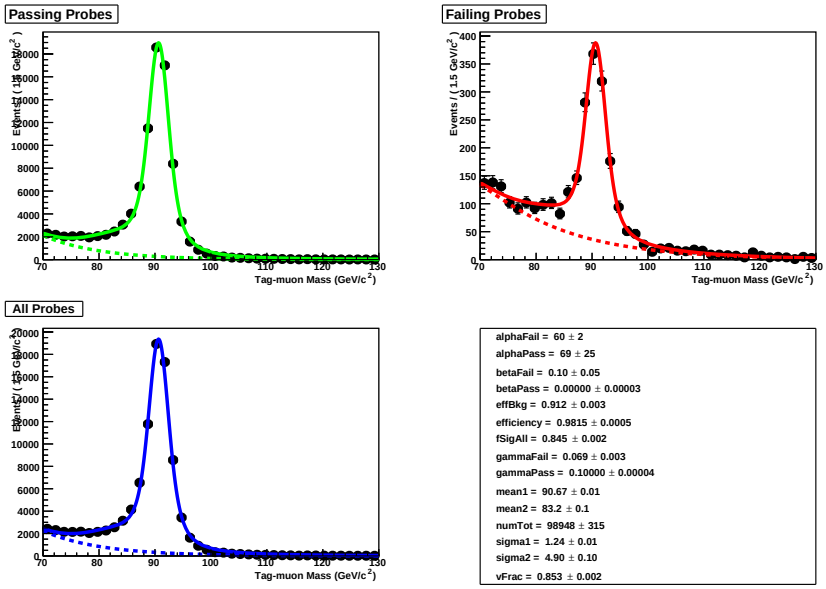

Figure 7: ID fits for bin $20 < p_T < 25$ GeV, $-0.3 < \eta < -0.2$ in 2017 data. Fit results are shown in the bottom right panel.

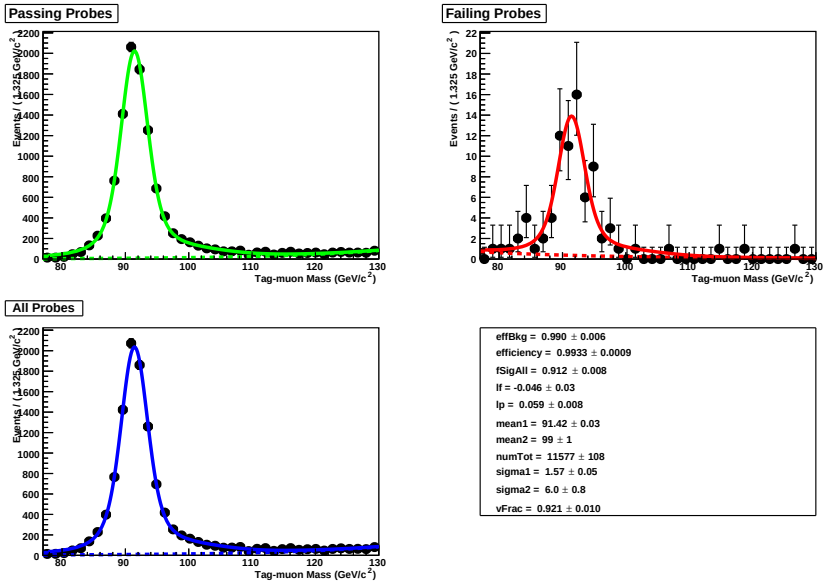

Figure 8: ISO fits for bin $60 < p_T < 100$ GeV, $-1.6 < \eta < -1.2$ in 2017 MC. Fit results are shown in the bottom right panel.

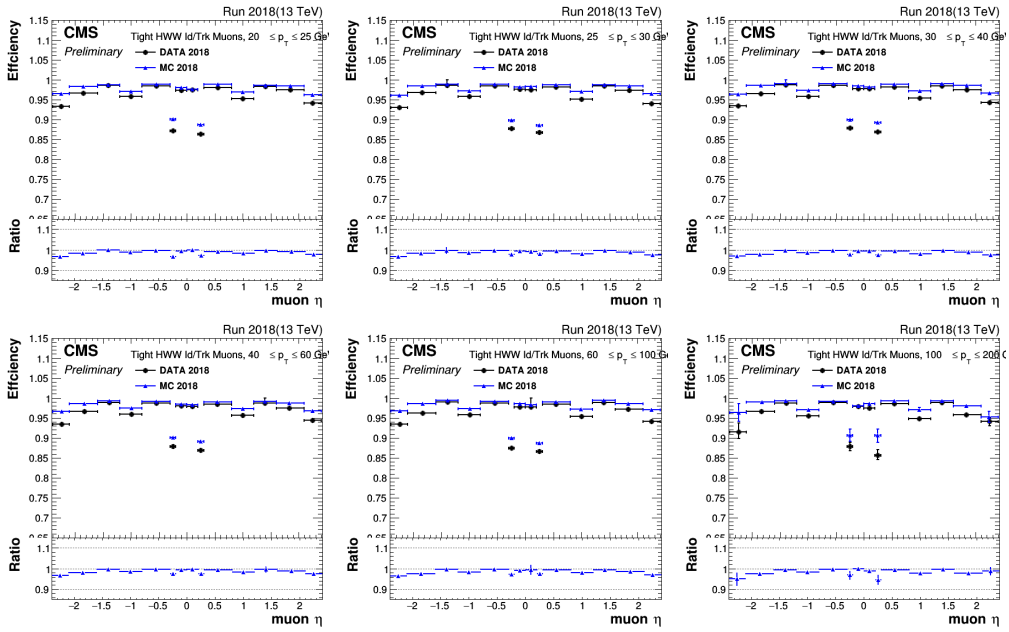

Figure 9: ID efficiency distributions for 2018 data (black) and MC (blue) as function of η for each p_T bin (written in the legend). The ratio in η each bin, so-called scale factor, is shown on the bottom of each figure.

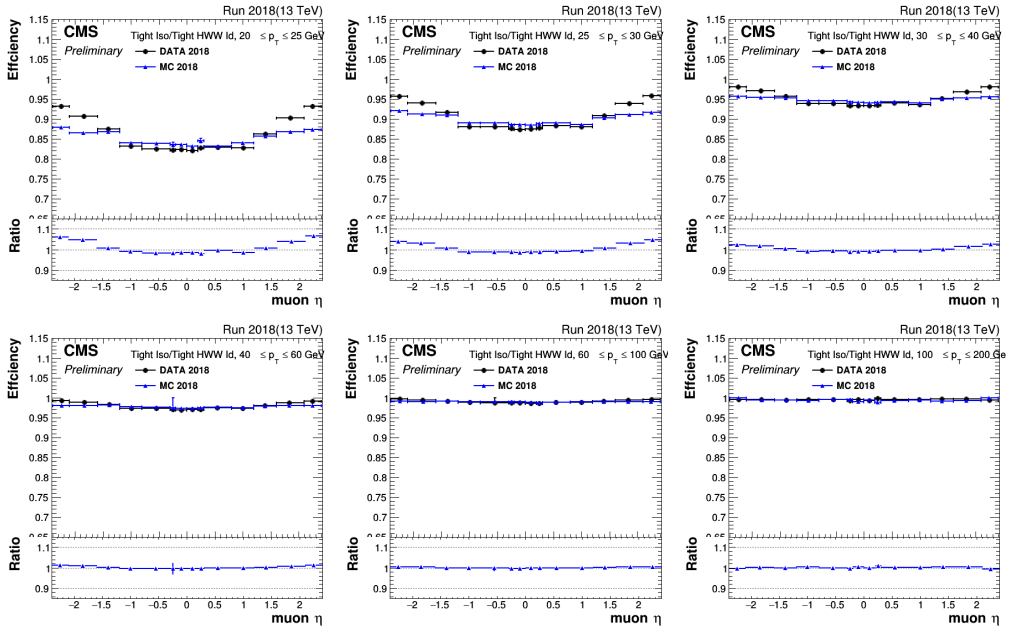

Figure 10: ISO efficiency distributions for 2108 data (black) and MC (blue) as function of η for each p_T bin (written in the legend). The ratio in each η bin, so-called scale factor, is shown on the bottom of each figure.

[77,130] GeV to [80,140] GeV and to [70,120] GeV. The *Tag-And-Probe* efficiencies are recalculated for all the considered variations.

Once all the efficiencies have been computed for both data and simulation, the variations that maximizes (in each bin) the up and down shift on the scale factor value with respect to the nominal one are selected. Then, the associated systematic uncertainty for each p_T, η bin is computed by adding in quadrature both values.

Finally, scale and momentum corrections delivered by the Rochester group [83] are applied to mitigate potential biases in the muon momentum assignment due to detector misalignment, precision of the magnetic field, or possible problems in the muon reconstruction. The method compares the reconstructed Z peak from the $\mu^+\mu^-$ invariant mass with the theory value, and provides a experimental correction with proper systematic uncertainties to be applied to both data and simulation samples. The effect of the correction is shown in Figure 11 for the 2017 data set (similar behavior is observed for the other data periods).

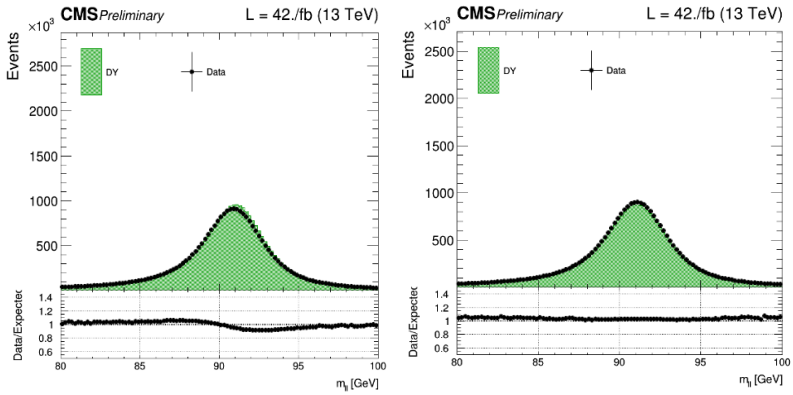

Figure 11: $\mu^+\mu^-$ invariant mass distribution in a DY control region before (left plot) and after (right plot) applying the 2017 Rochester corrections.

4.2 Electrons

As in the case of muons, the goal is to identify prompt electrons efficiently and to reject *fakes* as much as possible.

The looser electron definition used for estimation of the *non-prompt* electrons is based on the medium ID [84], on calorimetric observable requirements, and on d_0 and d_Z selections with respect to the PV, requiring $d_0 < 0.05$ (0.1) cm, $d_Z < 0.1$ (0.2) cm if $|\eta_{SuperCluster}| \leq 1.5$ ($1.5 < |\eta_{SuperCluster}| < 2.5$).

On top of the looser electron selections, the final electron definition is based on the *tight ID* criteria or on a selection on a Multivariate-Analysis (MVA) discriminator (depending on the studied analysis), both developed by the CMS collaboration [84]. In addition, a relative isolation selection, defined in a cone size of 0.3 around the electron direction, relative to electron p_T, is required to be less than 0.06. The MVA, used in the dark Higgs search, is trained with information related to the electron object reconstruction and isolation variables. Those features feed a Boosted Decision Tree (BDT) algorithm, trained on $Z + jets$ MC samples, with *prompt* electrons as signal and *non-prompt* electrons as background. A selection value on the BDT output discriminator that keeps 90% signal efficiency is set for each data period. On the other hand, the *tight ID*, used in the W^+W^-analysis, consists of a set of restrictive quality selections applied on the reconstructed electron track.

Electron efficiencies in data and MC are calculated with the *Tag-And-Probe* method described in Section 4.1. In this case, the signal is fitted by using MC templates that are derived from the simulated sample in the Z mass range between 60 and 120 GeV as function of the electron p_T and η. For the background fitting, a convolution of an exponential function and the error function has been used. The final electron efficiency is shown in Figure 12 for 2016 data (MVA case). Similar performance is observed for the other data periods.

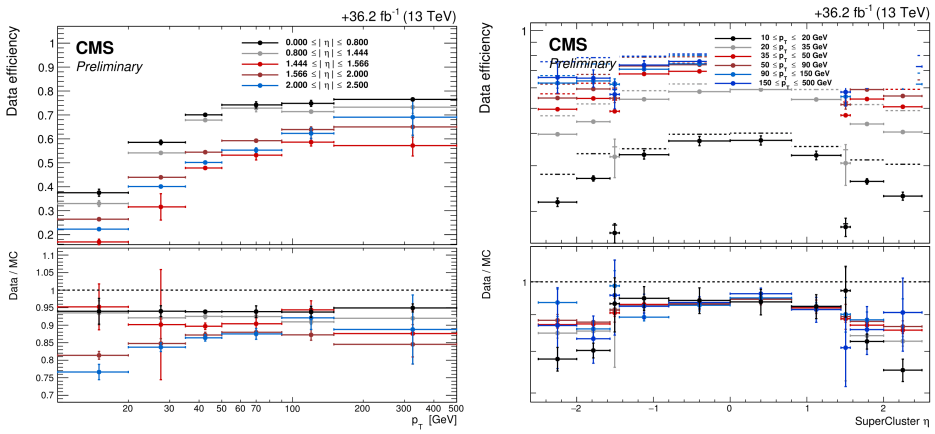

Figure 12: Efficiencies for electron ID selection (MVA case) as function of p_T (left) and η (right) for the 2016 data set. Scale factors are shown in the bottom panel.

For the systematic uncertainties estimation, some recommended variations are studied with respect to the nominal configuration. First, the signal and background fitting functions are varied to a Crystal-Ball function (Gaussian core and exponential tail) and to an exponential function respectively. Second, the DY

MC sample at LO precision that is used for getting the nominal scale factors is replaced by a NLO sample. Finally, the p_T selection on the *tag* electron is shifted from 30 GeV to 33 GeV. As in the case of muons, the associated systematic uncertainty for each p_T - η bin is estimated by taking the maximum variation in the up and down directions.

4.3 Jets

The jets are defined as objects identified by the $anti - k_T$ algorithm (see Section 2.2), with $|\eta| < 4.7$ and $p_T > 30$ GeV, to ensure that real and well measured jets are analyzed.

In order to remove jets originating from the calorimetric noise, tight identification criteria, provided centrally by the CMS collaboration [85], are applied. These ID criteria are essentially based on jet energy fraction and multiplicity variables. These are good quantities to discriminate between noise jets and physical jets, since the fractions of the jet energy carried by different types of PF candidates clustered into a jet, and the number of clustered PF candidates into the jet, are sensitive variables to several sources of noise from the calorimeters. In addition to that, jets that are within $\Delta R < 0.4$ of one of the identified leptons are disregarded.

4.4 B-Tagging

A fundamental aspect in many analyses is to identify events that involve the production of b quarks in their final states. b quarks have a long life time that causes their decay products to be measured from a secondary vertex displaced from the primary one, meaning that the particle moves a certain distance measurable by the detector before decaying. This particular information can be used to reconstruct secondary vertices and identify with a certain efficiency b quarks.

One of the most commonly used algorithms to identify b quarks (*b-tagger*) is the *DeepCSV* [79], which is based on secondary vertex and track-based information, and was built using a deep neural network with four hidden layer of a width of 100 nodes each aiming to improve the tagger performance. Once trained, the model is evaluated for the reconstructed jets in the events, providing for each of them a discriminator value that can be understood as a likelihood of being identified as a b-jet as shown in Figure 13.

A *b-tagger* will be used to identify or veto b-jets that may come from a *top* quark decay. The efficiency of the b-tagger depends on the algorithm that is used, on the flavour of the jets, and on the jet kinematics. For *DeepCSV*, the selection working point on the discriminator is chosen among the recommended selections provided centrally by the CMS collaboration aiming to have the maximum possible b-veto efficiency with a small misidentification probability. For each data

period, a discriminator cut (so-called *Loose* working point) is set, for which the rate for misidentifying a light jet as a b-jet is about 10% while having a b-veto efficiency of the order of 90%, as shown in Figure 13.

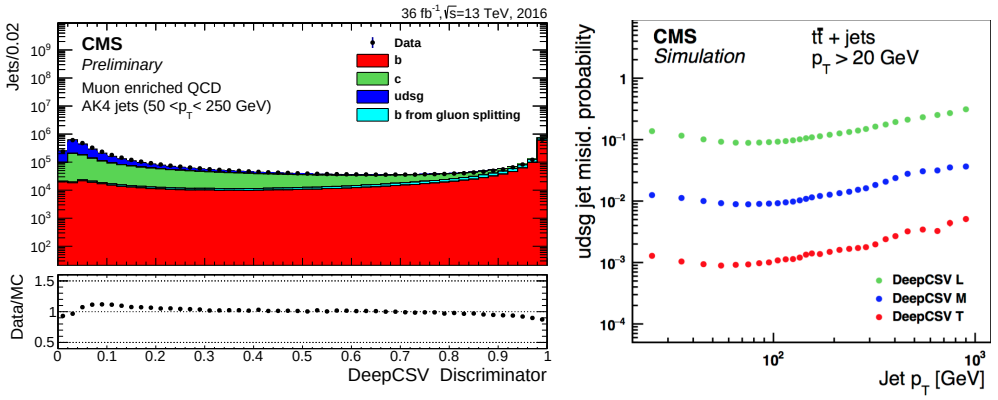

Figure 13: Left: Distribution of the 2016 DeepCSV discriminator for jets in a muon enriched jet sample. The black markers show the data distribution, while the filled histograms show the contributions of the different jet flavours in MC. The first and last bin of each histogram contain the underflow and overflow entries, respectively. Right: Misidentification probabilities for the DeepCSV tagger as function of the jet p_T for the different working points, where the chosen Loose working point is plotted in green. Figures taken from [86] and [79] respectively.

Once the selection working point has been defined, a correction scale factor is computed to account for the different efficiencies in data and simulation, such as the discrepancies related to different b-tagging efficiencies and misidentification rates. This correction is provided centrally as a weight per jet which depends on jet flavour and kinematics. Then, the MC events are reweighted using a global weight over all the jets in the event, defined as:

$$w = \prod_{i}^{N_{\text{jets}}} SF_{\text{jet}_i} \ , \tag{6}$$

where i runs over all the jets in the event for which b-tagging selection is applied. This kind of reweighting allows to correct for shape differences between data and MC but does not assure that the overall normalization of the MC samples is correct. To address this, a data-driven approach will be applied as will be detailed in Section 7.4.2.

The *DeepCSV* algorithm, which is based on deep learning techniques, is an improved version of the original *CSVv2* algorithm [79] that was used in most of the early *Run 2* CMS analyses. The former is used in the dark Higgs search, while the later is used in the W^+W^-analysis.

4.5 Missing Transverse Energy

The Missing Transverse Energy is constructed as the sum of the negative signed transverse momentum of all the reconstructed particles in the detector:

$$\vec{\mathrm{E}}_{\mathrm{T}}^{\mathrm{miss}} = -\sum_{PFcand} \vec{p_{T_i}} \,, \tag{7}$$

where p_{T_i} refers to the transverse momentum of the i PF candidate in the event.

In the dark Higgs search, a second algorithm, so-called PUPPI$\mathrm{E}_{\mathrm{T}}^{\mathrm{miss}}$ method (pileup per particle identification technique) [87, 88], is applied to further reduce the dependence on pileup. The method relies on a estimated likelihood that is assigned to each reconstructed particle in the event. This likelihood is then used to reweight each particle in the reconstruction process in order to give less importance to those that likely come from the pileup.

On top of that, reconstruction failures, pileup, or malfunctioning detectors can provide anomalous $\mathrm{E}_{\mathrm{T}}^{\mathrm{miss}}$. Recommended filters [87] are applied to minimize misreconstruction effects such as calorimeter noise, contamination from beam-gas interactions or beam-halo effects. The effect of applying the filters on a dijet selection is shown in Figure 14. Also, due to the resolution of the subdetectors, there is a certain instrumental $\mathrm{E}_{\mathrm{T}}^{\mathrm{miss}}$, even in physical processes that do not involve the production of neutrinos or new physics, such as DY events.

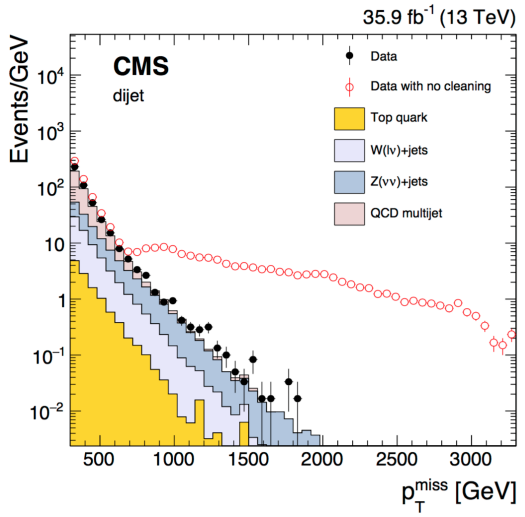

Figure 14: $\mathrm{p}_{\mathrm{T}}^{\mathrm{miss}}$ distribution for a 2016 dijet selection. Data with filters applied is shown as filled black markers, while data without filtering is represented as open red markers. Simulation is shown as solid histograms. Image taken from [87].

4.6 Objects summary

A summary of the applied identification and isolation requirements on the physics objects used in this work is given in Table 7.

Objects	Selections
Jets	PF jets, tight ID, cleaned from leptons in $\Delta R = 0.4$
E_T^{miss}	E_T^{miss} (for the W^+W^-analysis) or PUPPIE_T^{miss} (for the dark Higgs search)
B-tagging	CSVv2 (for W^+W^-) or DeepCSV (for dark Higgs). Loose working point
Muons	tight ID, ISO < 0.15 in $\Delta R = 0.4$, $d_0 < 0.01$ cm, $d_z < 0.1$ cm
Electrons	tight ID (for W^+W^-) or MVA ID (for dark Higgs), ISO < 0.06 in $\Delta R = 0.3$, $d_0 < 0.05$ (0.1) cm, $d_Z < 0.1$ (0.2) cm if barrel (endcaps)

Table 7: Summary of the used object selection in this work.

5 Signal extraction

To measure physics observables, such as the cross section of a certain process, a likelihood fit [89] is performed. The likelihood fit aims to estimate, from the observed data, the parameters of an hypothetical distribution defined by a given model.

The generic likelihood function is given by:

$$\mathcal{L} \sim p(data|\vec{\alpha}) \ , \tag{8}$$

where $\vec{\alpha}$ corresponds to the parameters of the model, and $p(data|\vec{\alpha})$ refers to the probability to observe the data for a given particular value of $\vec{\alpha}$.

The set of parameters $\vec{\alpha}$ can be split into physics parameters of interest (POIs, denoted as $\vec{\mu}$), and the nuisance parameters (NPs, denoted as $\vec{\theta}$), which typically are constrained by external measurements. This information can be included in the likelihood function in order to account for the fact that there is a known prior knowledge about what these NPs should be. Those constraint terms can be expressed as:

$$\pi(\vec{\theta_0}|\vec{\theta}) \sim p(\vec{\theta}|\vec{\theta_0}) \ , \tag{9}$$

where some observed (or externally measured) $\vec{\theta_0}$ values are introduced to relate π to the probability to observe the outcome value for the NPs from those external measurements.

Then, Eq. (8) can be written as:

$$\mathcal{L}(\vec{\mu}, \vec{\theta}) \sim p(data|\vec{\mu}, \vec{\theta}) \cdot \pi(\vec{\theta_0}|\vec{\theta}) \tag{10}$$

If a simply cut-and-count analysis is performed (just by counting the number of events in a single bin, denoted in the test as *one-bin* distribution), the data in this case is simply the observed number of events n, and the first probability term in Eq. (10) is given by a Poisson probability:

$$p(n|\lambda) = \frac{\lambda^n exp(-\lambda)}{n!} \tag{11}$$

Given that external measurements determine the nuisance parameters as $\theta \pm \sigma_\theta$, and in the absence of more information about the shape of the PDF, it is assumed that σ_θ represents 1σ of a Gaussian (valid if such measurements have been done with large statistics). Moreover, for simplicity, a Gaussian centered in zero with standard deviation equal to one is used. Using this prescription, when setting $\theta = 0$, the nominal number of observed events is recovered, while $\theta = \pm 1$ corresponds to the $\pm 1\sigma$ uncertainty. Following this logic, the second term in Eq. (10) can be written as:

$$\pi(\theta) = exp(-\frac{1}{2}\theta^2) \tag{12}$$

If one parameter modifies only the rate of events, it is known as a log-normal distributed nuisance parameter (based on multiplicative corrections on the event rate, such as the uncertainty on the luminosity). In case of a shape-analysis (where instead of having a single observation, distributions with several bins are considered), there are not only uncertainties affecting the event rate, but also uncertainties that modify the shape of the distributions. Those shape uncertainties can be easily introduced in the likelihood function by interpolating the $\pm 1\sigma$ shifted histograms with a spline method, aiming to associate a Gaussian distributed nuisance parameter for each shape uncertainty.

The models that will be considered in this work are used to determine the signal normalization, denoted commonly as signal strength r, from the maximum likelihood fit of the expected yields to the observed data. Thus, a single unconstrained POI (r) is measured. In that case, the product rule for probability can be used to account for the multiple i bins in a histogram and the several k systematic uncertainties affecting the expectations:

$$\mathcal{L}(r,\vec{\theta}) = \prod_i \frac{\left[r \cdot s_i(\vec{\theta}) + b_i(\vec{\theta})\right]^{n_i}}{n_i!} \exp\Big(-\left[r \cdot s_i(\vec{\theta}) + b_i(\vec{\theta})\right]\Big) \prod_k \exp\left(-\frac{1}{2}\theta_k^2\right), \tag{13}$$

where r refers to the signal strength, s_i to the expected signal yields in bin i, b_i to the expected background yields in bin i, and θ_k to the nuisance parameter associated to the uncertainty k. It should be noted that the observed data in each bin n_i is a constant value, so the likelihood is just a function of the POI and the nuisance parameters.

It is important to remark that only the POI is the interesting parameter to be measured. Also, since several nuisance parameters (systematic and statistical uncertainties) are commonly introduced, dealing with such multi-dimensional likelihood is usually not computationally feasible. To take both facts into account, the usual approach consists of removing the nuisance parameters dependence from the likelihood by profiling the likelihood function over the nuisance parameters, i.e., find the value for θ which maximises the likelihood at each value of r: $\hat{\theta}(r)$ (this nomenclature will be used from now on in the text to refer to maximum likelihood estimators). By doing that, $\mathcal{L}(r,\vec{\theta}) \rightarrow \mathcal{L}(r,\hat{\theta}(r))$, and removing the implicit dependence:

$$\mathcal{L}(r,\vec{\theta}) \rightarrow \mathcal{L}(r) \tag{14}$$

On the other hand, it is worth to note that the likelihood is an unnormalized function. Therefore, to avoid dealing with small or large values, the negative

logarithm function, $-\log\mathcal{L}(r)$, can be taken, so that the maximum likelihood is equivalent to the minimum negative log-likelihood. Also, since the value of the likelihood curve as function of the POI at the minimum, $\mathcal{L}(\hat{r})$, is not relevant, it can be subtracted to obtain the $-\Delta\log\mathcal{L}$ for each value of r:

$$-\log\mathcal{L}(r) \rightarrow -\log\mathcal{L}(r) - (-\log\mathcal{L}(\hat{r})) = -\Delta\log\mathcal{L}(r) = -\log\frac{\mathcal{L}(r)}{\mathcal{L}(\hat{r})} \tag{15}$$

This quantity multiplied by 2 is known as the profiled likelihood ratio.

From the Wilks theorem [90], in the limit of large sample sizes, the profile likelihood ratio is distributed as a χ^2 distribution with N degrees of freedom, where N is the difference in number of free parameters between the numerator and denominator of the likelihood ratio (1 in our case). Therefore, the quantile function of the χ^2 distribution can be used to define a 68% confidence interval (or Confidence Level, denoted as CL): $-2\times\Delta\log\mathcal{L}(r) < 1.0 \rightarrow -\Delta\log\mathcal{L}(r) < 0.5$. This strategy will be used in the W^+W^-analysis to quote the uncertainties on the cross section measurement.

In a new particle search, like the Dark Higgs analysis, two hypothesis are considered: signal+background (s+b) and background-only (b). Then, a hypothesis test based on the likelihood ratio is performed aiming to exclude one of those according to the data observation, so that for exclusion (discovery) the null-hypothesis corresponds to the signal+background assumption (background-only).

When calculating limits (setting upper limits on model parameters), it is commonly used the CLs criterion [91] to reject the null hypothesis (signal+background in this case). Taking this prescription as reference, we say that signal+background hypothesis is excluded at 95% CL if:

$$CLs = \frac{CL_{s+b}}{CL_b} \leq 0.05 \tag{16}$$

CL_{s+b} and CL_b, for a given test-statistic q_r, are defined by:

$$CL_{s+b} = p_r = P(q_r \geq q_r^{obs}|s+b) = \int_{q_r^{obs}}^{\infty} f(q_r|r,\hat{\theta}_r^{obs})\,dq_r\ , \tag{17}$$

$$CL_b = 1 - p_b = P(q_r \geq q_r^{obs}|b) = \int_{q_0^{obs}}^{\infty} f(q_r|0,\hat{\theta}_0^{obs})\,dq_r\ , \tag{18}$$

where the functions $f(q_r|r,\hat{\theta}_r^{obs})$ and $f(q_r|0,\hat{\theta}_0^{obs})$ are the Probability Density Functions (PDFs) of the quantity q_r, and q_r^{obs} is the observed value of the statistic obtained in the experiment.

At the LHC, the definition of q_r is chosen by convention:

$$q_r = -2\log\left[\mathcal{L}(data|r,\hat{\theta}_r)/\mathcal{L}(data|r=\hat{r},\hat{\theta})\right] \tag{19}$$

The value of q_r is set to 0 when $\hat{r} > r$ in order to get a one sided limit, and the r is constrained to take only positive values. Taking these two conditions into account, Eq. (19) can be written as:

$$q_r = \begin{cases} 0 & \text{if } \hat{r} > r \\ -2\log\left[\mathcal{L}(data|r,\hat{\theta}_r)/\mathcal{L}(data|r=0,\hat{\theta}_0)\right] & \text{if } \hat{r} < 0\ , \end{cases} \tag{20}$$

in which the nuisance parameters are profiled separately for $r = 0$ and r.

It should be taken into account that $\hat{r}$ and $\hat{\theta}$ correspond to the maximum likelihood estimators, so this test-statistic requires two fits, one for a fixed value of r (r=0) and one scanning it.

The value of the CLs for each possible r value can be calculated with frequentist Montecarlo toys, so that if CLs < 0.05 for a given r, we can say the signal is excluded at 95% CL. However, this approach can be time consuming, specially if several parameters are included in the model. To avoid that, the Asymptotic approximation of the test-statistic [92] can be used, allowing to compute quickly an estimate of the limits in a fairly accurate way. This approach relies again on the results from Wilks and Wald [93], that allow to approximate the test-statistic by a χ^2 distribution with one degree of freedom (one POI) in case the event yields are large enough, and thus the log-likelihood function is parabolic (typically works well for for event counts $\mathcal{O}(10)$ and above). If this condition is accomplished, simulation toys are not needed to build the PDFs in Eq. (17) and (18), so it is immediate to obtain the value of the integrals.

Similarly, to quantify a discovery, we intend to exclude the background-only hypothesis, for which a similar test-statistic can be defined:

$$q_0 = -2\log\left[\mathcal{L}(data|r=0,\hat{\theta}_0)/\mathcal{L}(data|\hat{r},\hat{\theta})\right]\ , \tag{21}$$

where $q_0 = 0$ is set when $\hat{r} < 0$.

Then, the rejection significance of the background-only hypothesis (r=0) is given by the p-value P_0, defined as:

$$P_0 = \int_{q_0^{obs}}^{\infty} f(q_0|r=0)\, dq_0 \tag{22}$$

To be able to confirm a discovery, the obtained P_0 must be at least 0.287×10^{-6} (5σ) by convention [94].

6 Uncertainties

The uncertainties that are included in the likelihood function as nuisance parameters are described in this section. Same kinds of uncertainties are taken into account in both the SM $W^+W^-$and in the dark Higgs analyses.

The uncertainties can be categorized as:

- Statistical uncertainties, due to the finite statistic of the used samples.
- Theoretical systematic uncertainties, due to knowledge and precision with which the MC processes are simulated, including for instance the precision of the used Probability Distribution Functions (PDFs) of the colliding protons, the precision of the QCD calculations, or the hadronization process.
- Experimental systematic uncertainties, due to the resolution, calibrations, and efficiency of the detector when performing any type of measurement.

6.1 Statistical uncertainties

The statistical uncertainty of the used MC samples is limited by the amount of generated events in each case, which is finite. To model the statistical uncertainties, a Poisson constrained parameter is assigned to each bin and to each MC process that is taken into account in the fit to the data distribution. This treatment is used because each bin of a certain distribution corresponds to an independent counting measurement.

However, although the likelihood function is well defined by Eq. (13), the number of needed Poisson parameters can be huge due to the different number of bins of the distributions, the number of regions, and the different physical processes considered. Consequently, from a technical point of view, the computation time and memory consumption required to perform the fit can increase considerably. To reduce the number of parameters that enter in the maximum likelihood fit, the Barlow-Beeston-lite approach [95] is used. This method aims to assign a single nuisance parameter, which is constrained by the total uncertainty, to scale the sum of the total number of events in each bin, in case the number of effective events is sufficiently large. On the other hand, if the number of effective MC events in a certain bin is small (typically in the tails of the kinematic distributions, where the amount of MC generated events is low), a Poisson constrained parameter is assigned to each process individually. To decide whether to use the generic Poisson assignment or the Barlow-Beeston-lite one, a threshold is set on the number of effective events in each bin, denoted as $n_{threshold}$.

The logic of the algorithm works as follows:

- For each bin, the number of effective events, n_{tot}^{eff}, is defined as $n_{tot}^{eff} = n_{tot}^2/e_{tot}^2$, where n_{tot} refers to the sum of the different processes yields, $n_{tot} = \sum_{i \in processes} n_i$, and e_{tot} to the sum of the corresponding statistical uncertainties, $e_{tot} = \sqrt{\sum_{i \in processes} e_i^2}$

- If $n_{tot}^{eff} \leq n_{threshold}$, separate uncertainties are accounted for each process by including in the model one Poisson-constrained parameter per each, given that a Gaussian-constrained is not a good approximation for very low stats .

- If $n_{tot}^{eff} > n_{threshold}$, a single Gaussian-constrained parameter is included, that scales the total yield in the bin.

This approach allows to reduce significantly the fit computation time, and increases the fit stability for complex models with large numbers of bins, such us the ones used in the analysis presented in this report, and specially for the dark Higgs analysis (see Section 8.4), where several bins are included in the global maximum likelihood fit.

Statistical uncertainties are treated as uncorrelated among the different bins of the fitted distributions of each data period, and uncorrelated among the different data periods.

6.2 Systematic uncertainties

Estimating the effect of the different systematic uncertainties on the measurements is a fundamental part of the considered analyses. In the following, the whole set of systematic uncertainties taken into account in the performed measurements are listed. The list includes those uncertainties which influence the overall normalization, such as the uncertainty on the luminosity measurement, and also the ones that affect the distribution of relevant kinematic quantities, such as the uncertainty on the jet energy scale, that are treated as shape uncertainties as explained in Section 5.

6.2.1 Theoretical uncertainties

Theoretical uncertainties are treated as fully correlated among the different bins of the fitted distributions of each data period, and fully correlated among the different data periods.

- PDFs: The choice of the PDFs affects the distribution shapes as well as the overall cross sections of the considered processes. The PDF uncertainty evaluation for the signal and background processes accounts for the effect of different PDF sets on MC simulation events, and is based on the PDF4LHC recommendations [96]. For the 2016 data set, the root mean square of

100 PDF variations is taken as total uncertainty (the PDF variations are based on MC replicas), while for the 2017 and 2018 data sets, individual shape uncertainties for 32 variations is taken (the PDF variations in this case contain hessian replicas). Its overall effect on the used MC samples is smaller than 0.1%.

- QCD scale: Missing higher-order terms in the perturbation series of the cross section calculations affects the shapes and the overall normalization. Renormalization and factorization scales are varied up and down by factors of 2 and 0.5 relative to the nominal value, and the up and down envelopes of the varied distributions are taken as one standard deviation variations. Its overall effect on the used MC samples is smaller than 0.1%.

- Underlying event (UE): Particle production not associated with the leading hardest parton-parton process is evaluated by comparing some of the MC efficiencies with samples with alternative underlying event parameters in simulation. These parameters come from phenomenological models and are tuned to reproduce real data. A normalization uncertainty of 1.5% has been assigned to cover the differences, as no kinematic shape dependencies are observed.

- Parton Shower (PS): Partons (quarks and gluons) radiate virtual gluons, which can emit more gluons or quark-antiquark pairs, producing as consequence parton showers whose effect is taken into account in simulation. Event reweighting with weights calculated by Pythia is used to evaluate this uncertainty. Reweighting factors correspond to per-event cross section variations with Initial State Radiation (ISR) and Final State Radiation (FSR) scales varied up and down by factor 2, based on the uncertainties in the PS tunning [97]. The envelope of the variation distributions is considered as up and down variations. Its overall effect on the used MC samples is smaller than 0.1%.

- Background corrections: Systematic uncertainties on the different background MC corrections are accounted. Regarding W^+W^-, recommended theoretical uncertainties from the NNLO-NNLL higher order corrections [98] are included by varying the resummation, and renormalization and factorization scales (details are given in Section 7.1). A systematic uncertainty on $t\bar{t}$ is added to cover the top quark p_T correction (described in Section 7.4).

6.2.2 Experimental uncertainties

Experimental uncertainties are treated as fully correlated among the different bins of the fitted distributions of each data period, and uncorrelated among the different data periods.

- Pileup (PU): Uncertainties on the amount of pileup present in the event are evaluated by varying the minimum bias cross section (see Section 3.2) used to generate the pileup distribution in MC by $\pm 1\sigma$. MC Events are reweighted to match these alternative distributions. Its overall effect on the used MC samples is of the order of 0.1%.

- Luminosity: The luminosity normalization uncertainties are derived from the van der Meer scan program [99] that is used for the luminosity calibration and corresponding measurement in each data period. The reported associated uncertainties are 1.2%, 2.3%, and 2.5% for the 2016, 2017, and 2018 luminosity respectively (see [100], [101], [102]).

- Trigger and lepton identification efficiencies: Uncertainties on trigger and lepton identification efficiencies are of the order of 1%. These uncertainties are computed by varying the tag-and-probe method parameters such as the tag selection or the used Z window (more details can be found in Section 4.1).

- Lepton momentum and electron energy scale: the lepton momentum scale uncertainty is computed by varying the momentum of the leptons by their uncertainties. The corresponding uncertainties in lepton $\mathrm{p_T}$-η bins, provided centrally by the *Muon Physics Object Group* of CMS [49, 84], are of the order of 0.8% for electrons and 0.2% for muons.

- $\mathrm{p_T^{miss}}$ energy scale: Uncertainties on $\mathrm{p_T^{miss}}$ are assessed by varying the momentum of each PF candidate by his own resolution as recommended by the *JetMET Physics Object Group* of CMS [88]. The overall effect on the rates ranges from 1% to 10% depending on the process.

- Jet energy scale (JES) and resolution (JER): The estimate of the jet energy scale uncertainty is performed varying the jet energy scale up and down by 1σ as measured by centrally by the *JetMET Physics Object Group* of CMS [103]. The variation corresponds to a simple re-scaling of the jet four-momentum as $P \to P \cdot (1 \pm \delta \mathrm{p_T^{JES}}/\mathrm{p_T})$, where $\delta \mathrm{p_T^{JES}}$ is the absolute uncertainty on the jet energy scale which is parametrized as function of the $\mathrm{p_T}$ and η of the jet. In order to account for the systematic uncertainty on the jet resolution smearing procedure, the resolution scale factors are varied up and down within their uncertainty. Their overall effect on the used MC samples is about 5% when selecting 0 or 1 jets in the event, and about 1% in inclusive measurements.

- B-tagging efficiency: Uncertainties on the b-tagging scale factor are evaluated by shifting the per-jet scale factors by ranges provided centrally by the *b-tag & Vertexing Physics Object Group* of CMS [79], accounting for both the statistical uncertainties of the used samples to compute the scale factors, and for the unknown jet flavor compositions of the samples. Its overall effect on the used MC samples is below 1%.

- Background estimation with data-driven methods: Uncertainties on non-prompt and DY estimation from the *tight-to-loose* and $R_{out/in}$ methods are included as described in Section 7.4.

In this context, it is worth to define the concept of the impact. The impact of a certain nuisance parameter (θ) on a parameter of interest, such as the signal strength (r), is defined as the shift in r, Δr, produced by setting the value of θ to its $\pm 1\sigma$ post-fit values, with all the other nuisance parameters of the model profiled. By this way, it is possible in each analysis to sort the nuisance parameters by their impact on the unconstrained parameter r, as will be shown in the following sections.

7 WW production

In this section the W^+W^-analysis (published in [104]) is described. The aim of this study is to measure the W^+W^-production cross section using the dileptonic decay channel with 2016 CMS data, together with fiducial and differential cross section measurements. Also, a search for potential anomalous couplings that could affect the W^+W^-production is performed, where limits on the corresponding coupling constants are set.

Previous results for these measurements are summarized in [31], where a total integrated luminosity of 2.3 fb^{-1} was used. This study aims to improve those by taking advantage of the greater luminosity and the better knowledge of the systematic uncertainties. In addition, events with a same-flavour lepton pair are analyzed for the fist time in this CMS analysis during the *Run 2*, in order to improve the experimental precision of the reported results. Direct comparisons among both results and with the theory prediction will be given in Section 7.5.

7.1 Signal modeling

The production of the W^+W^-process in proton-proton collisions at $\sqrt{s} = 13\ TeV$ occurs mainly (∼95% of the cases) by quark-antiquark annihilation ($qq \rightarrow W^+W^-$) in the t-channel and in the s-channel. On the other hand, and with a lower contribution to the production cross section of the process (∼5%), it can also be produced by gluon-gluon fusion ($gg \rightarrow W^+W^-$). Finally, the third possible production mode is the W^+W^-resonant production through a Higgs boson decay ($H \rightarrow W^+W^-$), that is considered as background in this analysis. The corresponding Feynman diagrams are shown in Figure 15.

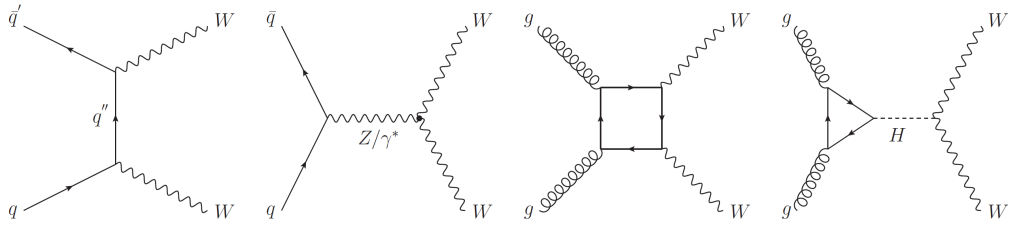

Figure 15: Feynman diagrams for the SM W^+W^-production. From left to right: $qq \rightarrow W^+W^-$ t-channel, $qq \rightarrow W^+W^-$ s-channel, non-resonant $gg \rightarrow W^+W^-$, and resonant $gg \rightarrow W^+W^-$ production through a Higgs boson decay. Image taken from [105].

The $qq \rightarrow W^+W^-$ signal is generated at NLO with POWHEG. Theory higher order corrections, which are not captured by the NLO order calculation, are included using a p_T resummation technique to match the NNLO-NNLL precision [98]. The p_T distribution of the W^+W^-system at generated level, p_T^{WW}, is used as a

probe of these higher orders corrections. In this way, the NLO p_T^{WW} spectrum given by POWHEG is corrected by using the prediction from the NNLO-NNLL resummation calculation. The applied event weights are taken from the theory paper recipe [98], together with an estimation of the theoretical uncertainties on the W^+W^-prediction as function of the p_T^{WW}, which are obtained by varying separately the renormalization and factorization scales[3] (μ_F, μ_R), and the resummation scale[4] (Q) within the calculation.

The effect of the correction and the corresponding scale uncertainties compared with the NLO POWHEG prediction at signal region selection level is shown in Figure 16.

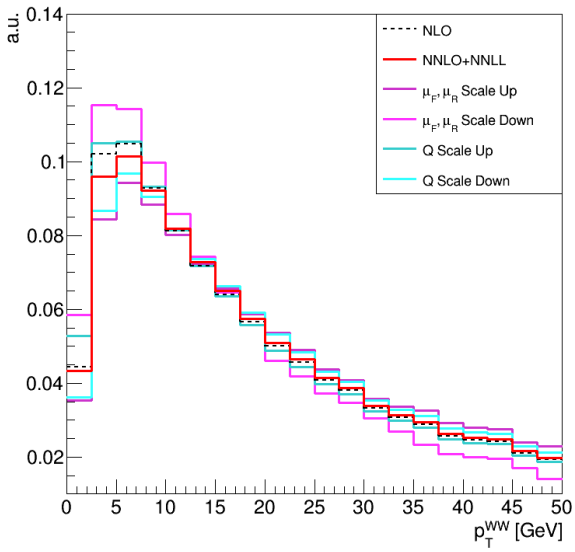

Figure 16: Effect of the higher order correction on the p_T^{WW} distribution at Table 8 selection level. The NLO distribution before reweighting (black dashed line), the reweighted distribution to match the NNLO-NNLL prediction (red line), the renormalization and factorization scale variations (magenta lines), and the resummation scale variations (blue lines) are shown normalized to unity.

On the other hand, the $gg \to W^+W^-$ contribution is generated at LO precision with MCFM and scaled to the NNLO cross section by a K-factor $= 1.4 \pm 0.4$ [107], since no strong shape dependencies are observed in the analyzed phase space.

[3] Regularization scales that are introduced in fixed-order perturbation theory calculations to avoid divergences [106] due to unaccounted diagrams.

[4] Defines the transition region where the p_T^{WW} distribution is mostly described by the resummed calculation ($p_T^{WW} < Q$), and where it is mostly described by the fixed order computation ($p_T^{WW} > Q$).

7.2 Main Backgrounds

The main backgrounds affecting the signal region of the analysis are the top quark background, the Drell-Yan (DY) background, and the non-prompt lepton background, denoted in the text simply as non-prompt background. These backgrounds present a final signature similar to the signal W^+W^-process, including at least two leptons and MET in their final state.

The non-prompt background comes mainly from W+jets (see Figure 17), semileptonic $t\bar{t}$, and single-top decays. It is an instrumental background, since at least one of the jets must be misidentified as a well identified and isolated lepton (*fake* lepton) in order to have two leptons in the final state. It should be noted that although the probability of misidentifying a jet as a lepton is very small, the production cross section of the processes involved is large (for instance, for W+jets is 61527 pb), and this fact makes it one of the main backgrounds of the analysis.

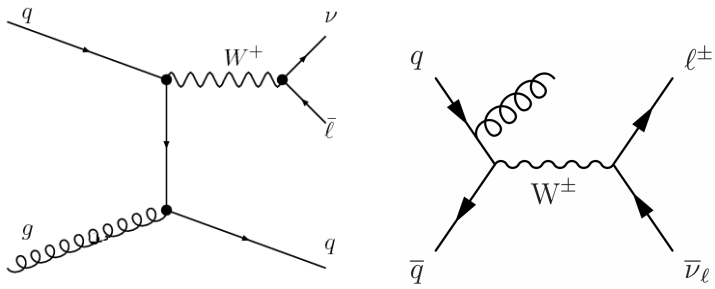

Figure 17: Low order Feynmann diagrams for W+jets production.

The top quark background in the dileptonic channel ($t\bar{t}$ pair production, associated production of a top quark and a W boson, denoted as tW, and single top production), which does not enter as non-prompt background, represents one of the dominant backgrounds in this analysis given its large cross section and its final state similar to the signal. Since *top* quarks decay in almost 100% of the cases into a W boson and a b quark [108], the peculiarity of this background is the presence of b-jets in the final state with a relatively high transverse momentum. Therefore, b-jet identification (b-tagging) is crucial to identify and reject top events in the analysis. Feynman LO diagrams for $t\bar{t}$ and tW processes are shown in Figure 18.

The Drell-Yan (DY) process (see Figure 19) takes place when a quark and an antiquark annihilate creating a virtual photon or a Z boson, and it decays into same-flavour leptons of opposite charge: $Z/\gamma^* \to \ell^+\ell^-$. The main difference between the W^+W^-signal and this background in the same-flavour decay channel (ee, $\mu\mu$ final states) is the absence of real $E_{\mathrm{T}}^{\mathrm{miss}}$, since neutrinos are not produced in the final state and then the measured $E_{\mathrm{T}}^{\mathrm{miss}}$ is due to the resolution of the detector. In the different-flavour decay channel ($e\mu$, μe final states) the DY con-

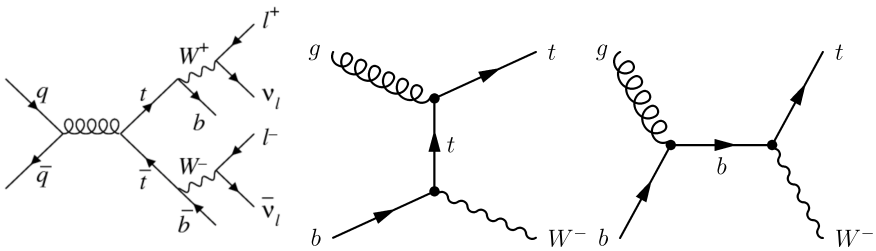

Figure 18: Feynman LO diagrams for $t\bar{t}$ (left) and tW (middle and right). Images taken from [109] and [110].

tribution comes from the $Z/\gamma^* \to \tau^+\tau^-$ decay, and the measured $E_{\mathrm{T}}^{\mathrm{miss}}$ in this case is due to the neutrinos produced in the subsequent τ decays: $\tau^+ \to \nu_\tau W^+$, $W^+ \to \ell^+\nu_\ell$, and $\tau^- \to \nu_\tau W^-$, $W^- \to \ell^-\nu_\ell$.

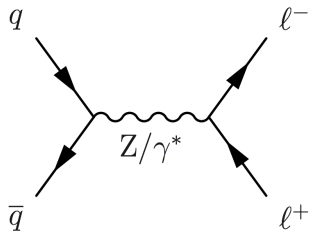

Figure 19: LO Feynman diagram of $Z/\gamma^* \to \ell^+\ell^-$production.

7.3 Event Selection

The target signature consists of two opposite charged leptons, and large transverse missing energy from the neutrinos. An event selection is defined for the different-flavour (DF) and the same-flavour (SF) final states separately.

For the DF category, leptons with leading lepton $\mathrm{p_T}$ ($\mathrm{p_T^{\ell\,max}}$) greater than 25 GeV and trailing lepton $\mathrm{p_T}$ ($\mathrm{p_T^{\ell\,min}}$) greater than 20 GeV are required, and events with additional loose leptons (defined in Section 4) with $\mathrm{p_T^{\ell}}$ greater than 10 GeV are vetoed. A minimum on the invariant mass of the dilepton system, $\mathrm{m_{\ell\ell}} > 20$ GeV, is set to suppress low mass resonances such as the J/psi (J/ψ) or the Upsilon (Υ) mesons. Also, a selection on the $\mathrm{p_T^{miss}}$, $\mathrm{p_T^{miss}} > 20$ GeV, and on the $\mathrm{p_T}$ of the dilepton system, $\mathrm{p_T^{\ell\ell}} > 30$ GeV, are applied to reject mainly DY and non-prompt backgrounds. In addition, a selection on the *mpmet* variable, defined in Eq. (25) using the projection of the $\mathrm{PFE_T^{miss}}$ and the $\mathrm{E_T^{miss}}$ measured in the CMS tracker over the lepton directions, *mpmet* > 20GeV, is applied to reduce instrumental $\mathrm{p_T^{miss}}$ due to mismeasurements of the lepton momentum. Finally, the b-veto is applied by rejecting b-tagged jets (as defined in Section 4) with $\mathrm{p_T}$ greater than

20 GeV to suppress the top quark contribution.

$$proj.\,Trk\mathrm{E}_{\mathrm{T}}^{\mathrm{miss}} = \begin{cases} Trk\mathrm{E}_{\mathrm{T}}^{\mathrm{miss}} & \text{if } \Delta\phi_{min}(\ell,\mathrm{Trk}\mathrm{E}_{\mathrm{T}}^{\mathrm{miss}}) \geq \pi/2 \\ Trk\mathrm{E}_{\mathrm{T}}^{\mathrm{miss}} \sin\Delta\phi_{min} & \text{if } \Delta\phi_{min}(\ell,\mathrm{Trk}\mathrm{E}_{\mathrm{T}}^{\mathrm{miss}}) < \pi/2 \end{cases} \quad (23)$$

$$proj.\,PF\mathrm{E}_{\mathrm{T}}^{\mathrm{miss}} = \begin{cases} PF\mathrm{E}_{\mathrm{T}}^{\mathrm{miss}} & \text{if } \Delta\phi_{min}(\ell,\mathrm{PF}\mathrm{E}_{\mathrm{T}}^{\mathrm{miss}}) \geq \pi/2 \\ PF\mathrm{E}_{\mathrm{T}}^{\mathrm{miss}} \sin\Delta\phi_{min} & \text{if } \Delta\phi_{min}(\ell,\mathrm{PF}\mathrm{E}_{\mathrm{T}}^{\mathrm{miss}}) < \pi/2 \end{cases} \quad (24)$$

$$mpmet = \min(proj.\,Trk\mathrm{E}_{\mathrm{T}}^{\mathrm{miss}}, proj.\,PF\mathrm{E}_{\mathrm{T}}^{\mathrm{miss}}) \quad (25)$$

For the SF category, harder selections on $\mathrm{E}_{\mathrm{T}}^{\mathrm{miss}}$ and on $\mathrm{m}_{\ell\ell}$, $\mathrm{E}_{\mathrm{T}}^{\mathrm{miss}} > 55$ GeV, $\mathrm{m}_{\ell\ell} > 40$ GeV, are applied to suppress the DY background, which is the dominant one on this category. On top of that, to further reject DY, events whose dilepton invariant mass is in a window of 15 GeV around the Z boson mass ($|m_Z - \mathrm{m}_{\ell\ell}| < 15$ GeV) are vetoed. Finally, a selection on a MVA discriminator developed for the CMS analysis done in the H→WW channel [80], denoted as DYMVA, is applied. The DYMVA is based on a Boosted Decision Trees (BDT) architecture that takes as input angular and energy related quantities from leptons, jets, $\mathrm{E}_{\mathrm{T}}^{\mathrm{miss}}$, and number of vertices, aiming to discriminate $\mathrm{H}\to\mathrm{W}^+\mathrm{W}^-$events from DY. In this analysis, a selection on the DYMVA estimator, DYMVA > 0.9, is applied. This selection keeps, at signal region selection level, a signal efficiency of about 80% while reducing the DY contamination by 90%.

The full set of selection cuts are listed in Table 8. Once the event selection is applied for the two decay channels, the remaining events are split into two categories each: events with zero reconstructed jets as defined in Section 4.3 (0-jets category) and events with one reconstructed jet (1-jet category).

7.4 Background estimation

In the following subsections, the procedures that have been followed to model the the non-prompt, top quark, and DY backgrounds are detailed, including the different control regions definitions.

The contribution of other sub-dominant backgrounds, such as HWW, $V\gamma/V\gamma^*$, VZ, and VVV, is obtained directly from the simulated samples.

7.4.1 Non-prompt background

The contribution of the non-prompt background is estimated in data with a method called *tight-to-loose*. Basically, the method aims to estimate the fake

Variable	Different-flavour	Same-flavour
Charge ℓmax $\times$ Charge ℓmin	< 0	< 0
$p_T^{\ell\,max}$ [GeV]	> 25	> 25
$p_T^{\ell\,min}$ [GeV]	> 20	> 20
p_T^{miss} [GeV]	> 20	> 55
mpmet [GeV]	> 20	> 20
$\lvert m_{\ell\ell} - m_Z \rvert$ [GeV]	-	> 15
DYMVA	-	> 0.9
$p_T^{\ell\ell}$ [GeV]	> 30	> 30
$m_{\ell\ell}$ [GeV]	> 20	> 40
Additional leptons ($p_T^{\ell} > 10$ GeV)	veto	veto
b-veto	applied	applied

Table 8: Summary of the event selection for the different-flavour and same-flavour final states.

and prompt rates based on the loose and tight identification criteria (see Sections 4.1 and 4.2), and use these rates to estimate the amount of non-prompt leptons in the signal region of the analysis.

The fake rate f is defined as the probability for a fake lepton passing the loose definition criteria to also pass the tight ones, and to therefore be considered as a real lepton in the analysis. It can be measured in a fake enriched region, for instance in a QCD region. In this case, this multijet region is defined by using the triggers listed in Table 9 to select events with at least one loose lepton and jets.

Electron HLT trigger paths	$\mathcal{L}_{int}$ [fb^{-1}]		
	2016	2017	2018
HLT_Ele8_CaloIdL_TrkIdL_IsoVL_PFJet30 ($p_T < 25$ GeV)	//	0.00397	0.00641
HLT_Ele12_CaloIdL_TrkIdL_IsoVL_PFJet30 ($p_T < 25$ GeV)	0.01485	//	//
HLT_Ele23_CaloIdL_TrkIdL_IsoVL_PFJet30 ($p_T \geq 25$ GeV)	0.06281	0.04347	0.03891
Muon HLT trigger paths	$\mathcal{L}_{int}$ [fb^{-1}]		
	2016	2017	2018
HLT_Mu8_TrkIsoVVL ($p_T < 20$ GeV)	0.00780	0.00290	0.00856
HLT_Mu17_TrkIsoVVL ($p_T \geq 20$ GeV)	0.21675	0.06594	0.04578

Table 9: Pre-scaled triggers used for defining the fake enriched region. The corresponding integrated luminosity, along with the lepton p_T range of application, is reported in each case.

Then, the following event selection is applied:

- $E_T^{miss} < 20$ GeV and $m_T^{\ell\,max, p_T^{miss}} < 20$ GeV, to remove real leptons from W

decays.

- Only one loose lepton in the event (to reduce contamination from Z events) recoiling against one jet, $\Delta R(\ell, jet) > 1.0$, is requested. The recoiling jet will be used to control the average p_T of the jet that fakes the lepton.

After applying the selection in the QCD enriched region, small contamination from the leptonic decay of some electroweak processes (EWK) is expected, mainly from W+jets, Z+jets and $t\bar{t}$. These backgrounds are estimated from MC and removed when computing the fake rate.

The fake rate is then given by the ratio between fake leptons passing the tight definition and those passing the loose definition, and it is measured as function of p_T and η of the lepton, as shown in Figure 20 for the 2016 data set. The effect of removing the EWK contamination from both the numerator and denominator of the fake rate calculation is also shown. Very similar dependence is observed for the other data periods.

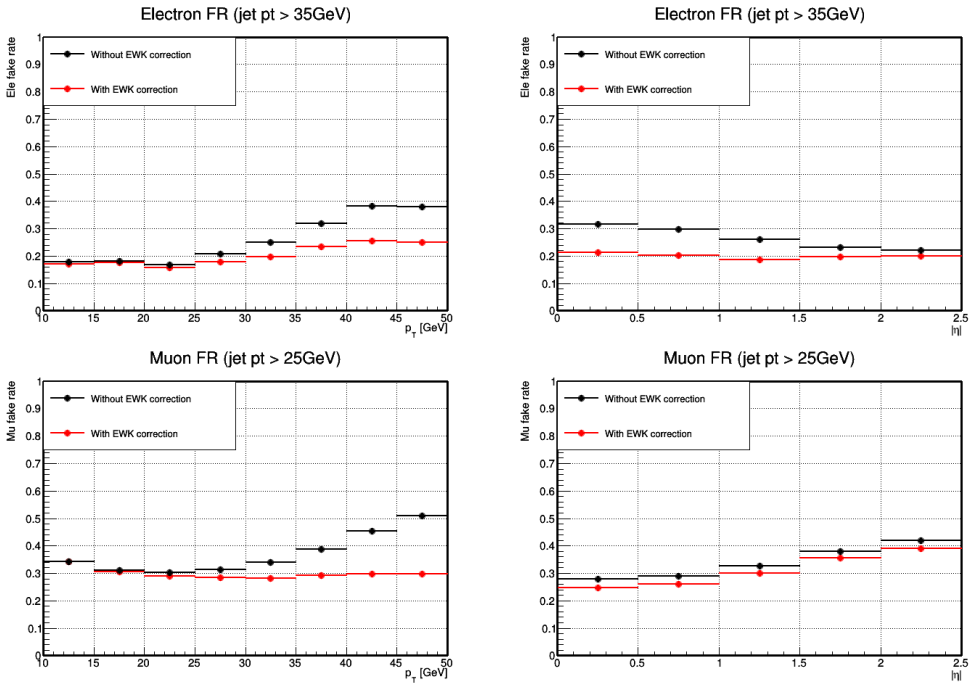

Figure 20: Electron (top) and muon (bottom) fake rate as a function of the loose lepton p_T (left) and η (right) from a control region sample obtained with a jet p_T threshold of 30 GeV, and for the 2016 data set. The effect of the EWK correction is shown in black and red.

The prompt rate p is the probability for a prompt lepton passing the loose criteria

to also pass the tight selection. It can be measured in a region enriched in prompt leptons, such as a Z boson enriched region. The prompt rate is measured in a Z+jets MC sample by requiring events with more than one reconstructed loose leptons with leading lepton $p_T > 25$ GeV and trailing lepton $p_T > 10$ GeV. The leading lepton is also required to pass the tight definition requirements, and then a loop over all the other loose leptons having the same-flavour is performed, selecting the lepton pair whose invariant mass is closer to the Z candidate. The prompt rate is then estimated by the ratio between the number of times the second lepton pass the tight definition as well over the total. It is measured as function of p_T and η of the lepton as shown in Figure 21 for the 2018 data set. Very similar dependence is observed for the other data periods.

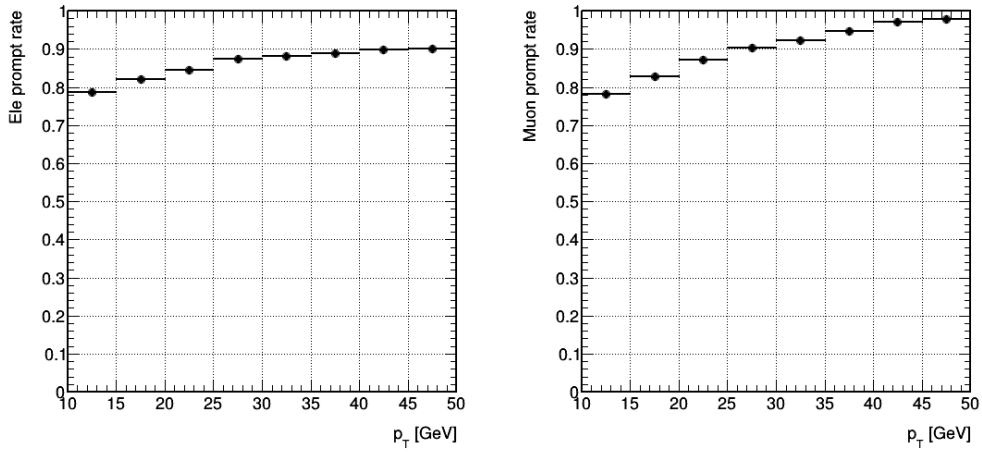

Figure 21: Electron (left) and muon (right) prompt rate as a function of the loose lepton p_T for the 2018 data set.

The last step consists of applying these rates to estimate the following quantities from data in the signal region of the analysis:

- N_{pp} events where both leptons are prompt.
- N_{fp} events where one lepton is prompt and the other is fake.
- N_{ff} events where both leptons are fake.

However, in data it is not possible to know which leptons are fake and which are prompt; the only quantity that can be measured with data is N_{tx} ($x = 0, 1, 2$), defined as the number of events with 0, 1 or 2 leptons passing the tight requirements. N_{tx} can be related to N_{pp}, N_{fp}, and N_{ff} by using the f and p rates as:

$$\begin{cases} N_{pp} + N_{fp} + N_{ff} = N_{t2} + N_{t1} + N_{t0} \\ N_{t0} = (1-p)^2 N_{pp} + (1-p)(1-f) N_{fp} + (1-f)^2 N_{ff} \\ N_{t1} = 2p(1-p) N_{pp} + (f(1-p) + p(1-f)) N_{fp} + 2f(1-f)^2 N_{ff} \\ N_{t2} = p^2 N_{pp} + pf N_{fp} + f^2 N_{ff} \end{cases} \tag{26}$$

Using matrix notation and isolating the N_{pp}, N_{fp}, and N_{ff} quantities:

$$\begin{pmatrix} N_{pp} \\ N_{fp} \\ N_{ff} \end{pmatrix} = \frac{f-p}{-(p-f)^3} \cdot \begin{pmatrix} f^2 & -f(1-f) & (1-f)^2 \\ -2fp & p(1-f) + f(1-p) & -2(1-p)(1-f) \\ p^2 & -p(1-p) & (1-p)^2 \end{pmatrix} \cdot \begin{pmatrix} N_{t0} \\ N_{t1} \\ N_{t2} \end{pmatrix} \tag{27}$$

From which N_{pp}, N_{fp}, and N_{ff} can be obtained for each event in the signal regions (see Section 7.3).

The estimation is performed in flavour categories (muon, electron) and in number of jets categories ($njets$: 0-jets, 1-jet, $\geq$2 jets) to account for the flavour of the jet that is misidentified as a well identified and isolated lepton. In case of the 0-jets category, the fakes come mainly W+jets, and the chosen nominal value for the recoiling jet E_T is 20 GeV for muons. In the 1-jet category, since the top contribution starts to be important, and hence we will have more fake contribution from b-quark jets, the nominal value is increased to 25 GeV. For the $\geq$2 jets category the nominal value is 35 GeV. The threshold for electrons is fixed to 35 GeV in all the $njets$ categories since no changes are observed in the fake rate as function of the recoiling jet E_T. The dependence of the fake rate as function of the recoiling jet E_T is shown in Figure 22 for the 2018 data set (similar dependence is observed for the other data periods).

To account for the systematic uncertainties of the method, the recoiling jet energy is shifted by 10 GeV up and down with respect to the nominal value. On the other hand, the non-prompt estimation is recomputed with the fake rate varied by the lepton statistical uncertainty in the QCD enriched region. Both variations are propagated independently in flavour categories and in $njets$ categories, and their effect on the non-prompt estimation is shown in Table 10.

To check if the method is able to properly reproduce the data, a validation region is defined with the same selections as the signal region, but inverting the dilepton charge sign, i.e., requiring same-sign charged leptons. Some distributions of the same-sign validation region are shown in Figures 23 and 24 for the different-flavour 0-jets category and for the different-flavour 1-jet category respectively. Similar agreement is observed for the same-flavour categories as shown in Appendix A. A flat 30% systematic uncertainty is added to this background to

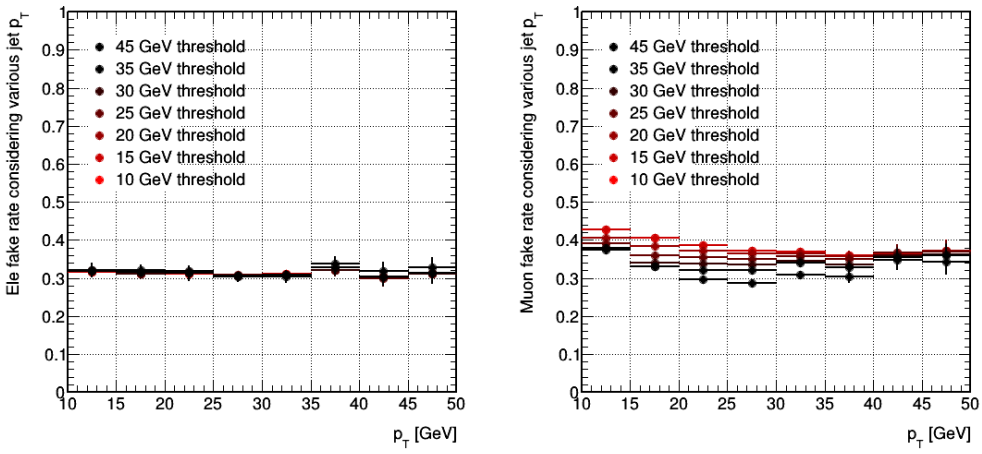

Figure 22: Electron (left) and muon (right) fake rate as a function of the loose lepton p_T for different jet p_T thresholds, and for the 2018 data set. The EWK correction is applied.

Systematic source	eμ 0-jets category	eμ 1-jet category	eμ $\geq$2 jets
2016 Electron jet E_T	2.0/-2.0%	1.7/-1.3%	2.0/-3.1%
2016 Electron statistical	12.3/-11.9%	9.6/-9.2%	8.7/-8.7%
2016 Muon jet E_T	6.6/-3.7%	8.8/-11.8%	10.7/-12.2%
2016 Muon statistical	1.6/-1.2%	3.0/-2.6%	4.6/-4.6%
2017 Electron jet E_T	9.0/-2.6%	8.0/-2.5%	7.0/-2.2%
2017 Electron statistical	20.0/-18.4%	17.5/-16.3%	21.4/-14.8%
2017 Muon jet E_T	6.1/-2.6%	8.3/-8.0%	10.3/-13.3%
2017 Muon statistical	1.9/-1.6%	3.7/-4.0%	6.6/-7.0%
2018 Electron jet E_T	4.3/-2.3%	4.3/-2.3%	4.8/-2.0%
2018 Electron statistical	17.3/-16.1%	12.2/-14.2%	14.0/-13.3%
2018 Muon jet E_T	6.3/-2.6%	8.1/-7.0%	9.6/-11.6%
2018 Muon statistical	1.7/-1.7%	4.3/-4.3%	6.8/-6.8%

Table 10: Systematics uncertainties associated to the non-prompt leptons data-driven estimation at Table 8 selection level in the eμ channel for the 0-jets, 1-jet and $\geq$2 jets categories, and for the three data periods.

cover the discrepancies observed in this validation region.

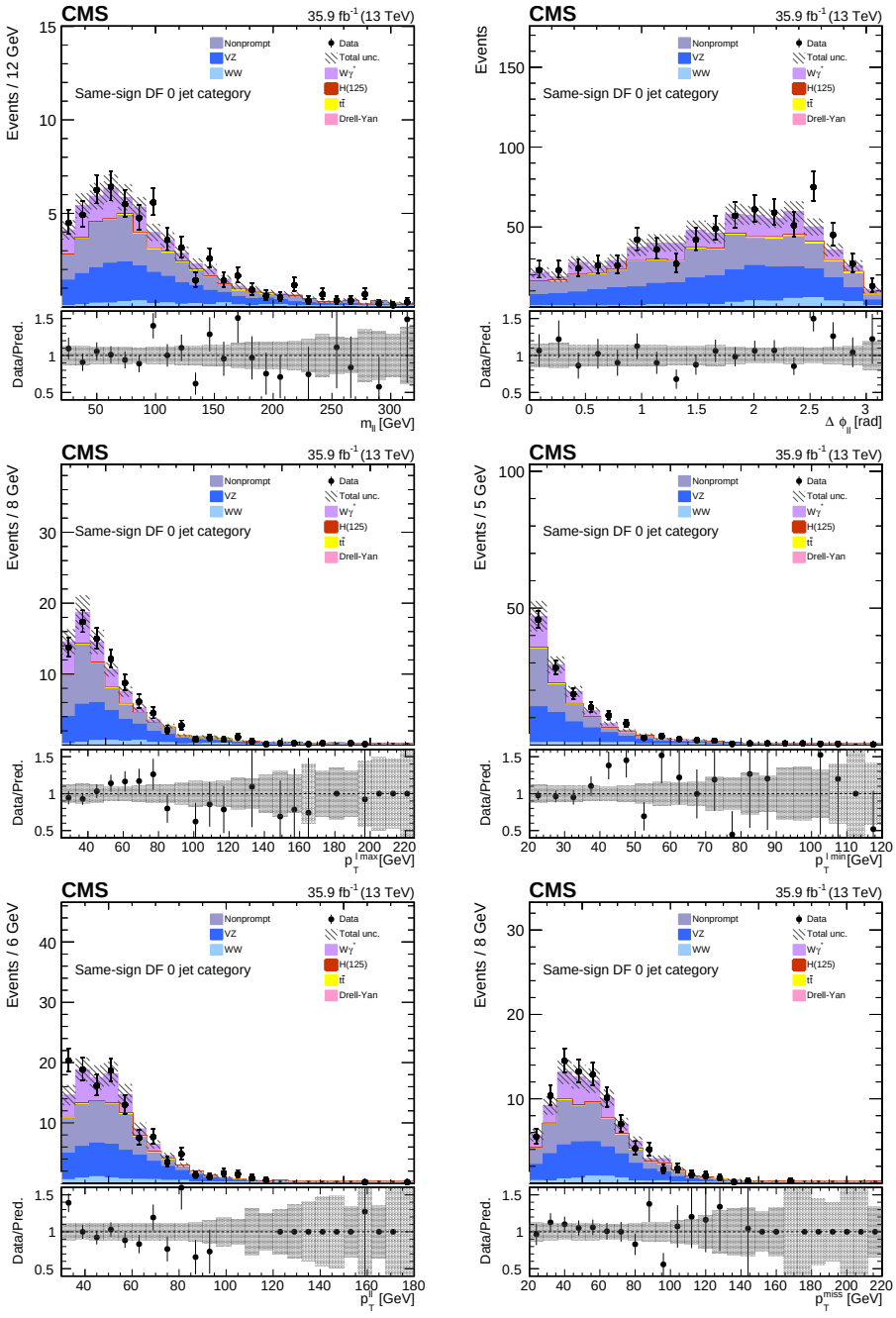

Figure 23: Distributions in $e\mu$ events for the same-sign 0-jets category region of the dilepton invariant mass ($m_{\ell\ell}$), azimuthal angle between the two leptons ($\Delta\phi(\ell,\ell)$), leading lepton p_T ($p_T^{\ell\ max}$), trailing lepton p_T ($p_T^{\ell\ min}$), dilepton p_T ($p_T^{\ell\ell}$), and missing transverse energy (E_T^{miss}). The hatched areas represent the statistical uncertainty in each bin. The ratio between data and prediction is shown in the bottom panel. The last bin includes the overflow.

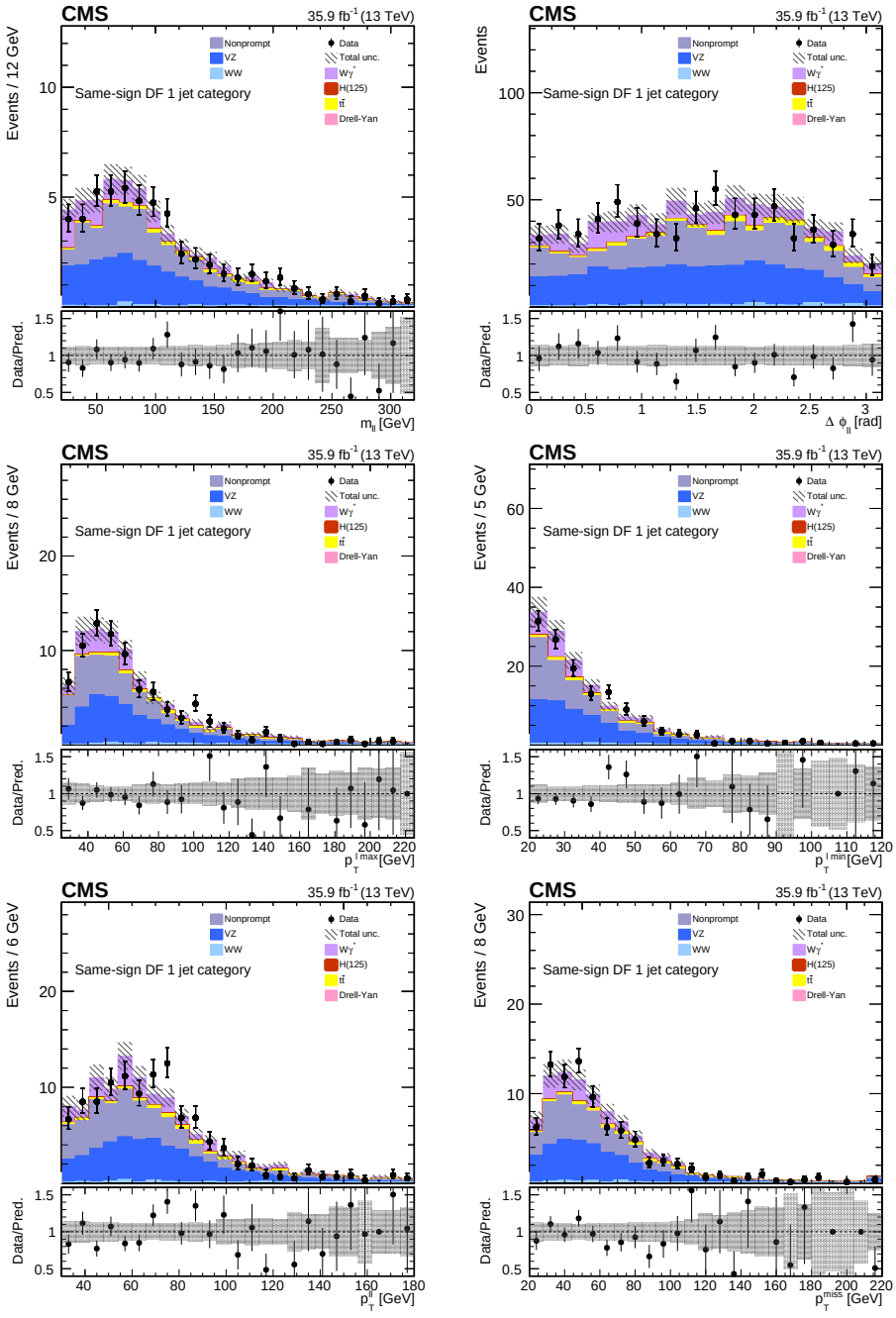

Figure 24: Distributions in $e\mu$ events for the same-sign 1-jet category region of the dilepton invariant mass ($m_{\ell\ell}$), azimuthal angle between the two leptons ($\Delta\phi(\ell,\ell)$), leading lepton p_T ($p_T^{\ell\ max}$), trailing lepton p_T ($p_T^{\ell\ min}$), dilepton p_T ($p_T^{\ell\ell}$), and missing transverse energy (E_T^{miss}). The hatched areas represent the statistical uncertainty in each bin. The ratio between data and prediction is shown in the bottom panel. The last bin includes the overflow.

7.4.2 Top background

To suppress the top background, the performance of b-tagging techniques is exploited. As detailed in Section 4.4, the *CSVv2* b-tagging algorithm is used to reject events that contain at least one jet likely coming from a B hadron decay, thus reducing significantly the amount of top quark background in the signal region.

In addition to that, the top quark p_T in $t\bar{t}$ data events is found significantly softer than those predicted by simulations based on either LO or NLO matrix elements interfaced with parton showers. The origin of this residual discrepancy might be due to higher order QCD and/or EWK corrections. The latest NNLO+EWK calculations integrate the most current theoretical knowledge of the SM $t\bar{t}$ production, and can be used to correct the top quarks p_T spectra in the used NLO $t\bar{t}$ MC. Taking this fact into account, a correction is applied on the $t\bar{t}$ events as a parametrised weight as function of the generator-level top and antitop p_T, obtained from the p_T distribution ratio of the NNLO+EWK and NLO samples [111]:

$$SF(p_T) = 0.103 \cdot e^{-0.0118 \cdot p_T} - 0.000134 \cdot p_T + 0.973 \,, \tag{28}$$

where an uncertainty of the order of the correction itself is assigned as theory uncertainty.

The top-enriched control region is defined by reverting b-veto selection on the reconstructed jets in the event. Data and simulation plots for this control region in the different-flavour channel are shown in Figures 25 and 26 for the 0-jets and 1-jet categories. Similar agreement is observed for the same-flavour categories as shown in Appendix A.

7.4.3 Drell-Yan background

The $Z/\gamma^* \to \tau^+\tau^-$ background in the different-flavour channel is estimated from simulation, where the normalization is scaled to data using a control region enriched in these events. This region is defined as the W^+W^-signal region, but inverting the $p_T^{\ell\ell}$ selection, $p_T^{\ell\ell} < 30$ GeV, and requiring $m_{\ell\ell} < 80$ GeV. In this way the purity of the $Z/\gamma^* \to \tau^+\tau^-$ sample is larger than 80%, both in the 0-jets and 1-jet categories. Some distributions of the $Z/\gamma^* \to \tau^+\tau^-$ enriched region are shown in Figures 27 and 28.

The contribution of the $Z/\gamma^* \to \ell^+\ell^-$ process to the same-flavour final states is estimated from data with the $R_{out/in}$ data-driven method, since the instrumental E_T^{miss} is not properly simulated by MC.

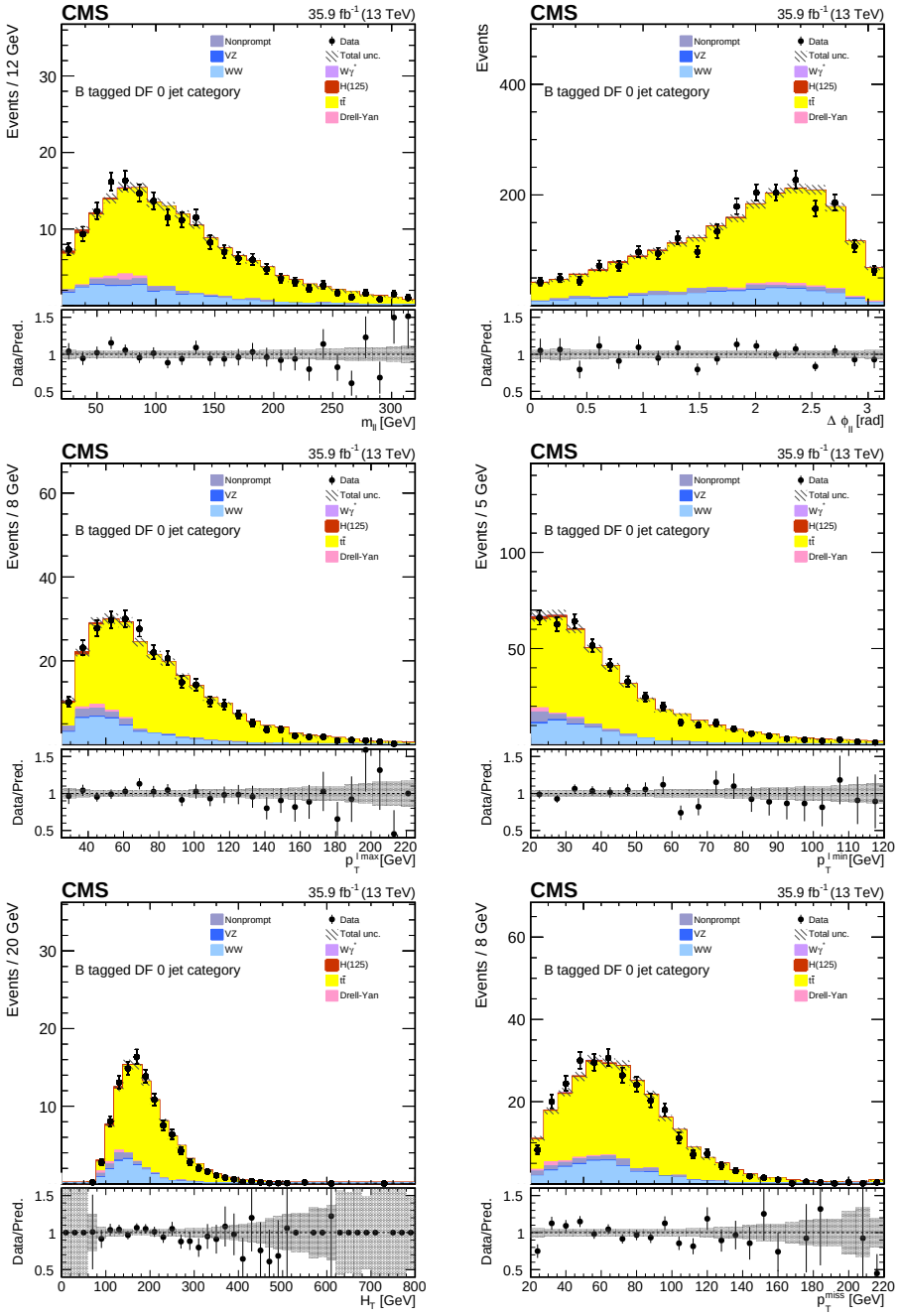

Figure 25: Distributions in $e\mu$ events for the top 0-jets category region of the dilepton invariant mass ($m_{\ell\ell}$), azimuthal angle between the two leptons ($\Delta\phi(\ell,\ell)$), leading lepton p_T ($p_T^{\ell\ \max}$), trailing lepton p_T ($p_T^{\ell\ \min}$), the p_T of the the two leptons plus E_T^{miss} plus jets system (H_T), and missing transverse energy (p_T^{miss}). The hatched areas represent the statistical uncertainty in each bin. The ratio between data and prediction is shown in the bottom panel. The last bin includes the overflow.

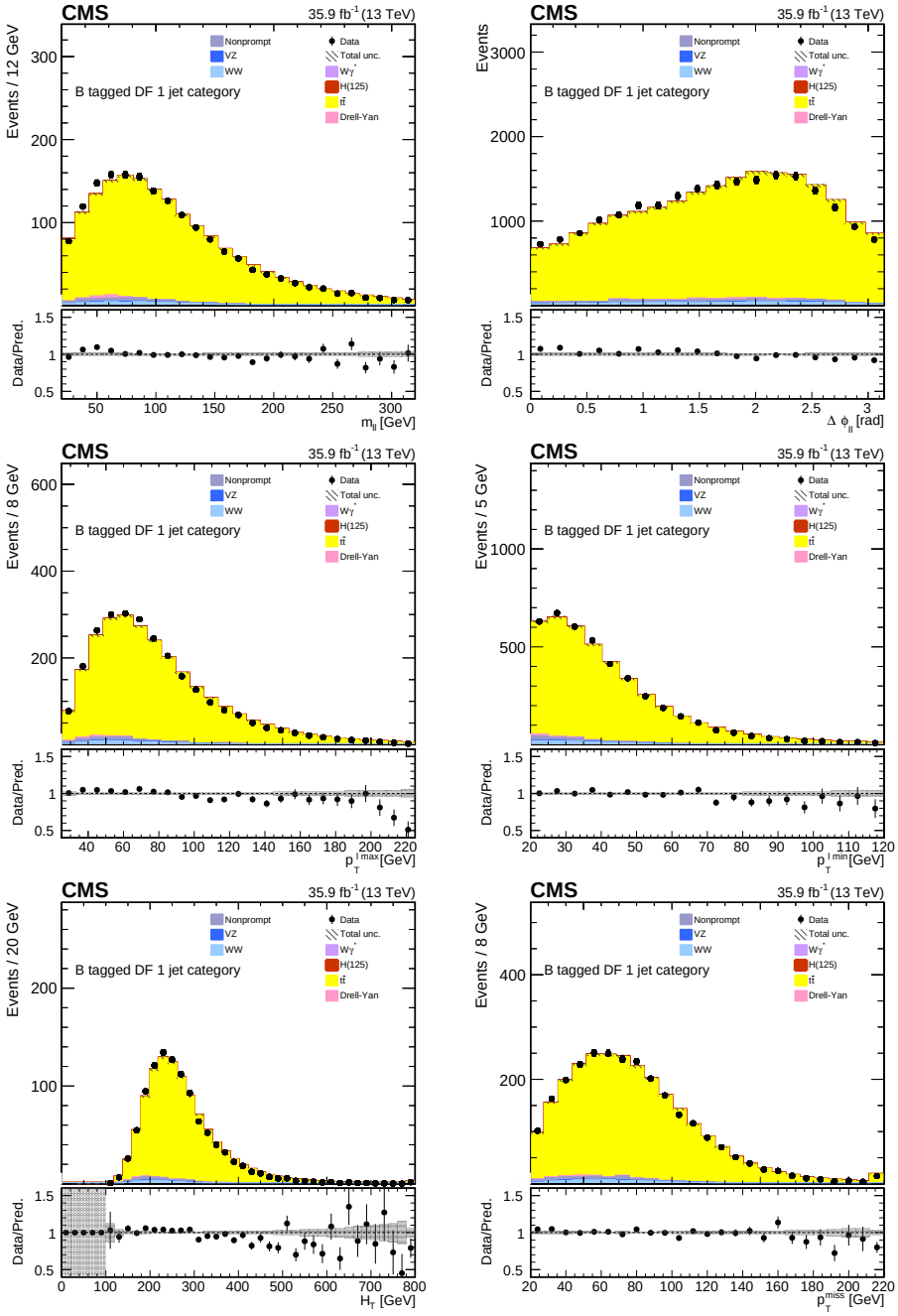

Figure 26: Distributions in $e\mu$ events for the top 1-jet category region of the dilepton invariant mass ($m_{\ell\ell}$), azimuthal angle between the two leptons ($\Delta\phi(\ell,\ell)$), leading lepton p_T ($p_T^{\ell\ \mathrm{max}}$), trailing lepton p_T ($p_T^{\ell\ \mathrm{min}}$), the p_T of the the two leptons plus E_T^{miss} plus jets system (H_T), and missing transverse energy (p_T^{miss}). The hatched areas represent the statistical uncertainty in each bin. The ratio between data and prediction is shown in the bottom panel. The last bin includes the overflow.

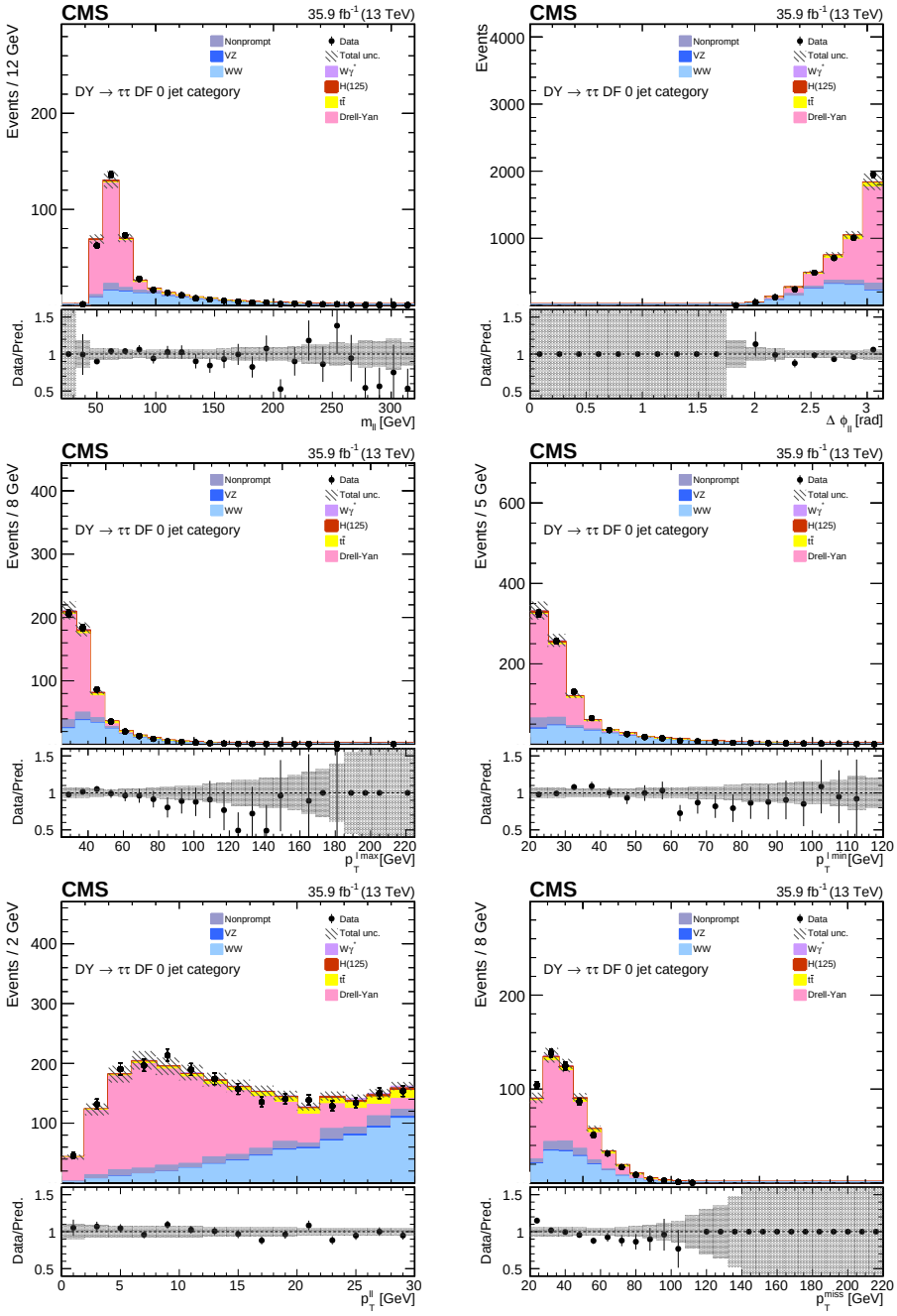

Figure 27: Distributions in $e\mu$ events for the 0-jets $Z/\gamma^* \to \tau^+\tau^-$ control region without applying the tighter $m_{\ell\ell}$ requirement of the dilepton invariant mass ($m_{\ell\ell}$), azimuthal angle between the two leptons ($\Delta\phi(\ell,\ell)$), leading lepton p_T ($p_T^{\ell\ \max}$), trailing lepton p_T ($p_T^{\ell\ \min}$), dilepton p_T, and missing transverse energy (p_T^{miss}). The hatched areas represent the statistical uncertainty in each bin. The ratio between data and prediction is shown in the bottom panel. The last bin includes the overflow.

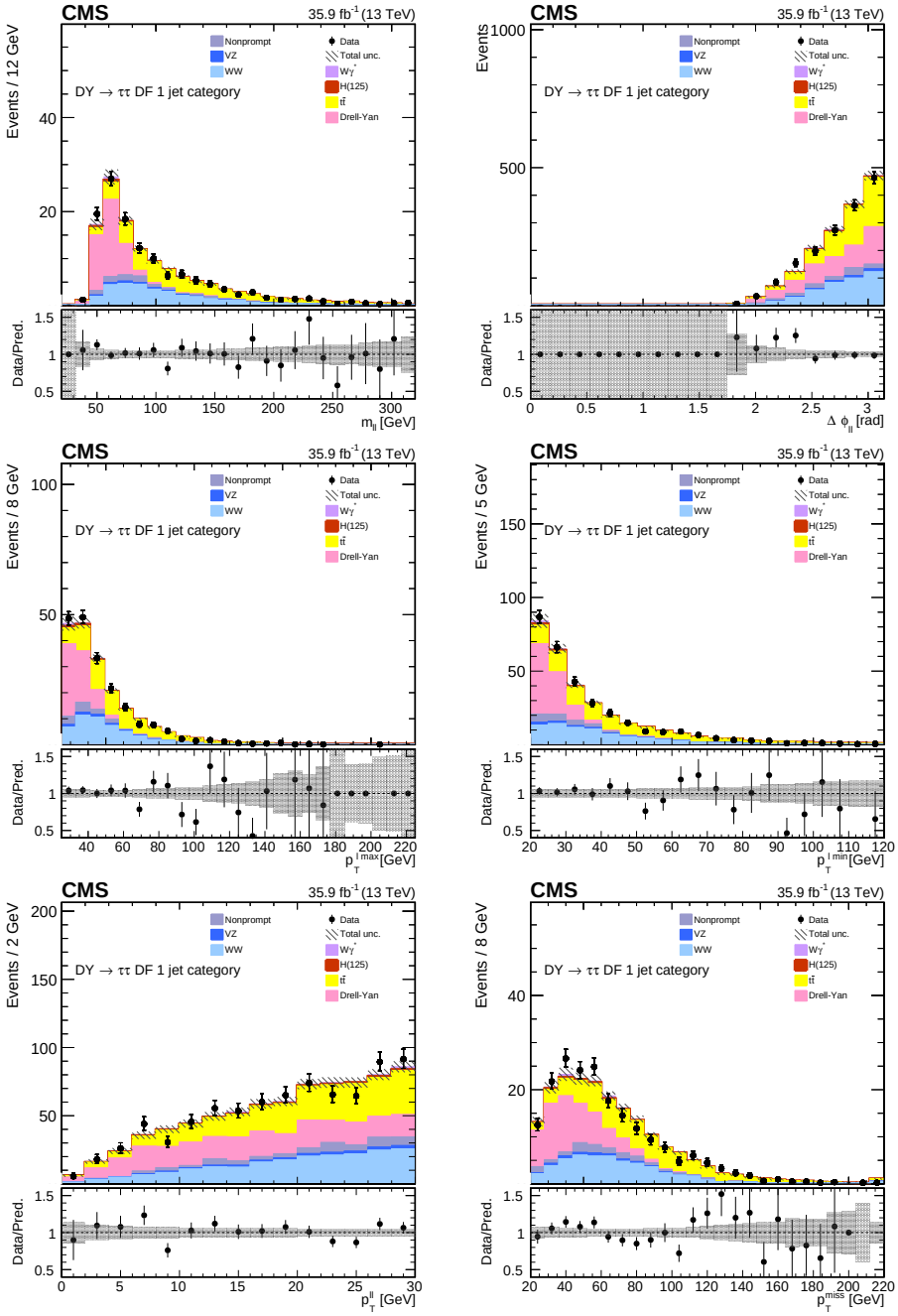

Figure 28: Distributions in $e\mu$ events for the 1-jet $Z/\gamma^* \to \tau^+\tau^-$ control region without applying the tighter $m_{\ell\ell}$ requirement of the dilepton invariant mass ($m_{\ell\ell}$), azimuthal angle between the two leptons ($\Delta\phi(\ell,\ell)$), leading lepton p_T ($p_T^{\ell\ \mathrm{max}}$), trailing lepton p_T ($p_T^{\ell\ \mathrm{min}}$), dilepton p_T, and missing transverse energy (p_T^{miss}). The hatched areas represent the statistical uncertainty in each bin. The ratio between data and prediction is shown in the bottom panel. The last bin includes the overflow.

The method aims to estimate the expected contribution from $Z/\gamma^* \to \ell^+\ell^-$ events outside the Z boson mass region in data (signal region) from the number of events inside the Z boson mass region in data (control region). The control region is defined with the same selections as the signal region but inverting the $|m_{\ell\ell} - m_Z|$ requirement, i.e., $|m_{\ell\ell} - m_Z| < 15$ GeV. Then, the number of events in the control region are scaled to the fraction of events outside and inside the Z boson mass region in simulation ($R_{out/in}$), after subtracting other physics processes that are not DY. These non-DY processes can be split into two categories:

1. Non resonant processes in the Z boson mass region, such as W^+W^-, $t\bar{t}$ or W+jets (flat dilepton mass shape around the Z window), equally decay into all the dilepton states (ee, $\mu\mu$, $e\mu$, μe), so their contribution to the Z boson mass region in data can be estimated from $e\mu$ data events ($N_{e\mu}^{in,data}$) by applying a correction factor to account for the different detection efficiency for muons and electrons (k_{ee}, $k_{\mu\mu}$).

2. Resonant processes in the Z boson mass region (peak in the dilepton invariant mass distribution at Z boson mass), such as WZ and ZZ, are estimated with simulated samples.

Thus, the estimated number of $Z \to e^+e^-$and $Z \to \mu^+\mu^-$data events inside the Z boson mass region, $N^{in,data}_{Z\to e^+e^-}$ and $N^{in,data}_{Z\to \mu^+\mu^-}$, can be written as:

$$\begin{aligned} N^{in,data}_{Z\to e^+e^-} = \Bigg[& N^{in,data}_{ee} - \frac{1}{2} k_{ee} \left(N^{in,data}_{e\mu} - N^{in,WZ\ MC}_{e\mu} - N^{in,ZZ\ MC}_{e\mu} \right) \\ & - N^{in,WZ\ MC}_{ee} - N^{in,ZZ\ MC}_{ee} \Bigg] , \end{aligned} \tag{29}$$

$$\begin{aligned} N^{in,data}_{Z\to \mu^+\mu^-} = \Bigg[& N^{in,data}_{\mu\mu} - \frac{1}{2} k_{\mu\mu} \left(N^{in,data}_{e\mu} - N^{in,WZ\ MC}_{e\mu} - N^{in,ZZ\ MC}_{e\mu} \right) \\ & - N^{in,WZ\ MC}_{\mu\mu} - N^{in,ZZ\ MC}_{\mu\mu} \Bigg] , \end{aligned} \tag{30}$$

where $k_{ee} = \sqrt{\frac{N^{in,data}_{ee}}{N^{in,data}_{\mu\mu}}}$, $k_{\mu\mu} = \sqrt{\frac{N^{in,data}_{\mu\mu}}{N^{in,data}_{ee}}}$.

Furthermore, $R_{out/in}$ is calculated from $Z/\gamma^* \to \ell^+\ell^-$simulation for both ee and $\mu\mu$ channels as:

$$R^{\ MC}_{ee\ out/in} = \frac{N^{out,DY\ MC}_{ee}}{N^{in,DY\ MC}_{ee}} , \tag{31}$$

$$R_{\mu\mu\ out/in}^{\ MC} = \frac{N_{\mu\mu}^{out,DY\ MC}}{N_{\mu\mu}^{in,DY\ MC}}\ , \tag{32}$$

where $N_{ee}^{out,DY\ MC}$ and $N_{ee}^{in,DY\ MC}$ correspond to the number of simulated DY events outside and inside the Z boson mass region respectively in the ee decay channel (same for the $\mu\mu$ decay channel).

Finally, the estimated amount of $Z/\gamma^* \to \ell^+\ell^-$ events outside the Z boson mass in the signal region, $N_{Z\to e^+e^-}^{out,data}$ and $N_{Z\to \mu^+\mu^-}^{out,data}$, are given by:

$$N_{Z\to e^+e^-}^{out,data} = N_{ee}^{in,data} \times R_{ee\ out/in}^{\ MC} \tag{33}$$

$$N_{Z\to \mu^+\mu^-}^{out,data} = N_{\mu\mu}^{in,data} \times R_{\mu\mu\ out/in}^{\ MC} \tag{34}$$

Scale factors, defined as the ratio of the estimated DY events in data and the predicted DY events from MC in the signal region, are applied to correct the differences between data and simulation as function of the DYMVA estimator for the 0-jets category and for the 1-jet category separately as shown in Figure 29.

Since the scale factors have a strong dependence with the DYMVA variable in the 0-jets signal region ($0.9 <$ DYMVA < 1.0), three scale factor bins have been considered in order to transfer properly this dependence: $0.9 <$ DYMVA < 0.95; $0.95 <$ DYMVA < 0.98; $0.98 <$ DYMVA < 1.0. In the case of the 1-jet category, the dependence is smaller, so only one scale factor bin is taken into account: $0.9 <$ DYMVA < 1.0.

The $R_{out/in}$ dependence with the DYMVA selection value is shown in Figure 30 and in Figure 31 for the 0-jets category and for the 1-jet category respectively. The maximum variation is taken as systematic uncertainty of the method (30%), and it is applied as normalization uncertainty on the DY data-driven prediction.

7.5 Results

The resulting yields from the event selection and background estimation are shown in Table 11 for data, signal, and background in the $e\mu$ channel. Some relevant distributions are shown in Figure 32 for the 0-jets category, and in Figure 33 for the 1-jet category. The data over MC agreement is reasonably good for all the

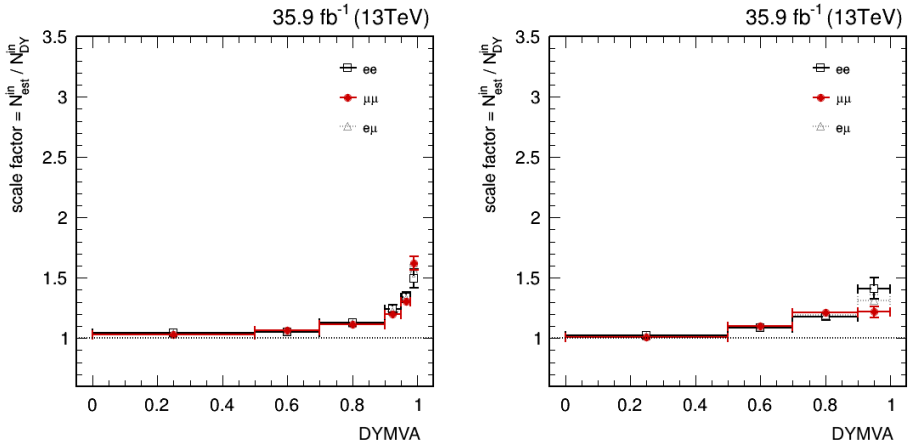

Figure 29: Estimated scale factors from the data-driven method as function of the DYMVA variable for the 0-jets bin category (on the left), and for the 1-jet bin category (on the right). The error bars represent the statistical uncertainty in each bin.

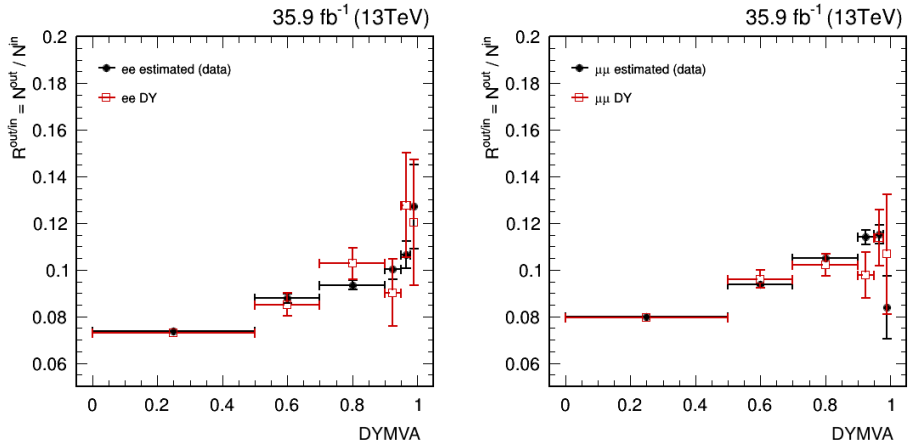

Figure 30: $R_{out/in}$ dependence on the DYMVA variable for the 0-jets category. The ee events dependence is shown on the left, while the $\mu\mu$ events dependence is shown on the right. The error bars represent the statistical uncertainty in each bin.

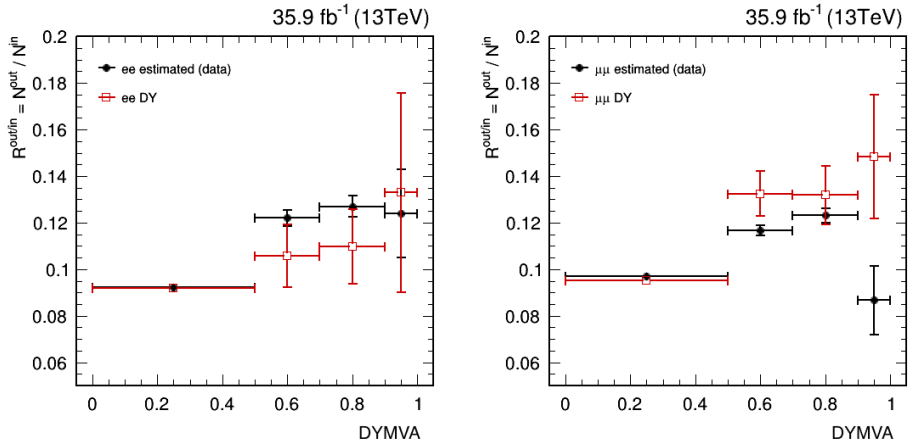

Figure 31: $R_{out/in}$ dependence on the DYMVA variable for the 1-jet bin category. The ee events dependence is shown on the left, while the $\mu\mu$ events dependence is shown on the right. The error bars represent the statistical uncertainty in each bin.

kinematic quantities within the total uncertainty.

Yields for the $ee/\mu\mu$ channel are shown in Table 12. Some relevant distributions are shown in Figure 34 for the 0-jets category, and in Figure 35 for the 1-jet category. Again, the data over MC agreement is reasonably good.

Process	0-jets category	1-jet category
$qq \to W^+W^-$	6432.2 ± 250.5	2532.0 ± 145.3
$gg \to W^+W^-$	520.6 ± 66.1	290.8 ± 38.5
Total W^+W^-	6952.8 ± 259.1	2822.8 ± 150.3
Top-quark	2113.5 ± 111.0	5002.2 ± 120.6
$Z/\gamma^* \to \ell^+\ell^-$	129.3 ± 10.5	497.8 ± 38.1
VV	226.9 ± 13.4	270.2 ± 13.4
VVV	11.4 ± 0.9	28.7 ± 2.3
Wγ^*	146.8 ± 16.9	135.5 ± 13.0
Non-prompt	975.5 ± 227.2	550.2 ± 124.7
Higgs	269.2 ± 41.1	150.4 ± 25.2
Total bkg.	3872.6 ± 257.4	6635.0 ± 180.4
W^+W^- + Total bkg.	10825.4 ± 365.2	9457.8 ± 234.9
Data	10866	9404

Table 11: Data, signal and background yields for the $e\mu$ selection channel. Statistical and systematic uncertainties are reported.

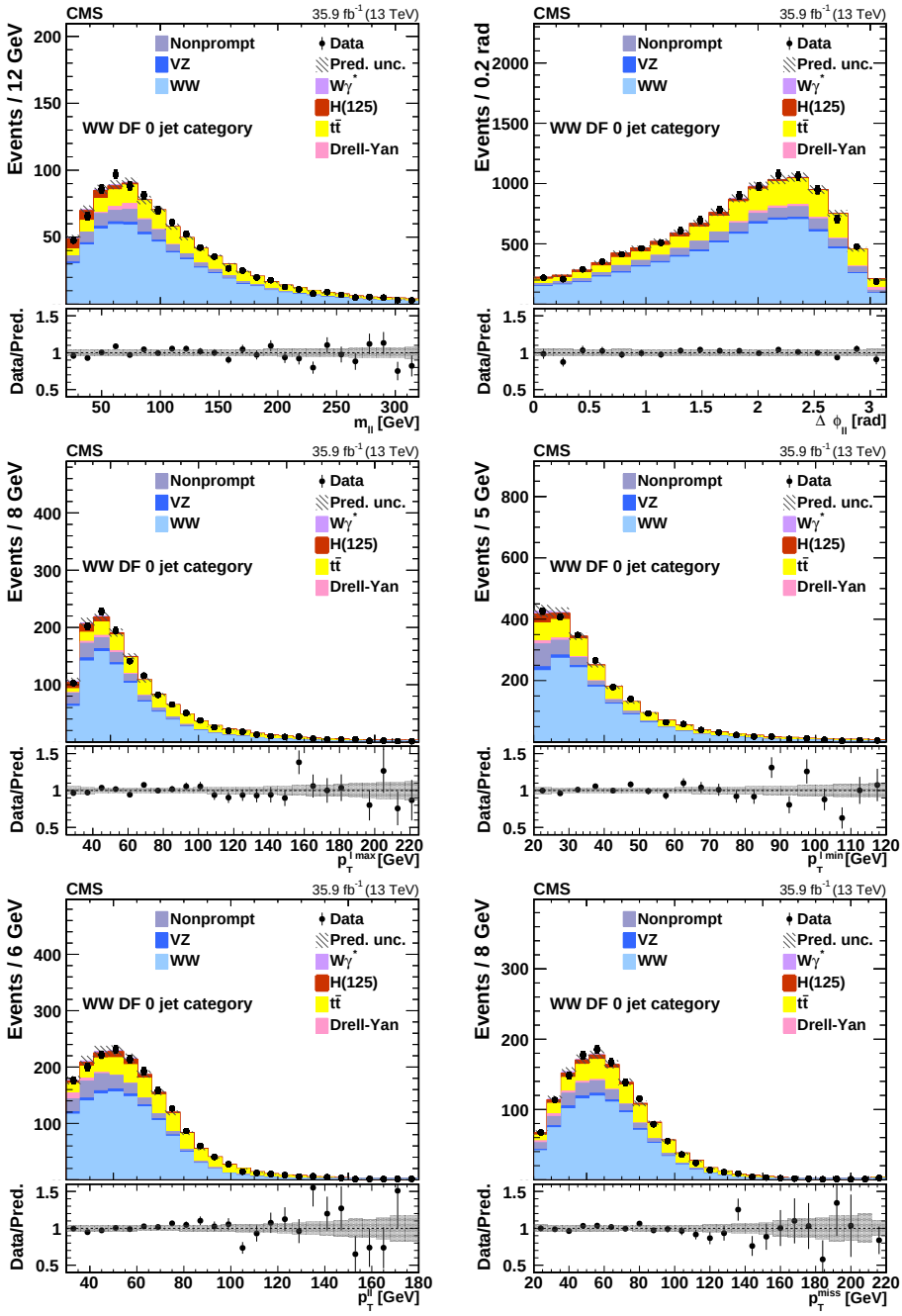

Figure 32: Distributions in $e\mu$ events for the 0-jets category of the dilepton invariant mass ($m_{\ell\ell}$), azimuthal angle between the two leptons ($\Delta\phi(\ell,\ell)$), leading lepton p_T ($p_T^{\ell\ max}$), trailing lepton p_T ($p_T^{\ell\ min}$), dilepton p_T ($p_T^{\ell\ell}$), and missing transverse energy (p_T^{miss}). The hatched areas represent the statistical and systematic uncertainty in each bin. The last bin includes the overflow.

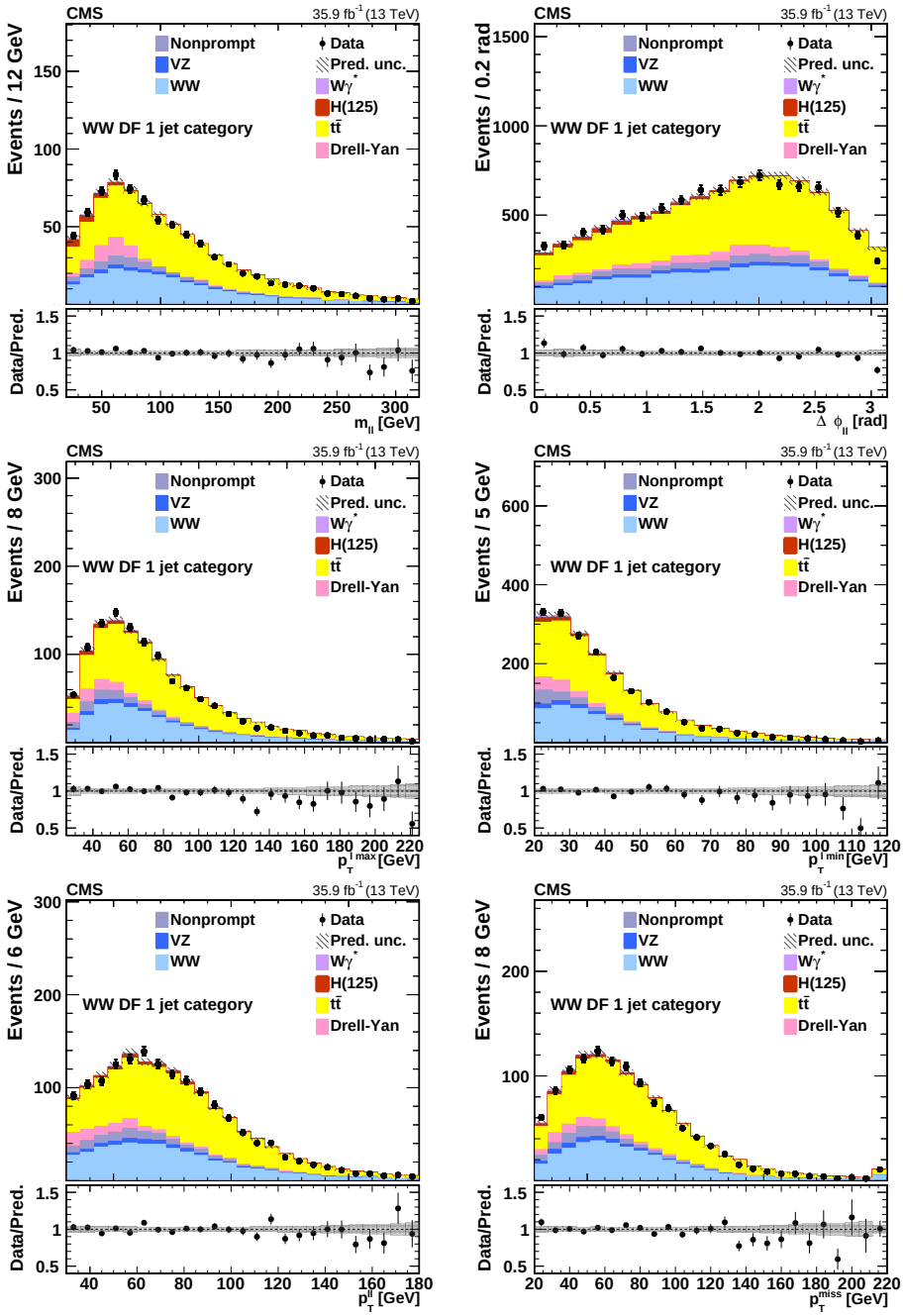

Figure 33: Distributions in $e\mu$ events for the 1-jet category of the dilepton invariant mass ($m_{\ell\ell}$), azimuthal angle between the two leptons ($\Delta\phi(\ell,\ell)$), leading lepton p_T ($p_T^{\ell\ \mathrm{max}}$), trailing lepton p_T ($p_T^{\ell\ \mathrm{min}}$), dilepton p_T ($p_T^{\ell\ell}$), and missing transverse energy (p_T^{miss}). The hatched areas represent the statistical and systematic uncertainty in each bin. The last bin includes the overflow.

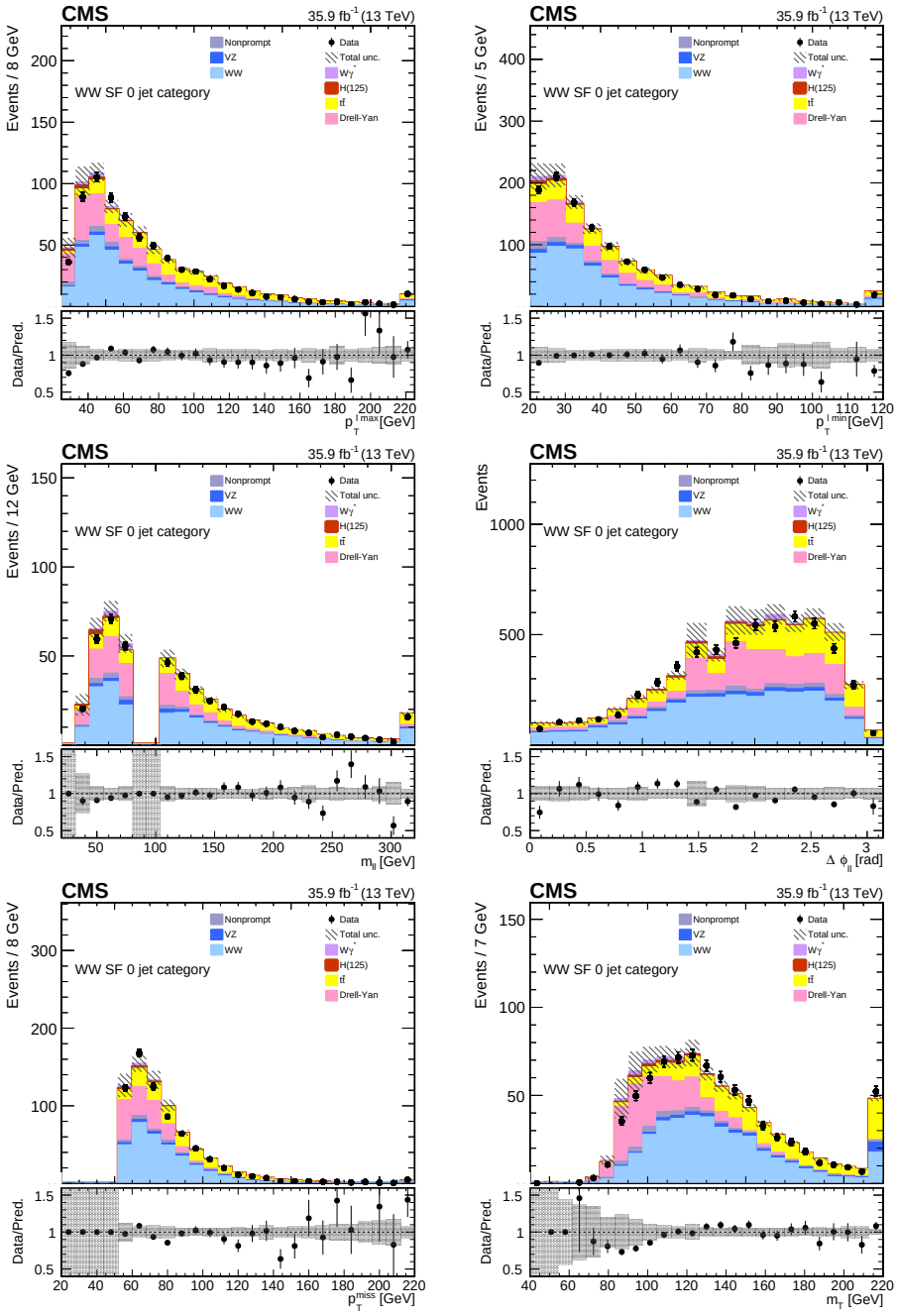

Figure 34: Distributions in $ee/\mu\mu$ events for the 0-jets category of the leading lepton p_T ($p_T^{\ell\ \max}$), trailing lepton p_T ($p_T^{\ell\ \min}$), dilepton invariant mass ($m_{\ell\ell}$), azimuthal angle between the two leptons ($\Delta\phi(\ell,\ell)$), the missing transverse energy (p_T^{miss}), and the transverse mass of the two leptons plus E_T^{miss} system (m_T). The hatched areas represent the statistical and systematic uncertainty in each bin. The last bin includes the overflow.

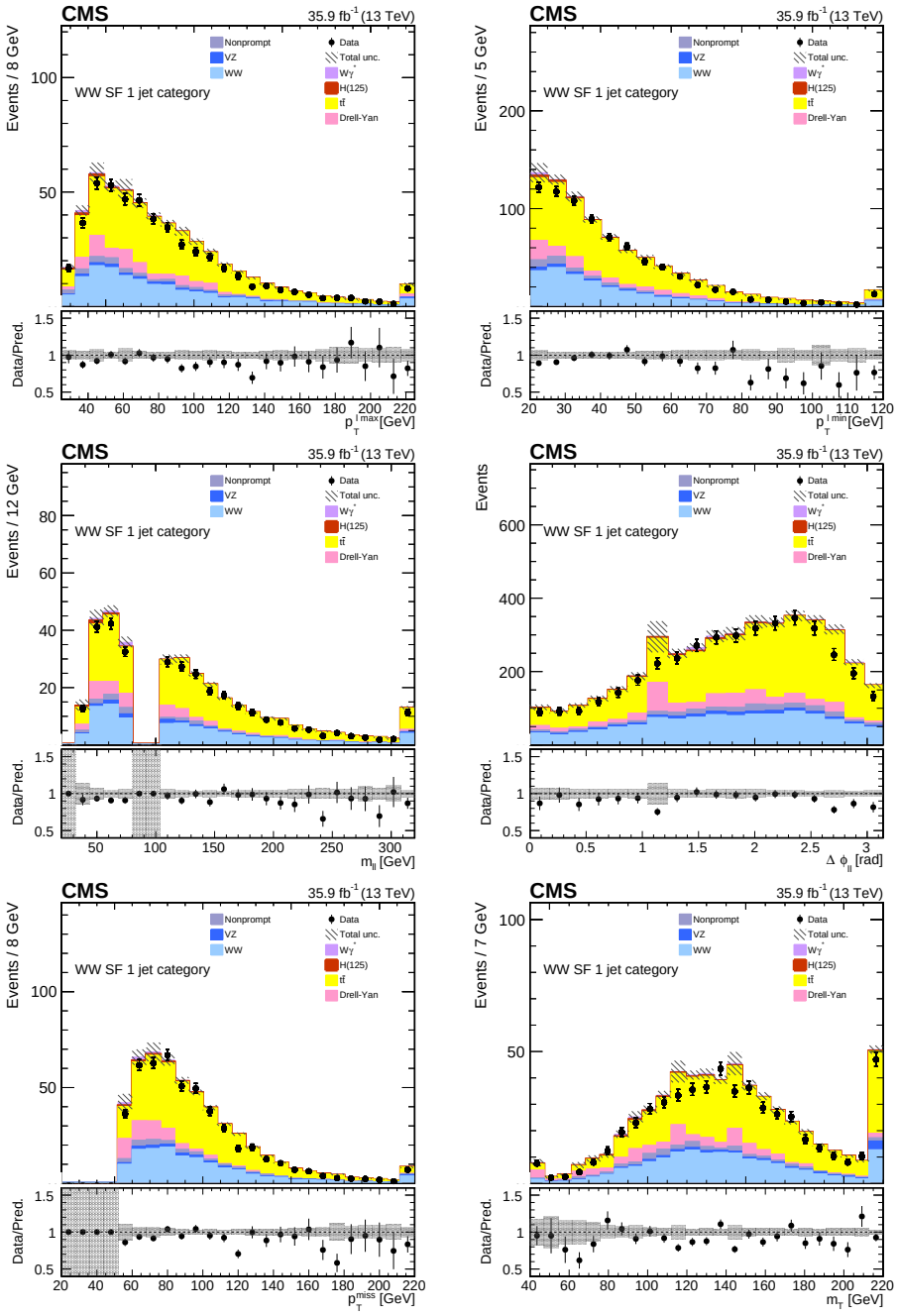

Figure 35: Distributions in $ee/\mu\mu$ events for the 1-jet category of the leading lepton p_T ($p_T^{\ell\ \mathrm{max}}$), trailing lepton p_T ($p_T^{\ell\ \mathrm{min}}$), dilepton invariant mass ($m_{\ell\ell}$), azimuthal angle between the two leptons ($\Delta\phi(\ell,\ell)$), the missing transverse energy (p_T^{miss}), and the transverse mass of the two leptons plus E_T^{miss} system (m_T). The hatched areas represent the statistical and systematic uncertainty in each bin. The last bin includes the overflow.

Process	0-jets category	1-jet category
$qq \to W^+W^-$	2500.7 ± 185.4	1018.5 ± 70.6
$gg \to W^+W^-$	228.3 ± 32.2	117.2 ± 15.2
Total W^+W^-	2729.0 ± 188.2	1135.7 ± 72.2
Top-quark	1201.7 ± 66.0	2210.6 ± 68.9
$Z/\gamma^* \to \ell^+\ell^-$	1230.5 ± 262.4	285.4 ± 85.7
VV	192.4 ± 12.1	109.9 ± 7.4
VVV	3.7 ± 0.2	6.2 ± 0.3
Wγ^*	122.9 ± 14.8	57.8 ± 6.4
Non-prompt	152.6 ± 39.2	126.9 ± 32.1
Higgs	50.3 ± 2.5	27.1 ± 1.1
Total bkg.	2953.9 ± 274.1	2823.9 ± 115.0
W^+W^- + Total bkg.	5682.9 ± 332.5	3959.6 ± 135.9
Data	5690	3914

Table 12: Data, signal and background yields for the $ee/\mu\mu$ selection channel. Statistical and systematic uncertainties are reported.

7.5.1 Total cross section measurement

To measure the cross section, a maximum likelihood fit is performed (see Section 5), where the predicted yields are fitted to the observed events. The global fit combines the four signal regions, 0-jets DF, 0-jets SF, 1-jet DF, 1-jet SF, and the four top control regions (used *one-bin* distributions). The signal strength r is the unconstrained parameter to be measured, and the top background normalization is left floating within the global fit. The whole set of uncertainties described in Section 6 are included in the likelihood function as nuisance parameters.

The propagation of the considered uncertainties to the final signal strength measurement is shown in Table 13, where it can be observed that the measurement is mainly affected by the total experimental systematic uncertainty, and in particular the uncertainty on the luminosity, on JES, on lepton quantities, and on top quark background normalization have the greatest impact on the result.

In addition to those uncertainties considered in the analysis so far, by extrapolating from the fully leptonic final states cross section to the full inclusive cross section, the branching fraction $\mathcal{B}(W \to \ell\nu)$ uncertainty (br) should be also considered. The most precise value is from the LEP measurements [112], assuming lepton universality: $\mathcal{B}(W \to \ell\nu) = 10.86 \pm 0.09\%$, which leads to 1.7% uncertainty in inclusive the cross section measurement.

The expected (using total MC prediction as pseudo-data when performing the maximum likelihood fit) and observed (using real data) signal strength measurements are reported for different different combinations of the four independent

Uncertainty source	Propagation to r (%)		
	DF	SF	DF+SF
B-tagging (b/c)	2.4	8.2	0.4
B-tagging (light)	2.3	3.6	1.0
Lepton efficiencies and p_T scale	2.1	3.2	2.1
JES	3.2	6.4	2.3
JER	0.1	0.1	0.1
Pileup	1.5	1.1	0.4
Top-quark normalization	1.8	1.5	2.0
Non-prompt estimation	2.5	1.9	1.9
Drell-Yan normalization	0.1	7.7	1.4
Simulation and data control regions sample size	0.7	4.3	1.0
Underlying event and parton shower	0.3	0.1	0.4
PDFs	0.4	0.1	0.4
QCD scales	0.7	0.4	0.5
Signal higher order effects	1.6	3.7	1.4
Luminosity	2.7	3.4	2.7
Total systematic uncertainty	7.0	15.5	5.6
Total experimental uncertainty (no lumi)	6.1	14.7	4.6
Total theoretical uncertainty	1.8	3.7	1.6
Statistical uncertainty	1.4	2.3	1.2
Total uncertainty	7.1	15.7	5.7

Table 13: Propagation of the considered uncertainties to the signal strength r measurement, in units of percent. The uncertainties are presented for the combination of the 0-jets and 1-jet categories using the different-flavour channels only, the same-flavour channels only, and both of them. It should be noted that the total uncertainty is slightly different from the square root of the sum of the squares, because it includes the correlations among the different sources of uncertainty.

channels in Table 14.

The cross section measurements (obtained simply by multiplying the observed signal strength by the signal sample cross section) for the different categories are shown in Table 15, where the combination of the 0-jets and 1-jet categories of the DF and SF final states corresponds to the final result.

The W^+W^-total production cross section is measured to be 117.6 ± 1.4 (stat) ± 5.5 (exp) ± 1.9 (theo) ± 3.2 (lumi) ± 2.0 (br) pb = 117.6 ± 6.8 pb, where (stat) refers to the uncertainty in the cross section due to statistical error in the data, (exp) to the total estimate of experimental systematic uncertainties, (theo) to the total estimate of theoretical systematic uncertainties, and (lumi) to the uncertainty on the integrated luminosity of the 2016 CMS data set.

Category	Expected r value ± total uncertainty	Observed r value ± total uncertainty
0-jet+1-jet DF	1.000 ± 0.073	1.027 ± 0.071
0-jets DF	1.000 ± 0.081	1.054 ± 0.083
1-jet DF	1.000 ± 0.132	0.930 ± 0.124
0-jet+1-jet SF	1.000 ± 0.140	0.892 ± 0.157
0-jets SF	1.000 ± 0.160	1.011 ± 0.160
1-jet SF	1.000 ± 0.210	0.757 ± 0.200
Full DF + SF combination	1.000 ± 0.058	0.990 ± 0.057

Table 14: signal strength r measurements for different combinations of the channels. The additional 1.7% uncertainty due to the $\mathcal{B}(W \to \ell\nu)$ is not considered in the results quoted in this table. Expected values are obtained by using total MC prediction as pseudo-data when performing the maximum likelihood fit, while the observed values are obtained with real data.

Category	Value ± stat ± exp syst ± theo syst ± lumi ± br [pb]
0-jet+1-jet DF	122.0 ± 1.7 ± 7.2 ± 2.1 ± 3.2 ± 2.1
0-jet+1-jet SF	106.0 ± 2.7 ± 17.5 ± 4.4 ± 4.0 ± 1.8
Full DF + SF combination	117.6 ± 1.4 ± 5.5 ± 1.9 ± 3.2 ± 2.0

Table 15: Cross section measurements (in pb) for the different categories and the combined result.

It is important to remark that the experimental measurement is compatible with the NNLO theoretical prediction within the uncertainties: $\sigma_{total}^{NNLO} = 118.8 \pm 3.6$ pb [29].

7.5.2 Fiducial and differential cross section measurements

Fiducial cross sections are defined within the acceptance phase space of the experiment, aiming to reduce the detector inefficiencies and thus minimize the extrapolation into the experimentally invisible phase space.

The fiducial definitions emulate the analysis selections as much as possible. In that way, the theoretical extrapolation from the reconstructed phase space and the fiducial one is minimized, and also the fraction of non-fiducial events (signal events that do not enter in the fiducial definitions) is reduced as well.

The fiducial region is defined at generation level, requiring two leptons in the event, electrons or muons, with $p_T > 20$ GeV and $|\eta| < 2.5$. Thus, in this case, tau leptonic decays are considered as non-fiducial events. In addition, the dilepton invariant mass must be greater than 20 GeV, the dilepton p_T must be greater than 30 GeV, and the p_T^{miss} is required to be greater than 20 GeV (where p_T^{miss} is calculated using the transverse momentum of the emitted neutrinos from the W boson decays).

The fiducial cross section measurement is performed by letting the fiducial signal events float to the data within the maximum likelihood fit, where the non-fiducial events are considered as background.

The measured fiducial cross section, combining the DF and SF channels and the 0-jets and 1-jet final states, is $\sigma^{fid} = 1.529 \pm 0.020$ (stat) ± 0.069 (exp) ± 0.028 (theo) ± 0.041 (lumi) pb $= 1.529 \pm 0.087$ pb, which agrees well with the theoretical prediction $\sigma^{\text{fid}}_{\text{NNLO}} = 1.531 \pm 0.043$ pb [29]. Based on 0-jets and 1-jet (reconstructed) categories only, the following results are obtained for the combination of the DF and SF channels: σ^{fid}(0-jets) $= 1.61 \pm 0.10$ pb and σ^{fid}(1-jet) $= 1.35 \pm 0.11$ pb.

The fiducial cross section for W^+W^-+0-jets category (adding the 0-jets requirement at generation level to the fiducial region definition) is also measured for several jet p_T thresholds. The results are shown in Figure 36 compared to the POWHEG and PYTHIA predictions, where the cross section is expected to increase with the jet p_T threshold because the phase space for 0-jets increases. It can be observed that the agreement is reasonable good within the uncertainties.

The inclusive fiducial cross section measurements report a single value for the given fiducial region, while the differential measurements report cross sections for a given distribution within the fiducial region. The technical implementation for the differential cross section measurements is simple: instead of having a single signal strength, there are as many of them as bins in the fiducial region; and the non-fiducial events are treated as an additional background process. Then, a

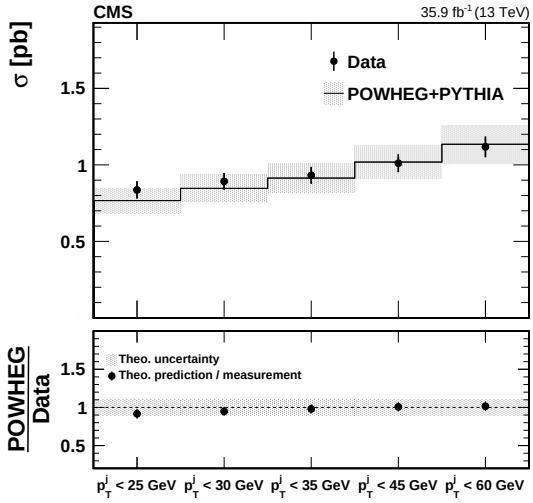

Figure 36: Fiducial cross section measurements for the combination of the different-flavour and same-flavour channels in the 0-jets category for several jet p_T thresholds, compared with POWHEG + PYTHIA predictions. The gray band around 1 in the ratio plots represent the systematic uncertainties, while the error bars on the markers show the statistical uncertainty on data.

multidimensional fit is performed to obtain the best fit value for all those signal strengths, where the simultaneous fit to all bins in a given histogram takes all the correlations into account.

The differential cross sections normalized to the total fiducial cross section, compared to the POWHEG and PYTHIA predictions, are shown in Figure 37 as function of $m_{\ell\ell}$, $p_T^{\ell\, max}$, $p_T^{\ell\, min}$, $p_T^{\ell\ell}$, and $\Delta\phi(\ell,\ell)$, where the binning in each case has been defined by setting approximately the same number of generated signal events per bin. It can be noticed that the measurements are in good agreement with the predictions within the uncertainties.

7.5.3 Limits on Wilson coefficients

The Effective Field Theory (EFT), postulates that any new physics can be written as an infinite series of the new interaction terms organized as an expansion in the mass dimension of the operators [113], where the first order term of the expansion corresponds to the dimension four operators in the SM. The momentum series is understood as coming from the integration of heavy fields in an UV-complete theory, that can be renormalizable and unitary. To probe experimentally the presence of these higher-dimensional operators, we consider the case in which just one or few operators have non-vanishing coupling constants. The truncated series

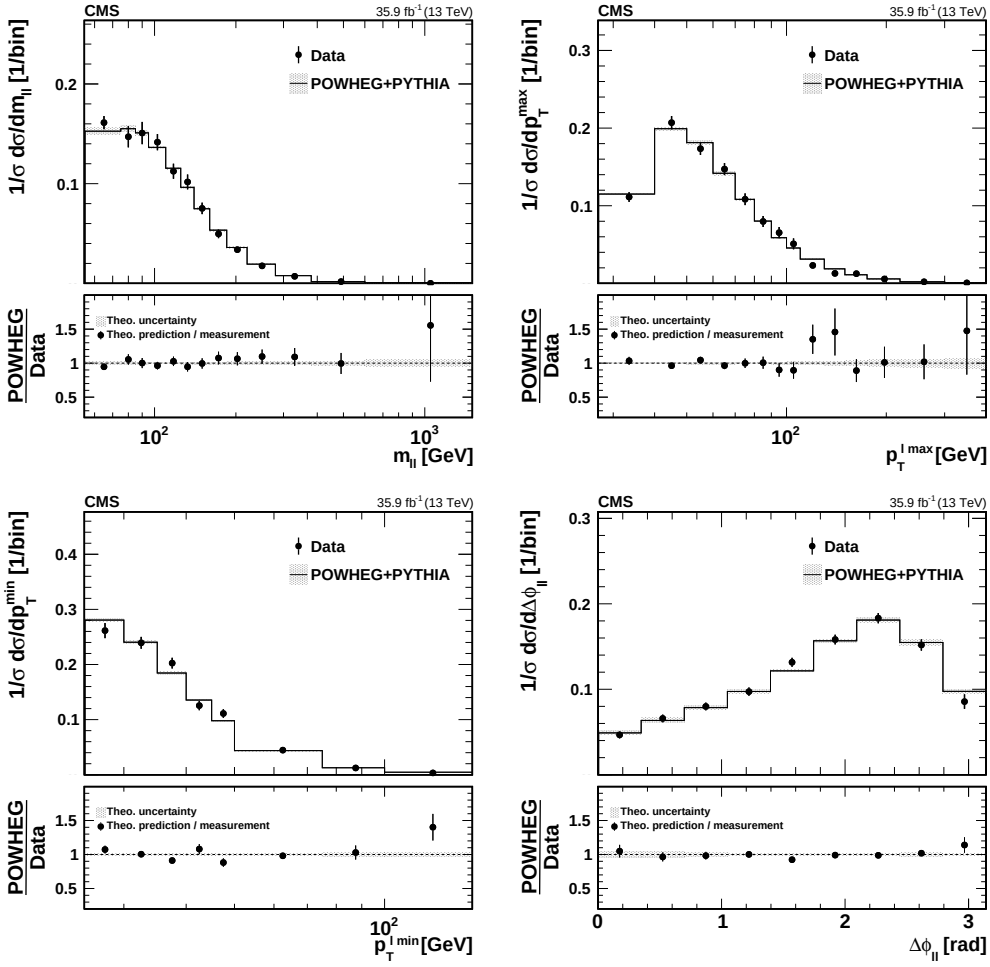

Figure 37: Differential cross sections measurements. The upper panels show the normalized differential cross sections with respect to the dilepton mass $m_{\ell\ell}$, leading lepton $p_T^{\ell\,max}$, trailing lepton $p_T^{\ell\,min}$, and dilepton azimuthal angular separation $\Delta\phi(\ell,\ell)$, compared to POWHEG predictions. The lower panels show the ratio of the theoretical predictions to the measured values. The error bars on the data points represent the total uncertainty of the measurement, and the shaded band depicts the uncertainty of the MC prediction.

is not renormalizable and will violate tree-level unitarity at some energy scale. Thus, it is only useful when the scale of new physics is large compared to the accessible energies in the scattering process, in which case the next momentum orders are heavily suppressed.

In the electroweak sector of the SM, the first higher-dimensional operators containing only massive boson are six-dimensional [114] and are listed below.

$$\begin{aligned}
\mathcal{O}_{WWW} &= \frac{c_{WWW}}{\Lambda^2} W_{\mu\nu} W^{\nu\rho} W_{\rho}^{\cdot\,\mu}, \\
\mathcal{O}_{W} &= \frac{c_{W}}{\Lambda^2} (D^{\mu}\Phi)^{\dagger} W_{\mu\nu} (D^{\nu}\Phi), \\
\mathcal{O}_{B} &= \frac{c_{B}}{\Lambda^2} (D^{\mu}\Phi)^{\dagger} B_{\mu\nu} (D^{\nu}\Phi), \\
\widetilde{\mathcal{O}}_{WWW} &= \frac{\widetilde{c}_{WWW}}{\Lambda^2} \widetilde{W}_{\mu\nu} W^{\nu\rho} W_{\rho}^{\cdot\,\mu}, \\
\widetilde{\mathcal{O}}_{W} &= \frac{\widetilde{c}_{W}}{\Lambda^2} (D^{\mu}\Phi)^{\dagger} \widetilde{W}_{\mu\nu} (D^{\nu}\Phi),
\end{aligned} \tag{35}$$

where $W_{\mu\nu}$ is the $SU(2)$ field strength, $B_{\mu\nu}$ is the $U(1)$ field strength, Φ is the Higgs doublet, and operators with tilde are the magnetic duals of the field strengths. The first three operators are CP-preserving, while the two last one are not.

In this analysis, we will assume models with CP-preserving operators turned on either individually (1D scan), or in pairs (2D scan). With these assumptions, the value of the coupling constants (c_{WWW}/Λ^2, c_W/Λ^2, c_B/Λ^2), commonly denominated as Wilson coefficients, will be measured.

These three interesting operators, denoted as aTGCs, have a rich phenomenology since they contribute to many of multiboson scattering processes. $\mathcal{O}_{WWW}$ modifies the vertices with 3 to 6 vector bosons, while $\mathcal{O}_W$ and $\mathcal{O}_B$ modify both HVV vertices and vertices with 3 or 4 vector bosons. A more detailed description of the phenomenology of these operators can be found in [115]. Here we will be interested in the modification to the vertices HWW, γWW and ZWW, since they modify the $pp \to W^+W^-$ cross-section via diagrams of the kind shown in Figure 38.

MadGraph5_aMC@NLO [72] is used for generating the aTGCs signal sample for the qq $\to$ $\mathrm{W^+W^-}$ induced production, while the showering and hadronization of the events are made with PYTHIA8. The simulated sample provides a SM event weight (considering only SM couplings), and aTGC weights based on a 3D grid in $c_{WWW}/\Lambda^2 \times c_W/\Lambda^2 \times c_B/\Lambda^2$, which is defined with the following discrete values: $c_{WWW}/\Lambda^2 = [-3, -1.5, 0, 1.5, 3]$ TeV^{-2}, $c_W/\Lambda^2 = [4, -2, 0, 2, 4]$ TeV^{-2}, and

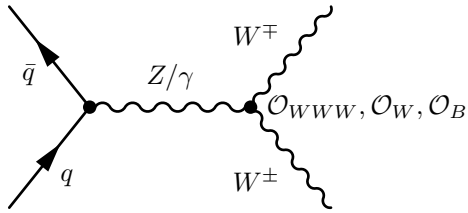

Figure 38: One of the Feynman diagrams through which 6-dimension electroweak operators modify the $pp \to W^+W^-$ cross section.

$c_B/\Lambda^2 = [-20, -10, 0, 10, 20]$ TeV^{-2}

The signal MadGraph5_aMC@NLO qq $\to$ W$^+$W$^-$ sample is scaled-up in order to account for the gg $\to$ W$^+$W$^-$ contribution. As the efficiency of the number of jets is different for gg $\to$ W$^+$W$^-$ and qq $\to$ W$^+$W$^-$, the scale factor is estimated separately for the 0-jets and 1-jet categories by taking into account the qq $\to$ W$^+$W$^-$ and gg $\to$ W$^+$W$^-$ yields at different-flavour selection level (see Section 7.3 and Table 11). The estimated scale factors to be applied to the qq $\to$ W$^+$W$^-$ sample are shown in Table 16.

Process	0-jets category	1-jet category
$qq \to W^+W^-$	6432.2 ± 250.5	2532.0 ± 145.3
$gg \to W^+W^-$	520.6 ± 66.1	290.8 ± 38.5
Scale factor	1.08 ± 0.09	1.11 ± 0.14

Table 16: Scale factor values to be applied to the MadGraph qq $\to$ W$^+$W$^-$ sample in order to take into account the gg $\to$ W$^+$W$^-$ contribution. The calculation is done by taking the qq $\to$ W$^+$W$^-$ and gg $\to$ W$^+$W$^-$ yields from the different-flavour analysis selection (see Section 7.3 and Table 11).

The aTGC samples have been validated by comparing MadGraph5_aMC@NLO with POWHEG predictions for the SM couplings as shown in Figure 39. This comparison has been done at the pre-selection level showed in Table 17, and the agreement between the two generators is reasonable good.

The chosen variable to measure the coupling constants is the invariant mass distribution of the two reconstructed leptons (m_{ll}). Being a well measured Lorentz invariant, this variable is robust against mismodeling and sensible to the aTGCs, so it is ideal for this purpose. The choice of the used binning is made to maximise the expected 95% CL intervals for all couplings while keeping enough MC statistic in each bin: [100, 200, 300, 400, 500, 600, 700, 750, 800, 850, 1000, Inf.] GeV,

Variable	Selection
$q_{\ell_1} \times q_{\ell_2}$	< 0
p_T^{ℓ} [GeV]	$> 25/20$
E_T^{miss} [GeV]	> 20
$p_T^{\ell\ell}$ [GeV]	> 30
$m_{\ell\ell}$ [GeV]	> 20
Additional leptons ($p_T^{\ell} > 10$ GeV)	veto

Table 17: Summary of the event selection for the aTGC samples validation.

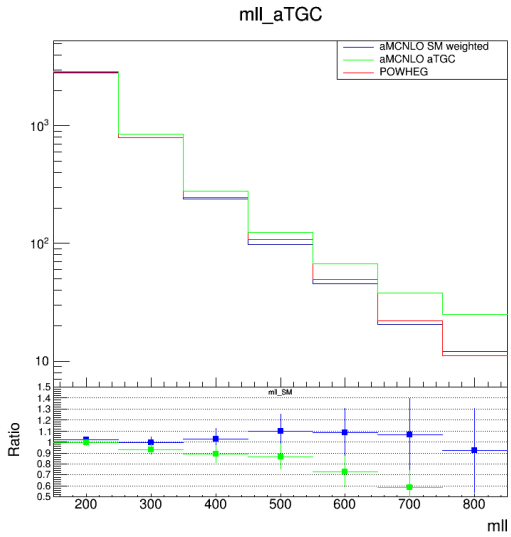

Figure 39: Comparison plot for the MadGraph5_aMC@NLO sample validation. The black line corresponds to the MadGraph5_aMC@NLO sample weighted by the SM weight (SM coupling), the green line corresponds to the MadGraph5_aMC@NLO sample weighted by the most sensitive aTGC weight, and the red one corresponds to the POWHEG prediction. The ratio plot is computed with respect the POWHEG sample.

where the last bin contains the overflow.

To perform the analysis, only the different-flavour events are studied, since the overwhelming amount of DY background in the same-flavour channel makes this channel insensitive to the aTGCs. Also, to suppress the Higgs boson contribution that should also be affected by the anomalous couplings but is not included in the simulated sample, the low di-lepton invariant mass region is removed by requesting $m_{\ell\ell} > 100$ GeV on top of the baseline selection from Section. 7.3.

The background estimation procedure is also identical to the one described in Section 7.4, where although the WZ and ZZ components of the background receive contributions from the dimension-6 operators, they are not varied since they represent a small component of the total yield after selection. Both the signal and top control regions are included in the global fit, where the signal region includes the shape information of the $m_{\ell\ell}$ variable, while in the top control region only *one-bin* distribution is considered. The top background is left floating and will be constrained in the global fit. The 0-jets and 1-jet categories are both used separately and combined to get the final results. Finally, since the sensitivity to aTGCs is concentrated at high energy regime, 5% of systematic uncertainty for $m_{\ell\ell} > 600$ GeV associated to the EWK corrections [116] has been included as nuisance in the model.

In order to build the m_{ll} templates, the associated weights calculated for each event are used to construct a parametrized model of the expected yield in each bin as a function of the values of the three coupling constants. More precisely, for each bin, we fit the ratios of the expected signal yield with dimension-6 operators to the one without (SM) in each point of 5×5 grid to a quadratic polynomial in two dimensions (equivalently, quadratic polynomial in one dimension when considering the hypothesis of a single dimension-6 operator turned on). The fits for the highest m_{ll} bins can be seen in Figure 40 for the 0-jets category. There are similar fits for the other bins and for the 1-jet category.

Figure 41 shows the $m_{\ell\ell}$ distributions for the 0-jets and 1-jet categories, where the expected signal distributions for three values of the coefficients close to the corresponding 95% CL expected limits are also plotted. It can be observed that the sensitivity is concentrated at $m_{\ell\ell} > 850$ GeV.

Figure 42 shows the expected and observed $-2\Delta \ln L$ distributions for the three dimension-6 operators considered, after combining the 0-jets and 1-jet categories. The corresponding 68% and 95% CL are reported in Table 18. Figures 43 show the expected and observed $-2\Delta \ln L$ contours (68% and 95% CL) for the three dimension-6 operators pairs considered. It should be noted that when performing the 1D scans, the other two coupling constants are set to zero, while when performing the 2D scans, the other coupling constant is also set to zero.

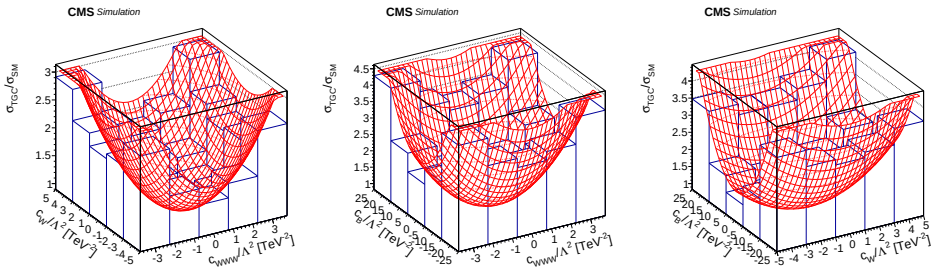

Figure 40: Quadratic polynomial fit for the $\mathcal{O}_{WWW} \times \mathcal{O}_W$ grid (left panel), $\mathcal{O}_{WWW} \times \mathcal{O}_B$ grid (central panel), and $\mathcal{O}_W \times \mathcal{O}_B$ grid (right panel). The vertical axis shows the ratio between the expected signal yield with dimension-6 operators to the SM for events with $m_{ll} > 850\,\text{GeV}$.

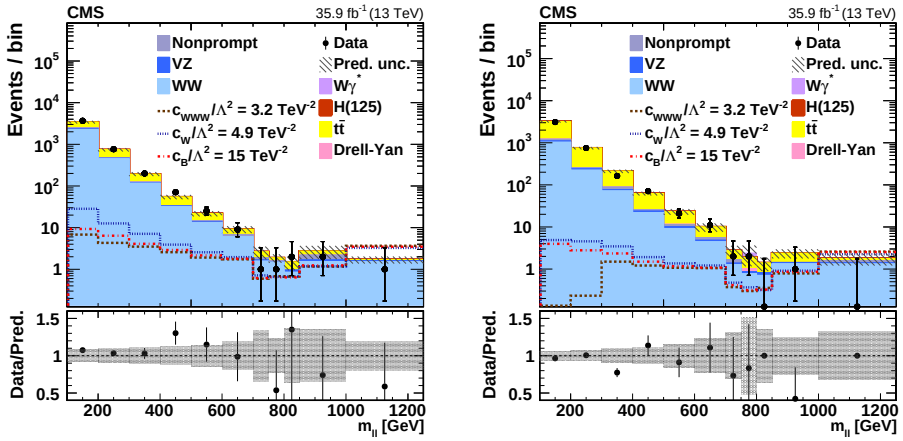

Figure 41: Comparison of the template fits to the observed $m_{\ell\ell}$ distributions in the 0-jets (left) and 1-jet (right) categories. The non-SM contributions for $c_{WWW}/\Lambda^2 = 3.2$ TeV^{-2}, $c_W/\Lambda^2 = 4.9$ TeV^{-2}, and $c_B/\Lambda^2 = 15.0$ TeV^{-2} are shown, not stacked on top of the other contributions. The last bin contains all events with reconstructed $m_{\ell\ell} > 1000$ GeV. The error bars on the data points represent the statistical uncertainties for the data, and the hatched areas represent the total uncertainty in each bin.

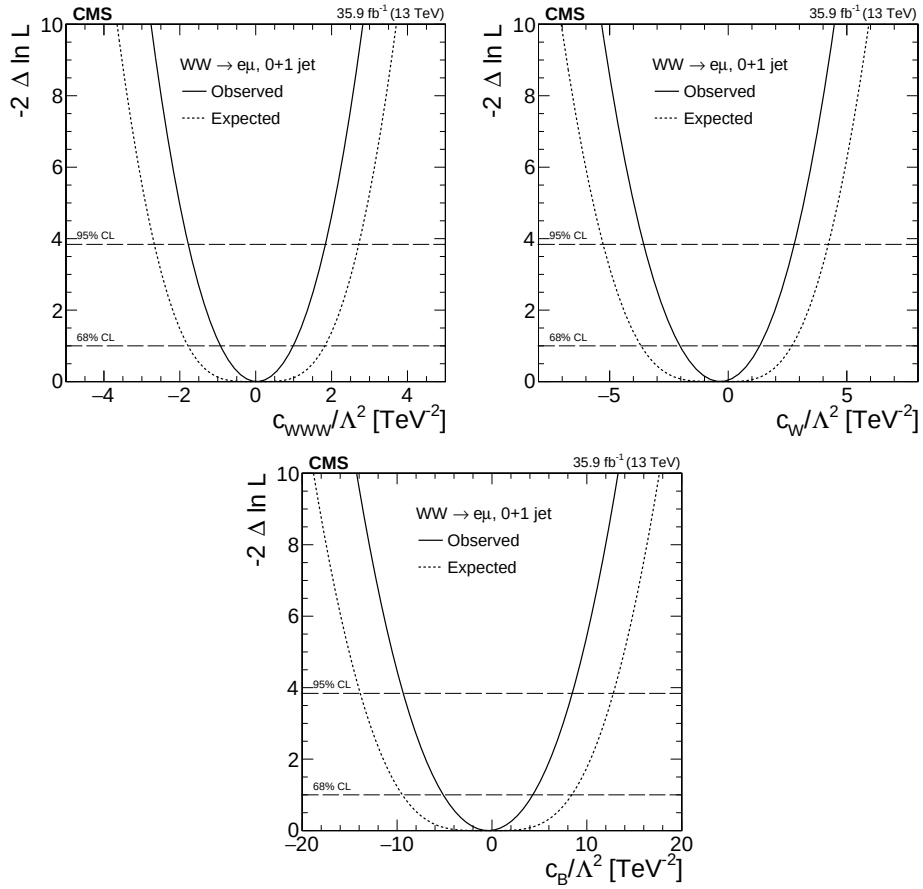

Figure 42: The expected and observed $-2\Delta \ln L$ values for the c_{WWW}/Λ^2, c_W/Λ^2, and c_W/Λ^2 1D scans combining the 0-jets and 1-jet categories.

Coupling constant	Exp. 68% (TeV^{-2})	Exp. 95% (TeV^{-2})	Obs. 68% (TeV^{-2})	Obs. 95% (TeV^{-2})
c_{WWW}/Λ^2	$[-1.78, 1.82]$	$[-2.67, 2.71]$	$[-0.93, 0.99]$	$[-1.78, 1.84]$
c_W/Λ^2	$[-3.67, 2.68]$	$[-5.28, 4.22]$	$[-2.03, 1.33]$	$[-3.56, 2.78]$
c_B/Λ^2	$[-9.45, 8.40]$	$[-13.88, 12.79]$	$[-5.14, 4.30]$	$[-9.35, 8.46]$

Table 18: Expected and observed 68% and 95% CL intervals on the measurement of the coupling constants associated to the three CP-preserving electroweak dimension-6 operators.

Comparing with previous W^+W^-CMS results [32], these limits are between a factor 2 and 3 stronger. Also, comparing with other results not only from CMS but also from ATLAS, D0, or LEP, it can be seen in Figure 44 that this analysis provides some of the strongest limits on the three Wilson coefficients.

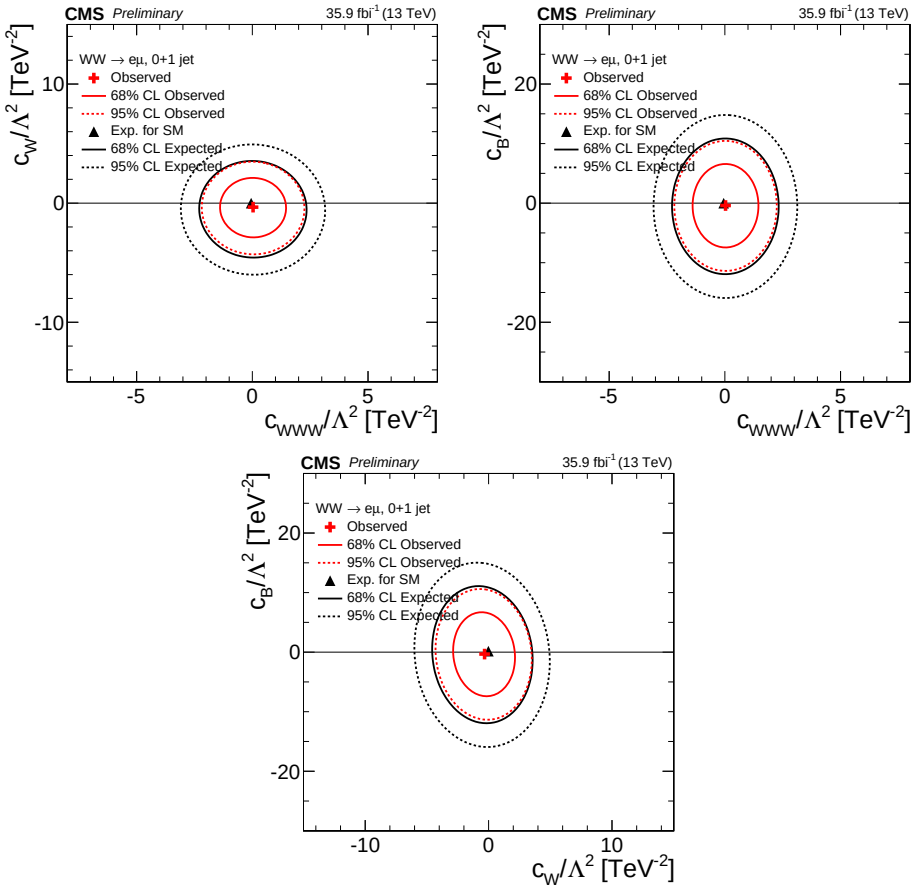

Figure 43: The expected and observed $-2\Delta \ln L$ values for the $c_{WWW}/\Lambda^2 \times c_W/\Lambda^2$, $c_{WWW}/\Lambda^2 \times c_B/\Lambda^2$, and $c_W/\Lambda^2 \times c_B/\Lambda^2$ 2D scans combining the 0-jets and 1-jet categories.

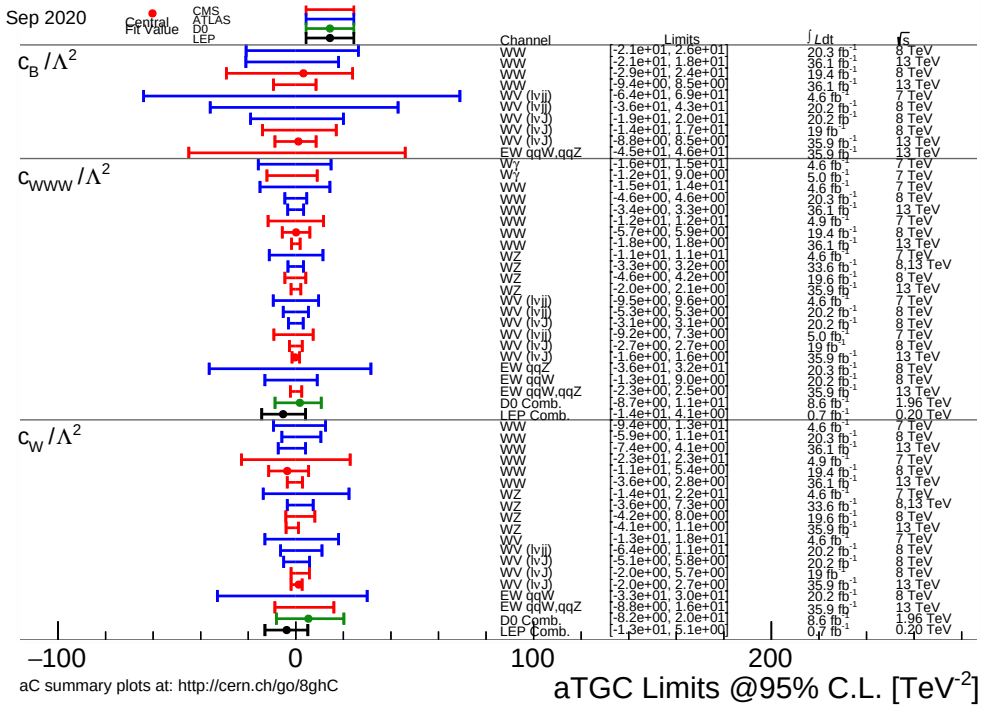

Figure 44: Limits on the Wilson coefficients using the effective field theory interpretation given by several analysis from CMS, ATLAS, D0 and LEP experiments. Figure provided by the CMS Collaboration for conference purposes.

8 Dark Higgs search

The simplified model used in this work, so-called the *dark Higgs* model [33], motivated in Section 1, predicts a new signature at the LHC with SM particles from the decay of the dark Higgs boson and a DM pair production. This signature is quite similar to the *mono-Higgs* searches [28], with the difference in this case the mass of the dark Higgs boson is a free parameter within the model.

The model assumes the emission of a dark Higgs boson, postulates a Majorana fermion χ as DM particle [117], and requires the presence of a Z' boson [118] vector mediator, to be able to produce DM particles in the final state. The independent parameters of the model are the dark Higgs boson mass m_s, the Z' mass $m_{Z'}$, the DM particle mass m_χ, the Z' coupling to quarks (g_q), the Z' coupling to DM particles (g_χ), and the mixing angle between the SM and the dark Higgs bosons ($\sin\theta$). The Feynman representation of the model is shown in Figure 45.

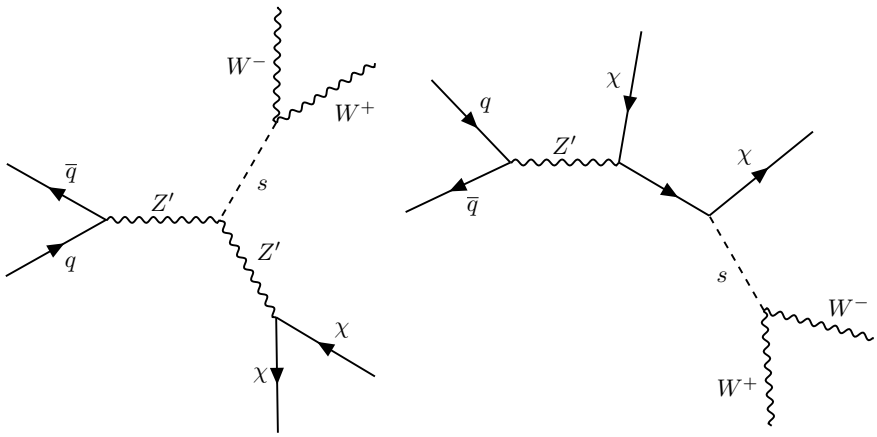

Figure 45: Representative Born-level Feynman diagrams for the benchmark signal model considered in this study: $q\overline{q} \to Z' \to s\chi\chi$, and $s \to W^+W^-$.

In this section the dark Higgs search is described, whose public results can be found in [119]. The aim of this analysis is to test the dark Higgs model using 2016, 2017, and 2018 CMS data. It is worth to remark that it has been the first time in which the CMS collaboration explores this BSM interpretation.

The $\mathrm{W^+W^-}$decay of the dark Higgs model is studied, whose branching fraction is greater than the other decay modes for $m_s > 160$ GeV [120] as shown in Figure 46. The subsequent leptonic decay of both W bosons is considered. Thus, the expected signature in the detector consists of large $\mathrm{p_T^{miss}}$ from the DM particles recoiling against the visible leptons. A CMS event display for one data event candidate illustrating this characteristic signature is shown in Figure 47.

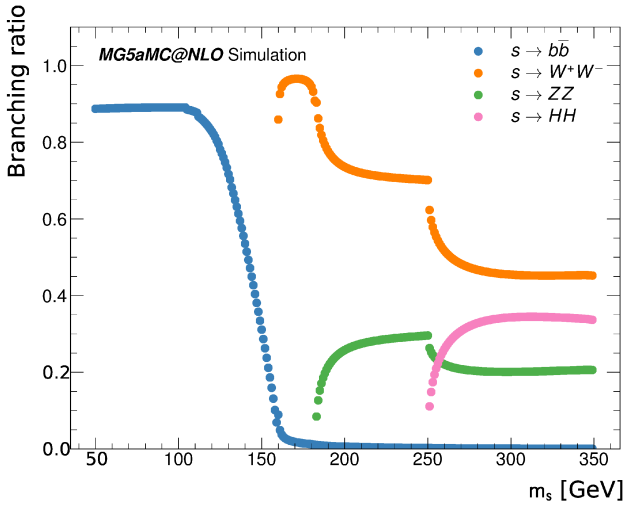

Figure 46: Branching fraction values of the dark Higgs boson s decay to a bottom quarks pair, ZZ, HH, and W^+W^-calculated in Madgraph at Leading Order. Image taken from [120].

8.1 Signal modeling

The dark Higgs signal events are generated with Madgraph5 at LO, including the dark Higgs decay to a pair of W bosons, and the subsequent decay of each W to a lepton and a neutrino.

In this analysis, the dark Higgs mass is set above the W^+W^-mass threshold ($m_s > 160$ GeV), where the branching fraction to $W^+W^-$is dominant among the possible dark Higgs decay modes. Following this criteria, five dark Higgs mass values have been chosen: 160, 180, 200 and 300 GeV. The selection of the masses has been made by evaluating the production cross section of the process in order to avoid regions where the W^+W^-decay channel is not sensitive.

For each chosen dark Higgs mass, the $m_{Z'} - m_\chi$ grids listed in Tables 19-22 have been generated, aiming to scan a substantially large part of the $m_s - m_{Z'} - m_\chi$ parameter space. One independent MC sample with one hundred thousand events is generated in each case, with the other parameters of the model fixed to the recommended values given by the ATLAS/CMS Dark Matter Forum [34]: $\sin\theta = 0.01$, $g_q = 0.25$, $g_\chi = 1.0$.

8.2 Event Selection

The first criterion to select a signal region (SR) is to define a phase space enriched in W^+W^-events, following the W^+W^-analysis event selection described in Section 7.3. The basic requirements of such selection consists of two well identified

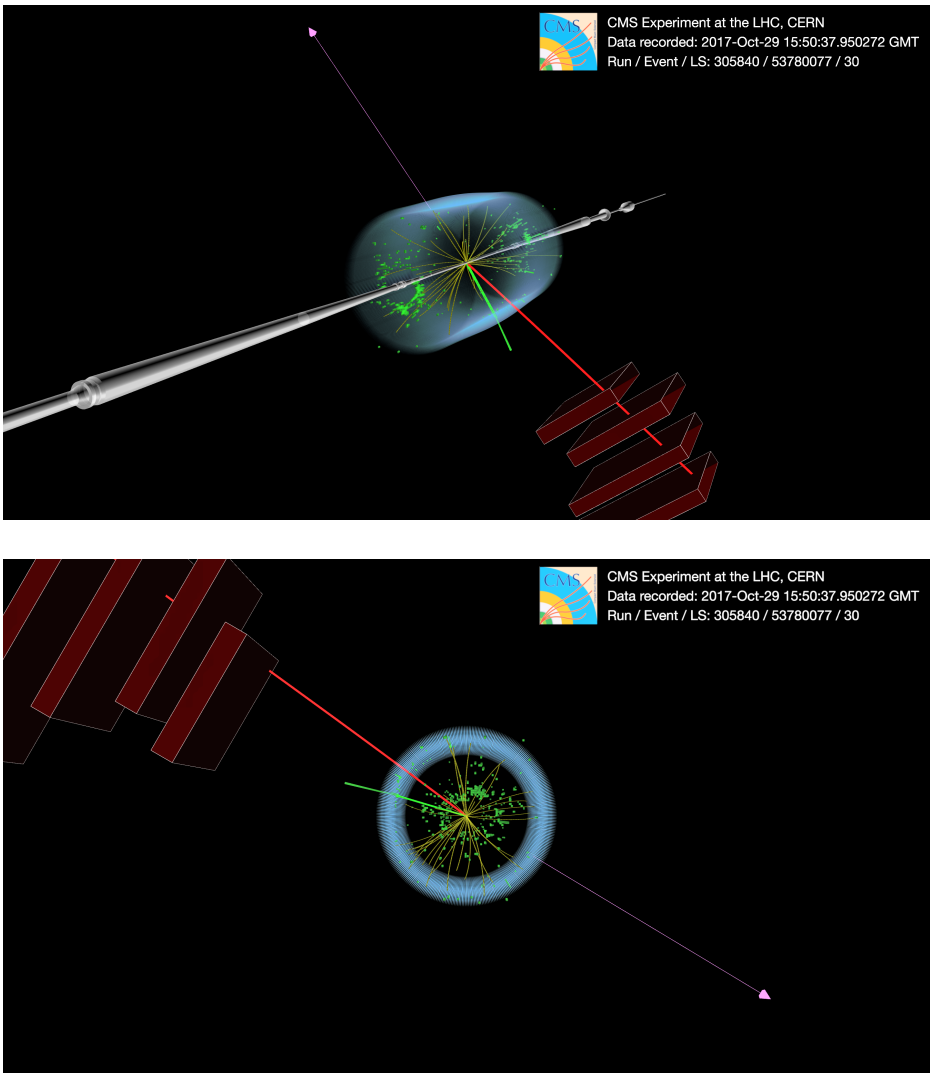

Figure 47: Event display of a particle collision recorded in the CMS detector in October, 2018. A pair of high energy charged leptons (a muon in red, and an electron in green) and large transverse momentum imbalance (pink arrow), in the direction where the undetectable dark matter particles might be gone, can be observed in the final state.

mZ' [GeV] / mχ [GeV]	200	300	400	500	800	1000	1200	1500	2000	2500
100	0.023	0.842	0.800	0.758	0.4544	0.275	0.164	0.077	0.023	0.007
150	0.004	0.025	0.382	0.417	0.335	0.226	0.142	0.070	0.022	0.007
200	0.003	0.004	0.015	0.191	0.225	0.173	0.119	0.062	0.020	0.007
300	-	-	-	-	0.085	0.089	0.074	0.045	0.017	0.006

Table 19: Cross section values (in pb) for the studied dark Higgs model: $q\overline{q} \rightarrow Z' \rightarrow s\chi\chi$, $s \rightarrow \mathrm{W}^{+}\mathrm{W}^{-}$. The mass points shown in the $m_{Z'} - m_{\chi}$ plane are generated for dark Higgs mass = 160 GeV. Samples with cross sections smaller than 0.003 pb (marked with the - character) have not been generated.

mZ' [GeV] / mχ [GeV]	200	300	400	500	800	1000	1200	1500	2000	2500
100	0.040	0.740	0.670	0.620	0.408	0.254	0.155	0.074	0.023	0.007
150	0.007	0.022	0.326	0.364	0.297	0.206	0.134	0.067	0.022	0.007
200	0.005	0.004	0.013	0.167	0.198	0.158	0.110	0.059	0.020	0.007
300	-	-	-	-	0.076	0.080	0.068	0.043	0.016	0.006

Table 20: Cross section values (in pb) for the studied dark Higgs model: $q\overline{q} \rightarrow Z' \rightarrow s\chi\chi$, $s \rightarrow \mathrm{W}^{+}\mathrm{W}^{-}$. The mass points shown in the $m_{Z'} - m_{\chi}$ plane are generated for $m_s = 180$ GeV. Samples with cross sections smaller than 0.003 pb (marked with the the - character) have not been generated.

mZ' [GeV] / mχ [GeV]	200	300	400	500	800	1000	1200	1500	2000	2500
100	0.022	0.440	0.400	0.367	0.258	0.167	0.103	0.050	0.016	0.005
150	0.004	0.013	0.200	0.225	0.187	0.135	0.089	0.046	0.015	0.005
200	0.003	0.002	0.008	0.104	0.124	0.103	0.074	0.040	0.014	0.005
300	-	-	-	-	0.049	0.051	0.044	0.029	0.011	0.004

Table 21: Cross section values (in pb) for the studied dark Higgs model: $q\overline{q} \rightarrow Z' \rightarrow s\chi\chi$, $s \rightarrow \mathrm{W}^{+}\mathrm{W}^{-}$. The mass points shown in the $m_{Z'} - m_{\chi}$ plane are generated for $m_s = 200$ GeV. Samples with cross sections smaller than 0.003 pb (marked with the - character) have not been generated.

mZ' [GeV] / mχ [GeV]	200	300	400	500	800	1000	1200	1500	2000	2500
100	-	-	-	-	-	-	-	-	-	-
150	-	-	0.044	0.052	0.042	0.036	0.027	0.016	-	-
200	-	-	-	0.025	0.029	0.027	0.022	0.014	-	-
300	-	-	-	-	0.013	0.013	0.012	-	-	-

Table 22: Cross section values (in pb) for the studied dark Higgs model: $q\overline{q} \to Z' \to s\chi\chi$, and $s \to \mathrm{W^+W^-}$. The mass points shown in the $m_{Z'} - m_{\chi}$ plane are generated for $m_s = 300$ GeV. Samples with cross sections smaller than 0.003 pb (marked with the - character) have not been generated.

and isolated leptons of opposite charge and different-flavour with $\mathrm{p_T^{\ell\,max}} > 25$ GeV, $\mathrm{p_T^{\ell\,min}} > 20$ GeV, and events with additional loose leptons with $\mathrm{p_T^{\ell}}$ greater than 10 GeV are vetoed. The invariant mass of the dilepton system is required to be not be compatible with low resonances ($\mathrm{m_{\ell\ell}} > 12$ GeV), and $\mathrm{p_T^{\ell\ell}}$ to be greater than 30 GeV to reject non-prompt and DY events. A selection on the $\mathrm{E_T^{miss}}$ variables ($\mathrm{p_T^{miss}} > 20$ GeV, *mpmet* > 20 GeV), and on the transverse mass of the dilepton plus $\mathrm{E_T^{miss}}$ system, $\mathrm{m_T^{ll,p_T^{miss}}} > 50$ GeV, are applied to suppress the DY contamination, whose final state leptons comes from a lower-mass resonance than the dark Higgs mass. Finally, in order to reduce the large background induced by top quark production, events with b-tagged jets with $\mathrm{p_T}$ larger than 20 GeV are rejected.

One important remark is that, compared with the $\mathrm{W^+W^-}$analysis shown in Section 7, this selection does not require a certain number of jets in the event. Also, the same-flavour decay mode is not considered in this analysis since the overwhelming amount of DY background makes this channel insensitive compared to the different-flavour channel, and on the other hand, the DY MC modeling is quite poor at the high $\mathrm{p_T}$ and high $\mathrm{p_T^{miss}}$ regime that this search targets, in contrast to the $\mathrm{W^+W^-}$analysis.

By studying the signal kinematic distributions, one more selection has been applied: the angular distance between the two leptons in the (η, ϕ) plane, denoted as $\Delta\mathrm{R}(\ell,\ell)$, is set to be lower than 2.5 in order to account for the boost of the dark Higgs boson decay products (visible system) recoiling against the dark matter system. The whole set of selections are listed in Table 23.

To define the signal regions of the analysis, the events that pass the selection criteria are split into three categories: $\Delta\mathrm{R}(\ell,\ell) < 1.0$ (high-boost), $1.0 < \Delta\mathrm{R}(\ell,\ell) < 1.5$ (medium-boost), and $1.5 < \Delta\mathrm{R}(\ell,\ell) < 2.5$ (low-boost), where the bounds are selected by taking into account the strong dependence of the dark Higgs boson mass with the $\Delta\mathrm{R}(\ell,\ell)$ variable, shown in Figure 48. In Figure 49, the obtained

significance curves as function of $\Delta R(\ell,\ell)$ are shown for the 2017 data set, where the significance is defined as the number of expected signal events divided by the sum of signal events and the total background (similar behavior is observed for the other data periods). The three signal regions will be denoted in the text as SR1 (high-boost), SR2 (medium-boost), and SR3 (low-boost) respectively, where the corresponding $\Delta R(\ell,\ell)$ selections are applied on top of the selection described in Table 23.

Quantity	Selection
Number of leptons	2
Lepton flavours	eμ, μe
Charge ℓmax $\times$ Charge ℓmin	< 0
Additional leptons ($p_T^{\ell} > 10$ GeV)	0
$p_T^{\ell\,max}$ [GeV]	> 25
$p_T^{\ell\,min}$ [GeV]	> 20
$m_{\ell\ell}$ [GeV]	> 12
$p_T^{\ell\ell}$ [GeV]	> 30
p_T^{miss} [GeV]	> 20
mpmet [GeV]	> 20
$m_T^{ll,p_T^{miss}}$ [GeV]	> 50
$\Delta R(\ell,\ell)$	< 2.5
b-veto	applied

Table 23: Summary of the event selection applied in the dark Higgs search.

Some of the most relevant variables considered in the analysis are shown in Figures 50-52 for the three data periods and for the three signal regions respectively.

8.3 Background estimation

The main background processes that affect the signal regions of this analysis arise from $t\bar{t}$ and non-resonant W^+W^-events.

As in the SM W^+W^-analysis (see Section 7), the non-prompt background contribution is estimated using data with the *tight-to-loose* method and it is validated in a same-sign validation region.

Regarding W^+W^-, DY, and top quark backgrounds, control regions (CRs) are defined for each process, consisting of phase spaces that are as close as possible to the signal regions, with the inversion of one specific cut in each case, aiming to enrich each region by one background at a time. The corresponding number of events in W^+W^-, DY, and top quark CRs are simultaneously fitted to the data

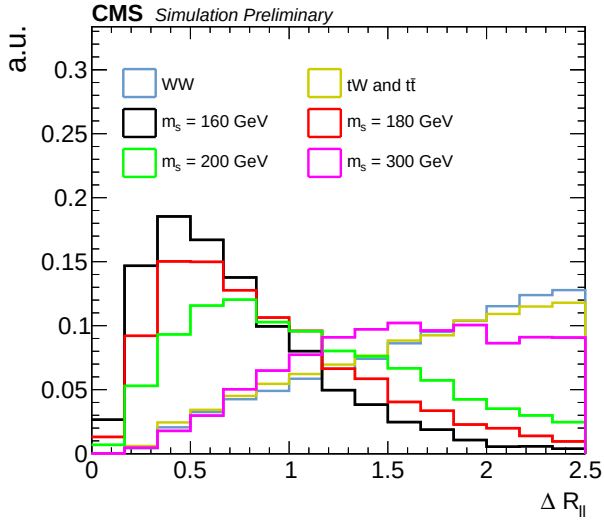

Figure 48: $\Delta R(\ell,\ell)$ distributions normalized to unity for signals with m_s = 160 GeV, m_s = 180 GeV, m_s = 200 GeV, and m_s = 300 GeV (m_χ = 150 GeV, $m_{Z'}$ = 800 GeV) shown as black, red, green, and magenta solid lines respectively. Predictions of the two main backgrounds of the analysis, WW and top, are shown as blue and yellow solid lines respectively. The distributions are obtained after applying the selection criteria from Table 23. The last bin includes the overflow.

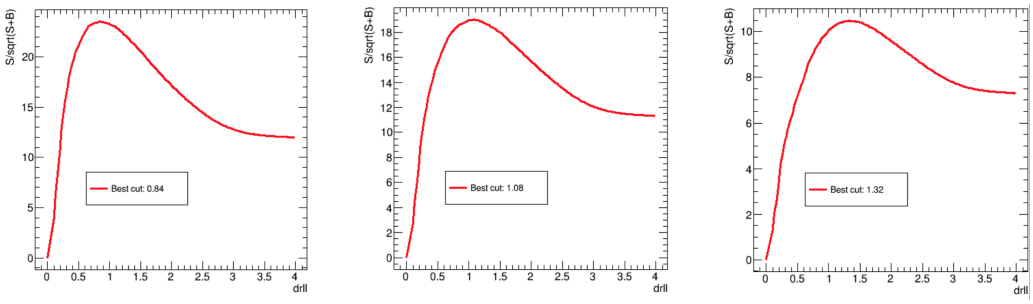

(a) m_s = 160 GeV (b) m_s = 180 GeV (c) m_s = 200 GeV

Figure 49: 2017 significance curves for $\Delta R(\ell,\ell) < x$ at selection level for m_s = 160, 180, 200 GeV respectively, where x refers to the $\Delta R(\ell,\ell)$ scanned value. For m_s = 300 GeV the selection on this variable does not improve the signal significance (flat shape at $\Delta R(\ell,\ell) > 1.5$ regime), so no further categorization is set from this dark Higgs mass.

together with the signal regions, where their normalizations are free parameters to be determined by the ML fit. The contribution of other sub-dominant backgrounds, such as HWW, $V\gamma/V\gamma^*$, VZ, and VVV, is obtained directly from the simulated samples.

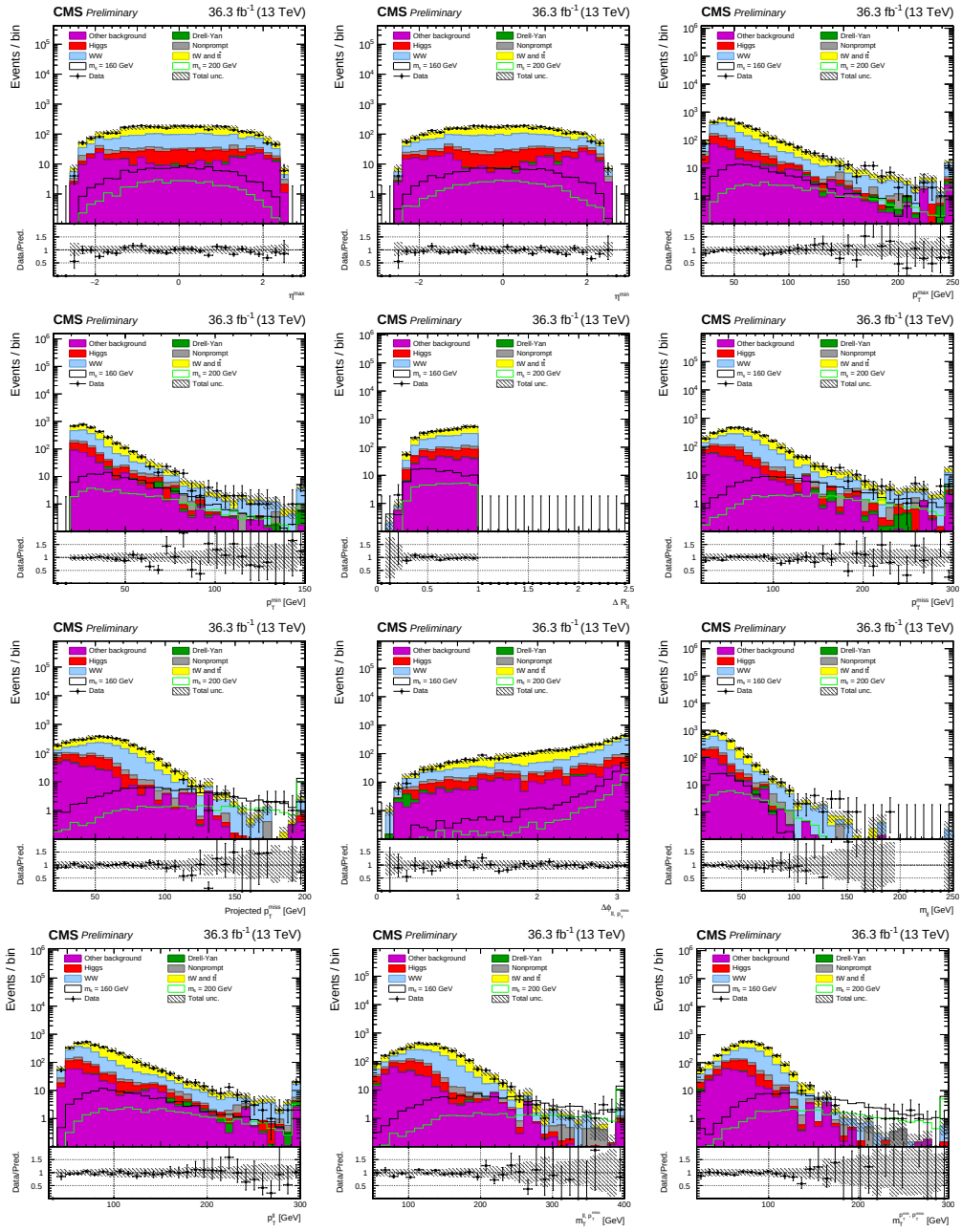

Figure 50: Pre-fit distributions for 2016 events in SR1. The distributions show the leading (a) and trailing (b) lepton η, the leading (c) and trailing (d) lepton p_T, $\Delta R(\ell, \ell)$ (e), p_T^{miss} (f), mpmet (g), azimuthal angle between the dilepton system and the p_T^{miss} (h), $m_{\ell\ell}$ (i), $p_T^{\ell\ell}$ (j), $m_T^{ll,p_T^{miss}}$ (k), and $m_T^{\ell min,p_T^{miss}}$ (l). The error bars on the data points represent the statistical uncertainty, and the hatched areas represent the combined systematic and statistical uncertainty of the predicted background. Black and green lines correspond to the signal predictions of $m_s = 160$ GeV and $m_s = 200$ GeV respectively, with $m_\chi = 100$ GeV, $m_{Z'} = 500$ GeV. The last bin includes the overflow.

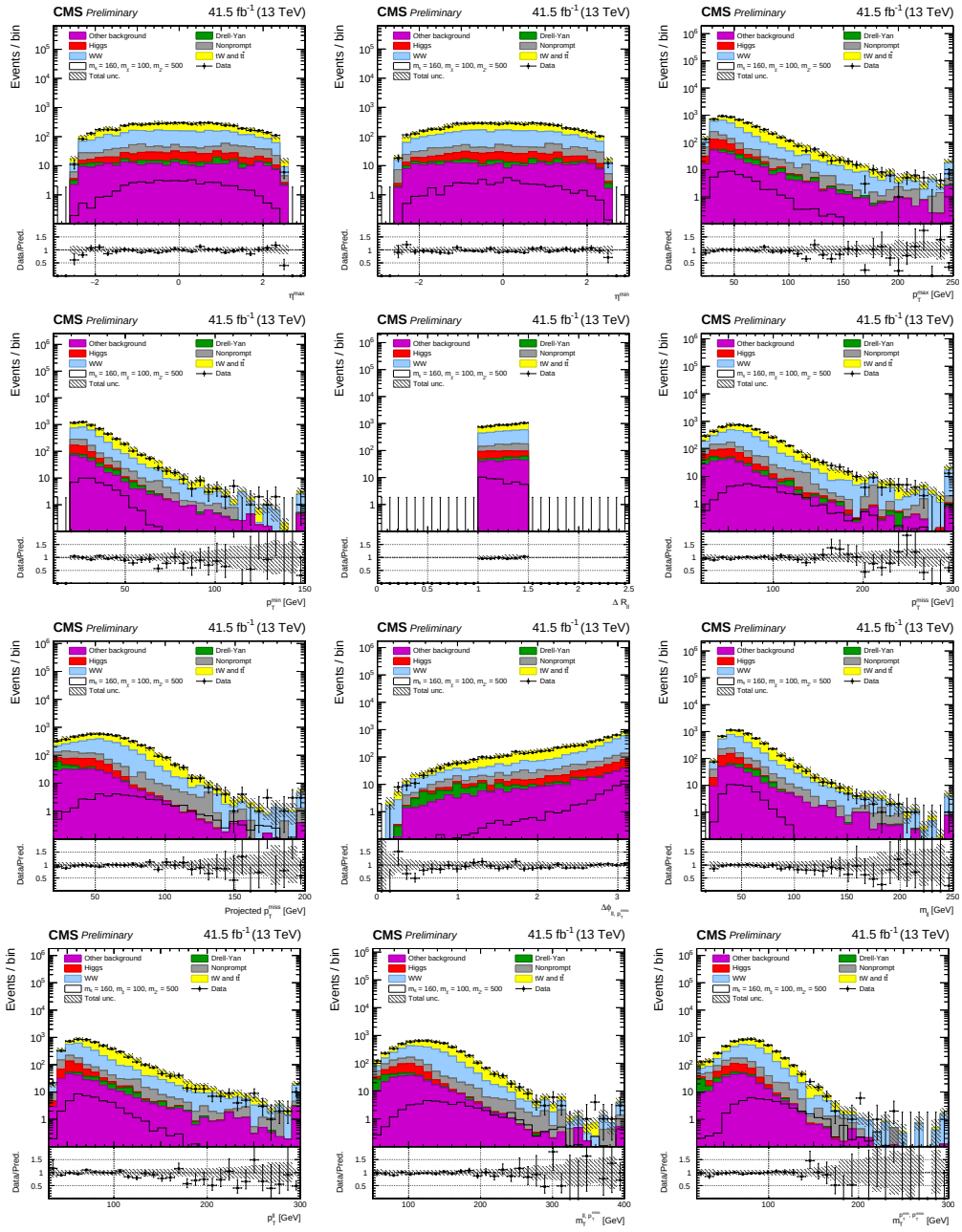

Figure 51: Pre-fit distributions for 2017 events in SR2. The distributions show the leading (a) and trailing (b) lepton η, the leading (c) and trailing (d) lepton p_T, $\Delta R(\ell,\ell)$ (e), p_T^{miss} (f), mpmet (g), azimuthal angle between the dilepton system and the p_T^{miss} (h), $m_{\ell\ell}$ (i), $p_T^{\ell\ell}$ (j), $m_T^{ll,p_T^{miss}}$ (k), and $m_T^{\ell min,p_T^{miss}}$ (l). The error bars on the data points represent the statistical uncertainty, and the hatched areas represent the combined systematic and statistical uncertainty of the predicted background. Black and green lines correspond to the signal predictions of $m_s = 160$ GeV and $m_s = 200$ GeV respectively, with $m_\chi = 100$ GeV, $m_{Z'} = 500$ GeV. The last bin includes the overflow.

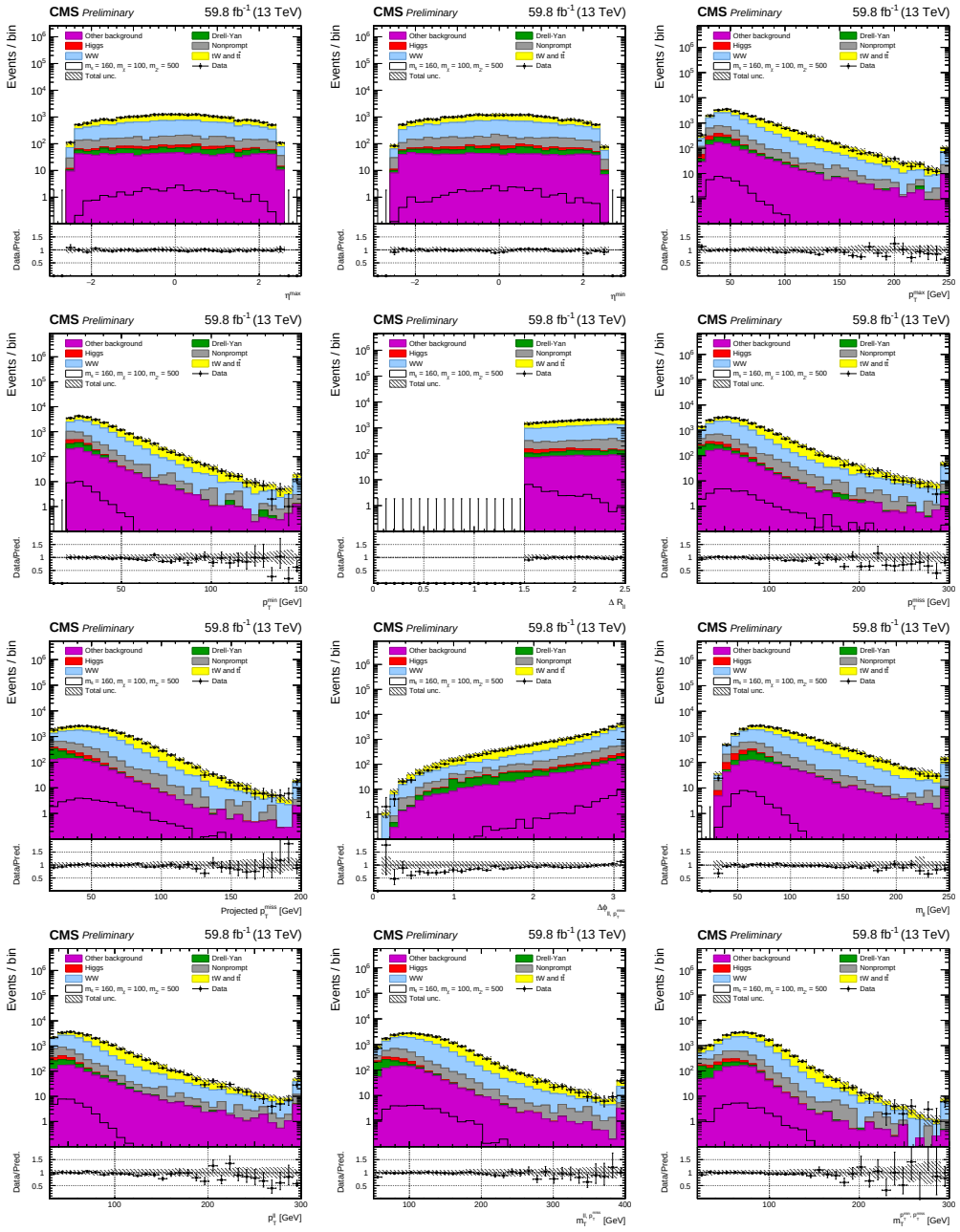

Figure 52: Pre-fit distributions for 2018 events in SR3. The distributions show the leading (a) and trailing (b) lepton η, the leading (c) and trailing (d) lepton p_T, $\Delta R(\ell, \ell)$ (e), p_T^{miss} (f), mpmet (g), azimuthal angle between the dilepton system and the p_T^{miss} (h), $m_{\ell\ell}$ (i), $p_T^{\ell\ell}$ (j), $m_T^{ll,p_T^{miss}}$ (k), and $m_T^{\ell min,p_T^{miss}}$ (l). The error bars on the data points represent the statistical uncertainty, and the hatched areas represent the combined systematic and statistical uncertainty of the predicted background. Black and green lines correspond to the signal predictions of $m_s = 160$ GeV and $m_s = 200$ GeV respectively, with $m_\chi = 100$ GeV, $m_{Z'} = 500$ GeV. The last bin includes the overflow.

In the following subsections, the procedures that have been followed to model the the non-prompt, WW, top, and DY backgrounds are detailed, including the different control regions definitions.

8.3.1 Non-prompt background

The non-prompt background contribution in the analysis regions is estimated with the *tight-to-loose* data-driven method described in Section 7.4.1, that provides a measurement of its yield and kinematic shapes.

In order to validate the data-driven approach, a validation region is defined by simply reverting the opposite-charge requirement of the two leptons, but keeping the same selections shown in Table 23. This region is enriched in $V\gamma/V\gamma^*$ and non-prompt events. Data and MC distributions for the non-prompt validation region for the 2016 data set are shown in Figure 53, where the $V\gamma/V\gamma^*$ contribution enters in the *Other background* categorization. Similar data/MC agreement is observed for the other data periods.

8.3.2 WW background

Standard Model non-resonant W^+W^-production is a very important background, as the detectable particles in the dileptonic final state are exactly the same as the signal ones, the cross section is significantly larger, and there are neutrinos in the final state that can produce large E_T^{miss}. On the other hand, resonant $H\to W^+W^-$production gives rise to a similar case, but its smaller cross section makes its contribution in the signal regions of the analysis less important.

Same corrections are applied on the W^+W^-modeling as described in Section 7.1: K-factor to scale the $gg \to W^+W^-$ contribution to the NNLO precision, and the p_T^{WW} reweighting is applied to the $qq \to W^+W^-$ contribution to match the NNLO + NNLL accuracy. On top of those, since this analysis targets the high-energy regime, higher-order electroweak corrections are included [116], which have an effect of about 5% for $m_{\ell\ell} > 200$ GeV.

The W^+W^-control region is orthogonalized to the signal regions by reverting the $\Delta R(\ell,\ell)$ selection shown in Table 23, i.e., $\Delta R(\ell,\ell) > 2.5$. Data and MC distributions for the W^+W^-control region for the 2017 data set are shown in Figure 54. Similar agreement data/MC is observed for the other data periods.

8.3.3 Top background

The production of top quarks ($t\bar{t}$, tW, and single top production) corresponds to one of the dominant backgrounds in the signal regions of this analysis, since its dileptonic decay produces a very similar final state compared to the signal regions,

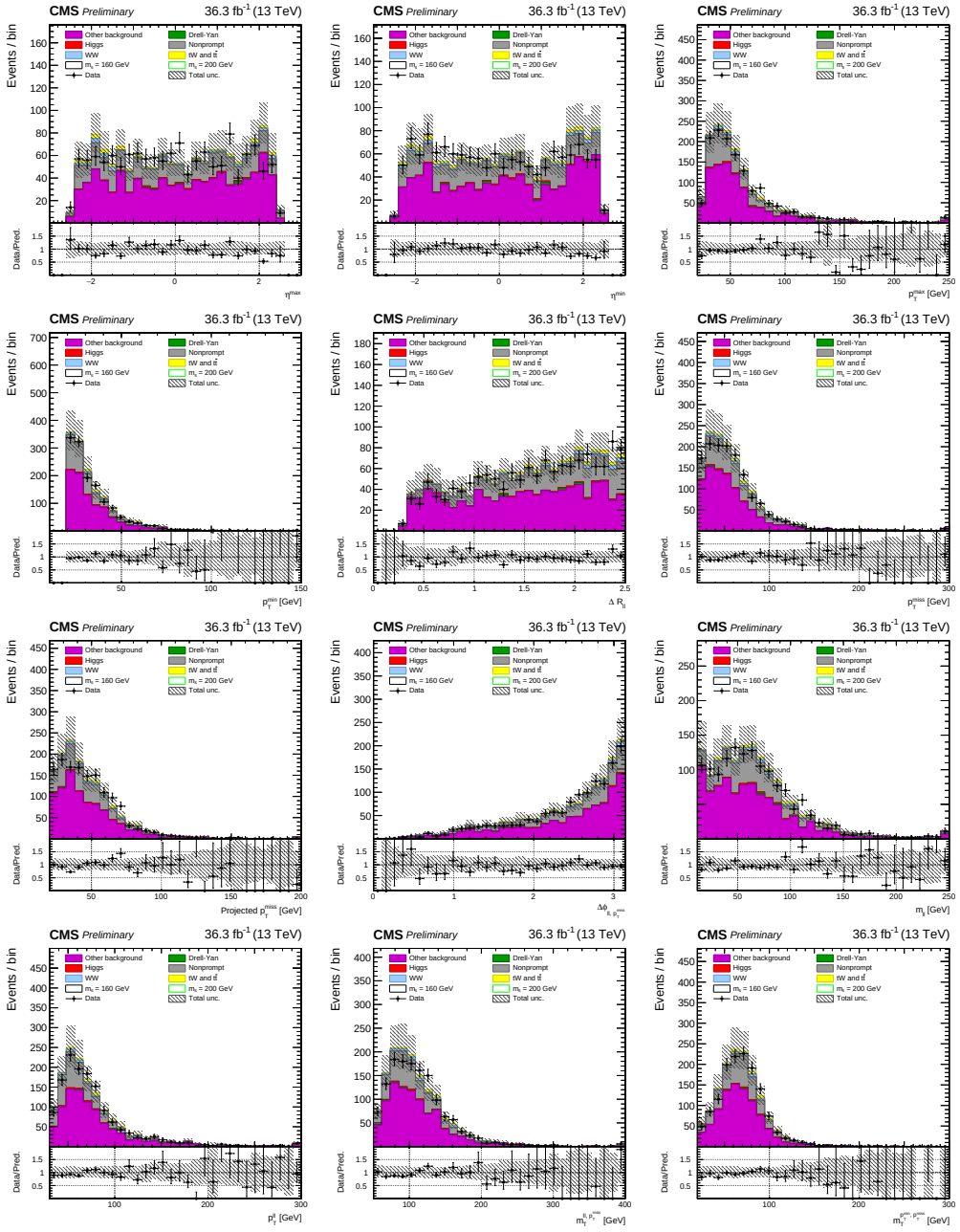

Figure 53: Pre-fit kinematic distributions for 2016 events in non-prompt validation region. The distributions show the leading (a) and trailing (b) lepton η, the leading (c) and trailing (d) lepton p_T, $\Delta R(\ell,\ell)$ (e), p_T^{miss} (f), mpmet (g), azimuthal angle between the dilepton system and the p_T^{miss} (h), $m_{\ell\ell}$ (i), $p_T^{\ell\ell}$ (j), $m_T^{ll,p_T^{miss}}$ (k), and $m_T^{\ell\,min,p_T^{miss}}$ (l). The error bars on the data points represent the statistical uncertainty, and the hatched areas represent the combined systematic and statistical uncertainty of the predicted background. Black and green lines correspond to the signal predictions of $m_s = 160$ GeV and $m_s = 200$ GeV respectively, with $m_\chi = 100$ GeV, $m_{Z'} = 500$ GeV. The last bin includes the overflow.

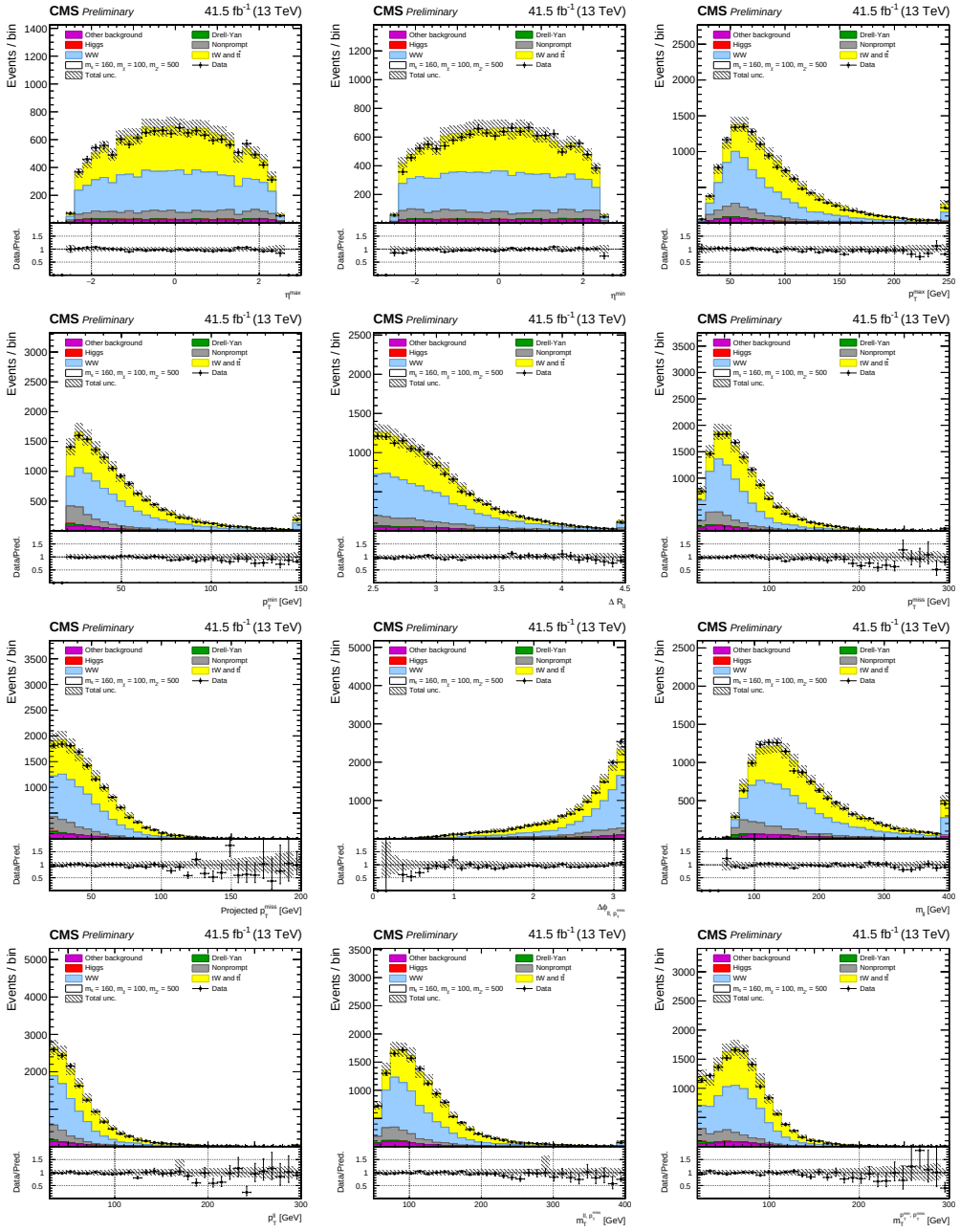

Figure 54: Pre-fit kinematic distributions for 2017 events in WW CR. The distributions show the leading (a) and trailing (b) lepton η, the leading (c) and trailing (d) lepton p_T, $\Delta R(\ell,\ell)$ (e), p_T^{miss} (f), mpmet (g), azimuthal angle between the dilepton system and the p_T^{miss} (h), $m_{\ell\ell}$ (i), $p_T^{\ell\ell}$ (j), $m_T^{ll,p_T^{miss}}$ (k), and $m_T^{\ell\,min,p_T^{miss}}$ (l). The error bars on the data points represent the statistical uncertainty, and the hatched areas represent the combined systematic and statistical uncertainty of the predicted background. Black and green lines correspond to the signal predictions of $m_s = 160$ GeV and $m_s = 200$ GeV respectively, with $m_\chi = 100$ GeV, $m_{Z'} = 500$ GeV. The last bin includes the overflow.

and because of its large cross section.

As described in Section 7.4.2, the top p_T spectra correction on the $t\bar{t}$ MC is applied in order to improve the MC modeling. Also, a top-enriched control region is defined by requiring b-tagged jets in the event instead of vetoing, i.e., the *DeepCSV* selection on the reconstructed jets with $p_T > 20$ GeV is inverted. Data and MC distributions for the 2018 data set are shown in Figure 55. Similar agreement data/MC is observed for the other data periods.

8.3.4 Drell-Yan background

The production of a Z boson can mimic the signal signature in case of dileptonic decay.

The Z boson decay to ee or $\mu\mu$ is suppressed by requiring two different-flavour leptons in the event, so the DY contribution that affects this analysis is $Z/\gamma^* \rightarrow \tau^+\tau^-$. If the taus decay leptonically in the detector, a final state similar to the signal regions is obtained (two leptons of different-flavour and two neutrinos).

The $Z/\gamma^* \rightarrow \tau^+\tau^-$control region is defined by applying the same selections as listed in Table 23 but inverting the $m_T^{ll,p_T^{miss}}$ requirement, i.e., $m_T^{ll,p_T^{miss}} < 50$ GeV. Data and MC distributions for the 2017 data set are shown in Figure 56. Similar agreement data/MC is observed for the other data periods.

8.4 Analysis strategy

The approach chosen to get the best estimation of the discovery confidence level or the exclusion limits consists of a binned shape analysis (see Section 5) based on $m_{\ell\ell}$, $\Delta R(\ell,\ell)$, and $m_T^{\ell\,min,p_T^{miss}}$ distributions, which correspond to the three variables that show the greater power to separate the signal from the main backgrounds. The $m_{\ell\ell}$ and $m_T^{\ell\,min,p_T^{miss}}$ distributions for some reference signals and for the main backgrounds are shown in Figure 57, where it can be observed that the signal populates more the tails of the $m_T^{\ell\,min,p_T^{miss}}$ distribution compared to the $W^+W^-$and top quark backgrounds. Regarding $m_{\ell\ell}$, it can be seen that the signal shapes show a strong dependence with the dark Higgs mass.

As detailed in Section 8.2, the $\Delta R(\ell,\ell)$ variable is used to define the three signal regions considered. Then, for each $\Delta R(\ell,\ell)$ region, a 2D histogram on $m_{\ell\ell}$ - $m_T^{\ell\,min,p_T^{miss}}$ is defined. The $m_{\ell\ell}$ binning is set by taking into account the optimal selection based on the maximum of the significance curves for each dark Higgs mass value (see Figure 58), and the $m_T^{\ell\,min,p_T^{miss}}$ binning is set by maximizing the sensitivity while avoiding empty bins from background predicted events in each data period individually. This strategy makes the analysis flexible, allowing the

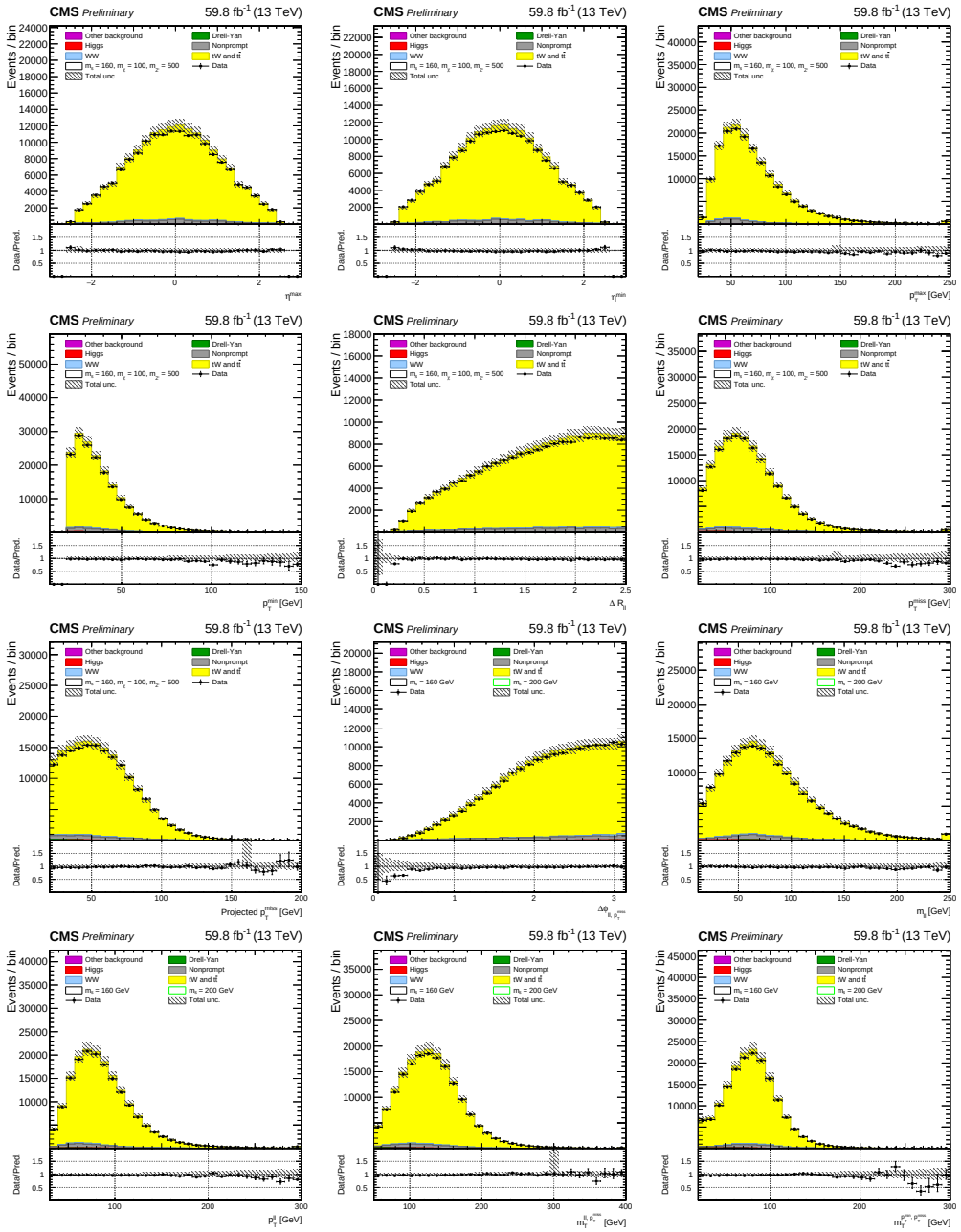

Figure 55: Pre-fit kinematic distributions for 2018 events in Top CR. The distributions show the leading (a) and trailing (b) lepton η, the leading (c) and trailing (d) lepton p_T, $\Delta R(\ell,\ell)$ (e), p_T^{miss} (f), mpmet (g), azimuthal angle between the dilepton system and the p_T^{miss} (h), $m_{\ell\ell}$ (i), $p_T^{\ell\ell}$ (j), $m_T^{ll,p_T^{miss}}$ (k), and $m_T^{\ell\,min,p_T^{miss}}$ (l). The error bars on the data points represent the statistical uncertainty, and the hatched areas represent the combined systematic and statistical uncertainty of the predicted background. Black and green lines correspond to the signal predictions of $m_s = 160$ GeV and $m_s = 200$ GeV respectively, with $m_\chi = 100$ GeV, $m_{Z'} = 500$ GeV. The last bin includes the overflow.

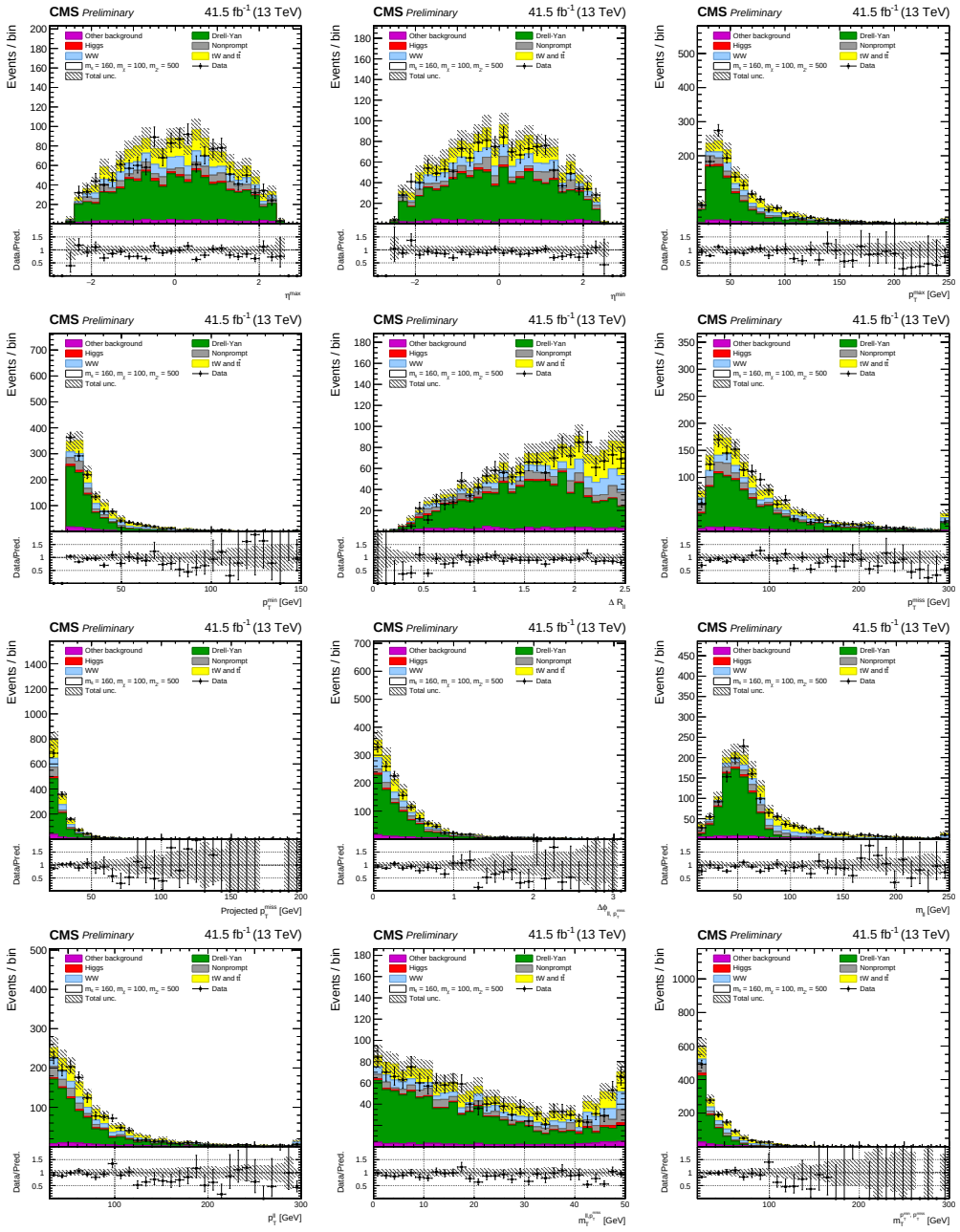

Figure 56: Pre-fit kinematic distributions for 2017 events in DY CR. The distributions show the leading (a) and trailing (b) lepton η, the leading (c) and trailing (d) lepton p_T, $\Delta R(\ell,\ell)$ (e), p_T^{miss} (f), mpmet (g), azimuthal angle between the dilepton system and the p_T^{miss} (h), $m_{\ell\ell}$ (i), $p_T^{\ell\ell}$ (j), $m_T^{ll,p_T^{miss}}$ (k), and $m_T^{\ell\,min,p_T^{miss}}$ (l). The error bars on the data points represent the statistical uncertainty, and the hatched areas represent the combined systematic and statistical uncertainty of the predicted background. Black and green lines correspond to the signal predictions of $m_s = 160$ GeV and $m_s = 200$ GeV respectively, with $m_\chi = 100$ GeV, $m_{Z'} = 500$ GeV. The last bin includes the overflow.

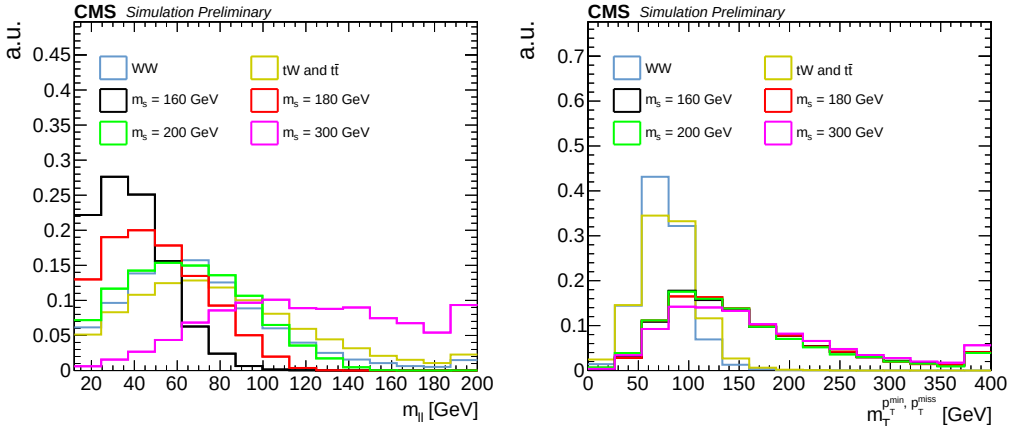

Figure 57: $m_{\ell\ell}$ (left) and $m_T^{\ell\,\mathrm{min},p_T^{\mathrm{miss}}}$ (right) distributions normalized to unity for signals with $m_s = 160$ GeV, $m_s = 180$ GeV, $m_s = 200$ GeV, and $m_s = 300$ GeV ($m_\chi = 150$ GeV, $m_{Z'} = 800$ GeV) shown as black, red, green, and magenta solid lines respectively. Predictions of the two main backgrounds of the analysis, WW and top, are shown as blue and yellow solid lines respectively. The distributions are obtained after applying the selection criteria from Table 23. The last bin includes the overflow.

different considered signals to freely populate the 3D phase space depending on the corresponding kinematics, while using the same background modeling procedure.

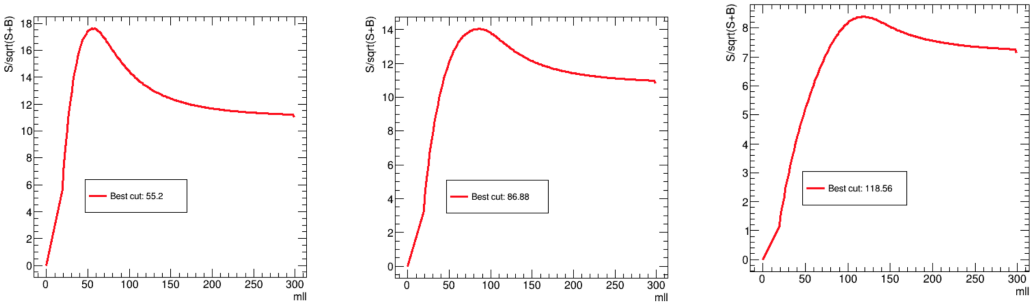

(a) $m_s = 160$ GeV (b) $m_s = 180$ GeV (c) $m_s = 200$ GeV

Figure 58: 2017 significance curves for $m_{\ell\ell} <$ x at selection level for $m_s = 160$, 180, 200 GeV respectively, where x refers to the $m_{\ell\ell}$ scanned value. For $m_s = 300$ GeV the selection on this variable does not improve the signal significance (flat shape at $m_{\ell\ell} > 120$ GeV regime), so no further categorization is set from this dark Higgs mass.

The chosen binning on $m_{\ell\ell}$ is [12,60,90,120,inf] GeV (same for the three data peri-

ods). Regarding $m_T^{\ell\,min,p_T^{miss}}$, differences among the years on the luminosity, on the b-tagger performance, and on the electron MVA ID performance, allow to set a different binning for each year by ensuring a reasonable signal sensitivity while avoiding empty bins. The following configuration has been chosen: [0,50,90,130,160,inf] GeV, [0,50,90,130,170,inf] GeV, and [0,50,90,130,180,inf] GeV for the 2016, 2017, and 2018 data sets respectively.

A global fit to the observed data in the three data periods is performed to get the final results, where all the analysis regions are simultaneously fitted, including the 2D histograms on $m_{\ell\ell}$ - $m_T^{\ell\,min,p_T^{miss}}$ for the three $\Delta R(\ell,\ell)$ signal regions, and the *one-bin* distributions from the W^+W^-, DY, and top CRs. It means that 18 regions (3 data periods, with 3 SRs and 3 CRs each) with a total of 189 bins (3 data periods, with 60 bins from the SRs and 3 bins from the CRs each) are fitted together, using the same systematic uncertainties as nuisance parameters as in the SM W^+W^-analysis (see Section 6).

8.5 Results

The different background normalization factors extracted from the global fit are registered in Table 24.

Post-fit background yields after applying the measured W^+W^-, DY and top quark normalization factors from the global fit, signal pre-fit yields, and the observed data events for the three considered signal regions and for the three data periods are shown in Table 25.

	2016	2017	2018
TopNorm	1.03 ± 0.06	1.01 ± 0.05	1.03 ± 0.05
WWNorm	1.02 ± 0.08	1.02 ± 0.07	1.09 ± 0.07
DYnorm	1.17 ± 0.15	1.01 ± 0.11	0.97 ± 0.10

Table 24: Background normalization extracted from the global fit to the data for the different data periods. Uncertainties are obtained from the maximum likelihood scan versus the corresponding parameters introduced in the model.

The unrolled[5] and equally spaced binned post-fit distributions (in $m_{\ell\ell}-m_T^{\ell\,min,p_T^{miss}}$ bins) with the chosen binning and for the full CMS Run2 luminosity of 137 fb^{-1} are shown in Figure 59. The corresponding $m_T^{\ell\,min,p_T^{miss}}$ 1D distributions can be found in Appendix B. No significant data excess over the expected background is

[5] One distribution is obtained for each $\Delta R(\ell,\ell)$ region. In each plot, every group of five bins (from left to right) corresponds to the $m_T^{\ell\,min,p_T^{miss}}$ distribution in a certain $m_{\ell\ell}$ bin.

Sample	2016 SR1	2016 SR2	2016 SR3	2017 SR1	2017 SR2	2017 SR3	2018 SR1	2018 SR2	2018 SR3
DY	16	41	251	42	65	348	53	103	429
top	1371	1844	5316	1694	2156	6491	2201	2806	8461
qqWW	1017	1461	4814	1361	1891	6562	2058	2805	9843
ggWW	184	216	491	260	302	693	364	422	973
Vg	132	66	167	152	81	189	221	112	270
VgS	168	99	321	180	150	394	241	196	532
VZ	6	8	17	8	9	20	11	12	28
VVV	6	8	18	8	9	26	12	12	32
Higgs	282	176	168	384	245	232	535	341	316
Non-prompt	107	203	669	302	367	1264	324	471	1557
Signal	118	35	18	180	47	23	264	66	33
Tot Bkg	3290 ± 36	4120 ± 36	12232 ± 70	4390 ± 41	5274 ± 40	16219 ± 80	6018 ± 56	7279 ± 48	22441 ± 95
DATA	3257	4114	12260	4369	5320	16100	6000	7200	22500

Table 25: Post-fit data and MC yields for the three considered signal regions and for the three data periods. Signal prediction corresponds to pre-fit yields of m_s = 160 GeV, m_χ = 100 GeV, $m_{Z'}$ = 500 GeV. Total post-fit uncertainty for the total background is shown.

observed, so limits on the dark Higgs model parameters are set.

The impacts of the top 30 uncertainties (see Section 6), ordered by decreasing importance for the full luminosity combination are shown in Figure 60. It can be observed that the signal strength is mainly affected by the statistical uncertainties of the MC samples in the most sensitive bins, and by the $t\bar{t}$ and $qq \to W^+W^-$ MC corrections.

8.5.1 Interpolation procedure

For the limits computation, the parameters of the model that have been scanned are the masses of the BSM particles (m_s,m_χ,$m_{Z'}$), where the used grid for the MC samples production, shown in Section 8.1, presents wide and discrete steps specially on $m_{Z'}$. Thus, in order to provide smoother limits, a interpolation procedure has been developed.

To do the interpolation between the produced signal MC samples, smaller MC samples (with ten thousand events each instead of one hundred thousand) have been generated with a finer binning. The chosen grid, that can be compared with Tables 19-22, has been the following:

- m_χ = 100, 150, 200, 300 GeV.
- $m_{Z'}$ = 200, 300, 400, 500, 600, 700, 800, 900, 1000, 1100, 1200, 1300, 1400,

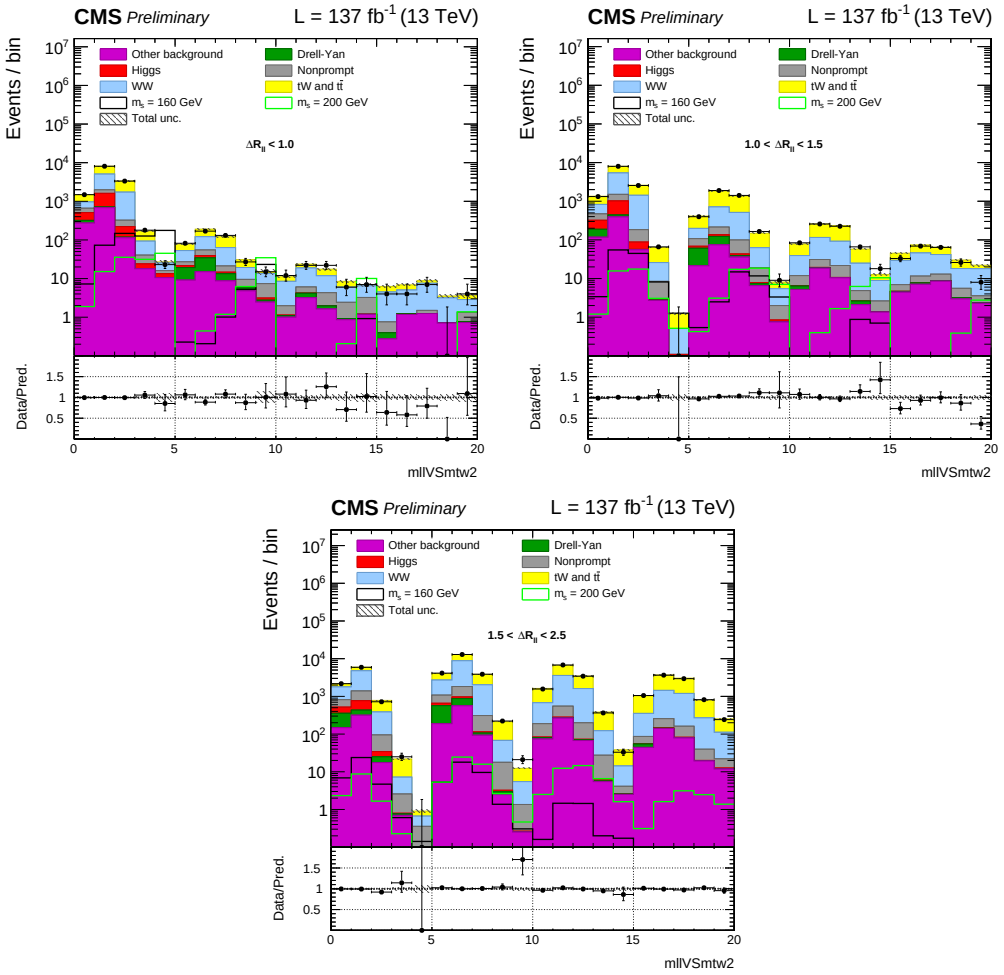

Figure 59: Unrolled and equally spaced binned $m_{\ell\ell}$-$m_T^{\ell\,\mathrm{min},p_T^{\mathrm{miss}}}$ post-fit distributions for the full data set in SR1 (top left), SR2 (top right), and SR3 (bottom). In each plot, every group of five bins (from left to right) corresponds to the $m_T^{\ell\,\mathrm{min},p_T^{\mathrm{miss}}}$ distribution in a $m_{\ell\ell}$ bin, placed in ascending order. Black and green lines correspond to the signal predictions of $m_s = 160$ GeV and $m_s = 200$ GeV respectively, with $m_\chi = 100$ GeV, $m_{Z'} = 500$ GeV.

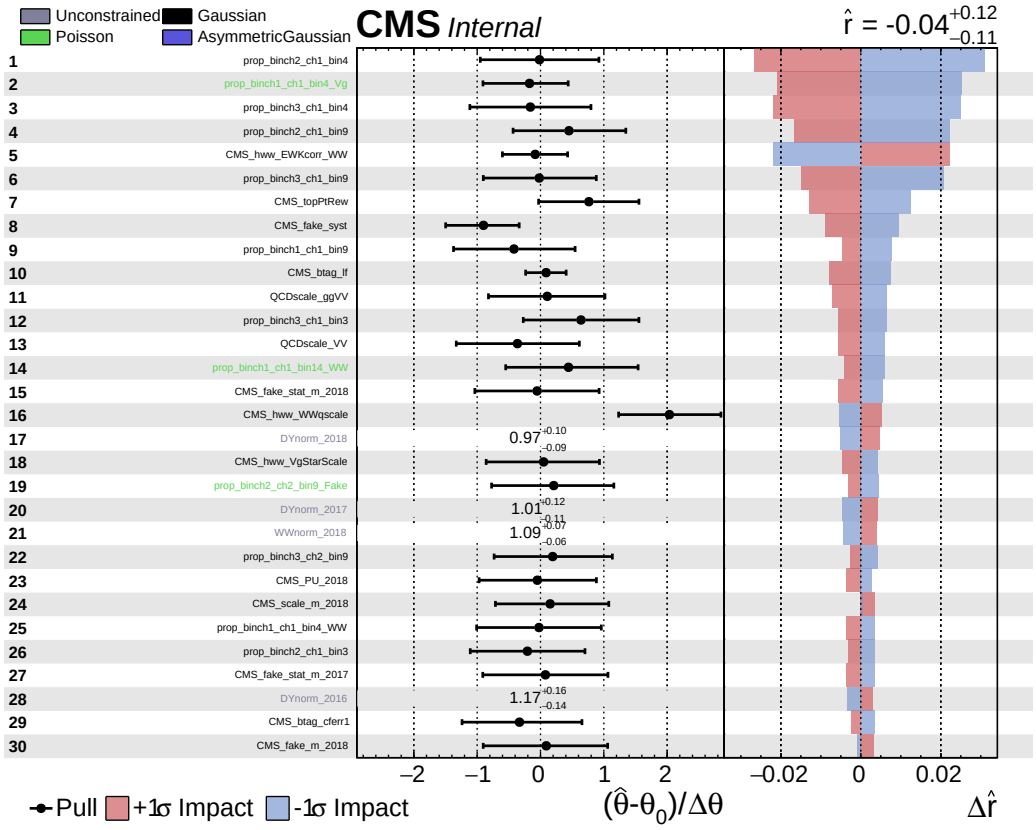

Figure 60: Observed top 30 uncertainties in the full combination of the dark Higgs analysis, sorted by the impact on the signal strength in decreasing order for the signal mass point m_s = 180 GeV, m_χ = 150 GeV, $m_{Z'}$ = 1200 GeV. The left panel shows the pulls, represented as black dots. The pull of a certain nuisance parameter is defined as $(\theta - \theta_0)/\sigma_{\theta_0}$, where θ and θ_0 corresponds to the post-fit and pre-fit value of the nuisance parameter respectively, and σ_{θ_0} corresponds to its pre-fit uncertainty. On the other hand, the error bars show the ratio of the post-fit and pre-fit uncertainties for each nuisance parameter. Thus, if the fit is able to constrain a certain nuisance parameter, its error bar will be smaller than ± 1. The best r value obtained from the maximum likelihood fit to the data in each case is shown on the top right corner. Statistical uncertainty of data period d (2016: 1, 2017:2, 2018:3), region c (SR1: 1, SR2: 2, SR3: 3, WW CR: 4, Top CR: 5, DY CR: 6), and bin number b (SRs: 0-19 taking the same order as shown in Figure 59, CRs: 0, since *one-bin* distributions are included in the fit) is denoted as prop_binch$< d >$_ch$< c >$_bin$< b >$ in case of single Gaussian-constrained uncertainty, and prop_binch$< d >$_ch$< c >$_bin$< b >$_$< ProcessName >$ in case of separate Poisson-constrained uncertainties (see Section 6.1).

1500, 1600, 1700, 1800, 1900, 2000, 2100, 2200, 2300, 2400, 2500 GeV.

- m_s = 160, 180, 200, 250, 300, 350, 400 GeV.

The interpolation is done between $m_{Z'}$ values at generation level by taking the dark Higgs p_T as key quantity. First, for each dark Higgs mass, a reference mass point is selected: m_χ = 150 GeV, $m_{Z'}$ = 1200 GeV, and a mass point that was not produced in the initial MC production (Tables 19-22) is targeted. Then, the ratio of the dark Higgs p_T distribution of each target sample with respect to the reference one is obtained as illustrated in Figure 61. Finally, every event in the reference sample is reweighted by its corresponding ratio value given by its dark Higgs p_T, and it is also scaled by the proper cross section value, i.e., the cross section of the target sample divided by the cross section of the reference sample.

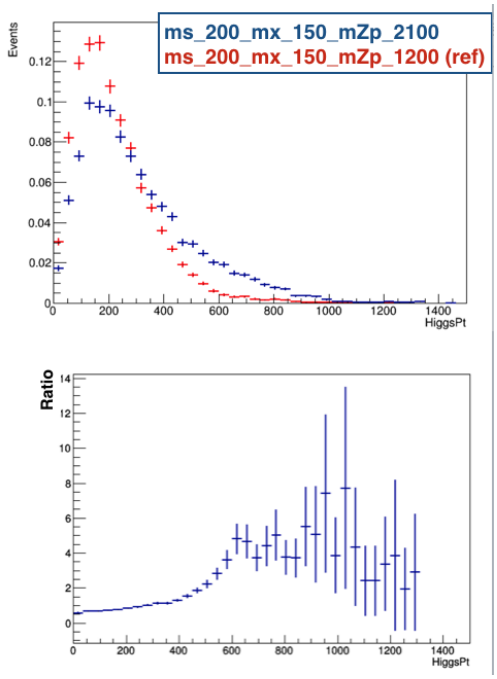

Figure 61: Upper plot: dark Higgs p_T distributions, normalized to unity, for one of the interpolated mass points, m_s = 200 GeV, m_χ = 150 GeV, $m_{Z'}$ = 2100 GeV in blue, and for the reference mass point m_s = 200 GeV, m_χ = 150 GeV, $m_{Z'}$ = 1200 GeV in red (which is reweighted). Bottom plot: Ratio values as function of the dark Higgs p_T.

On top of that, the final exclusion plots are smoothed by interpolating the limit values within the phase space using Delaunay triangles [121].

8.5.2 Limits on the dark Higgs model parameters

The obtained CLs limits (as defined in Section 5) for the dark Higgs model are shown in Figure 62, where the interpolated contours are gotten in the $m_s - m_{Z'}$ plane for each considered DM mass. In these plots, both the observed limits (using real data) and the expected limits (using total background prediction as pseudo-data) are shown. It can be noted that the observed limit is better than the expected one (within the one standard deviation band), due to the slight data deficit that is observed in the most sensitive bins with respect to the background prediction, as shown in Figure 59.

It can be seen that the most stringent limit is obtained for a $m_\chi = 150$ GeV (upper right plot), excluding m_s masses up to $\approx$ 300 GeV in a mass range $\approx 480 < m_{Z'} < 1200$ GeV.

Also, it should be noticed that only the visible decay of the dark Higgs to a pair of W bosons is considered, which corresponds to the dominant decay mode in the analyzed phase space. In the limit where $m_s \geq 2m_\chi$, the dark Higgs decaying to a pair of DM particles becomes the dominant mode, and as a consequence, above m_s = 200 GeV (m_s = 300 GeV) the sensitivity drops for a DM particle mass of 100 GeV (150 GeV) as can be seen in the upper-left (upper-right) plot of Figure 62. Similarly, the $m_{Z'} < 2m_\chi$ phase space is kinematically forbidden, since the two DM particles come from the $Z' \to \chi\chi$ decay (see Feynman diagrams in Figure 45).

The ATLAS Collaboration has recently published an analysis [122] which explores the dark Higgs model by considering the fully hadronic $s \to \mathrm{ZZ/W^+W^-}$ final states. Comparing the results, this analysis improves the excluded region in the m_s - $m_{Z'}$ mass plane, in the sense that, for $m_\chi = 200$ GeV, this analysis excludes up to $m_{Z'} \approx 2000$ GeV, for $m_s = 160$ GeV; and m_s masses up to ≈ 300 GeV for a $m_{Z'} = 700$ GeV. Also, a wider DM mass range is explored, from 100 GeV to 300 GeV.

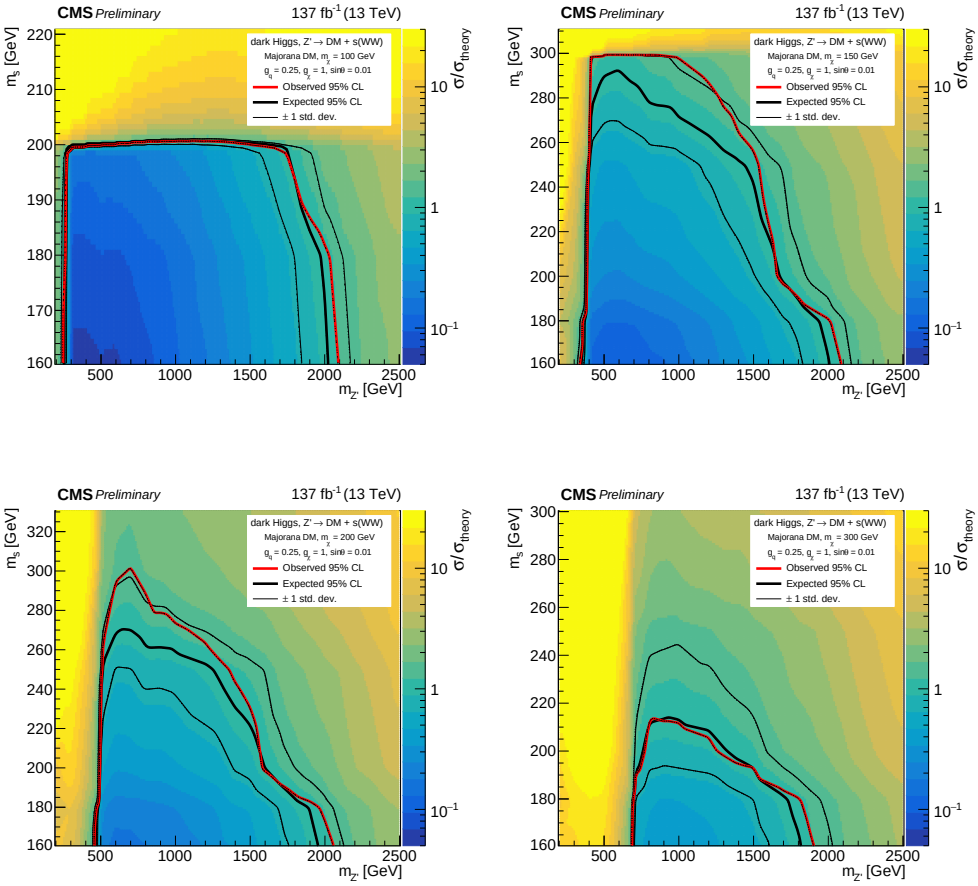

Figure 62: Combined observed (expected) exclusion regions at 95% CL for the dark Higgs model in the (m_s, $m_{Z'}$) plane, marked by the solid red (black) line. The expected $\pm$ 1σ band is shown as the thinner black line. Upper left: m_χ = 100 GeV, upper right: m_χ = 150 GeV, bottom left: m_χ = 200 GeV, bottom right: m_χ = 300 GeV.

9 Run 3 studies: Muon high momentum assignment

After the end of the *Run 2* era, the LHC is expected to deliver to the CMS experiment two times more luminosity during the next *Run 3* (2022-2024), that will allow, for instance, to improve the differential measurements and the sensitivity in searches for new physics. Apart from that, there are several ongoing studies, including new developments in triggers, upgrades in the different subdetectors, or improvements in the reconstruction and identification of physics objects, which will be integrated in the new era. In this section, novel techniques are studied aiming to improve the muon high p_T assignment in the CMS detector, and if so, consider including these types of methodologies in the future *Run 3*.

Muons are charged particles with spin 1/2 and mass approximately 200 times greater than the electron, being also unstable particles with a life time of 2.2 μs, which is high compared to other particles which show this property. High-$\mathrm{p_T}$ muons can be produced in BSM processes such as the decay of exotic particles like Z', W' [123, 124], or dark Higgs bosons, with masses on the TeV scale. The discovery of any of these particles would be a direct indication of new physics, so measuring the properties of these muons as accurately as possible in the detector is quite important. Specifically, the main objective of the study is to apply a regression technique based on a Deep Neural Network (DNN) [125] to estimate the transverse momentum of high-$\mathrm{p_T}$ muons in a precise way.

Experimentally, measuring the momentum of high-$\mathrm{p_T}$ muons raises several difficulties. First, it must be taken into account that the resolution of the $\mathrm{p_T}$ measurement from the muon track gets worse when the muon momentum increases, since the $\mathrm{p_T}$ is measured through the relation between curvature and momentum that establishes the Lorentz force. In this way, in the presence of a uniform magnetic field B, and with a radius of curvature of the track r, the transverse momentum $\mathrm{p_T}$ of a muon with charge q can be written as:

$$p_T[\mathrm{GeV}] = 0.3 \times B[\mathrm{T}] \times r[\mathrm{m}] \times q \tag{36}$$

The magnetic field inside the CMS solenoid is essentially uniform and known with great precision ($B = 3.8$ T), while the radius of curvature is related to the arc length L and the sagitta distance, s, defined in Figure 63, via:

$$r[\mathrm{m}] \approx L[\mathrm{m}]^2/8s[\mathrm{m}] \tag{37}$$

This approximation is valid for $L/r \ll 1$.

Combining the equations (36) and (37), we obtain:

$$s[\mathrm{m}] \approx (0.3B[\mathrm{T}]L[\mathrm{m}]^2/8)(q/p_T[\mathrm{GeV}]) = (0.3BL^2/8) \times (q/p_T) \tag{38}$$

It is observed that s is inversely proportional to the transverse momentum. Therefore, to improve the resolution in the measurement of p_T in the cases with small sagitta, the tracks of the muons in CMS are reconstructed in different subdetectors separated several meters from the collision point (as shown in Section 2). By doing that, longer tracks and consequently higher s values are obtained.

It is worth to keep in mind that measuring s with precision can be a great challenge. For instance, a muon with $p_T = 1$ TeV that passes through the CMS barrel ($L \approx 7.5$ m) has a sagitta value of the order of one centimeter, which requires muon detectors with excellent spatial resolution. On the other hand, even systematic uncertainties in the position of the different detectors can introduce a bias in the final measurement.

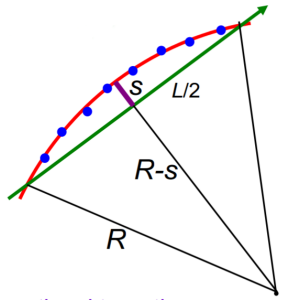

Figure 63: Definition of the sagitta distance, s, from the length of the reconstructed track L and its radius r.

Also, when the high-momentum muons pass through the dense components of the detector, mainly iron, they not only suffer energy loss by ionization, but also undergo other processes such as pair production, Bremsstrahlung, or photonuclear interactions. These processes can for instance modify the muon energy or generate additional particles, making the reconstruction process even more difficult. Figure 64 shows the dependence of the muon average energy loss when passing through different materials as a function of its energy.

It can be observed that the critical energy for iron, E_c^{iron}, where the ionization energy (in brown) is equal to the sum of all radiative losses (in purple), occurs at approximately 300 GeV. As a consequence, the main source of energy loss for a muon with $E > E_c^{iron}$ traveling in iron is due to electromagnetic radiation resulting from the production of electrons and photons. This electromagnetic radiation manifests itself as a shower of particles that produce additional signals in the detector, and can even change the direction of the muon trajectory, affecting the reconstruction of its track and consequently degrading the measurement of its momentum. It should be noted that because the CMS tracker is composed of a relatively light material, the probability of producing an electromagnetic shower

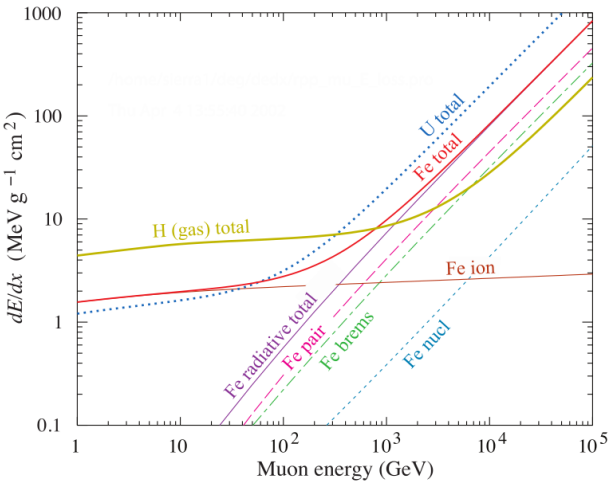

Figure 64: Average ionization and radiation energy loss of the muon in hydrogen, iron, and uranium, as a function of its energy. In the case of iron, contributions for pair production, Bremsstrahlung, and photonuclear interactions are separated. Figure taken from [112].

in this region of the detector is very low when a muon passes though it, so this phenomenon will be much more visible in the muon system.

The dedicated CMS track reconstruction algorithms, that are used for the muon high-p_T assignment, avoid dealing with shower emission cases (as will be explained in more detail in Section 9.2). Thus, for example, if several impacts are found on a subdetector that may be indicative that a shower has taken place, these signals are typically ignored when reconstructing the muon track. The objective of this study, instead, is to pick as much information as possible from the trajectory of the muons as they pass through CMS (including those signals from electromagnetic showers). To do that, highly energetic simulated muons with known generated p_T (the real momentum assigned in the particle simulation) are used. Then, a DNN is trained to do regression to the reconstructed p_T, aiming to provide a better transverse momentum scale and resolution than those provided by the CMS algorithms, and if so, consider including this kind of methodologies for the future *LHC Run 3* data taking.

To quantify the quality of the transverse momentum assignment, the R variable will be used, defined as:

$$R = \frac{|p_T^{GEN} - p_T^{RECO}|}{p_T^{GEN}} \,, \tag{39}$$

where p_T^{GEN} refers to the generated muon transverse momentum and p_T^{RECO} to

the reconstructed transverse momentum through its track in the detector.

It should be noted that the central value of the R distribution accounts for the existing bias in the estimation of the momentum, while its width accounts for the resolution of the system.

9.1 Machine learning and its use in High Energy Physics

Machine learning is a branch of artificial intelligence whose target is to develop algorithms that allow the machine to learn from the experience.

Since CMS has precise simulations that include the production, propagation, and measurement of these muons, where the real momentum of the particle is known, this study will focus on a supervised method. In this way, the mathematical model takes, in the training phase, both the characteristics of the muon (input data) as well as the real transverse momentum assigned in the simulation of the particle, so that at this stage the model can find correlations and behavior patterns in the input data that could improve the estimate of the muon $\mathrm{p_T}$ currently given by CMS. Later, in the testing process, the model must be able to give a prediction of the $\mathrm{p_T}$ quantity taking as input data from muons with unknown transverse momentum.

One of the different types of machine learning algorithms is the artificial neural networks, whose operation is inspired by the biological neural networks that make up the brain, with connected units called neurons that receive certain information, process it, and transmit it to the next neurons with which they are connected. The schematic structure of a neural network is shown in Figure 65. It is essentially made up of layers of neurons connected to each other, where each connection is associated with a weight that accounts for the importance of the information that goes from one neuron to another.

The transmission of the information goes from left to right: first the weights of the network are initialized (usually randomly), and the first layer of neurons corresponds to the different input variables. If all the neurons in one layer are connected to the neurons in the next layer, each neuron in the next layer will receive as input a sum of the information from each neuron in the previous layer multiplied by its associated weight, so that a a non-linear activation function is applied to this input and the information is again propagated to the following layers. Once the information reaches the final layer of the network, the error in the prediction is evaluated with respect to the known real value of the quantity to be predicted (in this case the p_T^{GEN}).

On the other hand, the learning process is done in the opposite direction: once

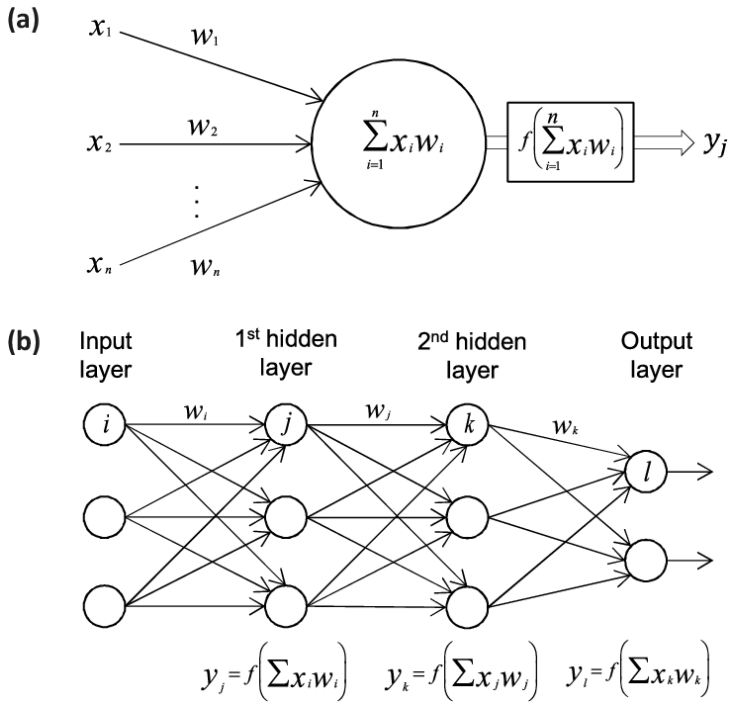

Figure 65: Graphic representation of the operation of an artificial neural network. a: processing of a neuron, where each input x_i is associated with a weight w_i, and the sum of all weighted inputs that reaches a certain neuron is passed to the next neuron after applying a non-linear activation function. b: example of a multilayer neural network, where the neurons of each layer are connected to all the neurons of the next layer. The information is propagated from the first layer to the final layer, where the error in the prediction is evaluated. Image taken from [126].

the prediction error is obtained, the weights are updated layer by layer backwards according to the direction of the gradient of the error function [127], so that in the next iteration the error in the prediction is expected to be smaller.

The DNN differs from the conventional neural network by having more hidden layers and a greater number of neurons in each layer, thus increasing the number of parameters, level of abstraction and complexity, and allowing higher performance in prediction for high-dimensional input data sets.

In High Energy Physics, the use of deep neural networks has spread in recent years, being one of the most widely used tools in the reconstruction of physical objects and in the classification of events in searches for new particles (see [128]).

9.2 Current muon high-p_T assignment in the CMS experiment

The momentum of a muon with p_T between 10 and 200 GeV is extracted from the reconstruction of its trajectory through the signals it leaves in the tracker together with the impacts on the muon chambers by means of a fit by a Kalman Filter (see Section 2.2).

In the case of high-p_T muons (p_T >200 GeV), the probability of emission of additional particles generated in electromagnetic showers is higher, and these showers typically leave additional signals (multiple segments) in the different muon chambers. These additional signals can be used in the Kalman Filter fit instead of the signals that actually come from the muon to be measured, or equivalently, a high number of segments in a particular chamber can degrade the reconstruction itself. This is why high-momentum muons require a more careful treatment of the information found in the muon system and are reconstructed using special algorithms called *refits*, which select which impacts are used in the track reconstruction process and which ones are not.

The following subsections provide an overview of the high-p_T muon *refits* currently being performed in CMS, as well as the algorithm used for final transverse momentum assignment: the *TuneP* algorithm.

9.2.1 TPFMS refit

The first refit, which is the simplest in terms of its implementation, is the TPFMS (Tracker-Plus-First-Muon-Station), which selects only the signals in the tracker and in the innermost station of the muon system (compatible with those found in the tracker). In this way, it is intended to ignore the impacts of the more distant stations and thus eliminate the possible contamination due to electromagnetic showers.

9.2.2 Picky refit

The Picky refit aims to find possible showers and eliminate those additional signals that do not belong to the original track of the muon. In this way, if more than n impacts are found within a cone around a specific impact, the station where these signals are found is marked as contaminated. Thus, when making the fit of the track, if its χ^2 is above a certain threshold, those impacts that are in contaminated chambers are eliminated from it and the fit is repeated again. The algorithm parameters n and χ^2 are optimized based on simulation studies.

9.2.3 DYT refit

When a muon loses a large fraction of its energy during its trajectory, its direction can change and the signals found in the following stations can be inconsistent with

the initial trajectory (see Figure 66). This fact causes problems in the reconstruction process of the track and consequently when trying to assign a proper value to its transverse momentum. In this case, the DYT refit (Dynamic truncation) considers it more convenient to stop the Kalman Filter once a change in the muon trajectory is detected.

In the DYT refit, an operator E that gives an idea of the compatibility of a certain segment in a chamber with the extrapolation of the internal track to this chamber is defined. Then, if this operator exceeds a predetermined value, the Kalman Filter stops and does not take into account those impacts found in the chambers after the identified change of trajectory.

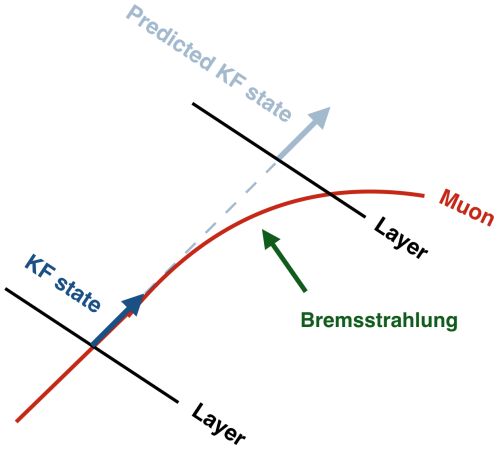

Figure 66: Graphical representation of the change in the muon trajectory after a large energy loss by Bremsstrahlung. KF stands for "Kalman Filter".

9.2.4 Final high-p_T assignment: the *TuneP* algorithm

Finally, the recommendation from the *Muon Physics Object Group* of CMS for the high-p_T muon assignment corresponds to that provided by the *TuneP* algorithm. The target of this algorithm is simply to choose which is the best possible reconstruction from the track reconstructed only in the tracker and the tracks obtained by the different *refits* (TPFMS, Picky and DYT). This choice is made taking into account jointly the χ^2/ndof and the σ_{p_T}/p_T of the considered tracks.

With all these considerations, CMS manages to measure the transverse momentum of the muons in the CMS barrel with a resolution of about 3% for $p_T < 1$ TeV, and about 6% for $p_T > 1.5$ TeV [129].

9.3 Proposed method

A regression algorithm using a DNN to predict the p_T of highly energetic muons is presented, aiming to improve the p_T assignment provided by the CMS algorithms.

Since part of the reconstruction problems of this type of muons has to do with the high multiplicity of segments found in the muon system due to the production of electromagnetic showers, the key element of the proposal is the study of the spacial distribution of the segments in the muon chambers. In particular, the sample that will be used for the DNN training is composed of the p_T provided by the *TuneP* algorithm, the information of the muon track reconstructed only in the tracker, and information about the number and spacial distribution of the segments found around the extrapolation.

In this section, the tools and methodology used to extract and process the data will be detailed.

9.3.1 Simulation sample

A total of 5 million of proton-proton collision MC events have been generated at a center of mass energy of $\sqrt{s} = 13$ TeV using Pythia, where each event contains a single muon. The generated muons have a total momentum randomly distributed in the range between 200 and 4000 GeV and spatially distributed in $|\eta| < 0.9$. The detector response is simulated with GEANT4.

The tracker track η and the generated p_T distributions of all the muons of the sample are shown in Figure 67.

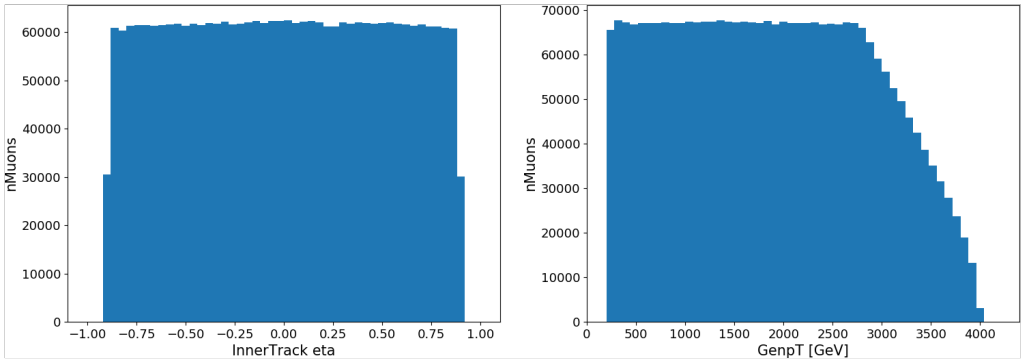

Figure 67: Distribution of the tracker track η (left) and the generated p_T (right) for the muons of the generated MC sample.

9.3.2 Muon and segments selection

The selection process of the muons and segments, as well as the production of the extrapolations from the simulation sample, consists of the following parts:

1. Data reading: in the input data, the muons and segments reconstructed in each event are stored in collections, which work as containers of information. Therefore, the first step is to read the collections to be able to iterate over them.

2. A loop over the muon collection is performed, and those that have a reconstructed track in the tracker with $p_T > 200$ GeV are selected. The chosen tracks are required to be close to the real generated track within a cone radius $\Delta\mathrm{R} = \sqrt{(\Delta\eta^2 + \Delta\phi^2)} < 0.3$. This is to ensure that the muon generated matches the reconstructed track.

3. Subsequently, a loop over the segments collection found in the event is performed, and their coordinates and the identifiers of the detectors where they are found are stored in case the segments are valid, meaning that the coordinates have been measured correctly, and are compatible with the initial path of the track, with a χ^2 of the fit of the hits that make up the segment smaller than 3.

4. The outermost position of the tracker track is selected and extrapolated to the surface of each of the muon chambers where at least one segment has been found. The extrapolation process is done by taking into account the trajectory of the muons by applying Lorentz's law, and their interactions with the detector material, such as ionization or multiple Coulomb scattering.

5. Of all the segments saved in step 3, those that are in chambers where the extrapolations are valid (compatible with the direction of the initial trajectory), go in the direction of the magnetic field imposed by the CMS solenoid, and comply that the distance between the center of the camera and the extrapolation itself does not exceed the size of the camera itself are selected. This last requirement is of vital importance, since the surfaces to which it is extrapolated are planes of infinite dimension (not delimited by the real dimensions of the cameras), and a generic charged particle in motion subjected to a magnetic field can always intersect a plane of infinite dimension when bending.

6. All variables of interest are stored: information about the muon track in the tracker, the coordinates and directions of the stored segments, and the coordinates of the extrapolations.

Figures 68 and 69 show the spatial positions of the extrapolations and the selected segments in the x-y and x-z planes.

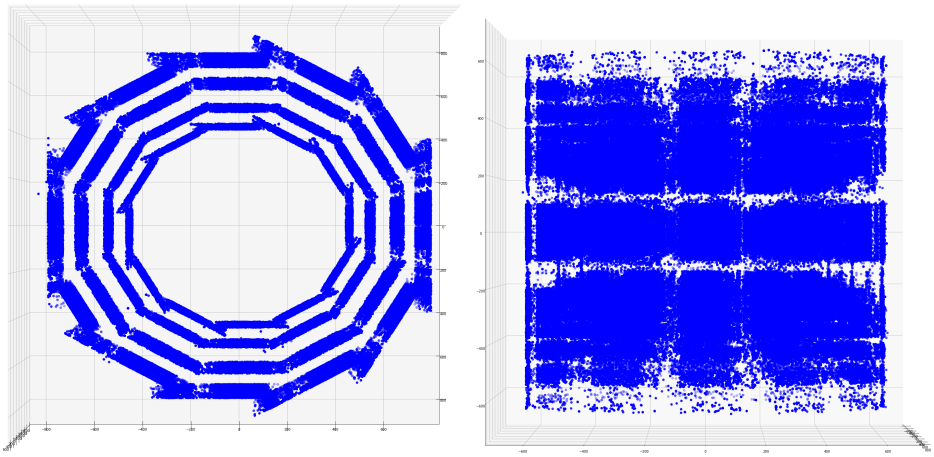

Figure 68: Geometric positions of all the selected extrapolations. Left: Extrapolations in the x-y plane. Right: Extrapolations in the x-z plane.

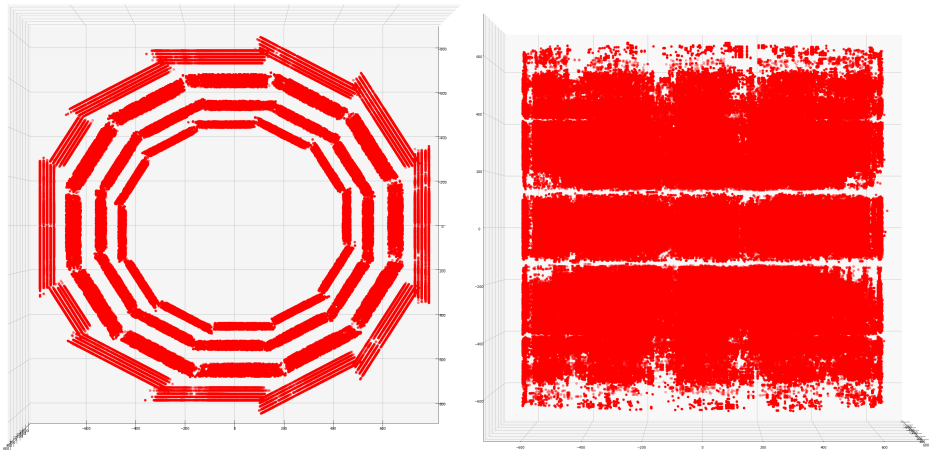

Figure 69: Geometric positions of all selected segments. Left: Segments in the x-y plane. Right: Segments in the x-z plane.

9.3.3 Control distributions

After defining the sample that will be used for the DNN training and testing, several checks have been carried out to ensure its quality and coherence.

First, muons with four or more segments in the DTs are selected, and these are

required to have at least one segment in each station. Then, the muons that match these conditions are separated into two categories: those that have exactly four segments (one in each station), and those that have more than four segments, so that the muons belonging to the second category could have emitted an electromagnetic shower. In this way, if the maximum value of distance between the segment and the extrapolation of all the segment-extrapolation pairs is plotted, one would expect to find relatively low values in the first category, and higher values in the second one, due to the presence of additional segments. The distributions for both groups are shown in Figure 70.

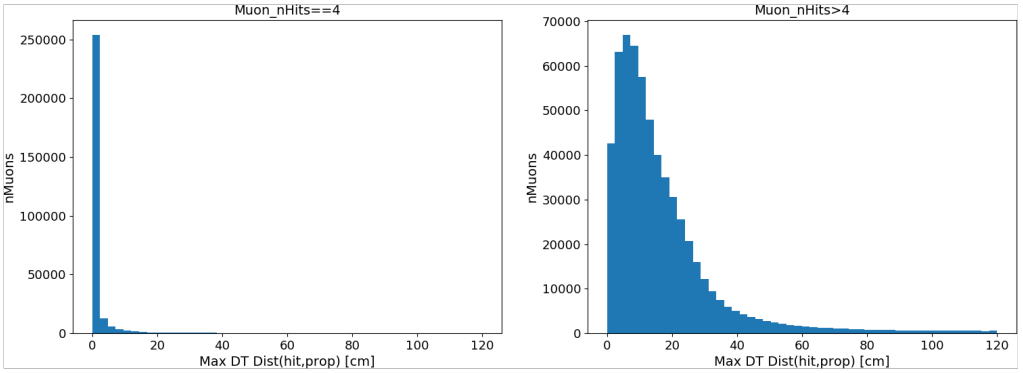

Figure 70: Distributions of the maximum value for the distance between the segment and the extrapolation (per muon). Left: Muons with four segments, one at each station. Right: Muons with more than four segments, and with at least one segment per station.

Figure 71 shows the dependence of the mean of the number of segments produced by each muon with the generated p_T for all the muons in the sample. In this case, it is observed that there is a clear upward trend in the average number of segments with the p_T, since the higher p_T the greater probability to emit showers, and therefore more signals are expected to be found in the muon chambers.

Figure 72 shows the dependence of the standard deviation and the average of R, defined in Eq. (39), with the generated p_T. It can be seen that the p_T assignment degrades with the generated p_T as expected.

Finally, for each muon, the variables that will be used in the DNN training are built: the total number of segments found in each DT station, the mean of the spatial distribution of segments per station, the standard deviation, the skewness, and the kurtosis.

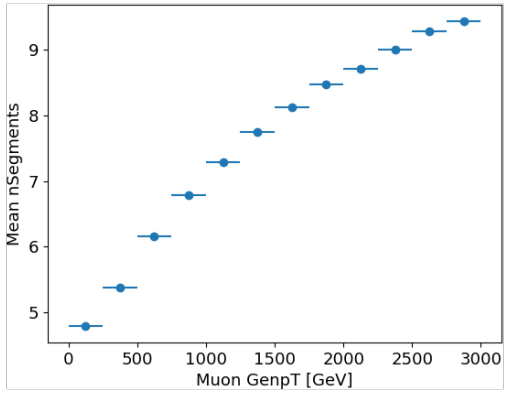

Figure 71: Average value of segments found per muon as a function of the transverse momentum generated, where the uncertainty in the abscissa axis corresponds to the standard deviation of the distribution of the number of segments per bin of p_T divided by the square root of the number of muons in each bin.

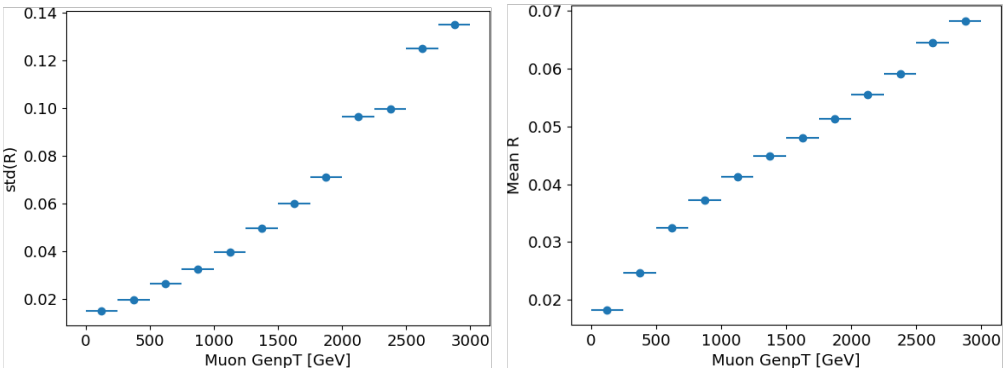

Figure 72: Dependence of the standard deviation and the mean value of R with the generated p_T. Left: Standard deviation of R on the y-axis. Right: Mean value of R as a function of the y-axis, where the uncertainty corresponds to the standard deviation of the distribution of R per bin of p_T divided by the square root of the number of muons in each bin.

9.4 DNN training

Once all the possible information has been obtained from the muons as they pass through CMS, the objective is to train a deep neural network taking as input the properties of the track in the tracker and the spatial information of the signals collected in the muon system. In this case, the loss function to be minimized will be a function that depends on the difference between the known generated p_T and the predicted value of p_T that the network returns, in order to learn the characteristics of muons (especially those that emit showers) and regress to their transverse momentum.

For simplicity, it should be noted that the training presented in this study is carried out with muons detected only in the DTs ($|\eta| < 0.9$), since the emission of showers depends fundamentally on the total momentum of the muon p. Thus, in the DTs $p_T \approx p$, while in the CSCs we have $p_T << p$.

The sample has been divided into 80% for the model training (of which 10% will be used as the validation data set), while 20% is used for testing it.

Regarding the type of network used, a *fully-connected* network has been trained, where all the neurons of each layer are connected with the neurons of the contiguous layers.

9.4.1 Input variables

The variables used for training are divided into three categories according to their nature, giving rise to a total of 53 variables:

- Features of the tracker track: p_T, η, ϕ, charge.
- Transverse momentum given by the track selected by the *TuneP* algorithm.
- Information on the set of segments collected in each DT station: the total number of segments in the station, the spatial mean in x, y, z, the standard deviation in x, y, z, the skewness in x, y, z, and the kurtosis in x, y and z.

Some distributions of the variables used in the training from the first two DT stations are shown in Figures 73 and 74.

9.4.2 DNN architecture

The following architecture has been used:

- Input layer with 53 neurons (training variables), and one neuron in the output layer. The number of hidden layers and neurons in each layer are varied to optimize the architecture.
- Activation: from the first to last layer the activation function *ReLu* [130] is used. It is one of the most appropriate activation functions for deep learning problems with high dimensionality because it always has a derivative equal to unity and thus the *vanishing gradient* [131] issue is avoided. In the last layer a linear activation function is used to do the regression to the transverse momentum.

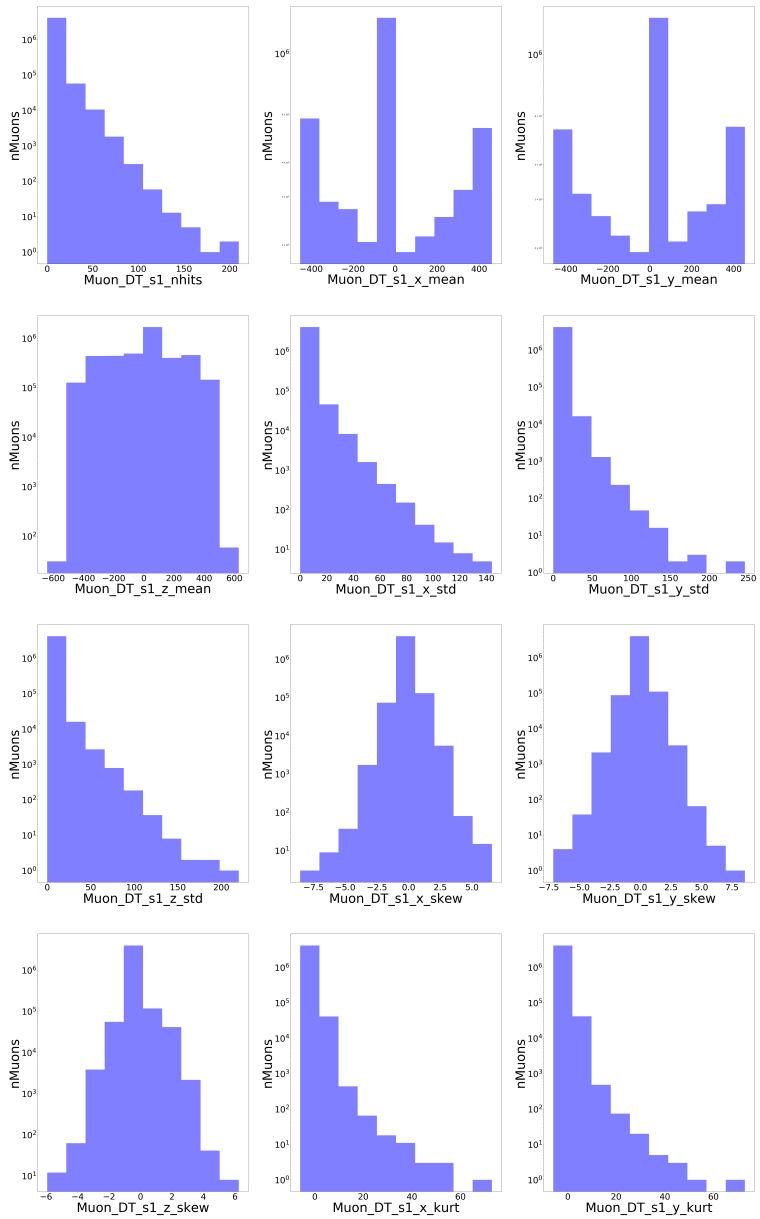

Figure 73: Distributions of the training variables the first two stations of the DTs (I).

- Loss function: *Mean Squared Error* (MSE), which is defined as the average of the squared errors as:

$$MSE = \frac{1}{n}\Sigma_{i=1}^{n}\left(p_T^{GEN^2}{}_i - p_T^{PRED^2}{}_i\right), \tag{40}$$

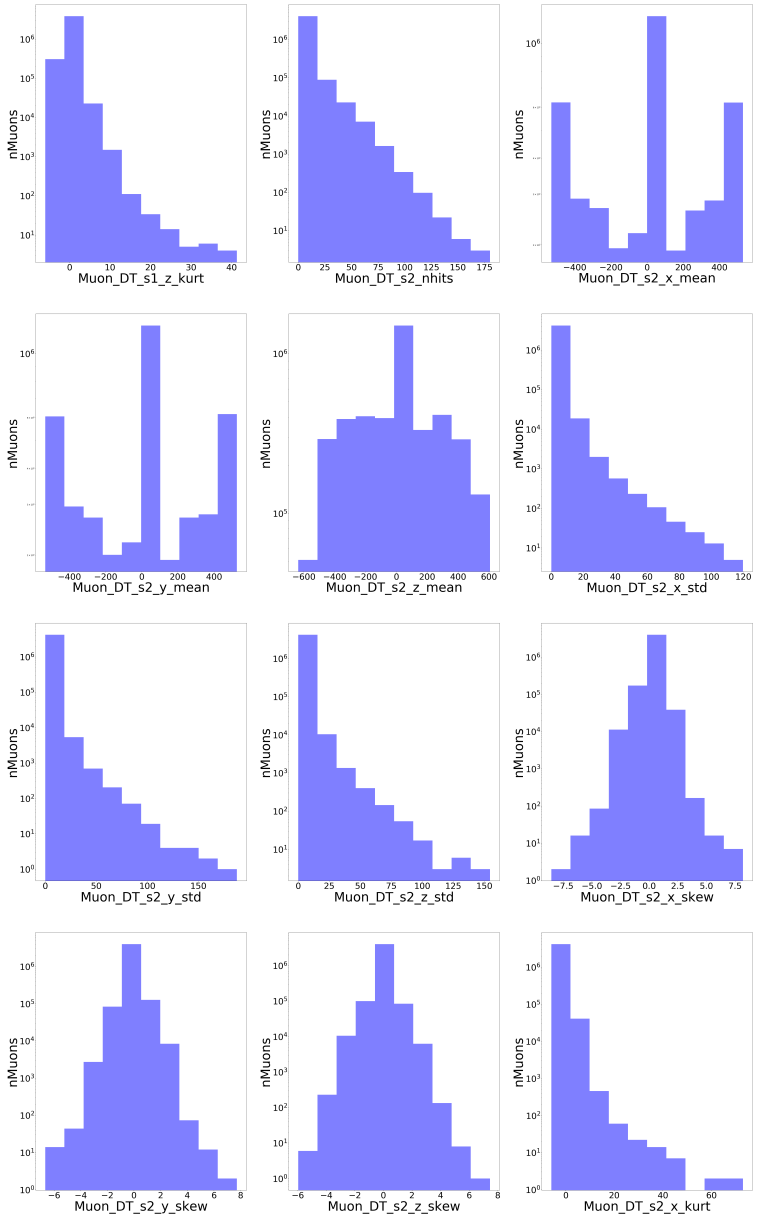

Figure 74: Distributions of the training variables of the first two stations of the DTs (II).

where n corresponds to the number of muons in the sample, ${p_T^{GEN}}_i$ refers to the generated transverse momentum of the muon i, and ${p_T^{PRED}}_i$ to the transverse momentum that the network predicts for it.

- Gradient descent: to speed up learning, the *mini-batch gradient descent* [132] technique is used, which consists of dividing the training data set into small

fragments called *mini-batches*, in such a way that the network parameters are updated for each fragment without having to go through the entire sample. This technique considerably improves the training speed while achieving a reasonably good convergence of the loss function to the minimum. The size of the *mini-batch* is a varied parameter within the optimization process.

- As optimizer in the search for the minimum of the loss function, the *Adaptive moment estimation* (Adam) is used, which combines the descent of the gradient with momentum [133] and the gradient descent with *RMSprop* [134]. The learning rate is varied as part of the optimization process, while the rest of the hyperparameters are taken as recommended by Adam's original article [135].

- Training epochs: 1000.

- To regularize, the *Early stopping* technique is evaluated in the loss of the validation data set (which is not used for training), with a patience of 50 epochs. In this way, the value of the MSE is obtained in the validation data set for each epoch. Then, if the MSE does not improve after 50 epochs, the training is stopped abruptly to prevent the model from overtraining, and the model found with the lowest MSE in validation is saved.

The optimized values of the different hyperparameters have been obtained after testing several configurations with a grid type search. The number of hidden layers is chosen randomly as an integer between 5 and 15. The number of neurons in each layer is chosen randomly among 128, 256, and 511 neurons. The learning rate is selected from a uniform distribution between 0 and 0.001. The *mini-batch* size is chosen randomly among 256, 511, 1024, 2048 muons.

A total number of 100 architectures have been trained, and the selected configuration has been the one that provides the smallest MSE value in the test data set, corresponding to: 13 hidden layers, with 512, 256, 128, 64, 64, 64, 32, 16, 16, 16, 16, 16, and 16 neurons respectively, learning rate of 0.0001856, and *mini-batch* size of 1024. This optimized architecture yields to a MSE of 35134.2 for the test data set.

9.5 Results

Figure 75 shows the value of MSE loss, defined in Eq. (40), as function of the training epoch.

Figure 76 shows two-dimensional distributions of the p_T predicted by the DNN and the p_T given by the *TuneP* algorithm as a function of the generated p_T for the muons in the test data set.

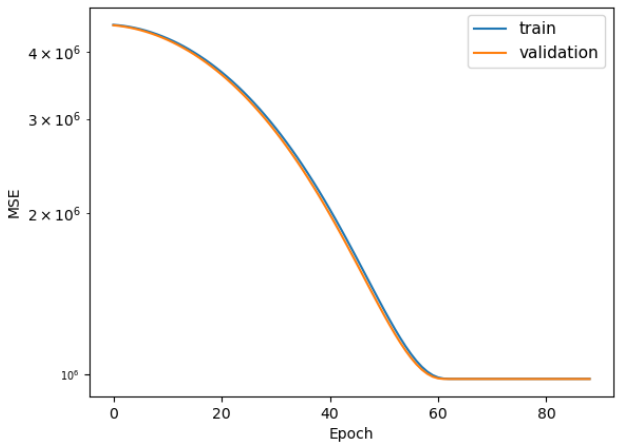

Figure 75: MSE value as a function of the training epoch for the training data set (in blue) and for the validation data set (in orange).

Figure 77 shows the dependence of the mean and the standard deviation of the R distribution with the generated p_T for the test data set muons, comparing in both cases the results obtained when introducing in Eq. (39) the p_T given by the *TuneP* algorithm, and the p_T predicted by the DNN. It is qualitatively observed that the DNN response is approximately flat for muons with $p_T > 1500$ GeV. In contrast, when the p_T provided by the *TuneP* algorithm is taken, the assignment of the transverse momentum is progressively degraded as the generated p_T increases. The fact that the resolution flattens for high values of p_T seems to indicate that the DNN is able to learn the shape of the showers as a function of the transverse momentum. Thus, the dependence of the p_T error with the p_T due to the sagitta measurement is reduced.

In order to quantify the results, it must be taken into account that the network has been fed with a sample of muons with a maximum value for the generated p_T of about 4000 GeV. Thus, it is natural to think that the model will tend to assign a transverse momentum equal to or less than this maximum value to the muons whose p_T is close to 4000 GeV. For this reason, and to be able to provide unbiased results, the evaluation of the method is performed for muons with transverse momentum generated in the range $1500 \leq p_T \leq 2500$ GeV. In this range, the response of the DNN is symmetric at both sides of the $Predicted\ p_T = Generated\ p_T$ line (see Figure 76), and the showering information is relevant enough to improve the p_T resolution compared to the *TuneP* assignment (see Figure 77).

For this range of p_T, the obtained standard deviation value of R for the test data set is $\sigma_{R_{TuneP}} = 0.0796$ when taking the p_T from the *TuneP* algorithm, and $\sigma_{R_{pred}} = 0.0598$ when taking the p_T predicted by the regression model. Therefore, the preliminary results show an improvement in the resolution of the transverse

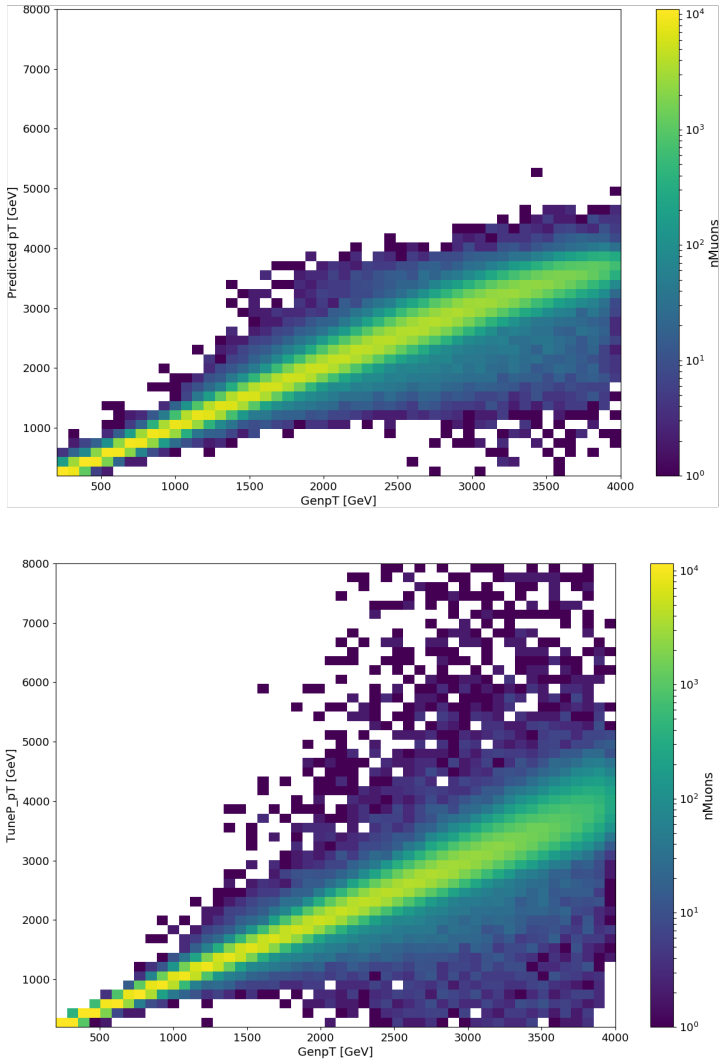

Figure 76: Two-dimensional distribution of the p_T as a function of the generated p_T for the muons of the test data set. Above: p_T predicted by the neural network on the y-axis. Bottom: p_T given by the *TuneP* algorithm on the y-axis.

momentum assignment of 25% compared to the transverse momentum provided by CMS. On the other hand, as can be seen in Figure 77, the improvement in the muon p_T scale seems to occur at larger p_T values, so further studies are needed to properly understand the reason behind.

Among the possible ways of expanding the work, which will be taken into account in future studies, are:

- Carry out detailed studies to characterize the emission of electromagnetic showers and its relationship with the p_T of the muon, and thus have a better

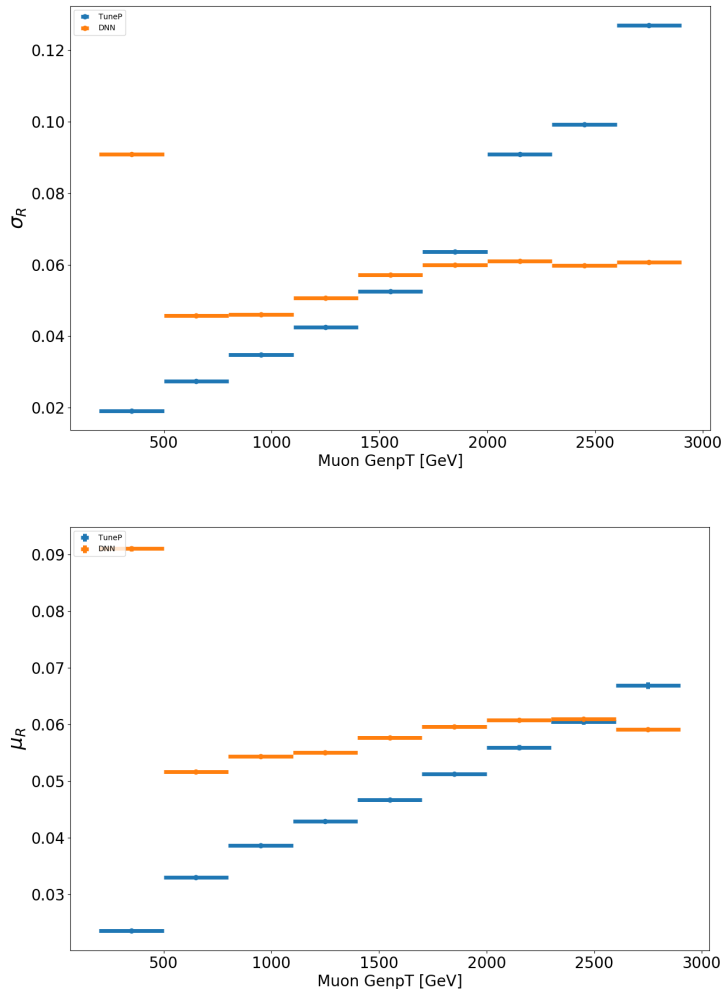

Figure 77: Dependence of the standard deviation σ (top) and the mean μ (bottom) of the variable R, defined in Eq. (39), with the generated p_T. Both quantities are calculated from the distribution of R in each bin of p_T. Blue: Taking the p_T provided by the *TuneP* algorithm in the definition of R. Orange: Taking the p_T predicted by the DNN in the definition of R.

understanding of how the DNN interprets this information.

- Simulate muons passing through the CSCs, and include them in the regression model, either as an independent training to that of the muons in the DTs, or ideally achieve a single training with all the muons (regardless of whether they pass through the DTs or CSCs).

- Convert the information from collected segments into images, and try a Convolutional Neural Network architecture [136], which has shown great performance in similar scenarios.

10 Summary and conclusions

Measurements of W^+W^-boson pair production in proton-proton collisions at $\sqrt{s}$ = 13 TeV have been performed. The analysis is based on data collected with the CMS detector at the LHC in 2016, corresponding to an integrated luminosity of 35.9 fb^{-1}. In the analysis, events with a pair of opposite charged and different-flavour leptons are selected. For the first time during the *Run 2* in CMS, also events with same-flavour leptons are considered in this analysis.

The reported measurements for the different-flavour and same-flavour channels are σ_{WW}^{DF} =122.0 ± 1.7 (stat) ± 7.2 (exp) ± 2.1 (theo) ± 3.2 (lumi) ± 2.1 (br) pb and σ_{WW}^{SF} = 106.0 ± 2.7 (stat) ± 17.5 (exp) ± 4.4 (theo) ± 4.0 (lumi) ± 1.8 (br) pb respectively, where (stat) refers to the uncertainty in the cross section due to statistical error in the data, (exp) to the total estimate of experimental systematic uncertainties, (theo) to the total estimate of theoretical systematic uncertainties, (lumi) to the uncertainty on the integrated luminosity of the 2016 CMS data set, and (br) to the branching fraction uncertainty on the leptonic decay of the W bosons. The combined production cross section is σ_{WW}^{DF+SF} =117.6 ± 1.4 (stat) ± 5.5 (exp) ± 1.9 (theo) ± 3.2 (lumi) ± 2.0 (br) pb = 117.6 ± 6.8 pb. These measured values are consistent with the theoretical prediction, σ_{WW}^{theo} =118.8 ± 3.6 pb, and the total measurement improves the precision of the previous CMS result by about 40%.

Fiducial and differential cross sections are also measured. The fiducial region is defined at generation level by requiring two leptons in the event, electrons or muons, with $p_T > 20$ GeV and $|\eta| < 2.5$, $m_{\ell\ell} > 20$ GeV, $p_T^{\ell\ell} > 30$ GeV, and $p_T^{miss} > 20$ GeV, in order to emulate the analysis selections as much as possible. The measured fiducial cross section combining the different-flavour and same-flavour channels is σ^{fid} = 1.529 ± 0.020 (stat) ± 0.069 (exp) ± 0.028 (theo) ± 0.041 (lumi) pb = 1.529 ± 0.087 pb, which agrees well with the theoretical prediction σ_{NNLO}^{fid} = 1.531 ± 0.043 pb. Fiducial cross sections adding the 0-jets selection to the fiducial region definition are measured as function of the jet transverse momentum threshold. The results, as shown in Figure 36, are in agreement with the POWHEG and PYTHIA predictions. The differential cross section measurements as function of $m_{\ell\ell}$, $p_T^{\ell\ max}$, $p_T^{\ell\ min}$, $p_T^{\ell\ell}$, and $\Delta\phi(\ell,\ell)$, shown in Figure 37, also agree well with the predictions from POWHEG and PYTHIA.

Finally, a search for anomalous triple gauge boson couplings that could affect the W^+W^-in the context of an effective field theory is performed. Constraints on the corresponding coupling constants are set using the invariant mass distribution of the two leptons as a probe. Comparing with previous W^+W^-CMS results, the reported limits are between a factor 2 and 3 stronger. Furthermore, comparing with other results from ATLAS, D0, or LEP, this analysis provides some of the strongest limits on the studied coefficients as shown in Figure 44.

As a possible extension of the work, the reported results on the differential cross section measurements and on the constraints on the effective field theory coefficients can be potentially improved by analyzing the full *Run 2* CMS data set, aiming to squeeze the whole available luminosity in those measurements which are limited by the statistical uncertainty. On the other hand, including the latest recipes for the experimental uncertainties over the full *Run 2* data set could also help to improve their precision. Lastly, a finer categorization of the events depending on the charge, on the p_T, and on the flavour of the leptons, could allow to further constraint the systematic uncertainties and then improve the precision of the total and fiducial cross section measurements.

A search for dark matter particles produced in association with a dark Higgs boson has been also performed. The analysis is based on data collected with the CMS detector at the LHC during the full *Run 2* (2016-2018), corresponding to an integrated luminosity of 137 fb^{-1}. The decay mode of the dark Higgs boson to a W^{+}W^{-}pair, for $m_s > 160$ GeV, and the subsequent leptonic decay of the W bosons to different-flavour leptons has been explored, being the first measurement carried out in the CMS experiment using this novel interpretation. The data from each year has been studied and analyzed separately, and the combined results include an adequate treatment of the correlations between the uncertainties that affect the different data periods. A global fit to the observed data in the three data periods is performed to get the final results, where all the analysis regions are simultaneously fitted. The fitted distributions from the signal regions are the $\text{m}_{\ell\ell}$, the $\Delta\text{R}(\ell,\ell)$, and the $\text{m}_{\text{T}}^{\ell\,\text{min,p}_{\text{T}}^{\text{miss}}}$, which correspond to the three variables that show the greater power to separate the signal from the main backgrounds. No significant deviations from the Standard Model predictions are observed. Thus, upper limits at 95% confidence level are set on the dark Higgs model parameters, where the most stringent limit found is set for $m_{DM} = 150$ GeV, excluding m_s masses up to ≈ 300 GeV in a mass range $\approx 480 < m_{Z'} < 1200$ GeV, and up to $m_{Z'} \approx 2000$ GeV for $m_s = 160$ GeV.

To extend the sensitive phase space, an additional analysis exploring the semileptonic decay of the W^{+}W^{-}pair is being performed at CMS, aiming to combine the results from both channels in a single publication. On the other hand, the expected increase in the luminosity during the next *LHC Run 3* will allow to access to a wider part of the $m_s - m_{Z'} - m_\chi$ parameter space. In addition, it would be also possible to extend the search to the plane of the couplings (g_q and g_χ), and as discussed previously, a finer categorization of the events may also enhance the statistical sensitivity of the analysis.

Looking ahead of the next *LHC Run 3* that will start in 2022, new techniques have been studied with the aim of improving the muon transverse momentum as-

signment provided by the current algorithms of the CMS Collaboration. For this purpose, a regression model has been trained through a DNN. The DNN takes as input the p_T given by the *TuneP* algorithm, the information on the reconstructed muon track in the tracker, and the information on the number and spacial distribution of the segments around the extrapolation of the tracker track to the muon chambers. The preliminary results obtained show a 25% improvement in the resolution of the transverse momentum (with respect to the generated p_T) for muons with $1500 \leq p_T \leq 2500$ GeV and $|\eta| < 0.9$. This promising methodology could be useful for most of the BSM searches at the LHC with boosted topologies including muons in the final state.

References

[1] Mary K. Gaillard, Paul D. Grannis, and Frank J. Sciulli. The standard model of particle physics. *Rev. Mod. Phys.*, 71:S96–S111, Mar 1999.

[2] Andrew Purcell. Go on a particle quest at the first CERN webfest. Le premier webfest du CERN se lance à la conquête des particules. Technical report, CERN, Aug 2012.

[3] Peter W. Higgs. Broken symmetries and the masses of gauge bosons. *Phys. Rev. Lett.*, 13:508–509, Oct 1964.

[4] F. Englert and R. Brout. Broken symmetry and the mass of gauge vector mesons. *Phys. Rev. Lett.*, 13:321–323, Aug 1964.

[5] Nima Arkani–Hamed, Savas Dimopoulos, and Gia Dvali. The hierarchy problem and new dimensions at a millimeter. *Physics Letters B*, 429(3):263–272, 1998.

[6] Michael Dine and Alexander Kusenko. Origin of the matter-antimatter asymmetry. *Rev. Mod. Phys.*, 76:1–30, Dec 2003.

[7] Gianfranco Bertone, Dan Hooper, and Joseph Silk. Particle dark matter: evidence, candidates and constraints. *Physics Reports*, 405(5):279–390, 2005.

[8] Fritz Zwicky. The redshift of extragalactic nebulae. *Helvetica Physica Acta*, 6:110–127, 1933.

[9] Vera C. Rubin. The rotation of spiral galaxies. *Science*, 220(4604):1339–1344, 1983.

[10] Peter Schneider, Jürgen Ehlers, and Emilio E. Falco. *Gravitational Lenses*. Springer Berlin Heidelberg, 1992.

[11] M. Markevitch, A. H. Gonzalez, D. Clowe, A. Vikhlinin, W. Forman, C. Jones, S. Murray, and W. Tucker. Direct constraints on the dark matter self-interaction cross section from the merging galaxy cluster 1e 0657-56. *The Astrophysical Journal*, 606(2):819–824, may 2004.

[12] The Plank Collaboration. Planck 2018 results. *Astronomy and Astrophysics*, 641:A6, Sep 2020.

[13] Ortwin E. Gerhard and David N. Spergel. Dwarf Spheroidal Galaxies and the Mass of the Neutrino. *Astrophysical Journal Letters*, 389:L9, April 1992.

[14] Gary Steigman and Michael S. Turner. Cosmological constraints on the properties of weakly interacting massive particles. *Nucl. Phys. B*, 253:375, 1985.

[15] Duccio Pappadopulo, Joshua T. Ruderman, and Gabriele Trevisan. Dark matter freeze-out in a nonrelativistic sector. *Phys. Rev. D*, 94:035005, Aug 2016.

[16] Kang Young Lee, Yeong Gyun Kim, and Seodong Shin. Singlet fermionic dark matter. *Journal of High Energy Physics*, 2008(05):100–100, May 2008.

[17] The ATLAS Collaboration. Search for dark matter and other new phenomena in events with an energetic jet and large missing transverse momentum using the ATLAS detector. *JHEP*, 01:126, 2018.

[18] The CMS Collaboration. Search for new physics in final states with an energetic jet or a hadronically decaying W or Z boson and transverse momentum imbalance at $\sqrt{s} = 13$TeV. *Phys. Rev. D*, 97:092005, 2018.

[19] The ATLAS Collaboration. Search for dark matter produced in association with bottom or top quarks in $\sqrt{s} = 13$ TeV pp collisions with the ATLAS detector. *Eur. Phys. J. C*, 78:18, 2018.

[20] The CMS Collaboration. Search for dark matter in events with energetic, hadronically decaying top quarks and missing transverse momentum at $\sqrt{s} = 13$ TeV. *JHEP*, 06:027, 2018.

[21] The ATLAS Collaboration. Search for dark matter at $\sqrt{s} = 13$ TeV in final states containing an energetic photon and large missing transverse momentum with the ATLAS detector. *Eur. Phys. J. C*, 77:393, 2017.

[22] The CMS Collaboration. Search for new physics in the monophoton final state in proton-proton collisions at $\sqrt{s} = 13$ TeV. *JHEP*, 10:073, 2017.

[23] The ATLAS Collaboration. Search for an invisibly decaying Higgs boson or dark matter candidates produced in association with a Z boson in pp collisions at $\sqrt{s} = 13$ TeV with the ATLAS detector. *Phys. Lett. B*, 776:318, 2018.

[24] The CMS Collaboration. Search for new physics in events with a leptonically decaying Z boson and a large transverse momentum imbalance in proton-proton collisions at $\sqrt{s} = 13$ TeV. *Eur. Phys. J. C*, 78:291, 2018.

[25] The ATLAS Collaboration. Search for dark matter in events with a hadronically decaying vector boson and missing transverse momentum in pp collisions at $\sqrt{s} = 13$ TeV with the ATLAS detector. *JHEP*, 10:180, 2018.

[26] The CMS Collaboration. Observation of a new boson at a mass of 125 gev with the cms experiment at the lhc. *Physics Letters B*, 716(1):30–61, Sep 2012.

[27] The ATLAS Collaboration. Observation of a new particle in the search for the standard model higgs boson with the atlas detector at the lhc. *Physics Letters B*, 716(1):1–29, Sep 2012.

[28] The CMS Collaboration. Search for dark matter particles produced in association with a higgs boson in proton-proton collisions at $\sqrt{\mathrm{s}} = 13$ tev. *Journal of High Energy Physics*, 2020(3), Mar 2020.

[29] T. Gehrmann, M. Grazzini, S. Kallweit, P. Maierhöfer, A. von Manteuffel, S. Pozzorini, D. Rathlev, and L. Tancredi. $\mathrm{W}^{+}\mathrm{w}^{-}$ production at hadron colliders in next to next to leading order qcd. *Physical Review Letters*, 113(21), Nov 2014.

[30] Adam Falkowski, Martín González-Alonso, Admir Greljo, David Marzocca, and Minho Son. Anomalous triple gauge couplings in the effective field theory approach at the lhc. *Journal of High Energy Physics*, 2017(2), Feb 2017.

[31] The CMS Collaboration. Measurement of the WW cross section pp collisions at $\sqrt{s} = 13$ TeV. Technical report, CERN, CMS-PAS-SMP-16-006, 2016.

[32] The CMS Collaboration. Measurement of the $w^{+}w^{-}$ cross section in pp collisions at $\sqrt{s} = 8$ tev and limits on anomalous gauge couplings. *The European Physical Journal C*, 76(7), Jul 2016.

[33] Michael Duerr, Alexander Grohsjean, Felix Kahlhoefer, Bjoern Penning, Kai Schmidt-Hoberg, and Christian Schwanenberger. Hunting the dark higgs. *Journal of High Energy Physics*, 2017(4), Apr 2017.

[34] Daniel Abercrombie, Nural Akchurin, Ece Akilli, Juan Alcaraz Maestre, Brandon Allen, Barbara Alvarez Gonzalez, Jeremy Andrea, Alexandre Arbey, Georges Azuelos, Patrizia Azzi, and et al. Dark Matter benchmark models for early LHC Run-2 Searches: Report of the ATLAS/CMS Dark Matter Forum. *Phys. Dark Univ.*, 27:100371, 2020.

[35] Tai Sakuma. Cutaway diagrams of CMS detector. Technical report, CERN, May 2019.

[36] The CMS Collaboration. CMS Tracking Performance Results from Early LHC Operation. *Eur. Phys. J. C*, 70(arXiv:1007.1988. CERN-PH-EP-2010-019. CMS-TRK-10-001):1165. 29 p, Jul 2010.

[37] The CMS Collaboration. Description and performance of track and primary-vertex reconstruction with the cms tracker. *Journal of Instrumentation*, 9(10):P10009–P10009, Oct 2014.

[38] The CMS Collaboration. Sketches of the cms tracker detector. `https://twiki.cern.ch/twiki/bin/view/CMSPublic/DPGResultsTRK`. Accessed: 2020-07-27.

[39] The CMS Collaboration. The CMS experiment at the CERN LHC. *Journal of Instrumentation*, 3(08):S08004–S08004, aug 2008.

[40] The CMS Collaboration. The CMS phase-1 pixel detector upgrade. *Journal of Instrumentation*, 16(02):P02027–P02027, feb 2021.

[41] Marco Cipriani. Performance of the CMS electromagnetic calorimeter during the LHC Run II and its role in precision physics measurements. Technical report, CERN, Geneva, Aug 2018.

[42] The CMS Collaboration. CMS ECAL performance with 2017 data. Technical report, CERN, Sep 2019.

[43] The CMS Collaboration. Performance of the cms hadron calorimeter with cosmic ray muons and lhc beam data. *Journal of Instrumentation*, 5(03):T03012–T03012, Mar 2010.

[44] Seth Isaac Cooper. Phase I Upgrade of the CMS Hadron Calorimeter. Technical report, CERN, Geneva, Oct 2014.

[45] The CMS Collaboration. Performance of the CMS Drift Tube Chambers with Cosmic Rays. *JINST*, 5:T03015, 2010.

[46] The CMS Collaboration. Performance of the CMS Cathode Strip Chambers with Cosmic Rays. *JINST*, 5:T03018, 2010.

[47] R Breedon and D Wenman. Images of the CMS Muons - Cathode Strip Chambers (CSC). CMS Collection., Nov 2008.

[48] The CMS Collaboration. The CMS RPC detector performance and stability during LHC RUN-2. *Journal of Instrumentation*, 14(11):C11012–C11012, nov 2019.

[49] The CMS Collaboration. Performance of the cms muon detector and muon reconstruction with proton-proton collisions at $\sqrt{s} = 13$ tev. *Journal of Instrumentation*, 13(06):P06015–P06015, Jun 2018.

[50] The CMS Collaboration. Particle-flow reconstruction and global event description with the CMS detector. *Journal of Instrumentation*, 12(10):P10003–P10003, oct 2017.

[51] R. E. Kalman. A New Approach to Linear Filtering and Prediction Problems. *Journal of Basic Engineering*, 82(1):35–45, 03 1960.

[52] Wolfgang Adam, R Frühwirth, Are Strandlie, and T Todor. Reconstruction of Electrons with the Gaussian-Sum Filter in the CMS Tracker at the LHC. Technical report, CERN, Geneva, Jan 2005.

[53] B.R. Webber. Fragmentation and Hadronization. *Int. J. Mod. Phys. AS*, 15S1:577–606. 31 p, Jan 2000.

[54] Matteo Cacciari, Gavin P Salam, and Gregory Soyez. The anti-ktjet clustering algorithm. *Journal of High Energy Physics*, 2008(04):063–063, Apr 2008.

[55] The CMS Collaboration. Performance of the cms level-1 trigger in proton-proton collisions at $\sqrt{s} = 13$ tev. *Journal of Instrumentation*, 15(10):P10017–P10017, Oct 2020.

[56] The CMS Trigger and Data Acquisition Group. The cms high level trigger. *The European Physical Journal C*, 46(3):605–667, Apr 2006.

[57] The CMS Collaboration. CMS Luminosity Measurements for the 2016 Data Taking Period. Technical Report CMS-PAS-LUM-17-001, CERN, Geneva, 2017.

[58] The CMS Collaboration. CMS luminosity measurement for the 2017 data-taking period at $\sqrt{s} = 13$ TeV. Technical Report CMS-PAS-LUM-17-004, CERN, Geneva, 2018.

[59] The CMS Collaboration. CMS luminosity measurement for the 2018 data-taking period at $\sqrt{s} = 13$ TeV. Technical Report CMS-PAS-LUM-18-002, CERN, Geneva, 2019.

[60] J. Allison et al. S. Agostinelli. Geant4—a simulation toolkit. *Nuclear Instruments and Methods in Physics Research Section A: Accelerators, Spectrometers, Detectors and Associated Equipment*, 506(3):250–303, 2003.

[61] Richard D. Ball, Valerio Bertone, Stefano Carrazza, Luigi Del Debbio, Stefano Forte, Alberto Guffanti, Nathan P. Hartland, and Juan Rojo. Parton distributions with QED corrections. *Nucl. Phys.*, B877:290–320, 2013.

[62] Richard D. Ball, Valerio Bertone, Francesco Cerutti, Luigi Del Debbio, Stefano Forte, Alberto Guffanti, Jose I. Latorre, Juan Rojo, and Maria Ubiali. Unbiased global determination of parton distributions and their uncertainties at NNLO and at LO. *Nucl. Phys.*, B855:153–221, 2012.

[63] Torbjorn Sjöstrand, Stephen Mrenna, and Peter Z. Skands. PYTHIA 6.4 physics and manual. *JHEP*, 05:026, 2006.

[64] Torbjorn Sjöstrand et al. An introduction to PYTHIA 8.2. *Comput. Phys. Commun.*, 191:159–177, 2015.

[65] The CMS Collaboration. Event generator tunes obtained from underlying event and multiparton scattering measurements. *Eur. Phys. J. C*, 76:155, 2016.

[66] The CMS Collaboration. Extraction and validation of a new set of CMS PYTHIA8 tunes from underlying-event measurements. *Eur. Phys. J. C*, 80:4, 2020.

[67] Simone Alioli, Paolo Nason, Carlo Oleari, and Emanuele Re. NLO vector-boson production matched with shower in POWHEG. *JHEP*, 07:060, 2008.

[68] Paolo Nason. A new method for combining NLO QCD with shower Monte Carlo algorithms. *JHEP*, 11:040, 2004.

[69] Stefano Frixione, Paolo Nason, and Carlo Oleari. Matching NLO QCD computations with parton shower simulations: the POWHEG method. *JHEP*, 11:070, 2007.

[70] S. Alioli, P. Nason, C. Oleari, and E. Re. A General Framework for Implementing NLO Calculations in Shower Monte Carlo Programs: the POWHEG BOX. *JHEP*, 06:043, 2010.

[71] John M. Campbell and R.K. Ellis. Mcfm for the tevatron and the lhc. *Nuclear Physics B - Proceedings Supplements*, 205-206:10–15, 2010. Loops and Legs in Quantum Field Theory.

[72] J. et al. Alwall. The automated computation of tree-level and next-to-leading order differential cross sections, and their matching to parton shower simulations. *JHEP*, 07:079, 2014.

[73] Simone Alioli, Paolo Nason, Carlo Oleari, and Emanuele Re. NLO Higgs boson production via gluon fusion matched with shower in POWHEG. *JHEP*, 04:002, 2009.

[74] Paolo Nason and Carlo Oleari. NLO Higgs boson production via vector-boson fusion matched with shower in POWHEG. *JHEP*, 02:037, 2010.

[75] Gionata Luisoni, Paolo Nason, Carlo Oleari, and Francesco Tramontano. $HW^{\pm}$/HZ + 0 and 1 jet at NLO with the POWHEG BOX interfaced to GoSam and their merging within MiNLO. *JHEP*, 10:083, 2013.

[76] The CMS Collaboration. Observation of $t\bar{t}h$ production. *Phys. Rev. Lett.*, 120:231801, Jun 2018.

[77] Torbjorn Sjostrand, Stephen Mrenna, and Peter Z. Skands. A Brief Introduction to PYTHIA 8.1. *Comput. Phys. Commun.*, 178:852–867, 2008.

[78] Sara Bolognesi, Yanyan Gao, Andrei V. Gritsan, Kirill Melnikov, Markus Schulze, Nhan V. Tran, and Andrew Whitbeck. On the spin and parity of a single-produced resonance at the LHC. *Phys. Rev. D*, 86:095031, 2012.

[79] The CMS Collaboration. Identification of heavy-flavour jets with the cms detector in pp collisions at 13 tev. *Journal of Instrumentation*, 13(05):P05011–P05011, May 2018.

[80] The CMS Collaboration. Measurements of properties of the higgs boson decaying to a w boson pair in pp collisions at $\sqrt{s} = 13$ tev. *Physics Letters B*, 791:96–129, Apr 2019.

[81] The CMS Collaboration. Search for neutral higgs bosons decaying to tau pairs in pp collisions at $\sqrt{s} = 7$TeV. *Physics Letters B*, 713(2):68–90, Jun 2012.

[82] The CMS Collaboration. Muon tracking performance in the CMS Run-2 Legacy data using the tag-and-probe technique. Technical report, CERN, Jul 2020.

[83] A. Bodek, A. van Dyne, J. Y. Han, W. Sakumoto, and A. Strelnikov. Extracting Muon Momentum Scale Corrections for Hadron Collider Experiments. *Eur. Phys. J. C*, 72:2194, 2012.

[84] The CMS Collaboration. Electron and photon reconstruction and identification with the cms experiment at the cern lhc. *Journal of Instrumentation*, 16(05):P05014, May 2021.

[85] The CMS Collaboration. Jet algorithms performance in 13 TeV data. Technical report, CERN, Geneva, 2017.

[86] The CMS Collaboration. Heavy flavor identification at CMS with deep neural networks. Technical report, CERN, Mar 2017.

[87] The CMS Collaboration. Performance of missing transverse momentum reconstruction in proton-proton collisions at $\sqrt{s} = 13$ tev using the cms detector. *Journal of Instrumentation*, 14(07):P07004–P07004, Jul 2019.

[88] The CMS Collaboration. Pileup mitigation at cms in 13 tev data. *Journal of Instrumentation*, 15(09):P09018–P09018, Sep 2020.

[89] Robert D. Cousins. What is the likelihood function, and how is it used in particle physics?, 2020.

[90] S. S. Wilks. The Large-Sample Distribution of the Likelihood Ratio for Testing Composite Hypotheses. *The Annals of Mathematical Statistics*, 9(1):60 – 62, 1938.

[91] A L Read. Presentation of search results: the CLs technique. *Journal of Physics G: Nuclear and Particle Physics*, 28(10):2693–2704, sep 2002.

[92] Glen Cowan, Kyle Cranmer, Eilam Gross, and Ofer Vitells. Asymptotic formulae for likelihood-based tests of new physics. *The European Physical Journal C*, 71(2), Feb 2011.

[93] Abraham Wald. Tests of statistical hypotheses concerning several parameters when the number of observations is large. *Transactions of the American Mathematical Society*, 54(3):426–482, 1943.

[94] Robert D. Cousins. The jeffreys–lindley paradox and discovery criteria in high energy physics. *Synthese*, 194(2):395–432, Jul 2014.

[95] Roger J. Barlow and Christine Beeston. Fitting using finite Monte Carlo samples. *Comput. Phys. Commun.*, 77:219–228, 1993.

[96] Jon et al. Butterworth. Pdf4llhc recommendations for lhc run ii. *Journal of Physics G: Nuclear and Particle Physics*, 43(2):023001, Jan 2016.

[97] P. Skands, S. Carrazza, and J. Rojo. Tuning pythia 8.1: the monash 2013 tune. *The European Physical Journal C*, 74(8), Aug 2014.

[98] Massimiliano Grazzini, Stefan Kallweit, Dirk Rathlev, and Marius Wiesemann. Transverse-momentum resummation for vector-boson pair production at NNLL+NNLO. *JHEP*, 08:154, 2015.

[99] Vladislav Balagura. Van der meer scan luminosity measurement and beam–beam correction. *The European Physical Journal C*, 81(1), Jan 2021.

[100] The CMS Collaboration. Precision luminosity measurement in proton-proton collisions at $\sqrt{s} = 13$ TeV in 2015 and 2016 at CMS. Technical report, CERN, Geneva, Apr 2021. Submitted to EPJC. All figures and tables can be found at http://CMS-results.web.cern.ch/CMS-results/public-results/publications/LUM-17-003 (CMS Public Pages).

[101] The CMS Collaboration. CMS luminosity measurement for the 2017 data-taking period at $\sqrt{s} = 13$ TeV. Technical report, CERN, Geneva, 2018.

[102] The CMS Collaboration. CMS luminosity measurement for the 2018 data-taking period at $\sqrt{s} = 13$ TeV. Technical report, CERN, Geneva, 2019.

[103] The CMS Collaboration. Jet energy scale and resolution in the cms experiment in pp collisions at 8 tev. *Journal of Instrumentation*, 12(02):P02014–P02014, Feb 2017.

[104] The CMS Collaboration. W^+W^- boson pair production in proton-proton collisions at $\sqrt{s} = 13$ TeV. *Physical Review D*, 102(9), Nov 2020.

[105] The ATLAS Collaboration. Measurement of fiducial and differential W^+W^- production cross-sections at $\sqrt{s} = 13$ tev with the atlas detector. *The European Physical Journal C*, 79, 10 2019.

[106] Tilman Plehn. LHC Phenomenology for Physics Hunters. In *Theoretical Advanced Study Institute in Elementary Particle Physics: The Dawn of the LHC Era*, pages 125–180, 2010.

[107] Fabrizio Caola, Kirill Melnikov, Raoul Röntsch, and Lorenzo Tancredi. Qcd corrections to ww production through gluon fusion. *Physics Letters B*, 754:275–280, Mar 2016.

[108] P.A. Zyla et al. Review of Particle Physics. *PTEP*, 2020(8):083C01, 2020.

[109] T. Aaltonen, B. Álvarez González, S. Amerio, D. Amidei, A. Anastassov, A. Annovi, J. Antos, G. Apollinari, J. A. Appel, T. Arisawa, and et al. Search for standard model higgs boson production in association with a w boson using a matrix element technique at cdf in pp collisions at $\sqrt{s} = 1.96$ tev. *Physical Review D*, 85(7), Apr 2012.

[110] The CMS Collaboration. Search for single top tW associated production in the dilepton decay channel in pp collisions at $\sqrt{s} = 7$ TeV. Technical report, CERN, Geneva, 2011.

[111] Michał Czakon, David Heymes, Alexander Mitov, Davide Pagani, Ioannis Tsinikos, and Marco Zaro. Top-pair production at the lhc through nnlo qcd and nlo ew. *Journal of High Energy Physics*, 2017(10), Oct 2017.

[112] M. et al. Tanabashi. Review of Particle Physics. *Phys. Rev.*, D98(3):030001, 2018.

[113] W. Buchmuller and D. Wyler. Effective Lagrangian Analysis of New Interactions and Flavor Conservation. *Nucl. Phys. B*, 268:621–653, 1986.

[114] B. Grzadkowski, M. Iskrzyński, M. Misiak, and J. Rosiek. Dimension-six terms in the standard model lagrangian. *Journal of High Energy Physics*, 2010(10), Oct 2010.

[115] C. Degrande, J.L. Holzbauer, S. C. Hsu, A.V. Kotwal, S. Li, et al. Studies of Vector Boson Scattering And Triboson Production with DELPHES Parametrized Fast Simulation for Snowmass 2013, 2013.

[116] Stefan Gieseke, Tobias Kasprzik, and Johann H. Kühn. Vector-boson pair production and electroweak corrections in herwig++, 2014.

[117] N. Majorana. A symmetric theory of electrons and positrons. *Ettore Majorana Scientific Papers: On occasion of the centenary of his birth*, pages 201–233, 01 2006.

[118] Thomas G. Rizzo. Z' phenomenology and the LHC. In *Theoretical Advanced Study Institute in Elementary Particle Physics: Exploring New Frontiers Using Colliders and Neutrinos*, pages 537–575, 10 2006.

[119] The CMS Collaboration. Search for dark matter particles produced in association with a dark Higgs boson decaying into W^+W^- in proton-proton collisions at $\sqrt{s} = 13$ TeV with the CMS detector. Technical report, CERN, Geneva, 2021.

[120] The ATLAS Collaboration. RECAST framework reinterpretation of an ATLAS Dark Matter Search constraining a model of a dark Higgs boson decaying to two b-quarks. Technical report, CERN, Geneva, Aug 2019.

[121] Mark de Berg, Marc van Kreveld, Mark Overmars, and Otfried Cheong Schwarzkopf. *Delaunay Triangulations*, pages 183–210. Springer Berlin Heidelberg, Berlin, Heidelberg, 2000.

[122] The ATLAS Collaboration. Search for dark matter produced in association with a dark higgs boson decaying into $W^{\pm}W^{\mp}$ or ZZ in fully hadronic final states from $\sqrt{s} = 13$ TeV pp collisions recorded with the ATLAS detector. *Phys. Rev. Lett.*, 126:121802, 2021.

[123] The CMS Collaboration. Search for resonant and nonresonant new phenomena in high-mass dilepton final states at $\sqrt{s} = 13$ tev. *Journal of High Energy Physics*, 2021(7), Jul 2021.

[124] The CMS Collaboration. Search for heavy gauge w' bosons in events with an energetic lepton and large missing transverse momentum at $\sqrt{s}$ =13 tev. *Physics Letters B*, 770:278 – 301, 2017.

[125] J. Schmidhuber. Deep learning. *Scholarpedia*, 10(11):32832, 2015.

[126] Sandra Vieira, Walter Pinaya, and Andrea Mechelli. Using deep learning to investigate the neuroimaging correlates of psychiatric and neurological disorders: Methods and applications. *Neuroscience and Biobehavioral Reviews*, 74, 01 2017.

[127] D. Rumelhart, Geoffrey E. Hinton, and Ronald J. Williams. Learning representations by back-propagating errors. *Nature*, 323:533–536, 1986.

[128] The CMS Collaboration. Identification of heavy, energetic, hadronically decaying particles using machine-learning techniques. *Journal of Instrumentation*, 15(06):P06005–P06005, June 2020.

[129] The CMS Collaboration. Performance of the reconstruction and identification of high-momentum muons in proton-proton collisions at $\sqrt{s} = 13$ TeV. *Journal of Instrumentation*, 15(02):P02027–P02027, Feb 2020.

[130] Abien Fred Agarap. Deep learning using rectified linear units (relu). *arXiv preprint arXiv:1803.08375*, 2018.

[131] S. Hochreiter. Untersuchungen zu dynamischen neuronalen Netzen. Diploma thesis, Institut für Informatik, Lehrstuhl Prof. Brauer, Technische Universität München, 1991.

[132] Michael P Perrone, Haidar Khan, Changhoan Kim, Anastasios Kyrillidis, Jerry Quinn, and Valentina Salapura. Optimal mini-batch size selection for fast gradient descent. *arXiv preprint arXiv:1911.06459*, 2019.

[133] Ning Qian. On the momentum term in gradient descent learning algorithms. *Neural networks : the official journal of the International Neural Network Society*, 12(1):145—151, January 1999.

[134] Tijmen Tieleman and Geoffrey Hinton. Lecture 6.5-rmsprop: Divide the gradient by a running average of its recent magnitude. *COURSERA: Neural networks for machine learning*, 4(2):26–31, 2012.

[135] Diederik P. Kingma and Jimmy Ba. Adam: A method for stochastic optimization. *CoRR*, abs/1412.6980, 2015.

[136] Dan Ciresan, Ueli Meier, Jonathan Masci, Luca Maria Gambardella, and Jürgen Schmidhuber. Flexible, high performance convolutional neural networks for image classification. In *IJCAI 2011, Proceedings of the 22nd International Joint Conference on Artificial Intelligence, Barcelona, Catalonia, Spain, July 16-22, 2011*, pages 1237–1242, 07 2011.

A WW production figures

Data and simulation plots for the non-prompt validation region in the same-flavour channel are shown in Figure 78 for the combination of the 0-jets and 1-jet categories.

Data and simulation plots for the top-enriched control region in the same-flavour channel are shown in Figures 79 and 80 for the 0-jets and 1-jet categories.

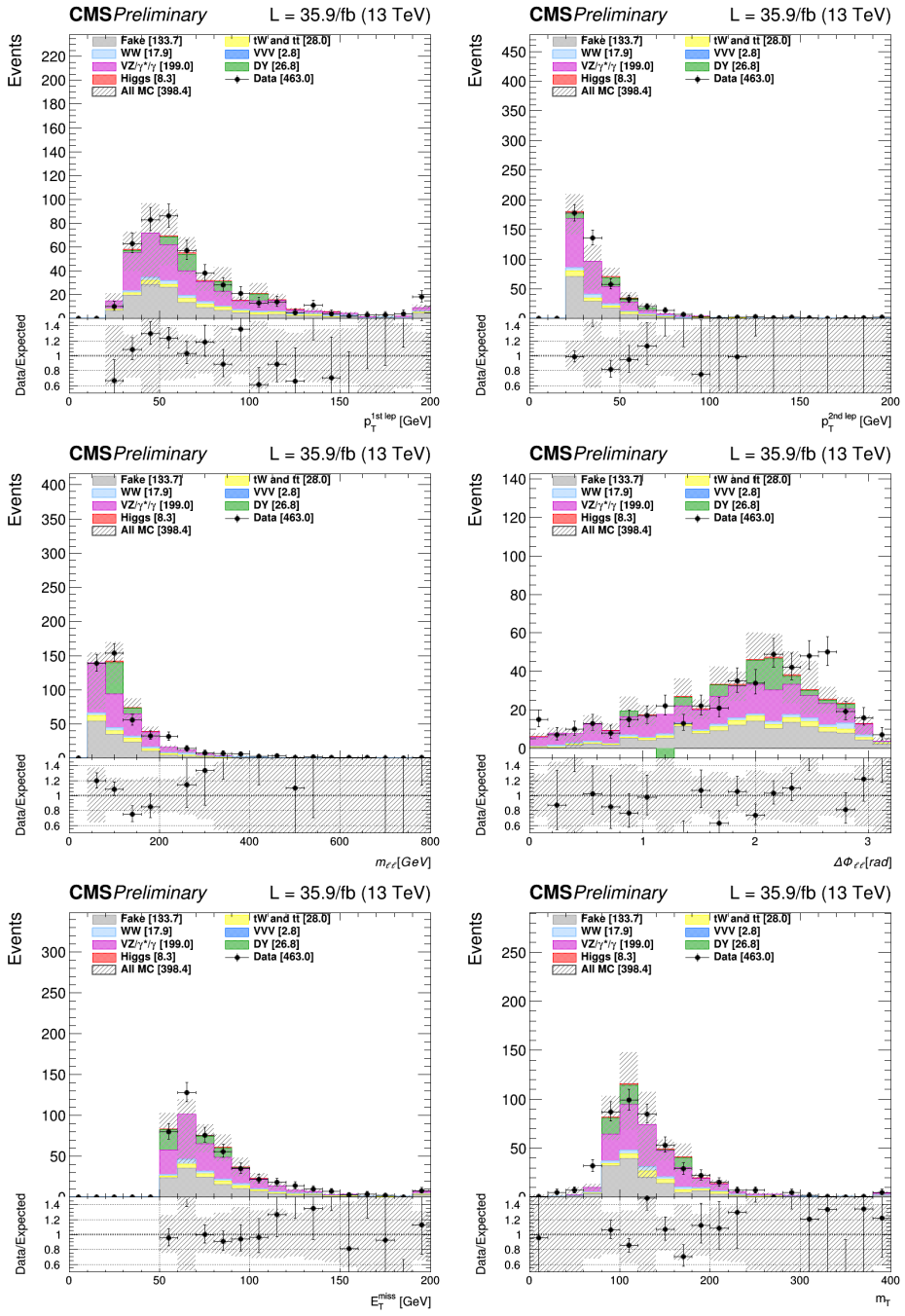

Figure 78: Distributions in $ee/\mu\mu$ events for the same-sign region of the leading lepton p_T ($p_T^{\ell\ max}$), trailing lepton p_T ($p_T^{\ell\ min}$), dilepton invariant mass ($m_{\ell\ell}$), azimuthal angle between the two leptons ($\Delta\phi(\ell,\ell)$), the missing transverse energy (p_T^{miss}), and the transverse mass of the two leptons plus E_T^{miss} system (m_T). The hatched areas represent the total uncertainty in each bin. The last bin includes the overflow.

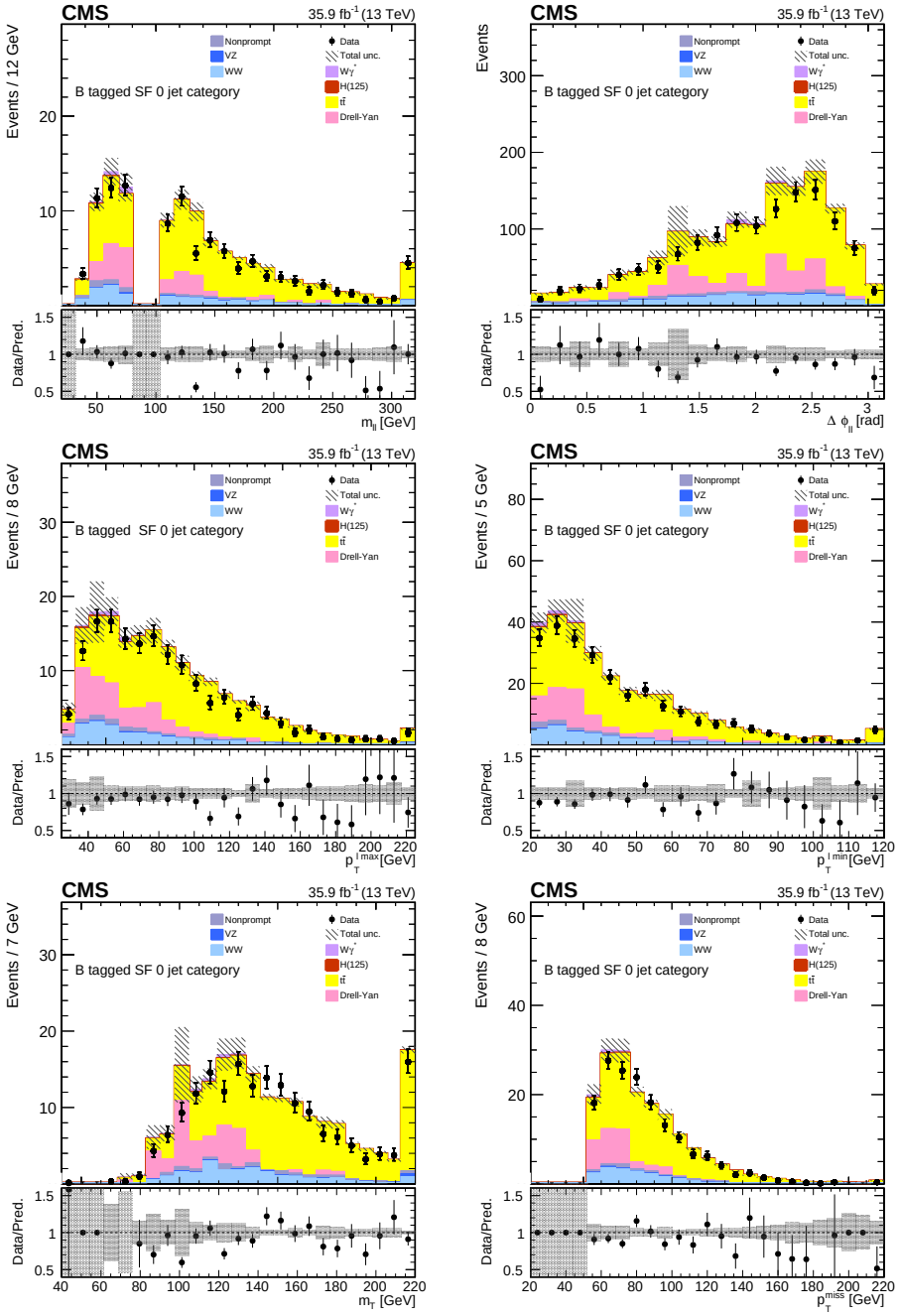

Figure 79: Distributions in $ee/\mu\mu$ events for the top 0-jets category region of the dilepton invariant mass ($m_{\ell\ell}$), azimuthal angle between the two leptons ($\Delta\phi(\ell,\ell)$), leading lepton p_T ($p_T^{\ell\ \max}$), trailing lepton p_T ($p_T^{\ell\ \min}$), transverse mass of the two leptons plus E_T^{miss} system (m_T), and missing transverse energy (p_T^{miss}). The hatched areas represent the statistical uncertainty in each bin. The ratio between data and prediction is shown in the bottom panel. The last bin includes the overflow.

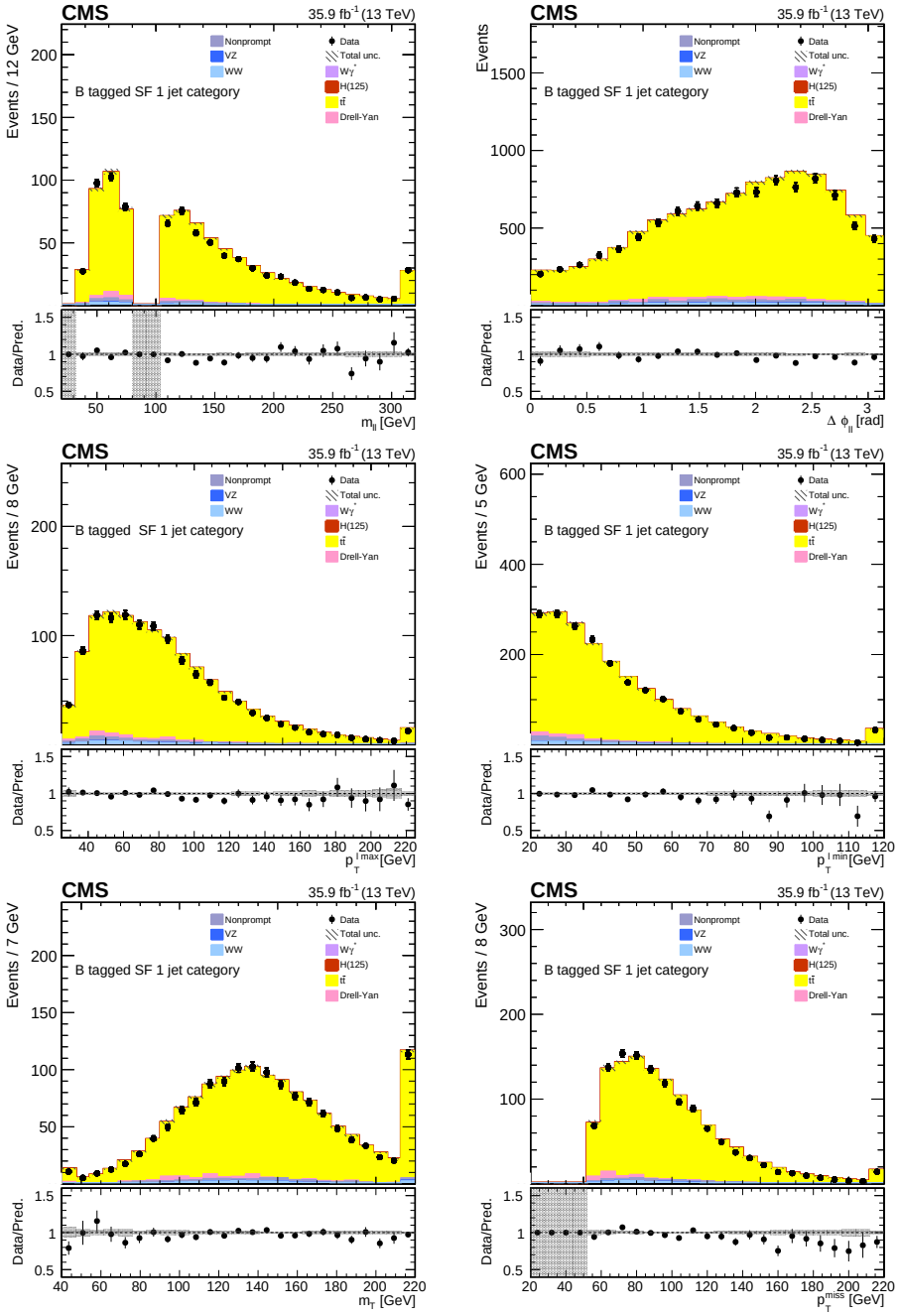

Figure 80: Distributions in $ee/\mu\mu$ events for the top 0-jets category region of the dilepton invariant mass ($m_{\ell\ell}$), azimuthal angle between the two leptons ($\Delta\phi(\ell,\ell)$), leading lepton p_T ($p_T^{\ell\ \max}$), trailing lepton p_T ($p_T^{\ell\ \min}$), transverse mass of the two leptons plus E_T^{miss} system (m_T), and missing transverse energy (p_T^{miss}). The hatched areas represent the statistical uncertainty in each bin. The ratio between data and prediction is shown in the bottom panel. The last bin includes the overflow.

B Dark Higgs search figures

The 1D $m_T^{\ell\,\mathrm{min},p_T^{\mathrm{miss}}}$ post-fit distributions from the signal regions are shown in Figures 81, 82, and 83 for 2016, 2017, and 2018 respectively.

Pre-fit kinematic distributions for all the analysis regions that have not been included in Section 8 are shown in Figures 84-97.

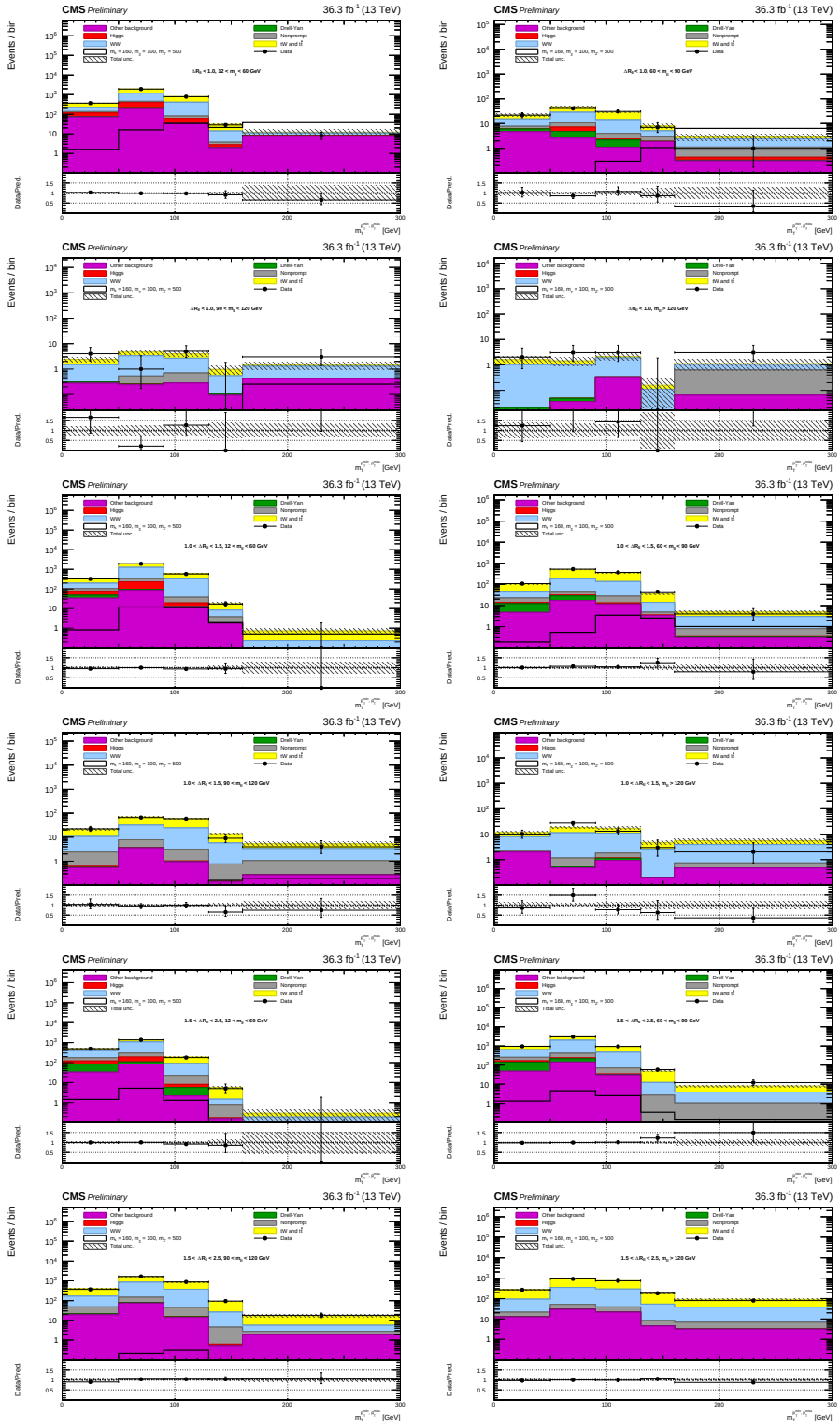

Figure 81: $m_T^{\ell\,\min,p_T^{miss}}$ distributions for the 2016 data set for the different signal regions. The black line indicates the signal prediction of $m_s = 160$ GeV, $m_\chi = 100$ GeV, $m_{Z'} = 500$ GeV.

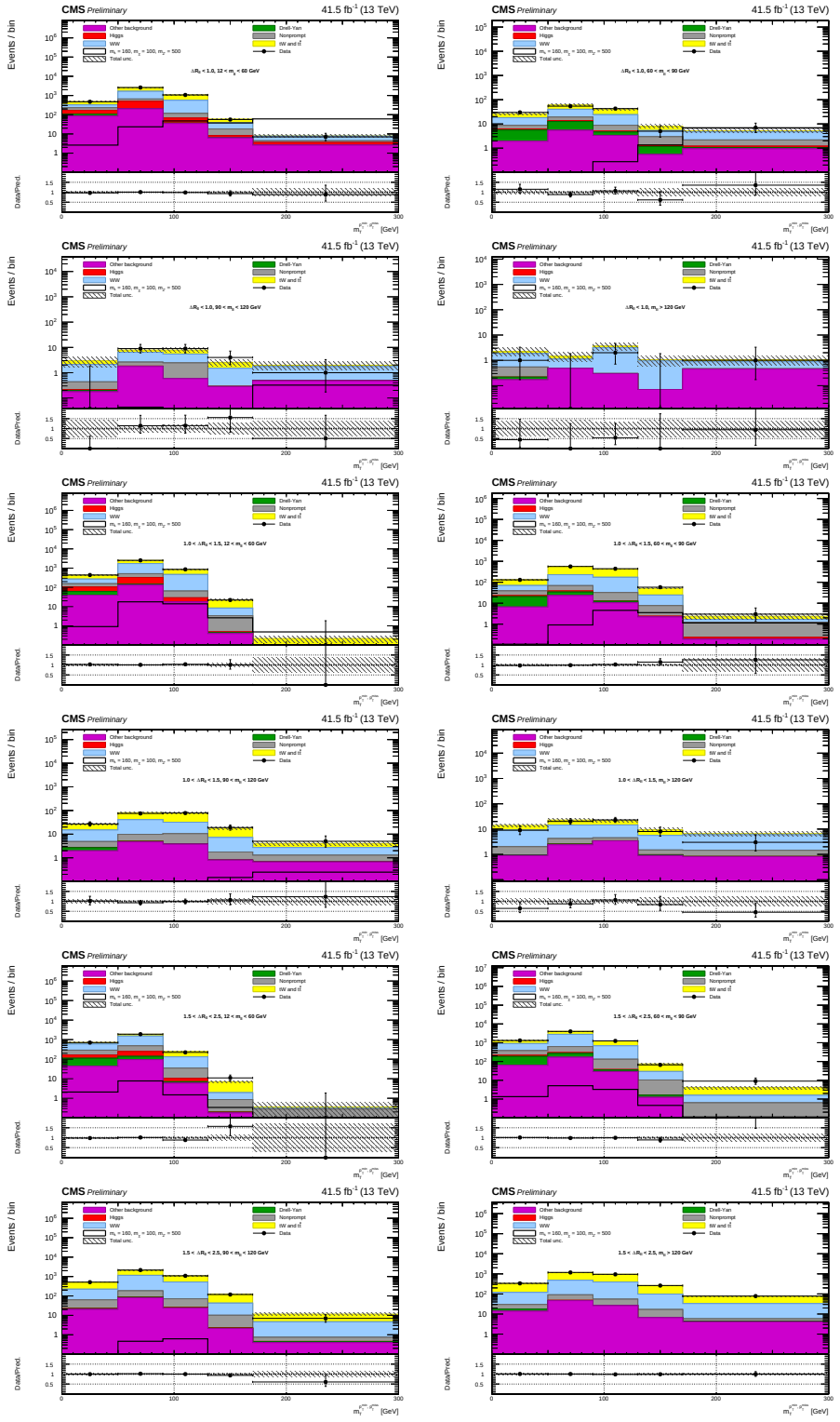

Figure 82: $m_T^{\ell\,\min,p_T^{miss}}$ distributions for the 2017 data set for the different signal regions. The black line indicates the signal prediction of $m_s = 160$ GeV, $m_\chi = 100$ GeV, $m_{Z'} = 500$ GeV.

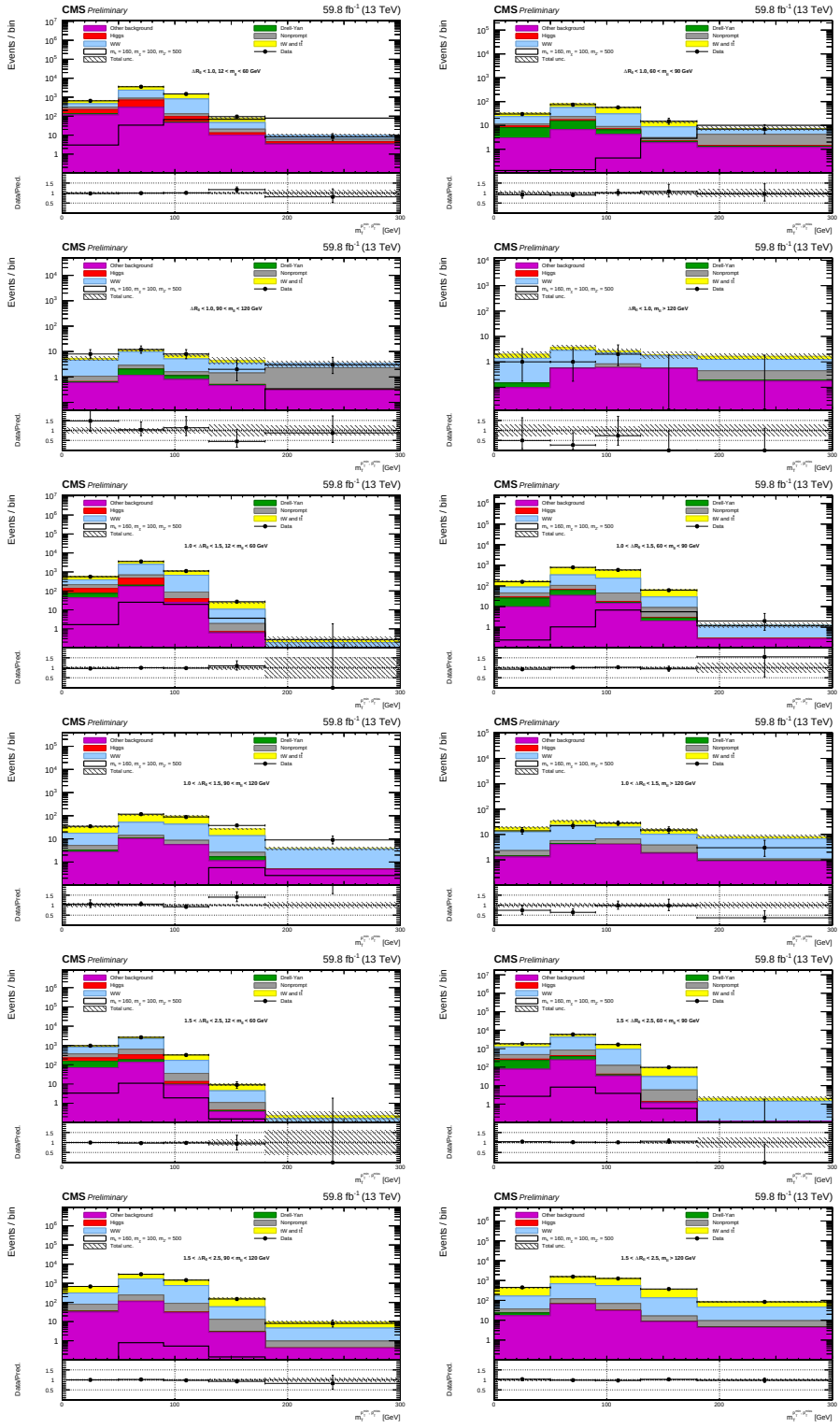

Figure 83: $m_T^{\ell\,\min,p_T^{miss}}$ distributions for the 2018 data set for the different signal regions. The black line indicates the signal prediction of $m_s = 160$ GeV, $m_\chi = 100$ GeV, $m_{Z'} = 500$ GeV.

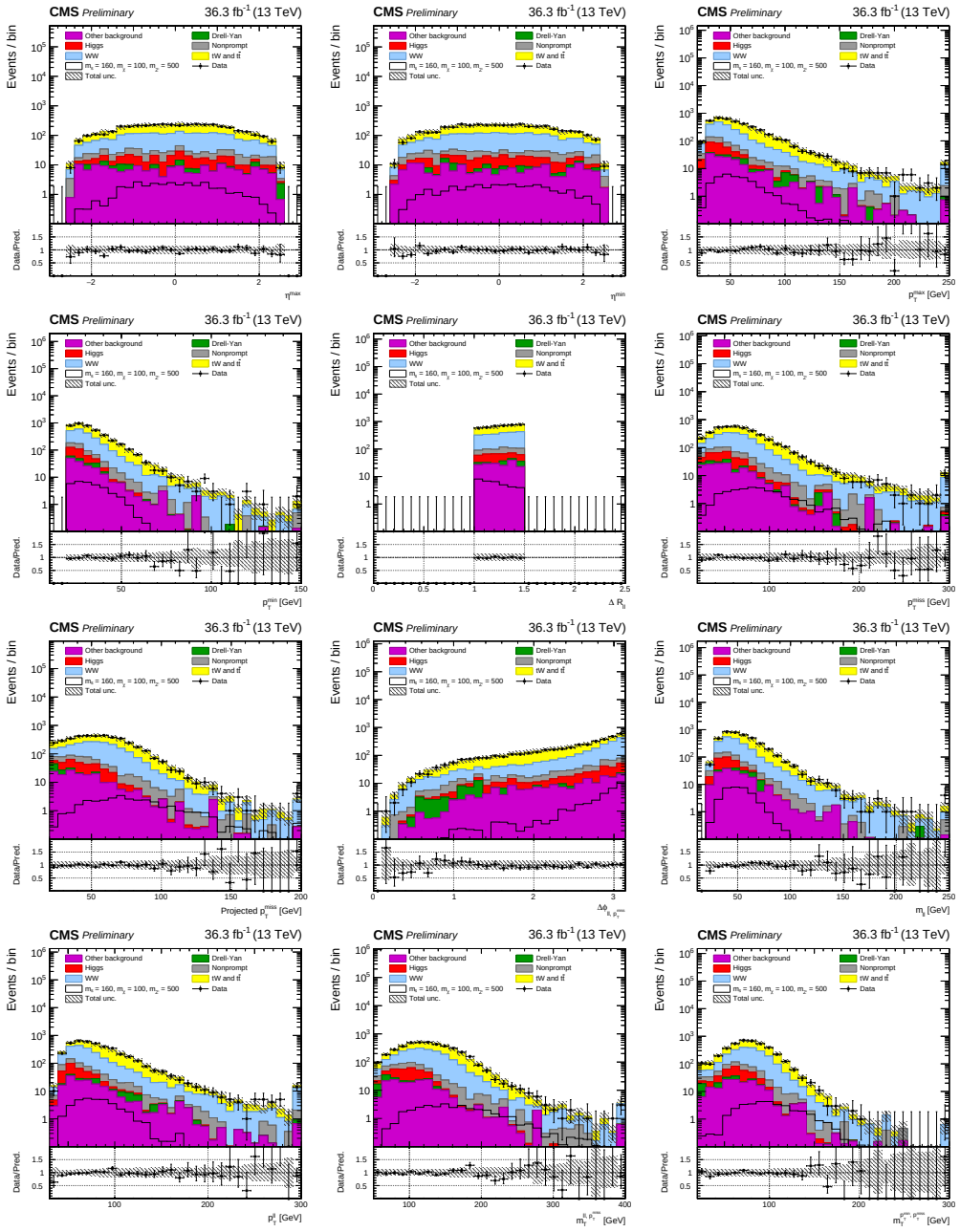

Figure 84: Pre-fit kinematic distributions for 2016 events in SR2. The distributions show the leading (a) and trailing (b) lepton η, the leading (c) and trailing (d) lepton p_T, $\Delta R(\ell,\ell)$ (e), p_T^{miss} (f), mpmet (g), azimuthal angle between the dilepton system and the p_T^{miss} (h), $m_{\ell\ell}$ (i), $p_T^{\ell\ell}$ (j), $m_T^{ll,p_T^{miss}}$ (k), and $m_T^{\ell\,min,p_T^{miss}}$ (l). The error bars on the data points represent the statistical uncertainty, and the hatched areas represent the combined systematic and statistical uncertainty of the predicted background. Black line corresponds to the signal prediction of $m_s = 160$ GeV, $m_\chi = 100$ GeV, $m_{Z'} = 500$ GeV. The last bin includes the overflow.

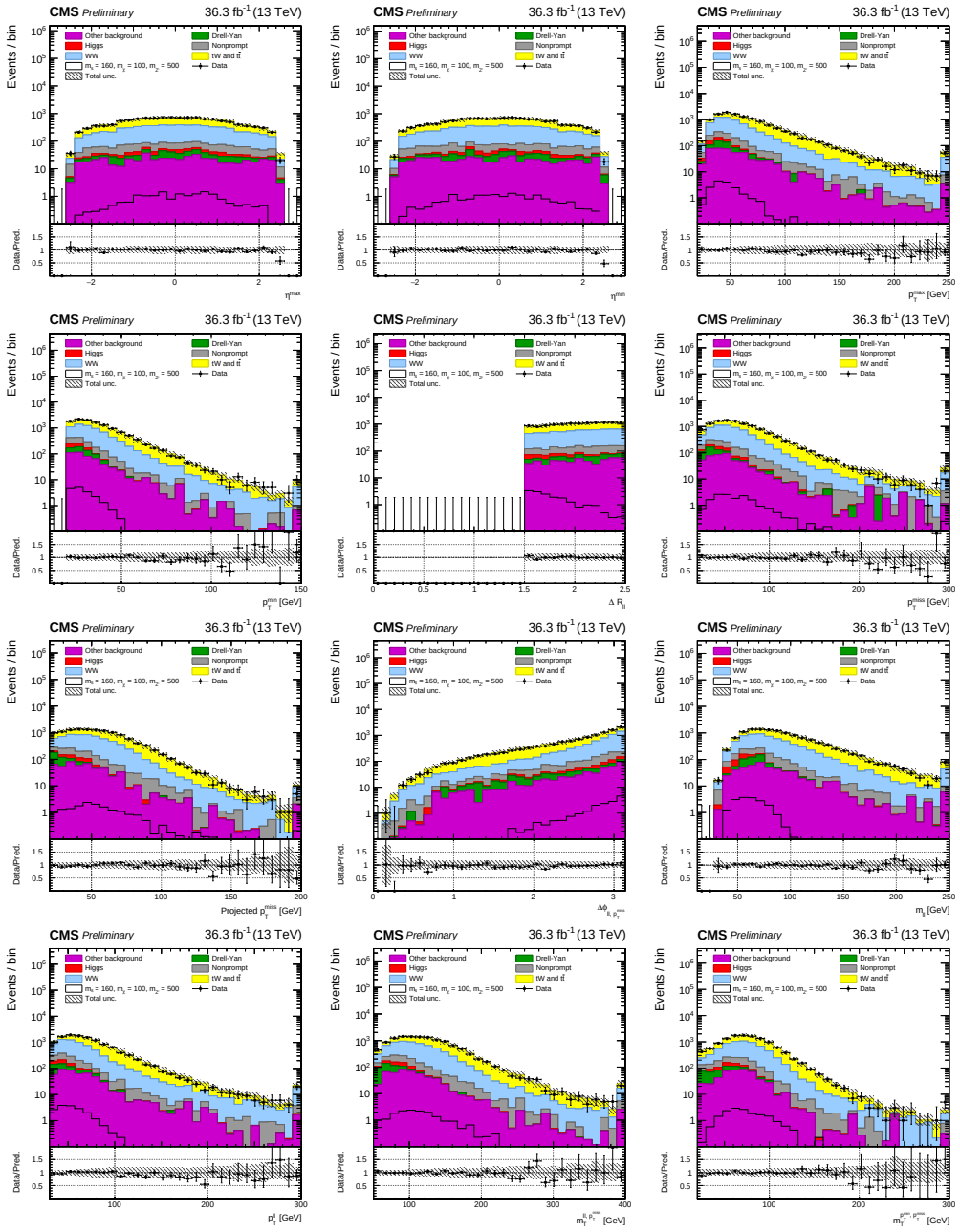

Figure 85: Pre-fit kinematic distributions for 2016 events in SR3. The distributions show the leading (a) and trailing (b) lepton η, the leading (c) and trailing (d) lepton p_T, $\Delta R(\ell,\ell)$ (e), p_T^{miss} (f), mpmet (g), azimuthal angle between the dilepton system and the p_T^{miss} (h), $m_{\ell\ell}$ (i), $p_T^{\ell\ell}$ (j), $m_T^{ll,p_T^{miss}}$ (k), and $m_T^{\ell\,min,p_T^{miss}}$ (l). The error bars on the data points represent the statistical uncertainty, and the hatched areas represent the combined systematic and statistical uncertainty of the predicted background. Black line corresponds to the signal prediction of $m_s = 160$ GeV, $m_\chi = 100$ GeV, $m_{Z'} = 500$ GeV. The last bin includes the overflow.

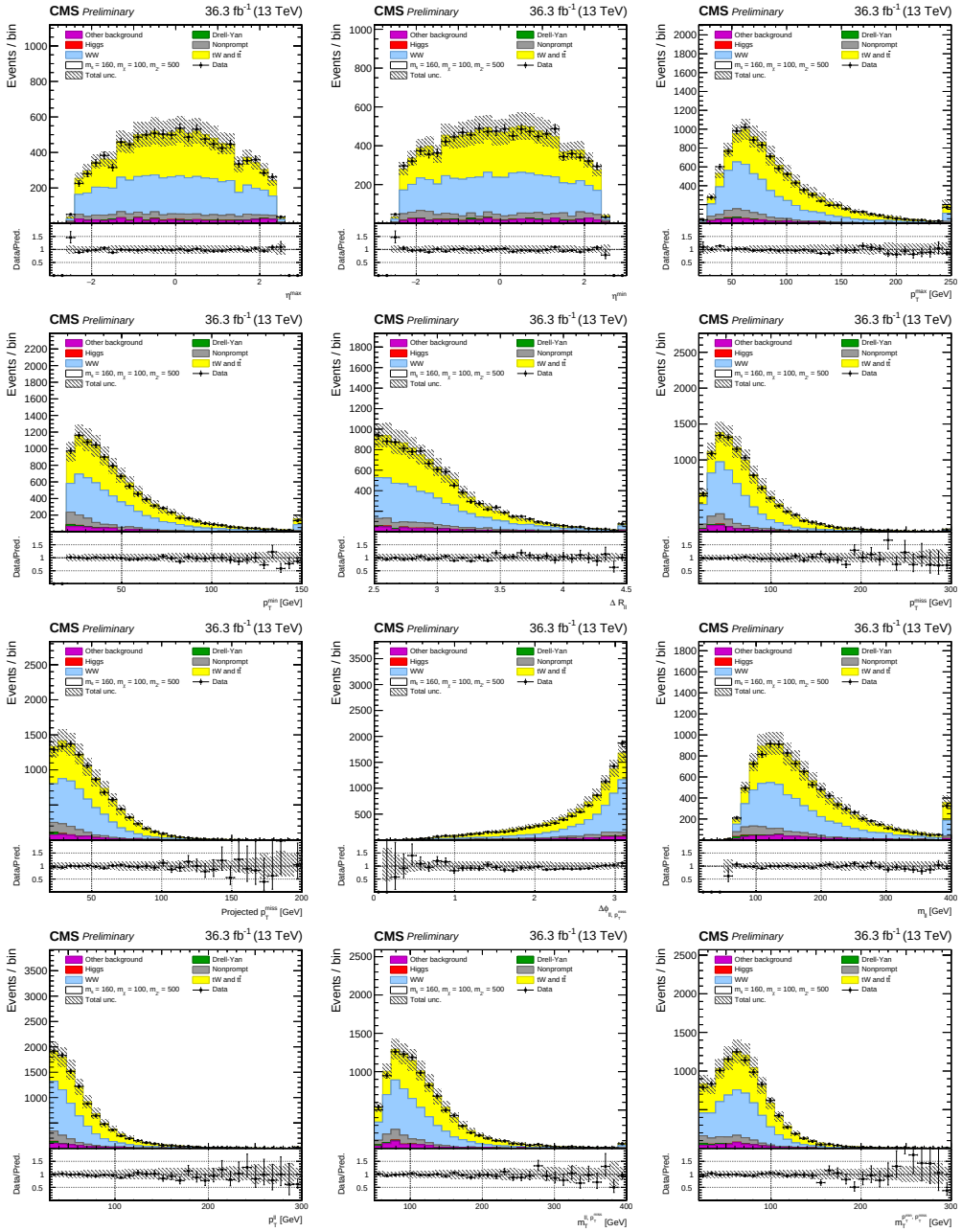

Figure 86: Pre-fit kinematic distributions for 2016 events in W^+W^- control region. The distributions show the leading (a) and trailing (b) lepton η, the leading (c) and trailing (d) lepton p_T, $\Delta R(\ell,\ell)$ (e), p_T^{miss} (f), mpmet (g), azimuthal angle between the dilepton system and the p_T^{miss} (h), $m_{\ell\ell}$ (i), $p_T^{\ell\ell}$ (j), $m_T^{ll,p_T^{miss}}$ (k), and $m_T^{\ell\,min,p_T^{miss}}$ (l). The error bars on the data points represent the statistical uncertainty, and the hatched areas represent the combined systematic and statistical uncertainty of the predicted background. Black line corresponds to the signal prediction of $m_s = 160$ GeV, $m_\chi = 100$ GeV, $m_{Z'} = 500$ GeV. The last bin includes the overflow.

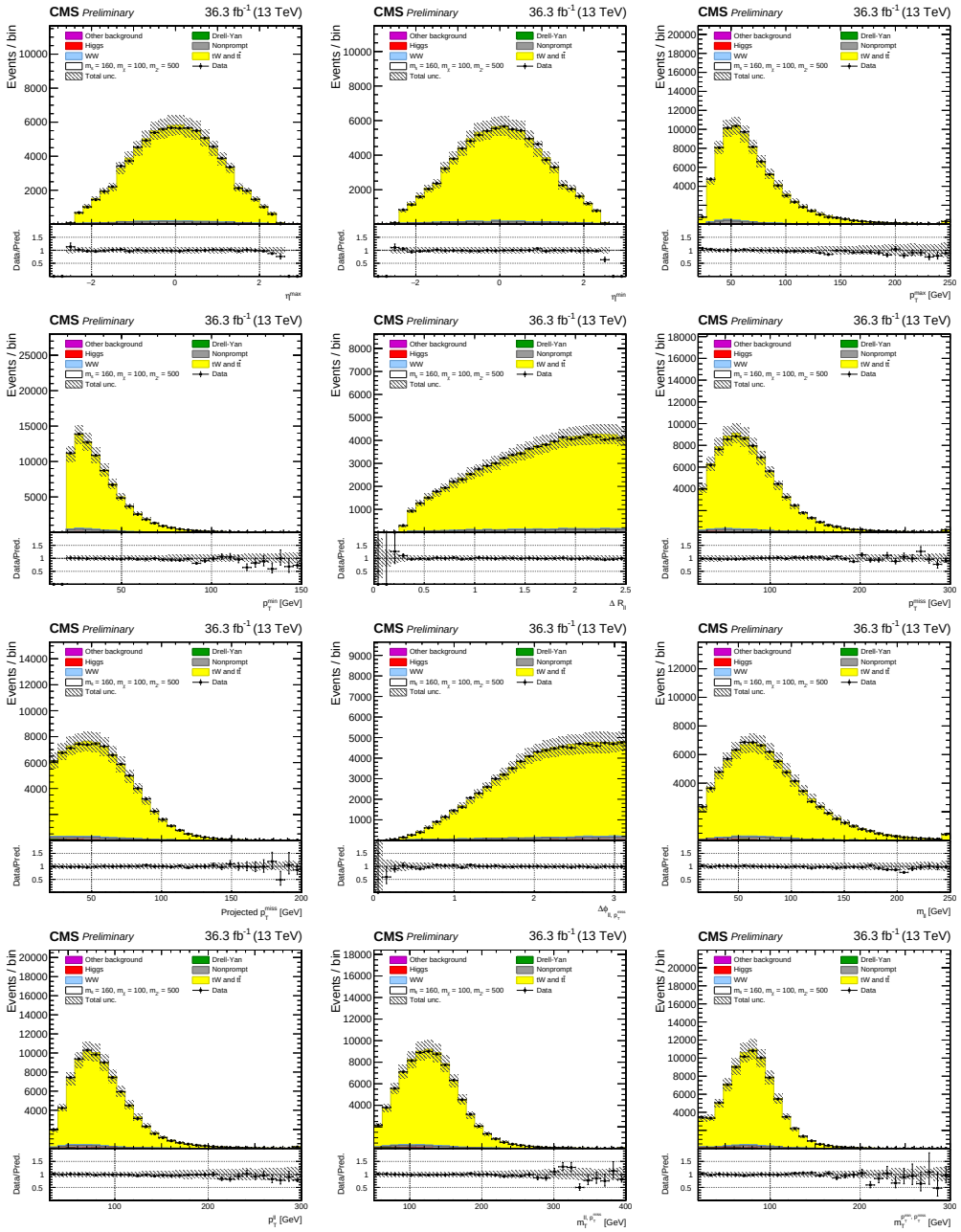

Figure 87: Pre-fit kinematic distributions for 2016 events in Top control region. The distributions show the leading (a) and trailing (b) lepton η, the leading (c) and trailing (d) lepton p_T, $\Delta R(\ell,\ell)$ (e), p_T^{miss} (f), mpmet (g), azimuthal angle between the dilepton system and the p_T^{miss} (h), $m_{\ell\ell}$ (i), $p_T^{\ell\ell}$ (j), $m_T^{ll,p_T^{miss}}$ (k), and $m_T^{\ell\,min,p_T^{miss}}$ (l). The error bars on the data points represent the statistical uncertainty, and the hatched areas represent the combined systematic and statistical uncertainty of the predicted background. Black line corresponds to the signal prediction of $m_s = 160$ GeV, $m_\chi = 100$ GeV, $m_{Z'} = 500$ GeV. The last bin includes the overflow.

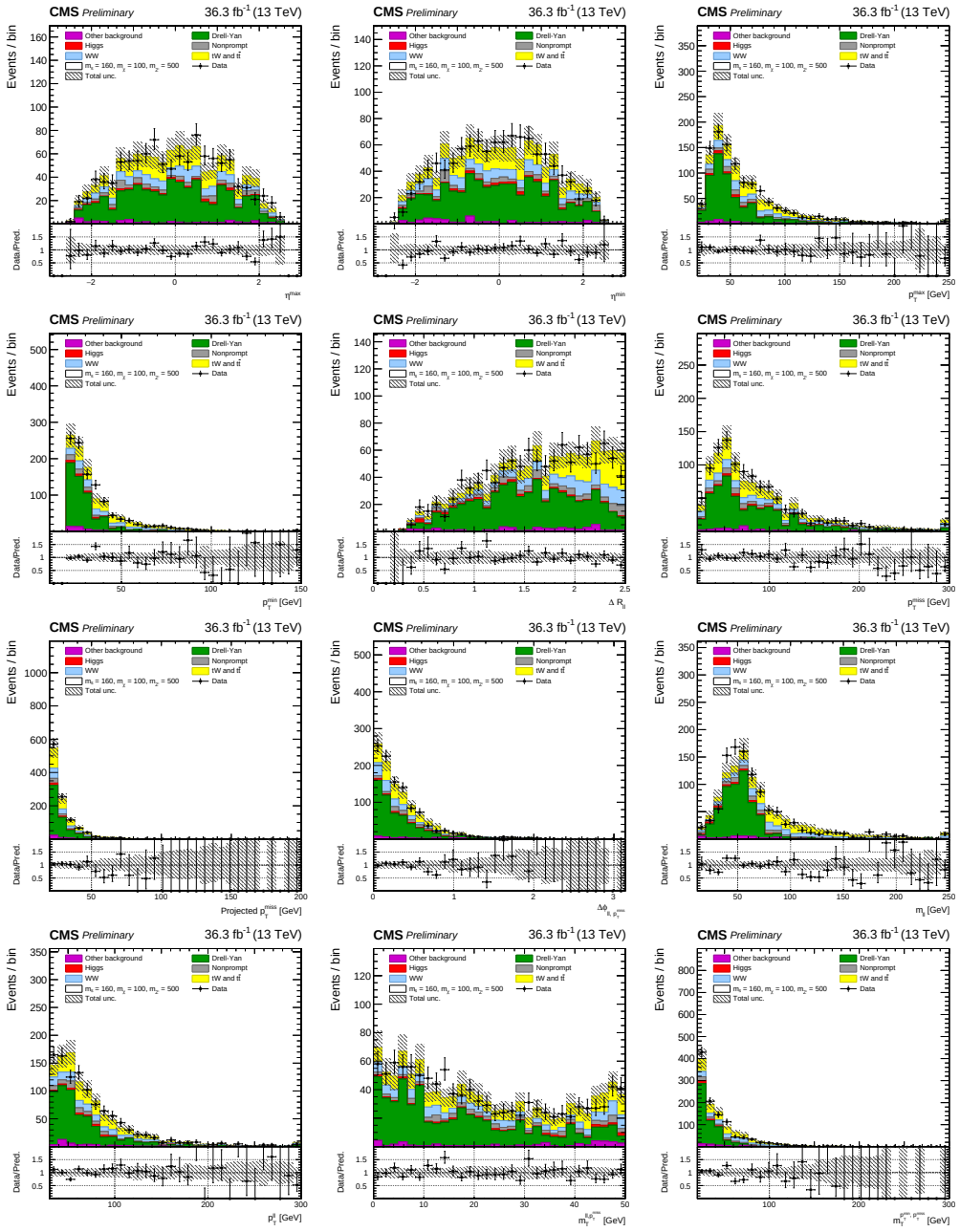

Figure 88: Pre-fit kinematic distributions for 2016 events in DY control region. The distributions show the leading (a) and trailing (b) lepton η, the leading (c) and trailing (d) lepton p_T, $\Delta R(\ell,\ell)$ (e), p_T^{miss} (f), mpmet (g), azimuthal angle between the dilepton system and the p_T^{miss} (h), $m_{\ell\ell}$ (i), $p_T^{\ell\ell}$ (j), $m_T^{ll,p_T^{miss}}$ (k), and $m_T^{\ell\,min,p_T^{miss}}$ (l). The error bars on the data points represent the statistical uncertainty, and the hatched areas represent the combined systematic and statistical uncertainty of the predicted background. Black line corresponds to the signal prediction of $m_s = 160$ GeV, $m_\chi = 100$ GeV, $m_{Z'} = 500$ GeV. The last bin includes the overflow.

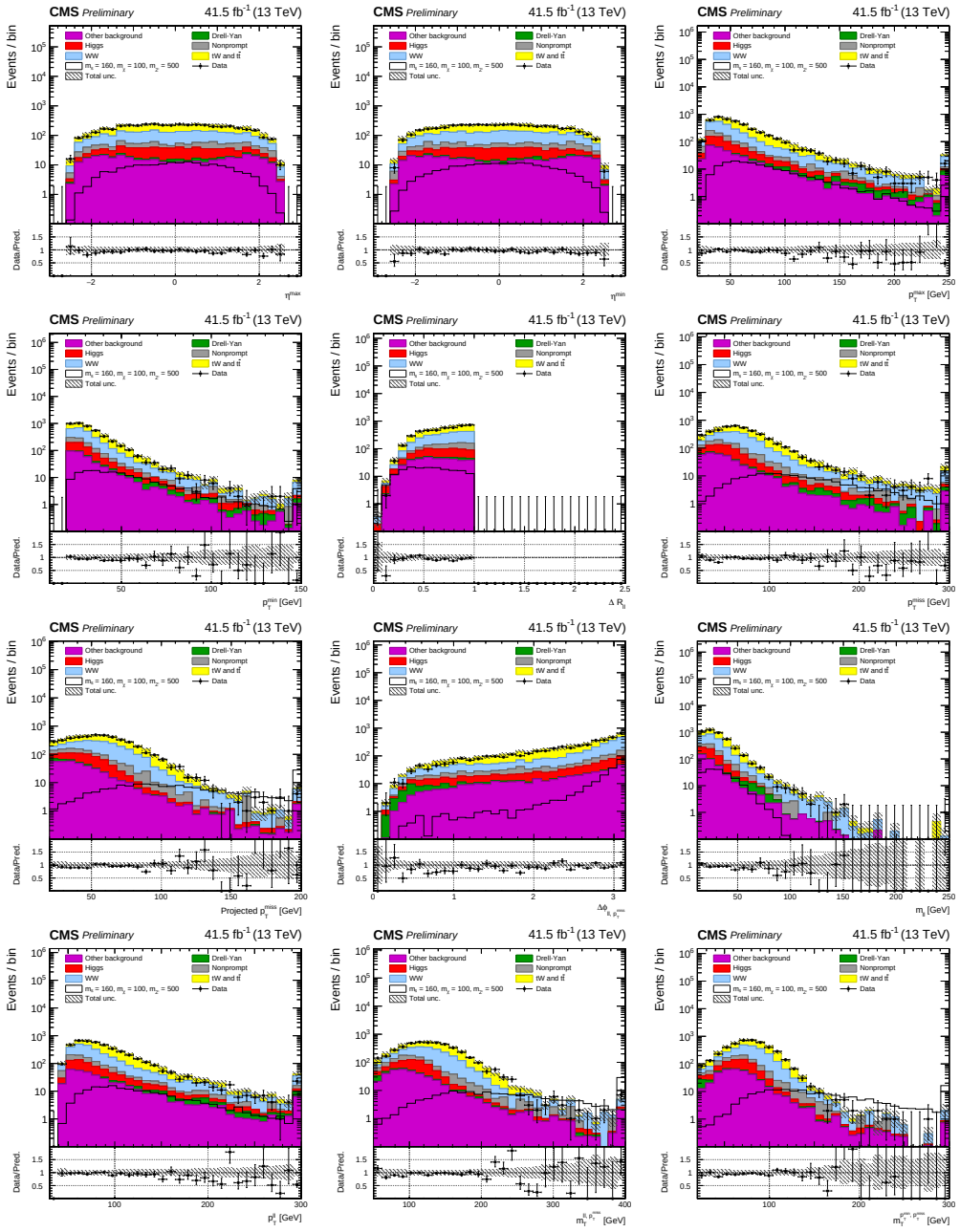

Figure 89: Pre-fit kinematic distributions for 2017 events in SR1. The distributions show the leading (a) and trailing (b) lepton η, the leading (c) and trailing (d) lepton p_T, $\Delta R(\ell,\ell)$ (e), p_T^{miss} (f), mpmet (g), azimuthal angle between the dilepton system and the p_T^{miss} (h), $m_{\ell\ell}$ (i), $p_T^{\ell\ell}$ (j), $m_T^{ll,p_T^{miss}}$ (k), and $m_T^{\ell min,p_T^{miss}}$ (l). The error bars on the data points represent the statistical uncertainty, and the hatched areas represent the combined systematic and statistical uncertainty of the predicted background. Black line corresponds to the signal prediction of $m_s = 160$ GeV, $m_\chi = 100$ GeV, $m_{Z'} = 500$ GeV. The last bin includes the overflow.

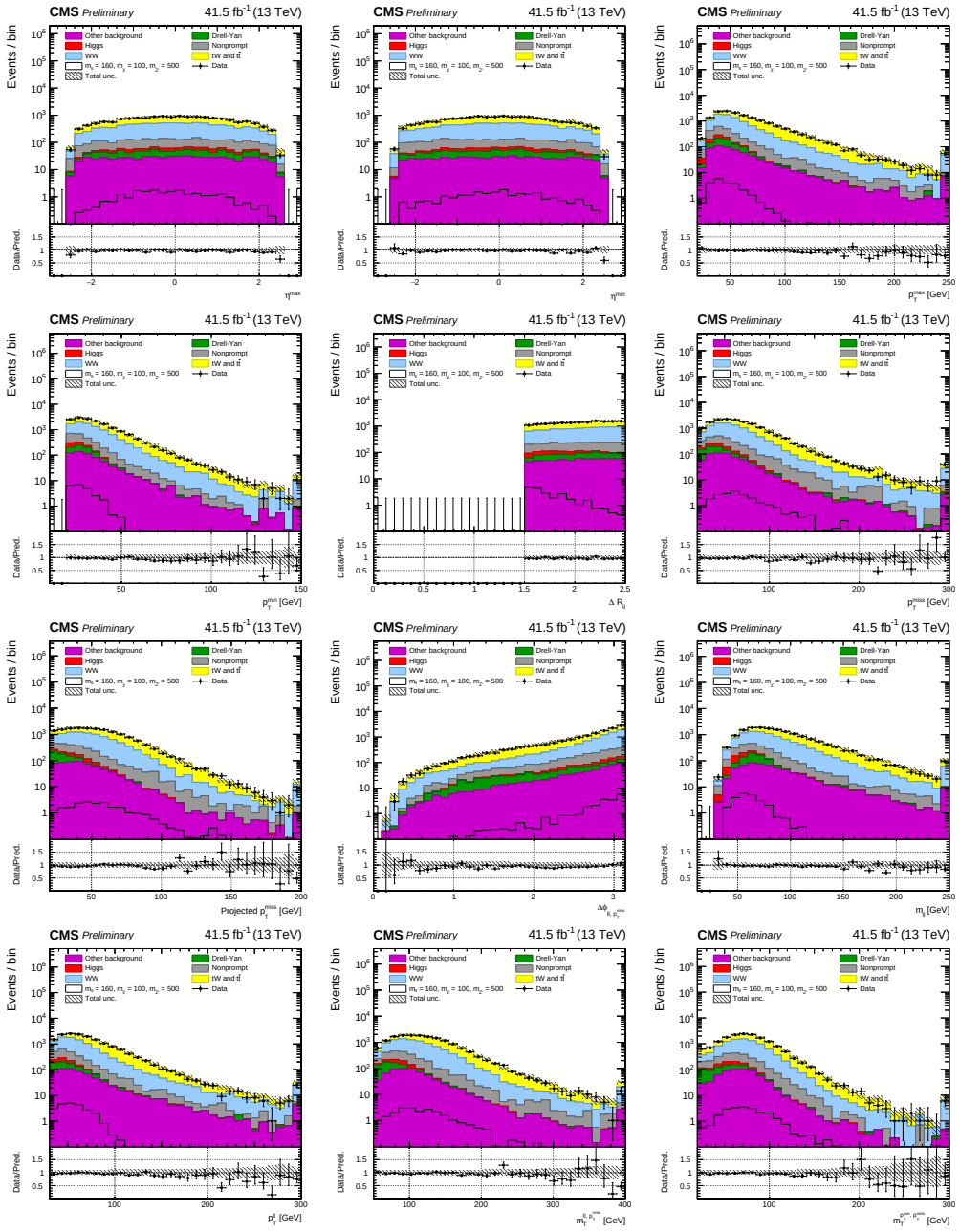

Figure 90: Pre-fit kinematic distributions for 2017 events in SR3. The distributions show the leading (a) and trailing (b) lepton η, the leading (c) and trailing (d) lepton p_T, $\Delta R(\ell,\ell)$ (e), p_T^{miss} (f), mpmet (g), azimuthal angle between the dilepton system and the p_T^{miss} (h), $m_{\ell\ell}$ (i), $p_T^{\ell\ell}$ (j), $m_T^{ll,p_T^{miss}}$ (k), and $m_T^{\ell\,min,p_T^{miss}}$ (l). The error bars on the data points represent the statistical uncertainty, and the hatched areas represent the combined systematic and statistical uncertainty of the predicted background. Black line corresponds to the signal prediction of $m_s = 160$ GeV, $m_\chi = 100$ GeV, $m_{Z'} = 500$ GeV. The last bin includes the overflow.

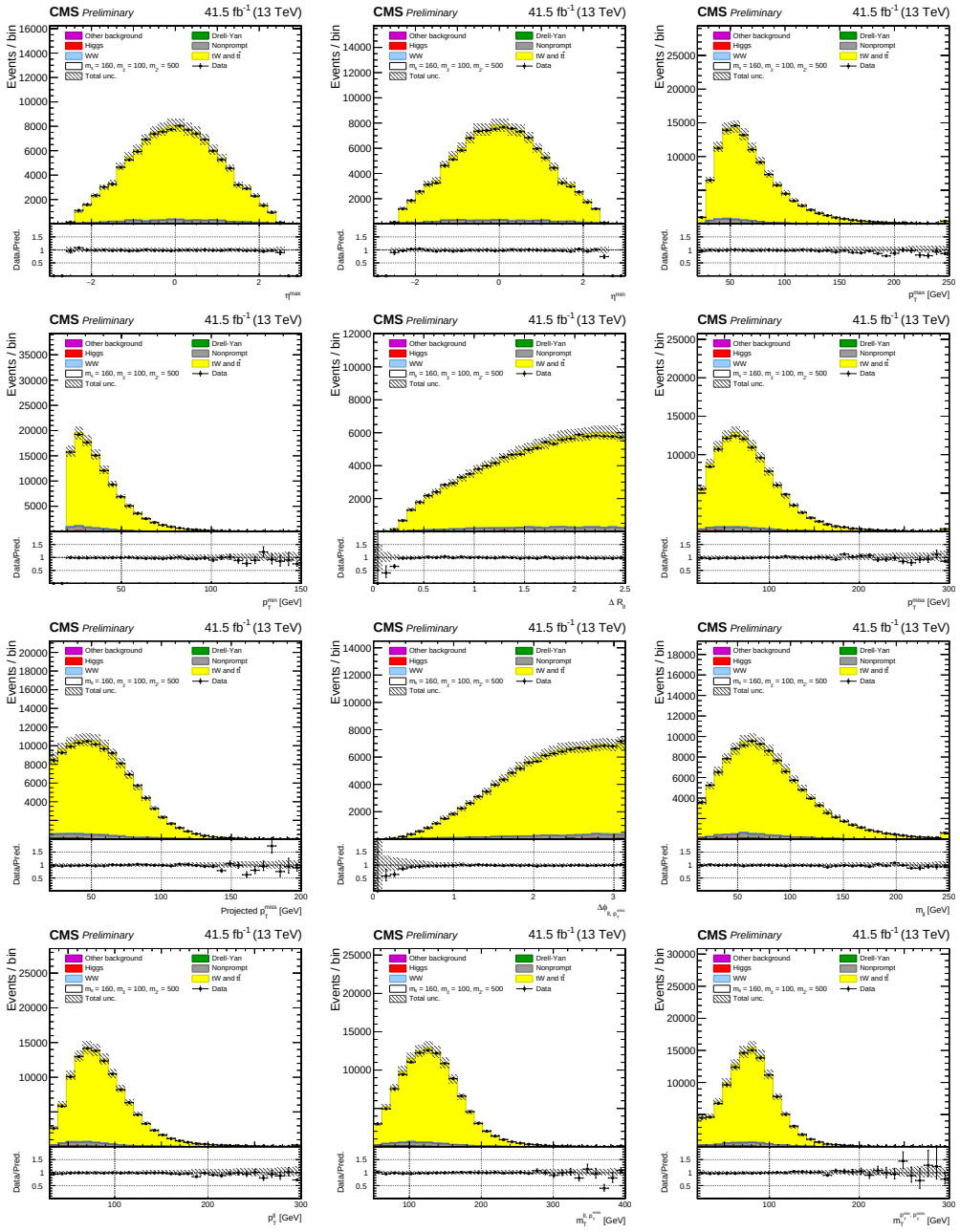

Figure 91: Pre-fit kinematic distributions for 2017 events in Top control region. The distributions show the leading (a) and trailing (b) lepton η, the leading (c) and trailing (d) lepton p_T, $\Delta R(\ell,\ell)$ (e), p_T^{miss} (f), mpmet (g), azimuthal angle between the dilepton system and the p_T^{miss} (h), $m_{\ell\ell}$ (i), $p_T^{\ell\ell}$ (j), $m_T^{ll,p_T^{miss}}$ (k), and $m_T^{\ell\,min,p_T^{miss}}$ (l). The error bars on the data points represent the statistical uncertainty, and the hatched areas represent the combined systematic and statistical uncertainty of the predicted background. Black line corresponds to the signal prediction of $m_s = 160$ GeV, $m_\chi = 100$ GeV, $m_{Z'} = 500$ GeV. The last bin includes the overflow.

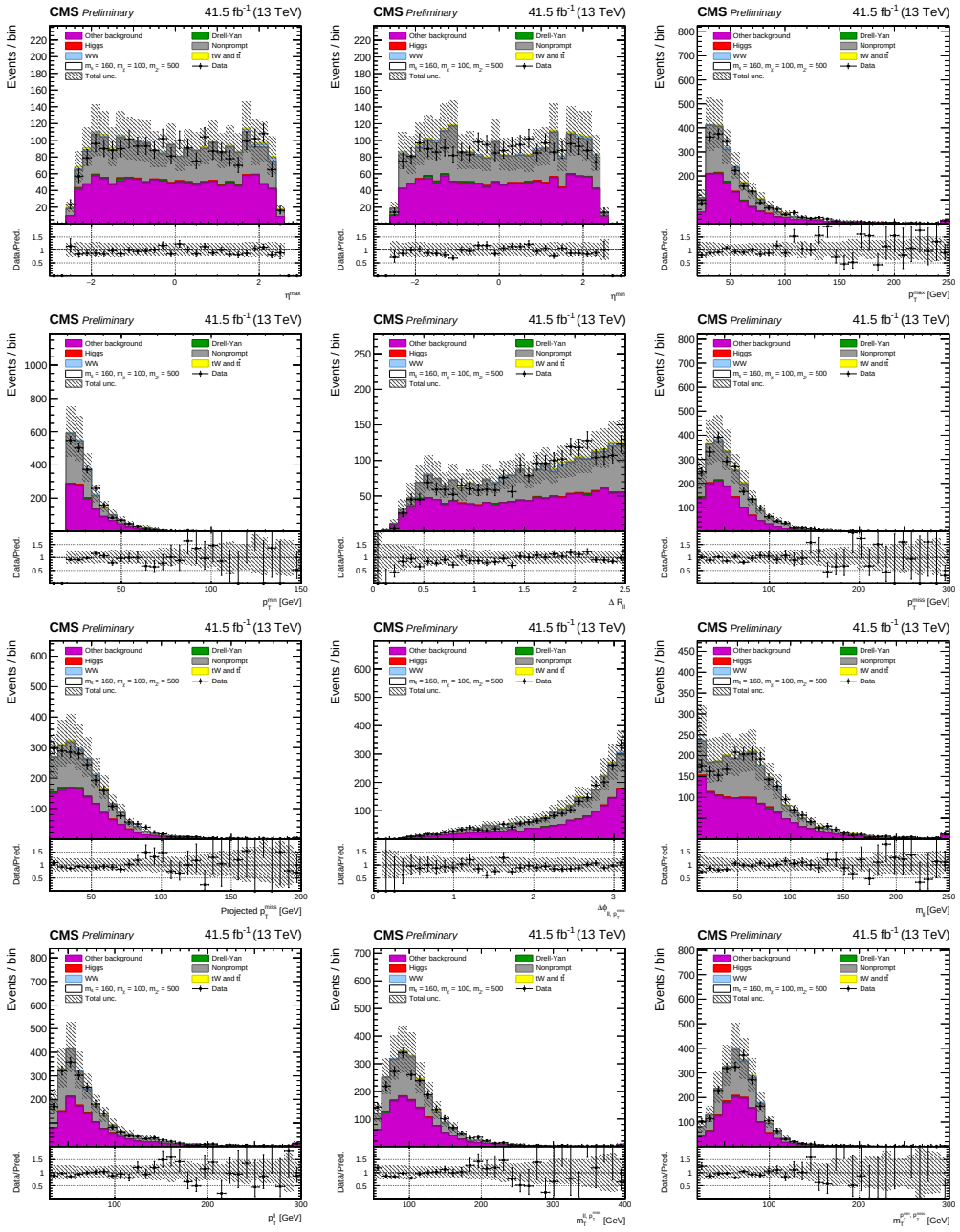

Figure 92: Pre-fit kinematic distributions for 2017 events in non-prompt validation region. The distributions show the leading (a) and trailing (b) lepton η, the leading (c) and trailing (d) lepton p_T, $\Delta R(\ell,\ell)$ (e), p_T^{miss} (f), mpmet (g), azimuthal angle between the dilepton system and the p_T^{miss} (h), $m_{\ell\ell}$ (i), $p_T^{\ell\ell}$ (j), $m_T^{ll,p_T^{miss}}$ (k), and $m_T^{\ell\,min,p_T^{miss}}$ (l). The error bars on the data points represent the statistical uncertainty, and the hatched areas represent the combined systematic and statistical uncertainty of the predicted background. Black line corresponds to the signal prediction of $m_s = 160$ GeV, $m_\chi = 100$ GeV, $m_{Z'} = 500$ GeV. The last bin includes the overflow.

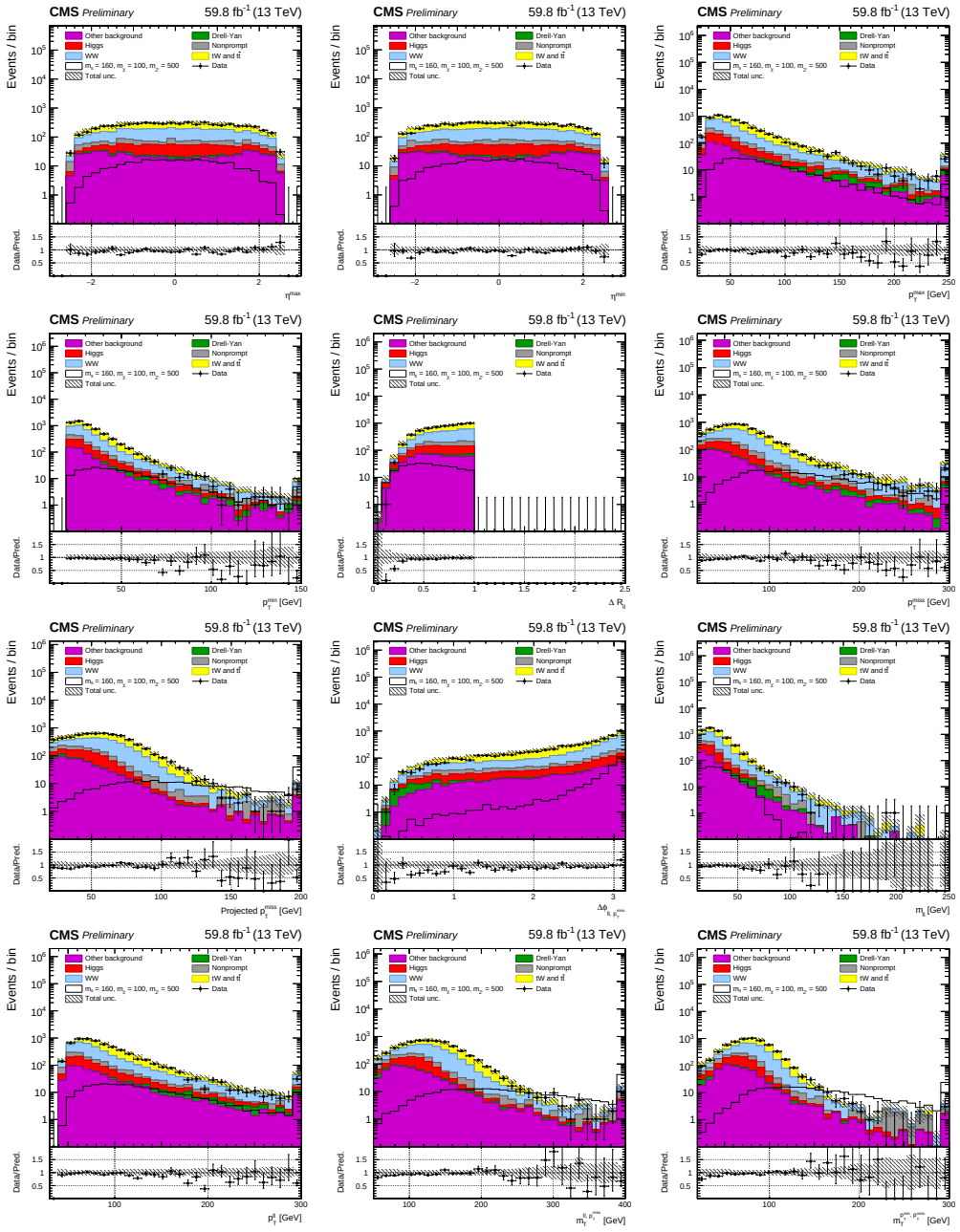

Figure 93: Pre-fit kinematic distributions for 2018 events in SR1. The distributions show the leading (a) and trailing (b) lepton η, the leading (c) and trailing (d) lepton p_T, $\Delta R(\ell,\ell)$ (e), p_T^{miss} (f), mpmet (g), azimuthal angle between the dilepton system and the p_T^{miss} (h), $m_{\ell\ell}$ (i), $p_T^{\ell\ell}$ (j), $m_T^{ll,p_T^{miss}}$ (k), and $m_T^{\ell\,min,p_T^{miss}}$ (l). The error bars on the data points represent the statistical uncertainty, and the hatched areas represent the combined systematic and statistical uncertainty of the predicted background. Black line corresponds to the signal prediction of $m_s = 160$ GeV, $m_\chi = 100$ GeV, $m_{Z'} = 500$ GeV. The last bin includes the overflow.

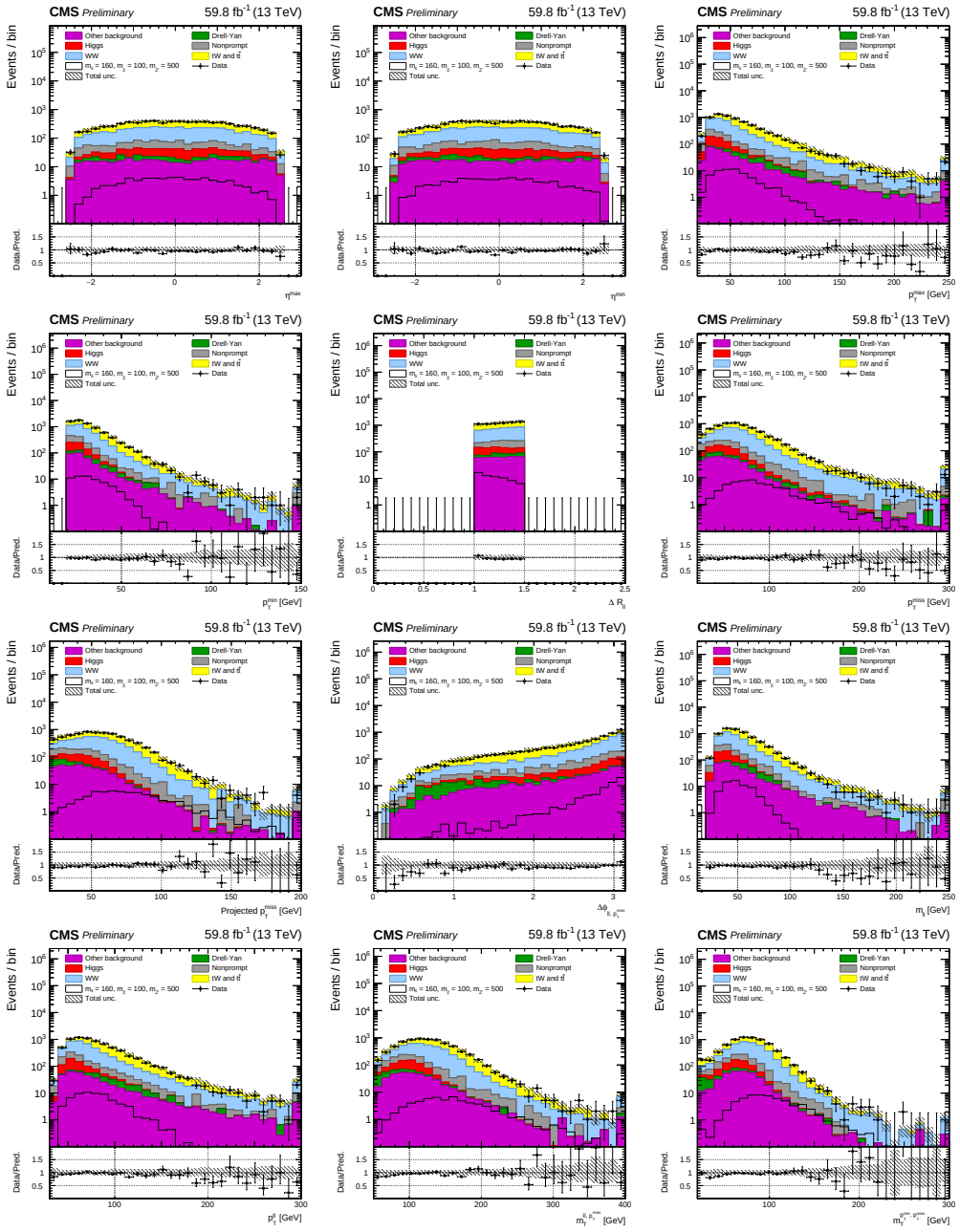

Figure 94: Pre-fit kinematic distributions for 2018 events in SR2. The distributions show the leading (a) and trailing (b) lepton η, the leading (c) and trailing (d) lepton p_T, $\Delta R(\ell,\ell)$ (e), p_T^{miss} (f), mpmet (g), azimuthal angle between the dilepton system and the p_T^{miss} (h), $m_{\ell\ell}$ (i), $p_T^{\ell\ell}$ (j), $m_T^{ll,p_T^{miss}}$ (k), and $m_T^{\ell\,min,p_T^{miss}}$ (l). The error bars on the data points represent the statistical uncertainty, and the hatched areas represent the combined systematic and statistical uncertainty of the predicted background. Black line corresponds to the signal prediction of $m_s = 160$ GeV, $m_\chi = 100$ GeV, $m_{Z'} = 500$ GeV. The last bin includes the overflow.

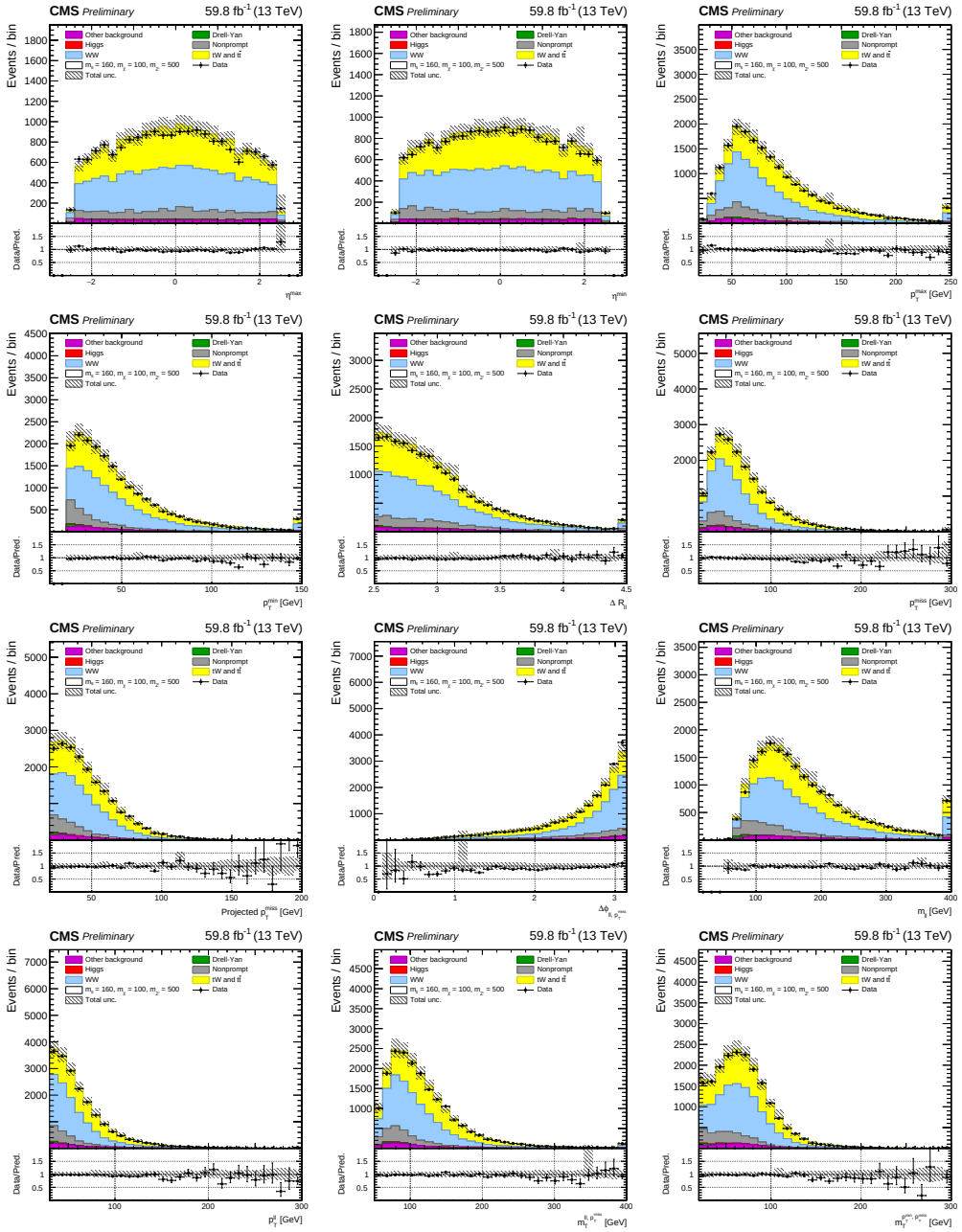

Figure 95: Pre-fit kinematic distributions for 2018 events in W^+W^- control region. The distributions show the leading (a) and trailing (b) lepton η, the leading (c) and trailing (d) lepton p_T, $\Delta R(\ell,\ell)$ (e), p_T^{miss} (f), mpmet (g), azimuthal angle between the dilepton system and the p_T^{miss} (h), $m_{\ell\ell}$ (i), $p_T^{\ell\ell}$ (j), $m_T^{ll,p_T^{miss}}$ (k), and $m_T^{\ell\,min,p_T^{miss}}$ (l). The error bars on the data points represent the statistical uncertainty, and the hatched areas represent the combined systematic and statistical uncertainty of the predicted background. Black line corresponds to the signal prediction of $m_s = 160$ GeV, $m_\chi = 100$ GeV, $m_{Z'} = 500$ GeV. The last bin includes the overflow.

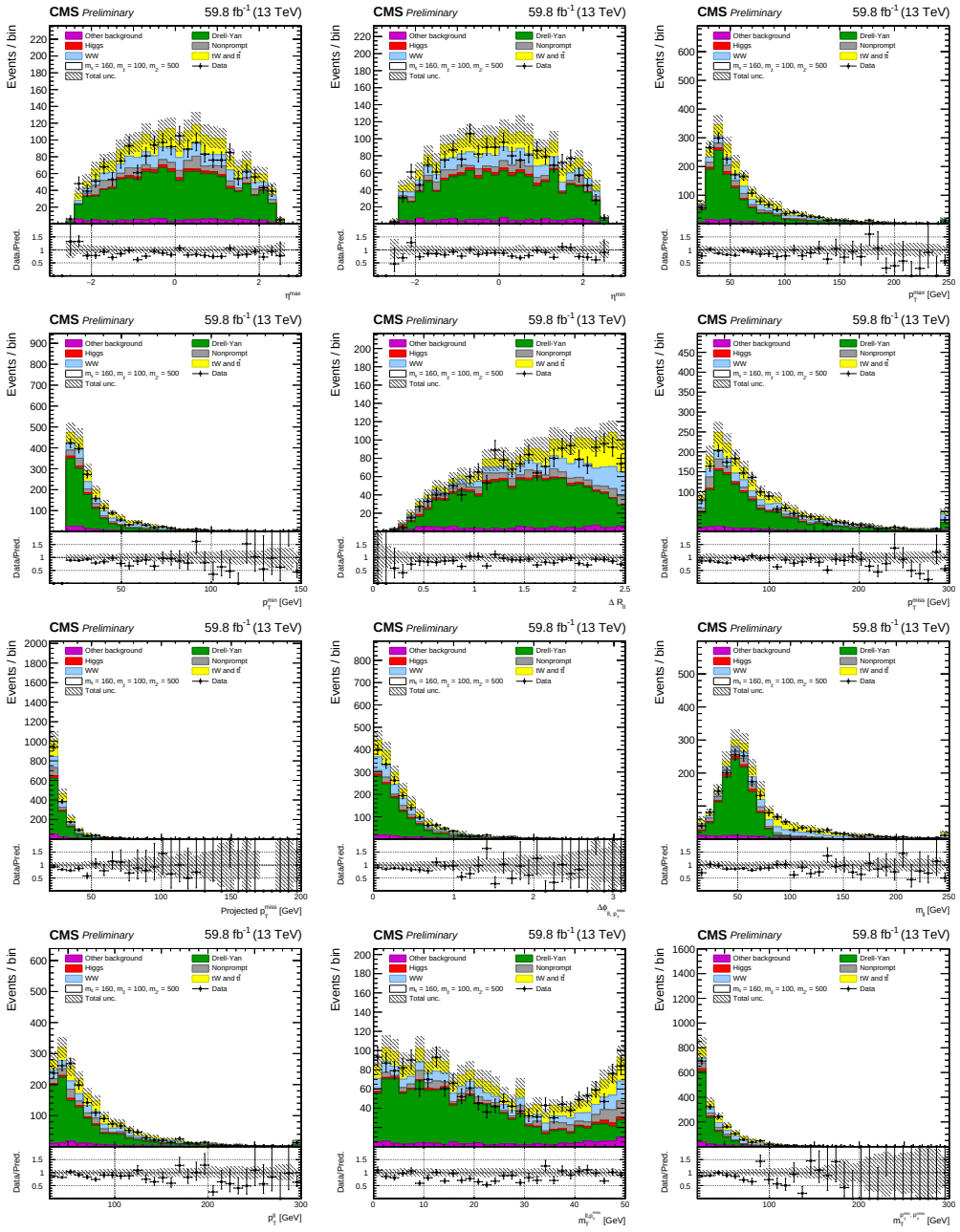

Figure 96: Pre-fit kinematic distributions for 2018 events in DY control region. The distributions show the leading (a) and trailing (b) lepton η, the leading (c) and trailing (d) lepton p_T, $\Delta R(\ell,\ell)$ (e), p_T^{miss} (f), mpmet (g), azimuthal angle between the dilepton system and the p_T^{miss} (h), $m_{\ell\ell}$ (i), $p_T^{\ell\ell}$ (j), $m_T^{ll,p_T^{miss}}$ (k), and $m_T^{\ell\,min,p_T^{miss}}$ (l). The error bars on the data points represent the statistical uncertainty, and the hatched areas represent the combined systematic and statistical uncertainty of the predicted background. Black line corresponds to the signal prediction of $m_s = 160$ GeV, $m_\chi = 100$ GeV, $m_{Z'} = 500$ GeV. The last bin includes the overflow.

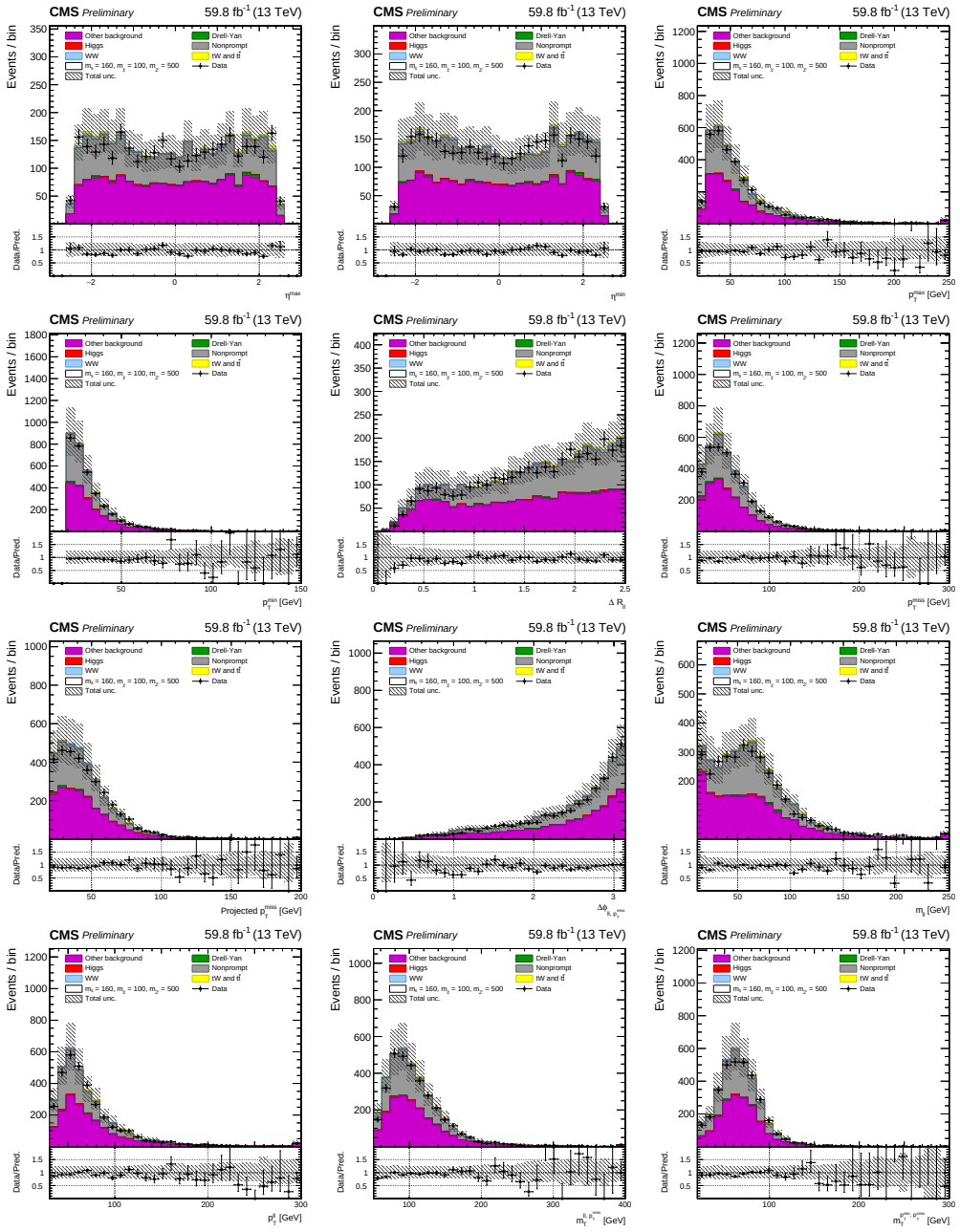

Figure 97: Pre-fit kinematic distributions for 2018 events in non-prompt validation region. The distributions show the leading (a) and trailing (b) lepton η, the leading (c) and trailing (d) lepton p_T, $\Delta R(\ell,\ell)$ (e), p_T^{miss} (f), mpmet (g), azimuthal angle between the dilepton system and the p_T^{miss} (h), $m_{\ell\ell}$ (i), $p_T^{\ell\ell}$ (j), $m_T^{ll,p_T^{miss}}$ (k), and $m_T^{\ell\,min,p_T^{miss}}$ (l). The error bars on the data points represent the statistical uncertainty, and the hatched areas represent the combined systematic and statistical uncertainty of the predicted background. Black line corresponds to the signal prediction of $m_s = 160$ GeV, $m_\chi = 100$ GeV, $m_{Z'} = 500$ GeV. The last bin includes the overflow.

C Resumen (summary in Spanish)

Se presentan medidas de la producción de pares de bosones W^+W^-en colisiones protón-protón a $\sqrt{s} = 13$ TeV. El análisis se basa en datos recopilados con el detector CMS en el LHC en 2016, que se corresponden con una luminosidad integrada de 35.9 fb^{-1}. En el análisis se seleccionan eventos con un par de leptones de distinto sabor y carga opuesta. Por primera vez durante el *Run 2* en CMS, también se incluyen en este análisis los eventos con leptones del mismo sabor.

Las medidas para los canales de diferente sabor y del mismo sabor son σ_{WW}^{DF} =122.0 ± 1.7 (stat) ± 7.2 (exp) ± 2.1 (theo) ± 3.2 (lumi) ± 2.1 (br) pb y σ_{WW}^{SF} = 106.0 ± 2.7 (stat) ± 17.5 (exp) ± 4.4 (theo) ± 4.0 (lumi) ± 1.8 (br) pb respectivamente, donde (stat) hace referencia a la incertidumbre en la sección eficaz debido a un error estadístico en los datos, (exp) a la estimación total de las incertidumbres sistemáticas experimentales, (theo) a la estimación total de las incertidumbres sistemáticas teóricas, (lumi) a la incertidumbre sobre la luminosidad integrada del conjunto de datos CMS de 2016, y (br) a la incertidumbre en la fracción de desintegración leptónica de los bosones W. La sección eficaz de producción combinada es σ_{WW}^{DF+SF} =117.6 ± 1.4 (stat) ± 5.5 (exp) ± 1.9 (theo) ± 3.2 (lumi) ± 2.0 (br) pb = 117.6 ± 6.8 pb. Estos valores medidos son consistentes con la predicción teórica, σ_{WW}^{theo} =118.8 ± 3.6 pb. Además, la medida final mejora la precisión del resultado CMS anterior en aproximadamente un 40%.

También se miden las secciones eficaces fiduciales y diferenciales. La región fiducial se define a nivel de generación requiriendo enventos con dos leptones, electrones o muones, con $p_T > 20$ GeV y $|\eta| < 2.5$, $m_{\ell\ell} > 20$ GeV, $p_T^{\ell\ell} > 30$ GeV y $p_T^{miss} > 20$ GeV, para emular las selecciones de análisis tanto como sea posible. La sección eficaz fiducial medida combinando los canales de diferente sabor y del mismo sabor es σ^{fid} =1.529 ± 0.020 (stat) ± 0.069 (exp) ± 0.028 (theo) ± 0.041 (lumi) pb = 1.529 ± 0.087 pb, que concuerda bien con la predicción teórica σ_{NNLO}^{fid} = 1.531 ± 0.043 pb. Además, se ha medido la sección eficaz fiducial añadiendo la condición de 0-jets a la definición de la región fiducial. Esta se obtiene como función del umbral del momento transverso del jet. Los resultados, mostrados en la Figura 36, están de acuerdo con las predicciones de POWHEG y PYTHIA. Las medidas diferenciales de la sección eficaz como función de $m_{\ell\ell}$, $p_T^{\ell\ max}$, $p_T^{\ell\ min}$, $p_T^{\ell\ell}$, y $\Delta\phi(\ell,\ell)$, que se muestra en la Figura 37, también concuerdan bien con las predicciones de POWHEG y PYTHIA.

Finalmente, se realiza una búsqueda de acoplamientos anómalos que podrían afectar a la producción de W^+W^-en el contexto de una teoría de campo efectiva. Los límites sobre las constantes de acoplamiento se obtienen utilizando la distribución de masa invariante de los dos leptones. En comparación con los resultados anteriores de W^+W^-CMS, los límites obtenidos son entre un factor 2 y 3 más restrictivos. Además, comparando con otros resultados de ATLAS, D0 o LEP,

este análisis proporciona algunos de los límites más restrictivos en los coeficientes estudiados, como se muestra en la Figura 44.

Como una posible extensión del trabajo, las medidas de las secciones eficaces diferenciales y la búsqueda acoplamientos anómalos pueden mejorarse mediante el análisis del conjunto completo de datos del *Run 2*, con el objetivo de exprimir toda la luminosidad disponible en estas medidas que están limitadas por la incertidumbre estadística. Por otro lado, incluir las últimas recomendaciones ara las incertidumbres experimentales sobre el conjunto de datos completo del *Run 2* también podría ayudar a mejorar la precisión de los resultados. Por otro lado, una categorización más fina de los eventos dependiendo de la carga, del p_T, y del sabor de los leptones, podría permitir restringir aún más las incertidumbres sistemáticas y por tanto mejorar la precisión de las medidas de las secciones eficaces total y fiducial.

Se realiza una búsqueda de partículas de materia oscura producidas en asociación con un bosón de Higgs oscuro. El análisis se basa en datos recopilados por el detector CMS en el LHC durante todo el *Run 2* (2016-2018), correspondiente a una luminosidad integrada de 137 fb^{-1}. Se ha explorado el modo de desintegración del bosón de Higgs oscuro a un par de bosones W^+W^-, para $m_s > 160$ GeV, y la posterior desintegración leptónica de los bosones W a leptones de distinto sabor, siendo la primera medida realizada en el experimento CMS utilizando esta nueva interpretación. Los datos de cada año han sido estudiados y analizados por separado, y los resultados combinados incluyen un tratamiento adecuado de las correlaciones entre las incertidumbres que afectan a los diferentes periodos de datos. Se realiza un ajuste global a los datos observados en los tres periodos de datos para obtener los resultados finales, donde todas las regiones de análisis se ajustan simultáneamente. Las distributiones de $\text{m}_{\ell\ell}$, $\Delta\text{R}(\ell,\ell)$ y $\text{m}_{\text{T}}^{\ell\,\text{min,p}_{\text{T}}^{\text{miss}}}$ en las zonas de señal, que se corresponden con las tres variables cinemáticas que muestran mayor poder para separar la señal de los fondos principales, se usan en el ajuste. No se observan desviaciones significativas de las predicciones del modelo estándar, por tanto, se obtienen límites superiores a un nivel de confianza del 95% en los parámetros del modelo, donde el límite más estricto encontrado se establece para $m_{DM} = 150$ GeV, excluyendo masas de hasta $m_s \approx 300$ GeV para $\approx 480 < m_{Z'} < 1200$ GeV, y hasta $m_{Z'} \approx 2000$ GeV para $m_s = 160$ GeV.

Para ampliar el espacio de fases sensible, se está realizando un análisis adicional en CMS que explora la desintegración semileptónica del par W^+W^-, con el objetivo de combinar los resultados de ambos canales en una misma publicación. Por otro lado, el aumento esperado de la luminosidad durante el próximo *LHC Run 3* también permitirá acceder a una parte más amplia del espacio de fases $m_s - m_{Z'} - m_\chi$. Además, también sería posible extender la búsqueda al plano de los acoplamientos (g_q y g_χ) y, como se discutió anteriormente, una categorización

más fina de los eventos también puede mejorar la sensibilidad estadística de la búsqueda.

De cara a la próxima era *LHC Run 3* que comenzará en 2022, se estudian nuevas técnicas con el objetivo de mejorar la asignación de momento transverso a los muones altamente energéticos proporcionada por los algoritmos actuales de la Colaboración CMS. Para ello, se entrena un modelo regresivo a través de una DNN. La DNN toma como entrada el p_T dado por el algoritmo *TuneP*, la información sobre la traza de los muones reconstruida en el tracker, y la información sobre el número y distribución de los segmentos encontrados alrededor de la extrapolación de la traza del tracker a las cámaras de muones. Los resultados preliminares obtenidos muestran una mejora del 25% en la resolución del momento transverso (con respecto al p_T generado) para muones con $1500 \leq p_T \leq 2500$ GeV y $|\eta| < 0.9$. Este tipo de metodología puede ser útil para la mayoría de las búsquedas de nueva física en el LHC que incluyan muones muy energéticos en su estado final, y se pretende hacer uso de la misma durante el próximo *LHC Run 3*.

List of Tables

List of Figures